FEDERAL UNIVERSITY OF SÃO CARLOS
CENTER OF EXACT SCIENCE AND TECHNOLOGY
POSTGRADUATE PROGRAM IN CIVIL ENGINEERING

VINICIUS MOURA DE OLIVEIRA

EXPERIMENTAL AND NUMERICAL ASSESSMENT OF GLOBAL AND LOCAL STABILITY OF STEEL-UHPC COMPOSITE ALVEOLAR BEAMS UNDER HOGGING BENDING

São Carlos - SP
2025

VINICIUS MOURA DE OLIVEIRA

EXPERIMENTAL AND NUMERICAL ASSESSMENT OF GLOBAL AND LOCAL STABILITY OF STEEL-UHPC COMPOSITE ALVEOLAR BEAMS UNDER HOGGING BENDING

A thesis presented to the Federal University of São Carlos, as a part of the exigencies of the Postgraduate Program in Civil Engineering, in the concentration area of Structures, to obtain the degree of Doctor of Philosophy.

Advisor: Carlos Humberto Martins

Co-advisor: Alexandre Rossi

São Carlos - SP
2025

UNIVERSIDADE FEDERAL DE SÃO CARLOS

Centro de Ciências Exatas e de Tecnologia
Programa de Pós-Graduação em Engenharia Civil

Folha de Aprovação

Defesa de Tese de Doutorado do candidato Vinícius Moura de Oliveira, realizada em 25/04/2025.

Comissão Julgadora:

Documento assinado digitalmente
gov.br **CARLOS HUMBERTO MARTINS**
Data: 25/04/2025 14:05:27-0300
Verifique em https://validar.iti.gov.br

Prof. Dr. Carlos Humberto Martins (UFSCar)

Documento assinado digitalmente
gov.br **EMERSON ALEXANDRO BOLANDIM**
Data: 28/04/2025 08:22:19-0300
Verifique em https://validar.iti.gov.br

Prof. Dr. Emerson Alexandro Bolandim (UNESP)

Prof. Dr. Luciano Rodrigues Ornelas de Lima (UERJ)

Documento assinado digitalmente
gov.br **LUCIANO RODRIGUES ORNELAS DE LIMA**
Data: 25/04/2025 14:32:36-0300
Verifique em https://validar.iti.gov.br

Documento assinado digitalmente
gov.br **RENATO SILVA NICOLETTI**
Data: 25/04/2025 15:57:59-0300
Verifique em https://validar.iti.gov.br

Prof. Dr. Renato Silva Nicoletti (USP)

Prof. Dr. Gustavo de Miranda Saleme Gidrão (UTFPR)

Documento assinado digitalmente
gov.br **GUSTAVO DE MIRANDA SALEME GIDRAO**
Data: 28/04/2025 10:57:55-0300
Verifique em https://validar.iti.gov.br

O Relatório de Defesa assinado pelos membros da Comissão Julgadora encontra-se arquivado junto ao Programa de Pós-Graduação em Engenharia Civil.

To my daughter, Maria Clara,
who made me a better man

ACKNOWLEDGEMENTS

First and foremost, I thank God for giving me strength and support on this journey. I am also grateful to my Lord for blessing me with my daughter, born during this period. May God be praised.

Heloísa, my love, I thank you for all that you do for our family, for all your care for our daughter, for choosing me as your life partner, and for making me a complete man. It is impossible to bring words to all my gratitude for having you in my life. Maria Clara, my angel, today you are only two years old, but I hope you read these words in the future and know that your father loves you more than everything in this life. You brought with you my best version, making me a better man.

I always thank my parents for shaping the person I am today. You are the main reason for this achievement. Thank you very much for constantly pushing me to reach my objectives. I am also very grateful to Janaína, Ademilson, and Heitor for being my family in Maringá. All your support was essential for this achievement.

Special thanks to my advisor, Professor Carlos Humberto Martins, and my co-advisor, Professor Alexandre Rossi, for their support and friendship. You always believed in me from the beginning, and I developed as a researcher with your collaboration. I also thank Professors Pablo Krahl, Daniel Cardoso, and Flávio de Andrade for collaborating on this research. Thanks so much to my research partners, Vinicius Brother and André Benedito, for their hard work and support during the tests and analyses. Together, we have been doing great work. Thanks to all the students and lab technicians from PUC-Rio for all the support in the tests. I am grateful to all my research group, Lucas, Douglas, Adriano, Gustavo, Jonas, Haron, and Igor.

Thanks to CAPES and CNPq for the scholarship and research funding, to PPGECiv and all its professors, and to the Department of Civil Engineering from UEM, especially my friend Juarez.

Finally, I want to thank everyone who contributed to my development and stayed by my side during this period, especially my friends Renan, Milena, Hadrian, and Valentin.

ABSTRACT

Continuous steel-concrete composite beams provide bending moment redistribution, slight deflection, the capability to cover longer spans, and cost-effectiveness. Employing steel alveolar I-sections, High-Strength Steel (HSS), and Ultra-High-Performance Concrete (UHPC) slabs in these composite beams can significantly dematerialize the structure. To the best of authors' knowledge, no studies have addressed the adoption of high-performance materials for composite alveolar beams. At the same time, composite alveolar beams under hogging bending with shear forces can reach local and global instability or the interaction between the modes, such as Lateral-Distortional Buckling (LDB) and Web-Post Buckling (WPB), requiring further investigation. The present study aimed to investigate the occurrence of LDB and WPB in composite alveolar beams, considering HSS I-sections and UHPC. For these objectives, both experimental and numerical analyses were conducted. Three-point bending tests were carried out in steel-UHPC composite castellated beams with I-sections of microalloyed steels with Niobium addition. The experimental results were used to validate the numerical model, and numerical parametric studies were also conducted. The specimens reached failure by WPB coupled with the Vierendeel mechanism (VM). This way, the length of the web openings' hexagon horizontal edge (tee length) influenced the bearing capacity of the castellated beam, in which the specimen with a higher tee length had a lower ultimate load, which was also observed in the numerical parametric study. In addition, the numerical models with the shortest web-post width were more critical for the WPB occurrence. The parametric study models also reached failure by LDB coupled with WPB, showing an elevated influence of the I-section steel yield strength, and composite castellated beams with UHPC slabs showed higher initial bending stiffness and ultimate loads than those with Normal Concrete (NC) slabs. Given this, some possibilities to dematerialize conventional composite beams under hogging bending by using HSS castellated I-sections and slabs of UHPC were verified. The dematerialization rate considered in the analysis regards the ratio between the volume of material consumption of the conventional element and the dematerialized element. Even when instability modes occur in the I-section, an I-section dematerialization rate of up to 55% can be reached using HSS castellated I-sections. In addition, only adopting the castellated I-sections, without changing the steel yield strength, can present an I-section dematerialization rate of up to 17.9%. The slab concrete can reach the dematerialization rate of 33.3% by utilizing UHPC instead of NC. Finally, the updates in ABNT NBR 8800:2024 presented a more accurate LDB resistance prediction than the previous version (ABNT NBR 8800:2008). In most cases, European codes (EC4/EC3) provided conservative LDB and WPB resistance prediction.

Keywords: Steel-concrete composite alveolar beams; Lateral-Distortional Buckling; Web-Post Buckling; High-strength steel; Ultra-high-performance concrete.

RESUMO

Vigas mistas aço-concreto contínuas fornecem redistribuição de momento de flexão, menor deflexão e capacidade de cobrir vãos maiores. Utilizar seções I alveolares de aço, Aço de Alta Resistência (AAR) e lajes de Concreto de Ultra Alto Desempenho (UHPC) nessas vigas compostas pode desmaterializar significativamente a estrutura. Até onde os autores sabem, faltam estudos com o uso de materiais de alto desempenho para vigas alveolares compostas. Ao mesmo tempo, estas vigas sob flexão simples negativa podem atingir instabilidade local e global ou a interação entre os modos, como Flambagem Lateral com Distorção (FLD) e Flambagem do Montante da Alma (FMA), necessitando de mais atenção. Este estudo tem como objetivo investigar a ocorrência da FLD e FMA em vigas alveolares mistas, considerando seções I de AAR e lajes de UHPC. Para isso, análises experimentais e numéricas são realizadas. Ensaios de flexão três pontos são realizados em vigas casteladas mistas aço-UHPC com seções I de aços microligados com adição de Nióbio. Os resultados experimentais são usados para validar o modelo numérico, e estudos paramétricos numéricos também são conduzidos. Os espécimes atingiram a falha por FMA acoplado ao mecanismo de Vierendeel (VM). Dessa forma, o comprimento do "tê" influenciou a capacidade dessas vigas, e aquela com maior comprimento do "tê" teve menor capacidade última, o que também foi observado no estudo paramétrico numérico. Além disso, os modelos com menor largura de montante da alma foram mais críticos para a ocorrência da FMA. No estudo paramétrico também foi observado modos de falha por FLD acoplado à FMA, mostrando uma influência elevada da resistência ao escoamento do aço da seção-I, e vigas casteladas mistas com lajes de UHPC tiveram maior rigidez inicial à flexão e cargas finais do que aquelas com lajes de Concreto Normal (CN). Diante disso, algumas possibilidades para desmaterializar vigas mistas convencionais sob flexão negativa usando seções I casteladas de AAR e lajes de UHPC são verificadas. A taxa de desmaterialização considerada na análise diz respeito à razão entre o volume de consumo de material do elemento convencional e do elemento desmaterializado. Mesmo quando ocorre instabilidade na seção-I, uma taxa de desmaterialização da seção-I de até 55% pode ser alcançada usando seções I casteladas de AAR. Além disso, adotando apenas as seções I casteladas, sem alterar a resistência ao escoamento do aço, pode-se apresentar uma taxa de desmaterialização da seção-I de até 17,9%. O concreto da laje pode atingir a taxa de desmaterialização de 33,3% utilizando UHPC em vez de CN. As atualizações na ABNT NBR 8800:2024 apresentaram uma previsão mais precisa da capacidade à FLD do que a versão anterior (ABNT NBR 8800:2008), e as normas europeias (EC4/EC3) forneceram previsões conservadoras para a capacidade à FLD e FMA.

Palavras-chave: Vigas alveolares mistas aço-concreto; Flambagem lateral com distorção; Flambagem do montante da alma; Aço de alta resistência; Concreto de ultra alto desempenho.

SUMMARY

CHAPTER 1

INTRODUCTION

This chapter provides a concise overview of the research topic's defining concepts, justifications, objectives, methodology employed in the work, thesis scope, and organization.

1.1 PROBLEM STATEMENT

Steel alveolar beams have many advantages, such as increasing the I-section depth without additional weight, high stiffness-to-weight ratio, easier access and services via the web openings, and visually appealing architecture (NAWAR; ARAFA; ELHOSSEINY, 2020). Various types of steel alveolar beams can be manufactured via longitudinal cutting and welding of the web. This process results in the cross-section height expansion without increasing material consumption and a steel beam with sequential web openings. Castellated and cellular beams are the most common, having hexagonal and circular sequential web openings, respectively. **Figure 1.1** illustrates the geometric parameters of castellated and cellular beams, in which the expanded height of the I-section is determined according to the expansion factor (d_g/d). The parameters in **Figure 1.1** are: b_f= flange width; b_w= web-post width and tee length of the castellated I-section; b_{we}= end-post width; D_0= opening depth or diameter; d= parent section depth; d_g= alveolar beam depth; p= length between the opening diameter centers; s= length of the hexagonal opening diagonal edge; t_f= flange thickness; t_w= web thickness.

For the castellated I-sections, the most common traces of hexagonal openings are the Litzka, Peiner and Anglo-Saxon patterns, as presented in **Figure 1.2** (MIRANDA *et al*., 2023; SILVEIRA, 2011; VIEIRA, 2015).

In recent years, the utilization of steel alveolar beams has been increasingly requested by architects and designers (HECHLER; MÜLLER; SEDLACEK, 2006). Moreover, the use of steel-concrete composite alveolar beams has also increased. Conventional composite beams consist of steel I-sections fixed by shear connectors in the top flange to a concrete or composite slab. Therefore, the bending resistance and the flexural stiffness of these beams are significantly higher than those with only the steel I-sections (CHUNG; LAWSON, 2001).

Structures requiring longer spans may benefit from the adoption of continuous steel-concrete composite cellular beams (JOHNSON, 2004; LAWSON *et al.*, 2006; LAWSON; SAVERIRAJAN, 2011). Steel cellular beams have been used in composite floor systems to create long-span beams (SHEEHAN *et al.*, 2016). However, continuous steel-concrete composite alveolar beams may experience Lateral-Distortional Buckling (LDB) in the hogging moment regions near the supports (GIZEJOWSKI; SALAH, 2008), which is not a concern for simply supported beams that are only subjected to sagging moment (HOSSEINPOUR *et al.*, 2022). The increase in the composite alveolar beam resistance over non-composite beams is more evident in long spans (BENINCÁ; MORSCH, 2020). **Figure 1.3** shows examples of composite castellated and cellular beams with steel deck slab, respectively.

Figure 1.1: Geometric parameters of alveolar beams.

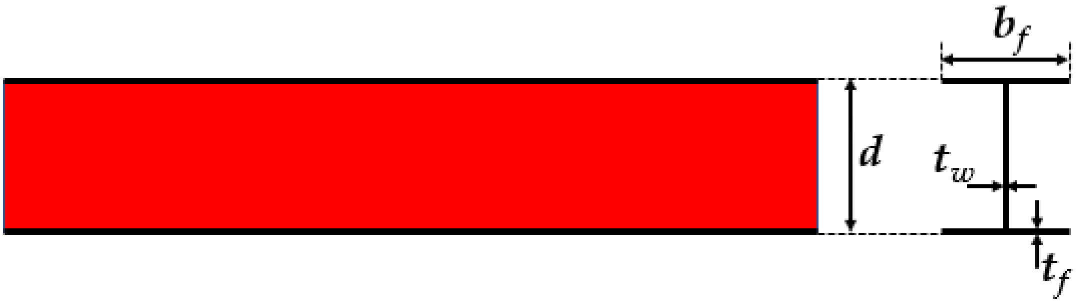

(a) Parent section

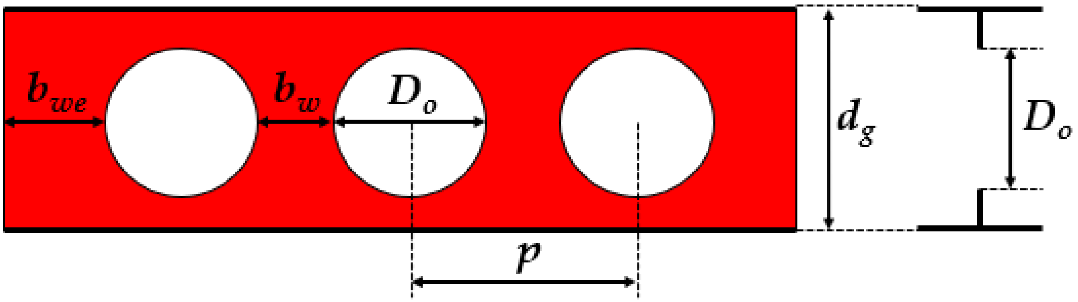

(b) Cellular section

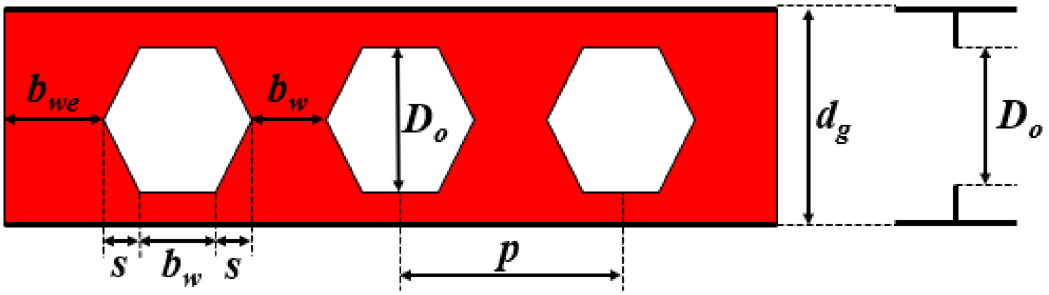

(c) Castellated section

Source: The author (2023).

Figure 1.2: Steel castellated I-section patterns.

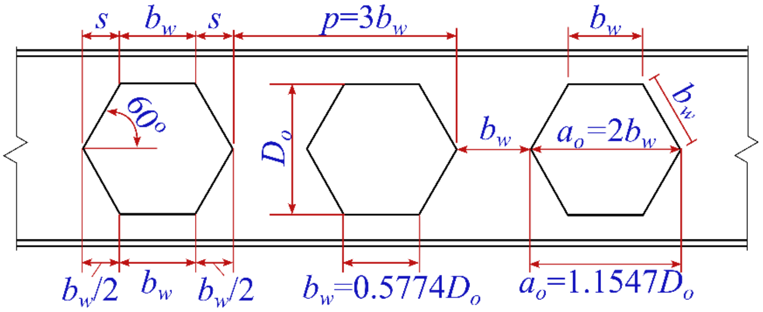

(a) Litzka

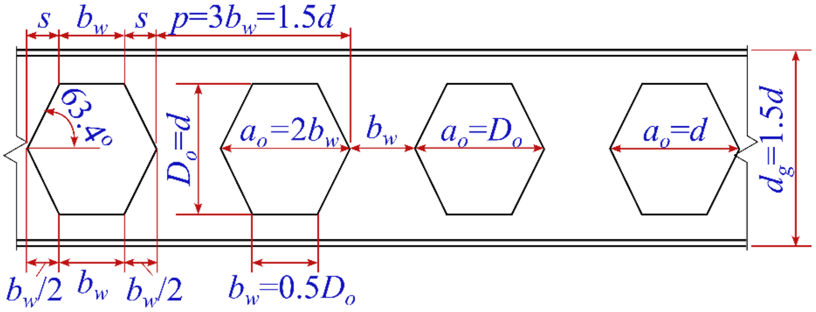

(b) Peiner

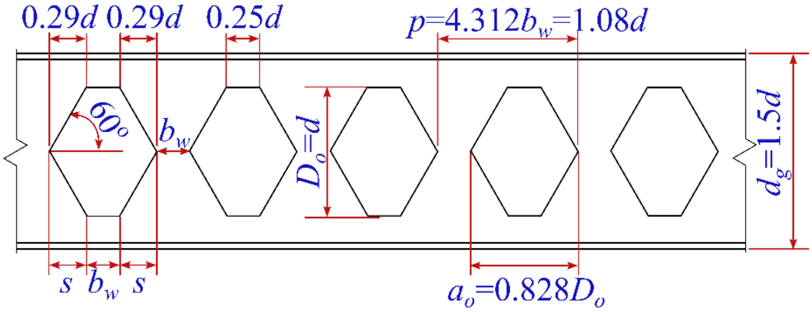

(c) Anglo-Saxon

Source: Adapted from Silveira (2011), Vieira (2015) and Miranda *et al*. (2023).

Figure 1.3: Applications of composite alveolar beams.

(a) With castellated section (b) With cellular section

Source: https://www.c-beams.com/.

Steel-concrete composite alveolar beams are subjected to hogging bending in regions near the supports of continuous and semi-continuous structural systems and along the span of cantilever elements. In these cases, global and local instability modes or their coupling may be reached (GENG *et al*., 2023; GIZEJOWSKI; SALAH, 2010a; OLIVEIRA, 2022; OLIVEIRA *et al*., 2022; SALAH, 2009). Regarding global instability, Lateral-Distortional Buckling (LDB) occurs due to the bottom flange, which does not have lateral restrictions, being submitted to compressive stresses. This way, LDB is characterized by the lateral curvature of the compressed flange with web distortion (**Figure 1.4a**) (ROSSI *et al*., 2020a). A local instability mode that may happen is the Web-Post Buckling (WPB), which results from intense shear force, presenting lateral displacements and torsion in the web-post as an "S" shape (**Figure 1.4b**) (FERREIRA; MARTINS; NARDIN, 2020a). In addition, the structures in question may also be susceptible to the formation of plastic mechanisms in the web-post and bottom tee (OLIVEIRA, 2022; OLIVEIRA *et al*., 2022).

Figure 1.4: Instability modes of composite alveolar beams in hogging moment regions.

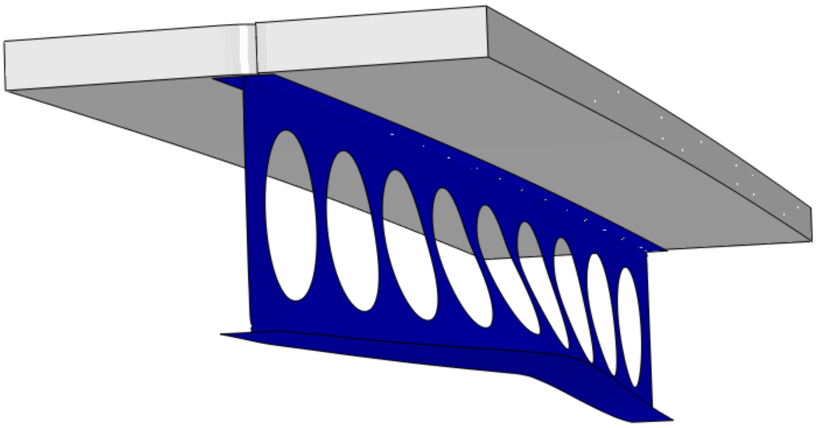

(a) Lateral-distortional buckling

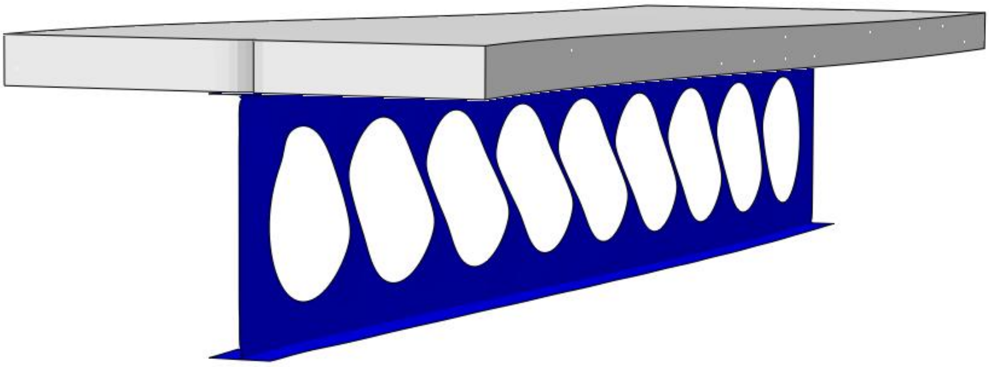

(b) Web-post buckling
Source: The author (2023).

The cracking resistance of the slab is significantly influential on the flexural behavior of continuous and cantilever composite beams, as in hogging moment regions, the concrete slab is under tensile stress. Therefore, the adoption of Ultra-High-Performance Concrete (UHPC) enhances the flexural capacity and cracking propagations of these beams (ZHAO *et al.*, 2023). Regarding the High-Strength Steel (HSS) I-sections (yield strength above 460MPa), these elements can have a reduction of their dimensions concerning normal strength steel, as the width and thickness of the plates. When both the I-section and concrete slab are made of high-performance materials, the composite beam can present an elevated dematerialization, decreasing the self-weight of the structure. However, the instability can limit the gain of bearing capacity even when using HSS, mainly if the composite alveolar beam reaches failure in the elastic regime (GÜNTHER, 2005). As Young's modulus is equal for normal and high-strength steel, the influence of the yield strength steel is only observed if the steel I-beams reach the ultimate load in the inelastic regime (VAROL; CASHELL, 2017). Finally, studies showed that with the increase of Niobium (Nb) content in microalloyed steels, the hardness, yield strength, and tensile strength are increased (KHAPLE *et al.*, 2020; BENEDITO *et al.*, 2024). In contrast, the elongation is decreased with the increase in Nb content, which is typical for HSS (BAN; SHI, 2018; KHAPLE *et al.*, 2020).

At the moment, considering high-performance materials, there are still no experimental or numerical investigations of the global and local stability behavior of composite alveolar beams in hogging moment regions. Therefore, this study aims to assess the LDB and WPB occurrence in these beams in the search for a way to characterize their structural behavior. Finally, some possibilities are verified to reduce the steel and concrete consumption of continuous conventional composite beams by adopting high-performance materials and alveolar I-sections.

Given the exposure, the question addressed in the present thesis is: "*Is it possible to reach elevated dematerialization rates in continuous conventional composite beams by using HSS alveolar I-sections and slabs of UHPC, even when instability occurs, while maintaining initial bending stiffness and ultimate loads?*".

1.2 JUSTIFICATION

High-performance materials go hand in hand with the dematerialization of structures. This way, HSS-UHPC composite beams can significantly reduce their weight-to-span ratio.

HSS offers numerous benefits compared to normal-strength steel, making it an interesting choice in contemporary building construction. Mainly, when the design is governed by strength rather than stiffness, it enables lighter and more efficient design options (WANG; BRADFORD; LIU, 2020). Additionally, since HSS requires less material, it helps reduce emissions and waste during production. Regarding UHPC, slab cracking is considerably enhanced in hogging moment regions of continuous composite beams, which justifies its adoption in the present study.

Continuous and cantilever composite alveolar beams can reach global and local instability modes in hogging moment regions, then LDB and WPB are addressed in this study. Standard procedures such as European (EN 1994-1-1: 2004 / prEN 1994-1-1), American (AISC 360-22 / AASHTO 2017), Australian (AS4100:2020 / AS/NZS2327-2017), and Brazilian codes (ABNT NBR 8800:2024) do not consider the LDB resistance prediction of steel-concrete composite alveolar beams, contemplating only beams without web openings. This way, the present study describes some adaptation approaches to these standard methodologies. There are design recommendations that include the resistance prediction of composite alveolar beams, such as SCI P355 (LAWSON; HICKS, 2011) and Steel Design Guide 31 (FARES; COULSON; DINEHART, 2016). However, these guides only address the WPB assessment, not including the LDB verification. Another area for improvement of the codes is that some approaches for HSS sections is the same for normal-strength steel, which can be inappropriate for predicting the bearing capacity of HSS elements and needs further investigation. In addition, some standard codes do not address the verification of HSS elements.

The scarcity of research, both in Brazil and globally, on the behavior of steel-concrete composite alveolar beams in hogging moment regions, mainly considering HSS I-sections and UHPC slabs, underscores and validates the need for this study. This lack of information highlights a requirement to address this knowledge gap, enhancing our understanding of these structural components and ensuring their safe usage. Consequently, the aim of this research is to tackle this issue, contributing to the advancement of the Brazilian civil construction sector.

1.3 OBJECTIVES

The general objective of the present study is to assess the dematerialization, with high-performance materials and alveolar I-sections, of conventional steel-concrete composite beams under hogging bending and to analyze the instability phenomenon in these structures. Based on this general objective, the following specific objectives are defined:

1) Conduct a thorough bibliographic analysis, identifying key areas that need more research on the subject and examining the trends in current analytical and standard processes;
2) Develop a Finite Element Model (FEM) using the ABAQUS program, searching for representing the local and global stability behavior of the analyzed beams with advanced numerical analysis. Therefore, the physical and geometrical nonlinearities and the structural imperfections are regarded;
3) Perform three-point hogging bending tests in steel-UHPC composite castellated beams with I-sections of ASTM A572 Gr60 steel (microalloyed steel with Niobium addition), focusing on analyzing the influence of opening patterns of these beams on their WPB resistance;
4) Assess via FEM the influence of parameters such as: loading configuration, I-section steel yield strength, cross-section of the steel alveolar profile; unrestrained length under hogging moment; concrete characteristic strength (f_{ck}), cross-section of the concrete slab, longitudinal reinforcement ratio; and the geometric opening parameters of the alveolar I-section.
5) Compare the behavior of conventional composite beams and those with high-performance materials and alveolar I-sections, analyzing the possibilities to reduce the material consumption in these structures and their dematerialization rates.

Consequently, this study aims to enhance comprehension of how steel-concrete composite alveolar beams with conventional and high-performance materials behave in areas affected by hogging moments.

1.4 SUMMARY OF THE METHODOLOGY

This study focuses on the assessment of LDB and WPB occurrence in steel-concrete composite alveolar beams in hogging moment regions. To accomplish this task, experimental and numerical models are used.

The **finite element modeling** is developed via ABAQUS software. These models enable the conduct of parametric studies, crucial for broadening and intensifying the analysis by considering changes in the geometry of the components of the composite beam. The numerical models serve a dual purpose in this research: initially, it assists in preliminary analyses to establish the geometric parameters for experimental testing, and later, it facilitates the execution of the parametric study. To verify the accuracy of these numerical models, they are validated against existing experimental results found in the literature. Thus, the role of numerical modeling in this study includes:

1) Definition of geometric parameters of the elements that compose the specimens of the experimental tests;
2) Previous verification of the numerical model with experimental results found in the literature;
3) Predicting the resistant capacity and failure modes of the specimens;
4) Validation of the numerical model with the results of experimental tests performed in this study;
5) Developments of parametric studies.

The **experimental program** is used as a methodology to investigate the WPB behavior of steel-UHPC composite castellated beams under the action of hogging bending (shear force and hogging moment), which is used in the numerical model validation, allowing greater reliability in all parametric studies. The experimental tests to be studied are composed of castellated I-sections of ASTM A572 Gr60 steel (415 MPa of yield stress), headed studs of 470 MPa steel, precast UHPC slabs (150 MPa of compressive characteristic strength), longitudinal reinforcement bars of GG70 steel (700 MPa of yield limit). The castellated I-sections are of Peiner and Anglo-Saxon Patterns. The connection between the UHPC slab and the steel castellated section is made by 19x60mm headed studs. Physical experimentation is planned on two specimens under a three-point bending test, in which the composite beam is inverted (slab on the supports and loading in the I-section. The variable to be studied are the opening pattern of the castellated I-section (Peiner and Anglo-Saxon).

After the development of the experimental tests, the so-called final numerical model is measured. An extensive parametric investigation is developed with the conformity between the experimental results and the final numerical model. In total, 360 models were assessed focusing in linear buckling analysis and 179 via geometrically and materially nonlinear analyses with imperfections. The parametric investigation determines the influence of many parameters on the LDB bearing capacity and WPB resistance of steel-concrete composite alveolar beams with conventional and high-performance materials (HSS and UHPC).

In the development of the parametric studies with the preliminary and final numerical models, the following variables are investigated:

- Type of alveolar I-beam, being cellular and castellated beams;

- Expansion factor (d_g/d) of the alveolar profiles;
- Opening parameters of cellular beams (opening diameter and web-post width);
- Opening patterns of castellated profiles (Litzka, Peiner and Anglo-Saxon);
- I-section dimensions (depth, flanges width and thickness and web thickness);
- Unrestrained length under hogging moment;
- Height of the concrete slab;
- The influence of high-performance materials (UHPC slabs and HSS I-sections);
- Loading configuration.

Figure 1.5 presents the flowchart of the described methodology to summarize the sequence of all performed tasks.

Figure 1.5: Flowchart of the methodology.

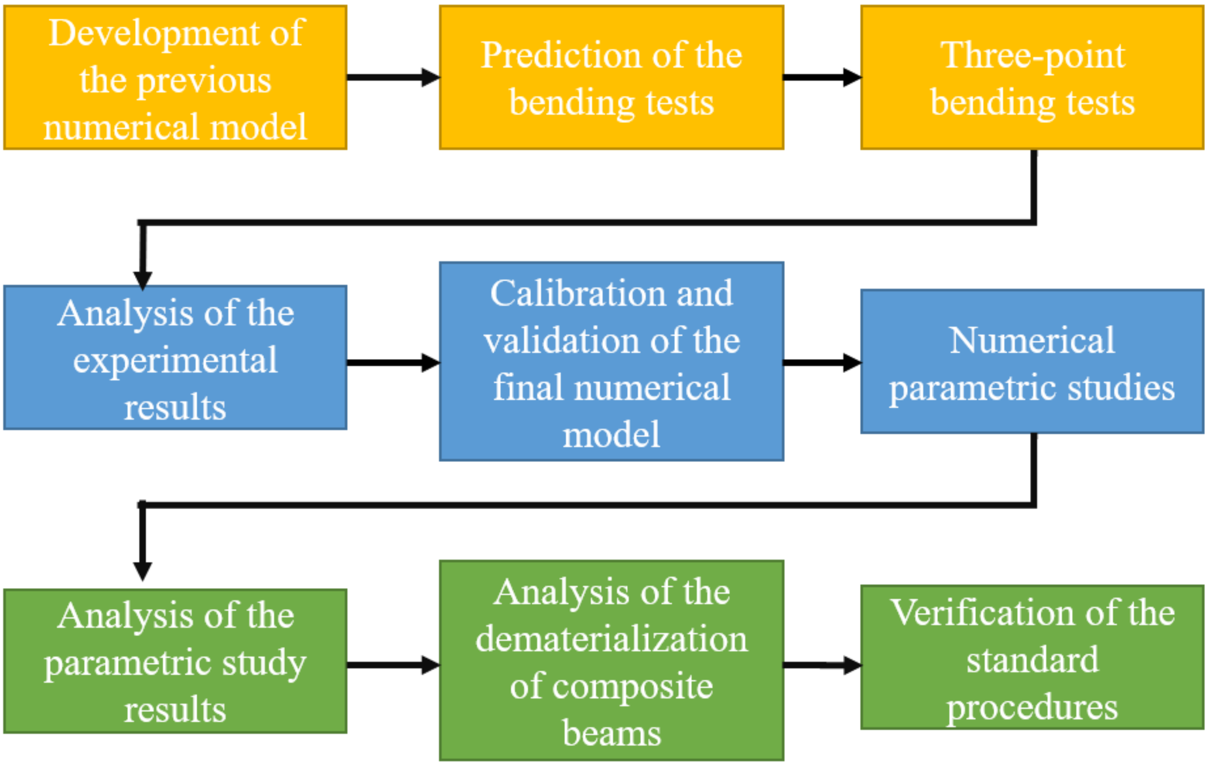

Source: The author (2023).

1.5 THESIS SCOPE AND ORGANIZATION

This thesis is a continuity of the master's dissertation of the present author, which numerically analyzed the stability behavior of steel-concrete composite cellular beams with conventional materials in hogging moment regions (OLIVEIRA, 2022). Both studies are part of those developed by the Research Group of Numerical Analysis (GPNUM www.gpnum.eng.br) from the State University of Maringá, supervised by Professor Carlos Humberto Martins. At the same time, this study is part of the research project entitled "*INOVA-Nióbio*" (CNPq/MCTI/FCNDT Call Nº 23/2022 – InovaNióbio, Grant number 408498/2022-6), which focuses on the assessment of the bending performance of composite and non-composite alveolar beams using I-sections of microalloyed steels with Niobium addition. In the case of composite beams, slabs of UHPC are adopted in the investigation. Given this, the present work addresses the part of this research project regarding the experimental and numerical analyses of steel-UHPC composite castellated beams under hogging moment, searching the possibilities for dematerializing conventional composite beams through the approach of using high-performance materials and the I-section height expansion method.

This thesis is organized into seven chapters, each briefly outlined below to clarify the sequence of the work. Chapter 1 presents the theme of the work, the justification, its objectives and a summary of the methodology used.

Chapter 2 outlines the study's theoretical basis, covering the state of the art on composite alveolar beams under hogging bending and their LDB and WPB resistance predictions, composite beams with HSS and UHPC, and the effect of structural and geometrical imperfections on the stability behavior of steel I-sections.

Chapter 3 deals with a theoretical study of the accuracy obtained by some approaches for LDB and WPB resistance prediction compared to experimental results from the literature.

Chapter 4 presents the three-point bending tests performed with steel-UHPC composite castellated beams, in which all materials and methods are detailed. The experimental results are discussed and used to verify the accuracy of WPB resistance predictions.

Chapter 5 describes the developed finite element modeling, which is divided into preliminary and final numerical models. The preliminary model was developed before the experimental tests were performed and validated against experimental results from the literature. Meanwhile, the final numerical model was calibrated with the test results of the present work.

Chapter 6 details the whole thesis's numerical parametric study, divided into three studies, each presenting its results and discussion. Each study is part of a different research article. The first study addressed the elastic stability behavior of composite cellular beams in hogging moment regions. The second study focused on the WPB resistance of steel-UHPC composite castellated beams under hogging bending. The third study analyzed the stability and dematerialization of continuous composite beams using HSS alveolar I-sections and UHPC slabs.

Finally, Chapter 7 presents the main conclusions and recommendations for future related works that can be developed.

Appendix A describes the review and research articles developed during the doctoral research, which were published in journals and international conference proceedings.

CHAPTER 2
STATE OF THE ART

This chapter provides a literature review of the subjects deemed essential for developing this work. The main research aimed at studying the hogging bending behavior of steel-concrete composite alveolar beams, focusing on the failure modes by Lateral-Distortional Buckling (LDB) and Web-Post Buckling (WPB). This part of the review study, presented in **section 2.1**, was published in a review article by Oliveira *et al*. (2023a).

Additionally, the review on the flexural behavior of composite beams with High-Strength Steel (HSS) I-sections and Ultra-High-Performance Concrete (UHPC) slabs, as there is no investigation of these composite beams with alveolar I-profiles. Finally, the chapter discusses the influence of physical and geometric imperfections on instability occurrences and includes research that contributes to the development of the numerical model featured in this study.

2.1 COMPOSITE ALVEOLAR BEAMS UNDER HOGGING MOMENT

Steel-concrete composite beams subjected to hogging moment are characteristics of continuous or cantilever elements. Continuous composite beams present hogging moments near to supports. On the other hand, cantilever composite beams are submitted to hogging moment in all their span.

The steel I-section is compressed in hogging moment regions of steel-concrete composite beams, and the concrete slab is tensioned (DE ANGELIS; PECCE; LOGORANO, 2019). Due to this, these beams can reach failure by Lateral Distortional Buckling (LDB), an instability mode characterized by a lateral displacement and rotation of the lower flange accompanied by web distortion (**Figure 2.1a**) (ROSSI *et al*., 2020b). Since the steel profile is subjected to compressive stress, the lower flange tends to move laterally out of the bending plane. When the profile web does not have enough flexural stiffness to contain this lower flange lateral displacement, the LDB can occur (AMARAL *et al*., 2018), as shown in **Figure 2.1b**.

Figure 2.1: Lateral distortional buckling in steel-concrete composite beams.

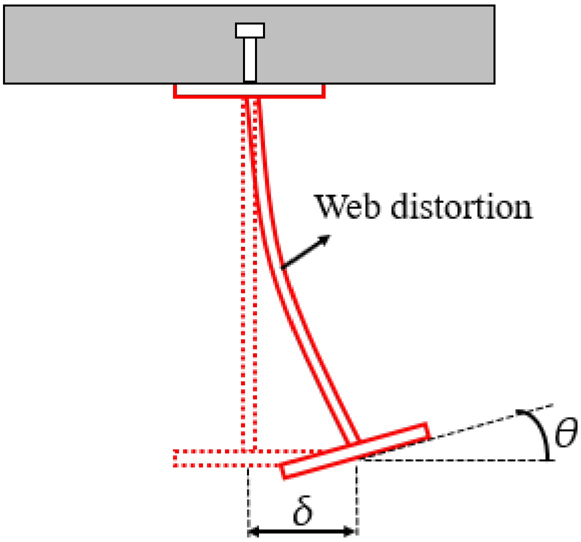

(a) Cross-section behavior

(b) Experimental tests by Kitaoka *et al*. (2017)

Source: Adapted from Rossi *et al*. (2020b) and Kitaoka *et al*. (2017).

LDB behavior of steel-concrete composite beams without web openings was considerably investigated. Elastic numerical analyses (ARAUJO *et al*., 2022; BRADFORD, 1998; BRADFORD; GAO, 1992; DEKKER; KEMP; TRINCHERO, 1995; ROSSI *et al*., 2021a; VRCELJ; BRADFORD, 2007), inelastic numerical analyses (BRADFORD, 2000; BRADFORD; JOHNSON, 1987; CHEN; JIA, 2010; CHEN; WANG, 2012; OLIVEIRA *et al*., 2021; ROSSI *et al*., 2020b, 2021b, 2021c; VRCELJ; BRADFORD, 2009), and experimental tests (CHEN, 1992; FAN, 1990; HOPE-GILL; JOHNSON, 1976; JOHNSON; CHEN, 1993; JOHNSON; FAN, 1991; KITAOKA *et al*., 2017; TONG *et al*., 2014; VASDRAVELLIS *et al*., 2012a, 2012b) were done. In addition to LDB, web local buckling has also been addressed by experimental and numerical investigations (BUI *et al*., 2020; MEN *et al*., 2021a, 2021b, 2023;

ZHOU *et al*., 2021). Additionally, studies have assessed ways to improve the cracking of the concrete slab of these beams, such as the use of high-performance concrete (HPC) (HAMODA *et al*., 2017), ultra-high-performance concrete (UHPC) (QI *et al*., 2020; WU *et al*., 2023; ZHANG *et al*., 2020), engineered cementitious composite (ECC) (FAN *et al*., 2020; WU *et al*., 2023), prestressed concrete slabs (WANG *et al*., 2020), and carbon fiber reinforced polymer (CFRP) (LIU *et al*., 2022). Other issues, such as the shear interaction steel beam-concrete slab (DING *et al*., 2021; FANG *et al*., 2021; JURKIEWIEZ; TOUT; FERRIER, 2021), beam-to-column joints (SONG *et al*., 2021), and residual deflections (SONG *et al*., 2018), also have been studied for the beams in question.

Few experimental studies evaluated the behavior of composite alveolar beams under hogging bending (GENG *et al*., 2023; GIZEJOWSKI; SALAH, 2010a; SALAH, 2009). In all, only five investigations that analyzed the structures in question are found, which **Table 2.1** summarizes the main focus of then. These assessments are discussed in **section 2.1.1**. Thus, it is clear that steel-concrete composite beams with full web are significantly more studied than those with web openings. The alveolar profiles are susceptible to local failure modes that do not occur in I-sections with solid web (ERDAL; SAKA, 2013; GRILO *et al*., 2018; KERDAL; NETHERCOT, 1984; PANEDPOJAMAN; THEPCHATRI; LIMKATANYU, 2014; WARREN, 2001). These local failure modes are Web-Post Buckling (WPB) and Vierendeel mechanism (VM) due to shear force and Tee Local buckling (TLB) caused by bending moment, which has been investigated in steel castellated beams (BRAGA *et al*., 2021; DE OLIVEIRA; CARDOSO; SOTELINO, 2019; DEEPHA; JAYALEKSHMI; JAGADEESAN, 2020; LIU *et al*., 2020; WEIDLICH; SOTELINO; CARDOSO, 2021), steel cellular beams (KANG; HONG; LIU, 2021; LIMBACHIYA; SHAMASS, 2021; MOHEBKHAH; AZANDARIANI, 2020; MORKHADE; GUPTA; MARTINS, 2022; QIAO; GUO; CHEN, 2022; SHAMASS; GUARRACINO, 2020; ZAHER *et al*., 2018; ZEWUDIE, 2022), steel beam with sequential sinusoidal and elliptically-based web openings (FERREIRA *et al*., 2022a, 2023; FRANÇA *et al*., 2022; NAWAR; ARAFA; ELHOSSEINY, 2020; SHAMASS *et al*., 2022), and steel-concrete composite cellular beams under sagging bending (BENINCÁ; MORSCH, 2020; FERREIRA *et al*., 2021a, 2021b, 2021c; FERREIRA; MARTINS; NARDIN, 2021). Due to shear force, WPB is characterized by a double curvature in the web-post region as an "S" shape with the web torsion (FERREIRA; MARTINS; NARDIN, 2020b). In contrast, VM is the distortion and formation of plastic hinges around the openings of steel alveolar I-beams that arise due to the so-called Vierendeel bending (TSAVDARIDIS; MELLO, 2012). Finally, TLB is the rotation of the compressed tee in the opening regions, being the coupling of the buckling in the flange and web of the tee caused by the compressive bending stresses (DE OLIVEIRA; CARDOSO; SOTELINO, 2019; WEIDLICH; SOTELINO; CARDOSO, 2021). These local failure modes are described and illustrated in **section 2.1.1**.

Table 2.1: Investigations on the behavior of composite alveolar beam under hogging moment.

Model	Reference	Highlight
Experimental	Salah (2009) and Gizejowski and Salah (2010)	Performed tests with steel-concrete composite beams with circular, hexagonal and rectangular web openings
Numerical	Geng *et al*. (2023)	Analyzed via four and three-point bending tests six composite castellated beams
	Gizejowski and Salah (2008)	Used geometrical nonlinear finite element models to analyze the stability behavior of continuous composite cellular beams
	Salah (2009) and Gizejowski and Salah (2010)	Carried out a calibration study with geometrical and physical nonlinear finite element models
	Oliveira *et al*. (2022) and Oliveira (2022)	Conducted nonlinear analysis to investigate the effect of the opening diameter, web post width, I-section dimensions, free span, and hogging moment distribution

Source: The author (2023).

Standards such as European (EN 1994-1-1: 2004 / prEN 1994-1-1), American (AISC 360-22 / AASHTO 2017), Australian (AS4100:2020 / AS/NZS2327-2017), and Brazilian codes (ABNT NBR 8800:2008 / ABNT NBR 8800: 2024) only specific the LDB resistance prediction of steel-concrete composite beams with full web. As these codes do not include composite alveolar beams, it is necessary to make adaptations for the beams in question to predict their bearing capacity to LDB.

The resistance of composite alveolar beams can be reached by an interaction between LDB and local failure modes, such as WPB and the formation of plastic mechanisms (GIZEJOWSKI; SALAH, 2008, 2010a; OLIVEIRA *et al*., 2022; SALAH, 2009). These interactions are disregarded in the analytical procedures for LDB resistance prediction analyzed in the present study. This is because the cited codes' formulations were not developed for beams with web openings. SCI P355 (LAWSON; HICKS, 2011) and Steel Design Guide 31 (FARES; COULSON; DINEHART, 2016) provide methodologies to evaluate the resistance to WPB and VM of composite and non-composite alveolar beams. However, do not present approaches for LDB.

The present state of the art section focuses on two issues: the gap in LDB and WPB behavior investigations in continuous and cantilever composite alveolar beams and the need for code procedures for LDB resistance prediction for these structures. Furthermore, it is discussed the parameters that need further assessment and describes some approaches for adapting the LDB resistance predictions developed for beams without web openings. The accuracy of these approaches is assessed with experimental results from Salah (2009), presented in **section 3.1**.

2.1.1 Experimental and numerical investigations

As mentioned, many studies have investigated steel-concrete composite beams without web openings in hogging moment regions. Regarding instability modes, these beams can reach the capacity by LDB, with single or double web curvature, Flange Local Buckling (FLB), Web Local Buckling (WLB), or by the interaction between these failure modes (ARAUJO *et al*., 2022; BRADFORD; JOHNSON, 1987; FAN, 1990; JOHNSON; FAN, 1991; ROSSI *et al*., 2020b, 2021b; TONG *et al*., 2014). **Figure 2.2** illustrates the deformed configurations of steel-concrete composite cross-sections. In addition to the deformed configurations shown in **Figure 2.2**, composite cellular beams in hogging moment regions can reach WPB. This failure mode was observed in those under considerable shear force (GIZEJOWSKI; SALAH, 2010a; OLIVEIRA *et al*., 2022; SALAH, 2009). In addition, studies showed that WPB becomes critical in cellular beams with short web-post width ($p/D_0 < 1.5$) (MORKHADE; GUPTA, 2017; PANEDPOJAMAN; SAE-LONG; CHUB-UPPAKARN, 2016; PANEDPOJAMAN; THEPCHATRI; LIMKATANYU, 2014). Furthermore, according to numerical investigations, non-composite beams with web openings can reach failure by Tee Local Buckling (TLB) in the central region of the alveolus (DE OLIVEIRA; CARDOSO; SOTELINO, 2019; WEIDLICH; SOTELINO; CARDOSO, 2021). This failure mode can also occur in composite cellular beams under hogging moment, as shown in **Figure 2.2**.

Gizejowski and Salah (2008) analyzed the continuous composite cellular beams behavior via geometrically nonlinear analysis. The authors noted that the buckling mode in short-span beams is characterized by the interaction between LDB and WPB. On the other hand, in long-span beams, the instability mode changes to LDB.

Figure 2.2: Failure modes of composite beams with and without web openings in hogging moment regions.

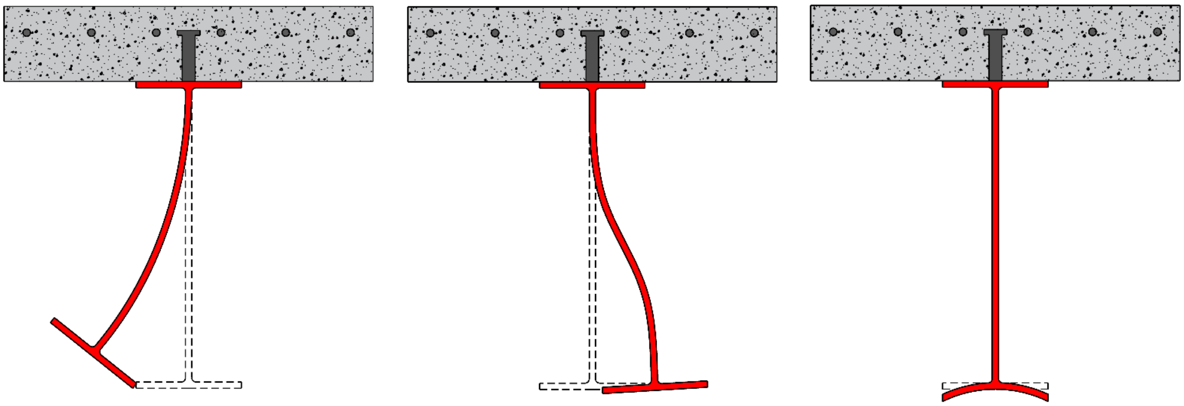

(a) Single curvature lateral distortional buckling (LDB)

(b) Double curvature lateral distortional buckling (LDB)

(c) Flange local buckling (FLB)

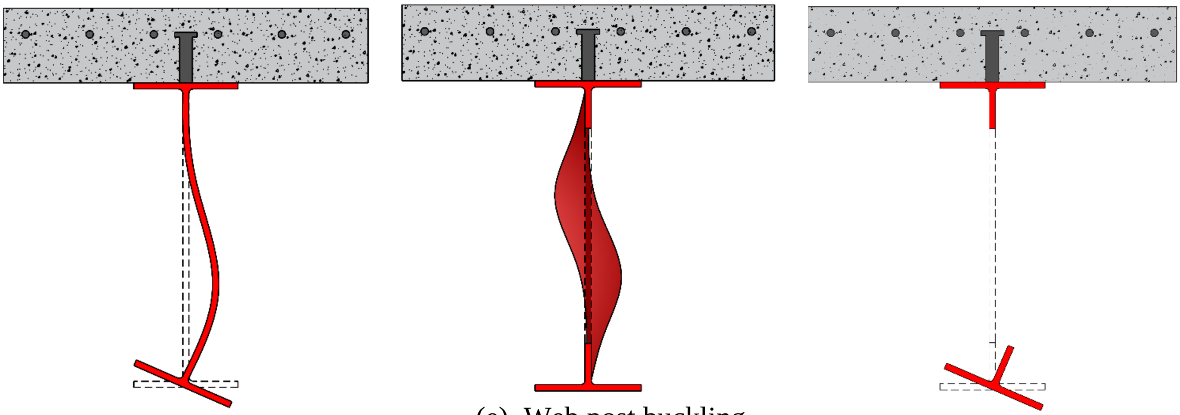

(d) Web local buckling (WLB)

(e) Web post buckling (WPB)

(f) Tee local buckling (TLB)

Source: Oliveira *et al*. (2023a).

Salah (2009) and Gizejowski and Salah (2010) carried out experimental investigations in twelve beams. Two sets of specimens were assessed, six with long spans and another six short spans. Both sets comprise two steel grades (S355 and S420) and three opening geometries (rectangular, circular and hexagonal). The alveolar I-sections were not manufactured by the height expansion method, in which these web openings were directly cut into the web of the solid I-sections. A lateral distortional mode predominance (LDB) was noted in the long-span beams with circular and hexagonal openings, showing a significant lateral displacement in the I-section compressed flange (**Figure 2.3a**). This failure occurred due to the significantly hogging moment and because these beams have longer unrestrained lengths than those with a short span, which favors global lateral instability. On the other hand, in the short-span beams occurred a torsional-distortional mode (WPB) with a not significant contribution of lateral compressed flange deformations (**Figure 2.3b**). This failure mode is characteristic of beams with a predominance of shear forces, the case of the short-span beams, in which the shear force was more critical than the hogging moment. In addition, this behavior was also noted in the beams with rectangular openings and long spans, as, due to the lower web post area than the ones with circular and rectangular openings, these beams are more susceptible to the local web post failure modes. Salah (2009) also developed numerical analyses, which showed that slender sections of composite beams reach LDB before the limit load of VM.

Figure 2.3: Experimental tests by Salah (2009) and Gizejowski and Salah (2010).

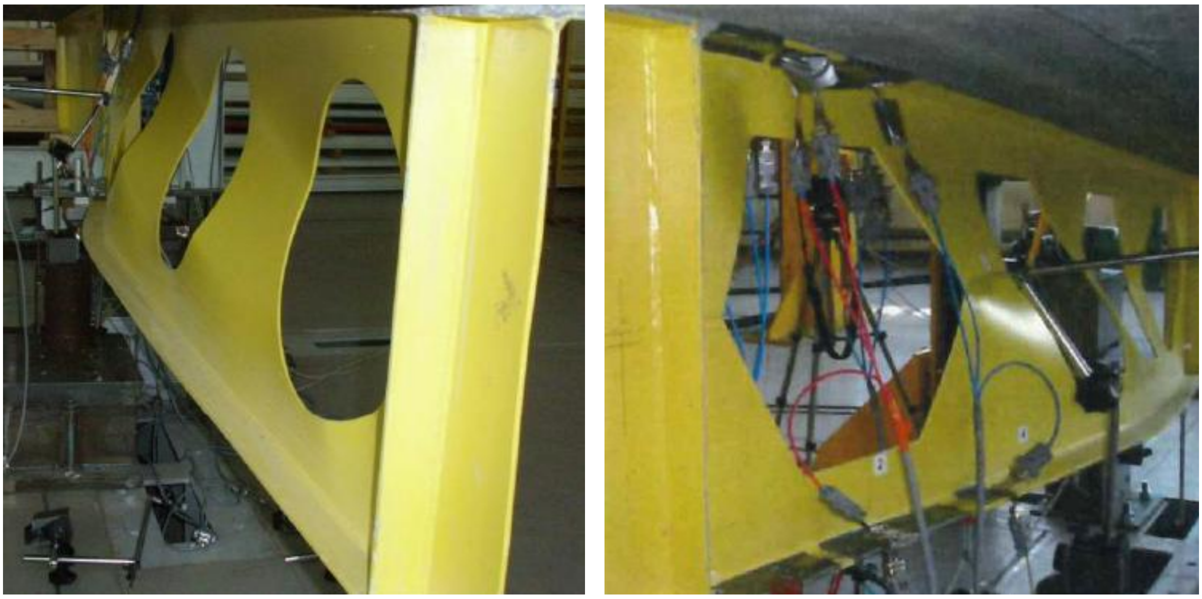

(a) Lateral distortional mode

(b) Torsional-distortional mode

Source: Salah (2009).

Oliveira *et al*. (2022) carried out numerical investigations of the behavior of composite cellular beams subjected to hogging moment. The authors observed that models subjected to uniform hogging moment distribution (without shear loads) reached failure by LDB or its interaction with Compression Tee Yielding (CTY). In contrast, the models subjected to linear hogging moment distribution (with shear loads) reached failure by WPB with the formation of plastic mechanism (PM), LDB, LDB+CTY, LDB+WPB+PM, LDB+WPB+PM+CTY, and LDB+WPB+CTY. According to the authors, in many models with lower global slenderness and subjected to linear hogging moment, the ultimate moment to LDB reached values above the plastic moment of the composite section. Oliveira *et al*. (2022) concluded that the I-section dimensions were the parameters that had the most significant influence on the load-carrying capacity of the models.

Geng *et al*. (2023) conducted four and three-point bending tests of composite castellated beams with I-sections of S355 steel and concrete of mean cubic compressive strength equal to 35.03MPa. Just like the beams of Salah (2009), the hexagonal web openings were directly cut into the web of the solid I-sections. Three specimens were adopted for each loading configuration and both sets with one composite castellated beam having transversal web stiffeners. The authors stated that all models of the four-point bending tests reached failure by compression flange buckling, which occurred in the opening regions (**Figure 2.4a**). In contrast, in the set of three-point bending tests, the models without web stiffeners characterized WPB+VM, and the one with web stiffeners had the coupling of VM and cracks around the opening (**Figure 2.4b**). Increasing the opening rate (D_o/d_g) from 0.47 to 0.6, the bending capacity decreased by 8.7% and 10.5% in four and three-point bending tests, respectively.

In this context, the behavior of composite cellular beams under hogging bending requires further investigation. There is still no knowledge about the influence of composite cellular beam parameters such as dimensions of the slab cross-section (height and width), slab typology, the longitudinal reinforcement ratio, shear interaction degree, expansion ratio of the cellular profile, mechanical properties of structural steel, and the use of asymmetric I-sections.

Due to the gap in studies that investigated composite alveolar beams under hogging bending, there are not studies that investigated all possible failure modes in these structures. However, based on the main observations by the works presented in this literature review, it was observed that the composite alveolar beams subjected to hogging bending could reach failure by LDB, WPB, the formation of plastic mechanisms, plastic behavior, and their interactions.

Figure 2.4: Hogging bending tests of composite castellated beams.

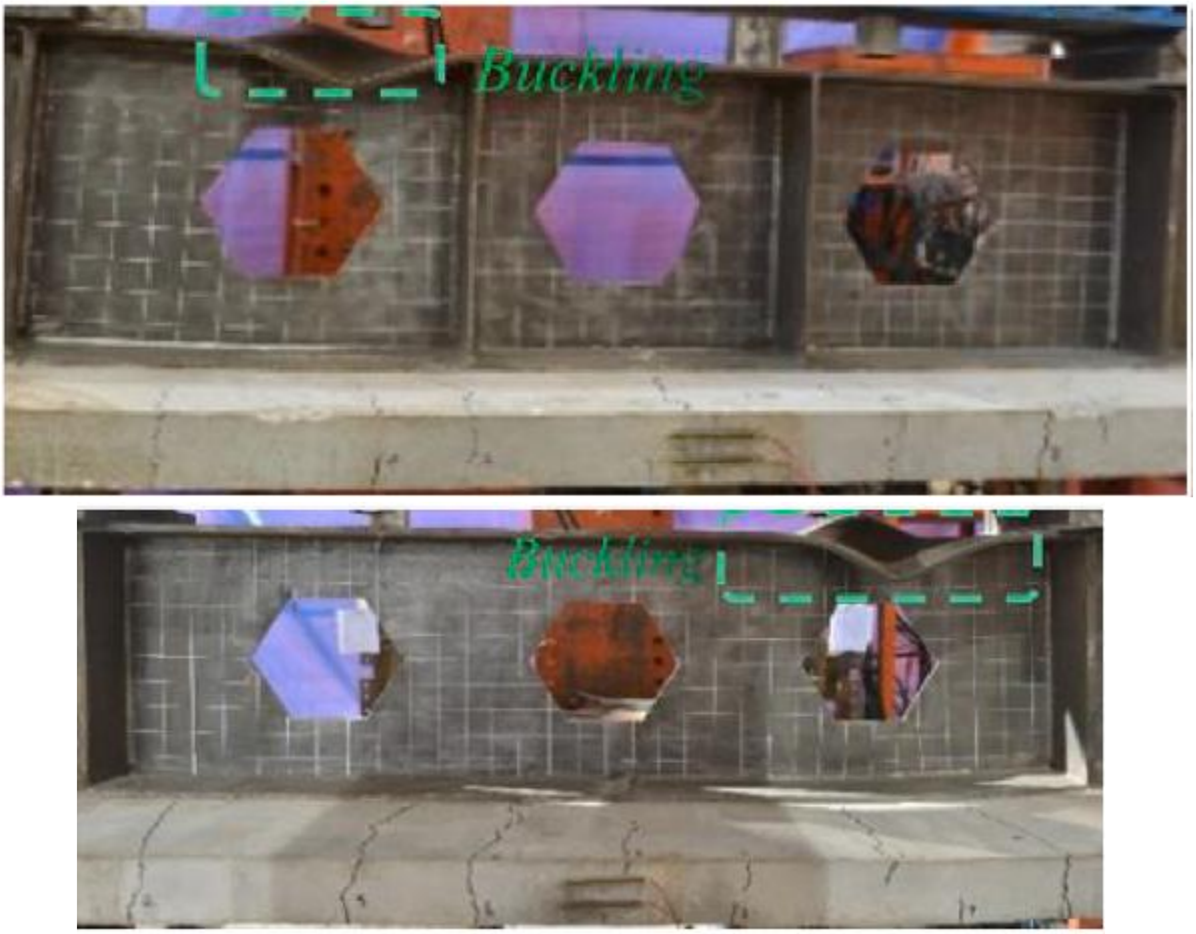

(a) Four-point bending tests

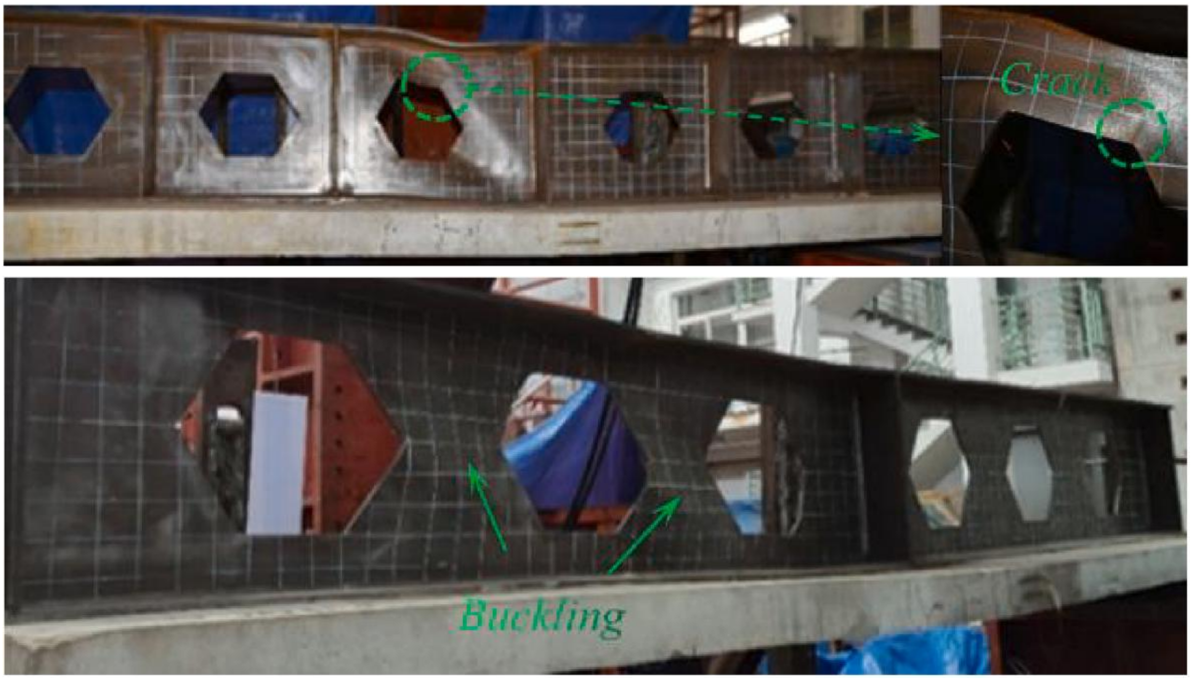

(b) Three-point bending tests

Source: Geng *et al*. (2023).

2.1.2 LDB standard codes and analytical methodologies

The standard procedures presented in this section do not specific the LDB verification approach on continuous steel-concrete composite beams with web openings. However, some authors give adaptations of these standards (MÜLLER *et al.*, 2006; SILVA *et al.*, 2019, 2020). In addition, assessments on the lateral-torsional buckling behavior of steel cellular beams show that methodologies developed for solid I-beams can be adapted to cellular I-beams, which must determine the cross-section geometric properties in the central region of the openings, the so-called double *T* section (CARVALHO *et al.*, 2023; DE CARVALHO *et al.*, 2023; DE CARVALHO; ROSSI; MARTINS, 2022; SONCK; BELIS, 2015, 2017). On the other hand, Sonck and Belis (2015, 2017) recommend that the torsional constant (J) must be obtained by an average ($J_{2T,Average}$) between the J of the I-section (J_{solid}) and the J of the double *T* section (J_{2T}) obtained through **Eq. 2.1**, where the parameters are: number of openings (n), equivalent opening length for the adapted torsion constant ($l_{0,avg}$), and I-section unrestrained length (L). The opening equivalent length ($l_{0,avg}$) for castellated and cellular I-section are determined as shown in **Figure 2.5** (SONCK; BELIS, 2015, 2017).

$$J_{2T,Average} = \frac{nl_{0,avg}}{L} J_{2T} + \left(1 - \frac{nl_{0,avg}}{L}\right) J_{solid} \tag{2.1}$$

Figure 2.5: Equivalent rectangular openings for calculation of the adapted torsion constant.

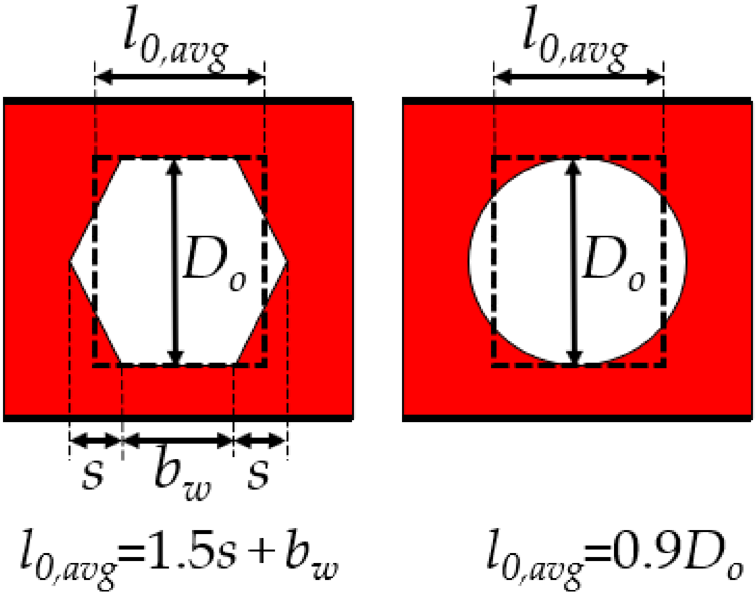

Source: Adapted from Sonck and Belis (2015,2017).

Other approaches were presented by Carvalho, Rossi and Martins (2022), which cover different methods in the determination of geometric properties: without web openings (*solid section*); the calculation of properties at the center of the opening (*double T*); and three approaches using average values between the properties of the solid section and the double *T* section, so-called "*average section*", "*linear weighting section*" and "*superficial weighting section*". The average value between the properties is used in the "*average section*". In addition, the weighting of the values, the total length of the web post, and the total length of the openings, are utilized in the "*linear weighting section*". Finally, the weighting of the values, the total area of steel in the web, and the total area of the web openings, are adopted in the "*superficial weighting section*". The last two approaches are detailed in **Figure 2.6**, where the parameters are: arbitrary geometric property (*GP*), arbitrary geometric property calculated at plain section web (GP_{sol}), and arbitrary geometric property calculated at middle of the opening (double *T* section).

Figure 2.6: Approaches to weighting the geometric properties of the cross-section.

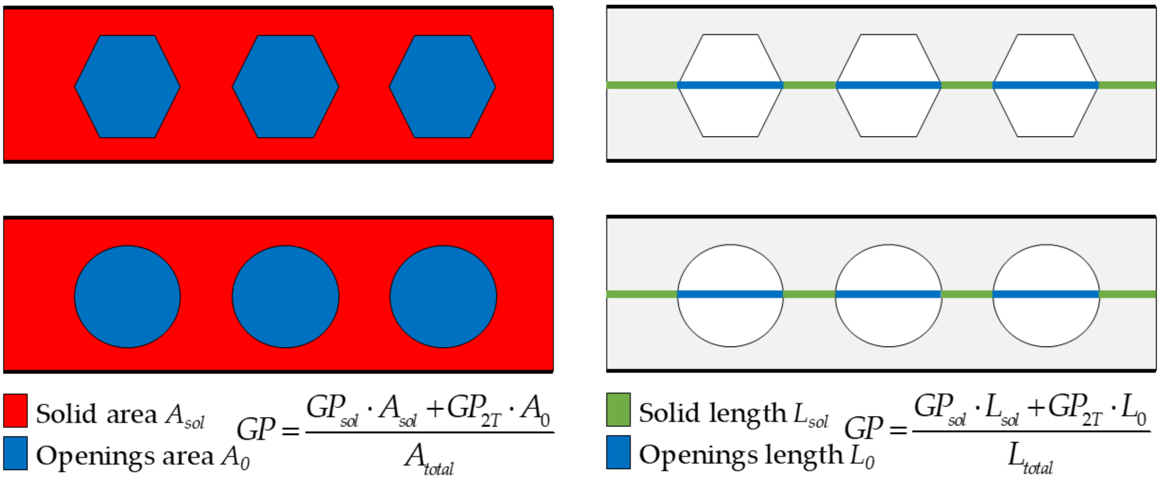

(a) Superficial way (b) Linear

Source: Adapted from Carvalho, Rossi and Martins (2022).

The resistance predictions of LDB addressed in the present study are based on the calculus of elastic critical moment. This way, design curves are applicated to obtain the ultimate moment. Thus, the elastic and ultimate moment formulations found in the literature are described in **sections 2.1.2.1** and **2.1.2.2**, respectively.

2.1.2.1 LDB elastic critical moment

The conventional LTB theories for partially constrained beams and the U-frame model are the typical methods employed by standard codes to verify LDB in steel-concrete composite beams (ROSSI *et al.*, 2020a). These approaches are depicted in **Figure 2.7**.

Figure 2.7: Models used by the standards.

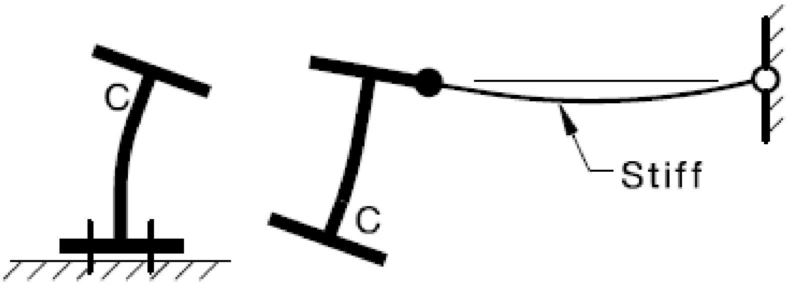

(a) Partially restricted beams

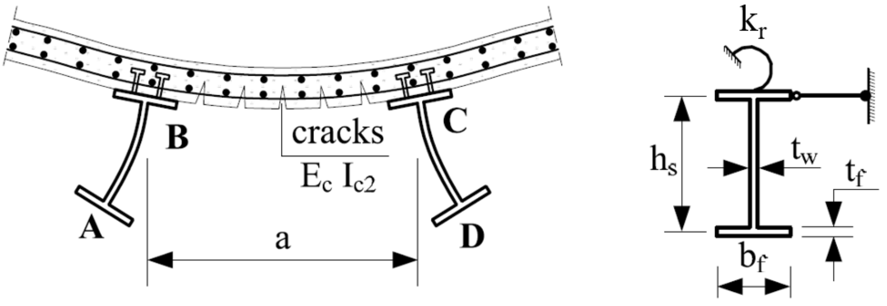

(b) Inverted U-frame model

Source: Adapted from AS4100:2020 and EN 1994-1-1: 2004.

European (EN 1994-1-1: 2004 / prEN 1994-1-1) and Brazilian standard (ABNT NBR 8800: 2008 / ABNT NBR 8800: 2024) use the inverted U-frame model to determine the elastic critical moment to LDB (M_{cr}). The U-frame model (**Figure 2.7b**) considers the composite beam cross-section as an I-section with its upper flange with lateral displacement completely prevented and rotation partially prevented by a flexural stiffness spring (k_r). The flexural stiffness k_r, given by **Eq. 2.2**, is composed of the bending stiffness of the slab (k_1, **Eq. 2.3**) per unit of beam length and the bending stiffness of the web I-section (k_2, **Eq. 2.4**):

$$k_r = \frac{k_1 k_2}{k_1 + k_2} \tag{2.2}$$

$$k_1 = \frac{\alpha\left(EI_c\right)_2}{a} \tag{2.3}$$

$$k_2 = \frac{E_a t_w^3}{4\left(1-\nu^2\right)h_0} \tag{2.4}$$

in which the parameters are: coefficient related to the I-section position (α), being equal to 2 for end beams, 3 for intermediate beams, and 4 for internal beams having four or more similar neighboring sections (AMARAL *et al*., 2018); flexural stiffness of the reinforced concrete slab with homogenized composite section per unit of beam length (EI_{c2}); distance between the I-sections; I-section elasticity modulus (E); web thickness (t_w); I-section Poisson ratio (v); and distance between the flanges centroids (h_0).

The study by Müller *et al*. (2006) was among the earliest in the literature to tackle the assessment of LDB resistance in composite beams with web openings, which introduced a modification to the European standard (EN 1994-1-1-2004), including the computation of k_2 for both composite cellular beams and composite beams with a single rectangular web opening. For calculating M_{cr}, Müller *et al*. (2006) recommended the method proposed by Hanswille *et al*. (1998), and k_2 is determined via **Eq. 2.5-2.6**.

$$k_2 = \frac{E t_w^3}{4\left(1-\nu^2\right)h_0} k_{hole}^* \tag{2.5}$$

$$k_{hole}^* = 1 - \frac{3D_0}{4p} \text{ for cellular beams.} \tag{2.6}$$

Studies of LDB in composite castellated beams also presented adaptations of k_2 flexural stiffness (SILVA *et al*., 2019, 2020). Basically, these propositions approach k_2 flexural stiffness determination of a composite alveolar beam from the adaptation of the k_2 of a composite beam without web opening, applying a reduction factor referring to the web openings. Silva *et al*. (2020) present a reduction factor equal to 0.51, and the method by Müller *et al*. (2006), for the experimental models of Salah (2009), provided a reduction factor equal to 0.524. Silva *et al*. (2019) determined the k_2 flexural stiffness via a simplified numerical model, considering the I-section web as a cantilever plate in the centroid of the upper flange and free in the centroid of the lower flange. The finite element models addressed cantilever plates with hexagonal web openings in compliance with the Litzka, Peiner and Anglo-Saxon patterns of castellated I-beams. Silva *et al*. (2019) observed reduction factor values (β) of 0.53, 0.54 and 0.55 for the Anglo-Saxon, Litzka and Peiner opening patterns, respectively. The authors proposed the determination of the flexural stiffness of castellated profiles considering the total height of the expanded I-section (*d_g*), which can be taken as:

$$k_2 = \beta \frac{E t_w^{\ 3}}{4 d_g \left(1 - \nu^2\right)} \tag{2.7}$$

Subsequently, Silva *et al.* (2020) presented a new equation for calculating k_2 very similar to the one shown by Silva *et al.* (2019). However, Silva *et al.* (2020) adopted the same parameters used in the standard procedures. This way, d_g was replaced by the distance between the flanges centroids (h_0). **Eq. 2.8** describes the formulation proposed by the authors, which is limited only to castellated composite beams with Anglo-Saxon pattern openings:

$$k_2 = 0{,}51 \frac{E t_w^{\ 3}}{4 h_0 \left(1 - \nu^2\right)} \tag{2.8}$$

Silva *et al.* (2020) verified the accuracy of their formulation with the results obtained by numerical analyses via ANSYS software. The authors stated that the proposed procedure is suitable for evaluating the LDB behavior of castellated composite beams, and it remains valid when the stiffness of the slab is varied.

In the previous version, the Brazilian standard (ABNT NBR 8800: 2008) presented the methodology proposed by Roik *et al.* (1990) to determine the M_{cr} based on the inverted U-frame model. That method was also presented in the previous version of EC4 (ENV 1994-1-1: 1992). Recently, the Brazilian standard (ABNT NBR 8800: 2024) has been updated and now presents the proposition of Dias *et al.* (2019) and Nery *et al.* (2023), also based on the inverted U-frame model, to determine the M_{cr}.

The current version of EC4 (EN 1994-1-1: 2004) does not present equations for determining the M_{cr}. However, it proposes using calculation methodologies based on the inverted U-frame model. This code is under an update process, in which the draft version (prEN 1994-1-1) shows the same considerations of the current version (EN 1994-1-1: 2004) to determine the M_{cr}.

Rossi *et al.* (2020a) stated that the LDB research methods for the elastic critical moment determination generally fall into two categories: studies based on the energy method (Galerkin method) or those based on the elastic foundation-beams theory. The formulations of Roik *et al.*

(1990) and Dias *et al*. (2019) are within the methodologies developed using the energy method as well as the propositions of Svensson (1985), Williams and Jemah (1987). On the other hand, Hanswille *et al*. (1998) utilized the elastic foundation-beams theory in their prediction procedure. The methods in question are objectively described below.

The first procedures found in the literature are based on the energy method, such as the works of Svensson (1985), Williams and Jemah (1987), and the methodologies proposed in these works are very similar. Starting with the method proposed by Svensson (1985), the author adopted the *T* section model (considers only an I-section associated with the slab) to evaluate the structure, in which it was considered that the I-section compressed flange could be treated as a column subjected to axial compressive loads. The author proposed a method that can be applied to several bending moment distributions. Svensson's formulation (1985) is described in **Eqs. 2.9-2.12**, where W_x is the elastic section modulus taken about the strong axis. **Eq. 2.12** and **Table 2.2** describe the formulation to obtain the slenderness parameter (λ).

$$M_{cr} = \frac{\pi^2 E}{\lambda_{el}^2} W_x \tag{2.9}$$

$$\lambda_{el} = \frac{L_{el}}{b_f / \sqrt{12}} \tag{2.10}$$

$$L_{el} = L \cdot \lambda^{-0.5} \tag{2.11}$$

$$\beta L = 1.35 \left(\frac{t_w{}^3 L^4}{d_g{}^3 t_f b_f} \right)^{1/4} \tag{2.12}$$

Williams and Jemah (1987) presented a proposal based on Svensson's method (SVENSSON, 1985). The authors considered that in addition to the compressed flange, a 15% portion of the web could also be analyzed as a column under compression (**Figure 2.8**). The proposition of Williams and Jemah (1987) is presented in **Eq. 2.13**. The slenderness parameter (λ_{el}) is obtained as described above.

Table 2.2: λ values for different bending moments (SVENSSON, 1985).

	λ values								
	Case								
βL	1	2	3	4	5	6	7	8	9
0	1.000	1.881	2.355	5.824	2.835	4.518	10.83	5.824	0.377
1	1.010	1.889	2.376	5.856	2.860	4.538	10.84	5.856	0.438
2	1.164	2.166	2.694	6.309	3.235	4.827	11.02	6.309	1.332
3	1.832	3.240	3.944	7.952	4.732	5.884	11.72	7.952	4.543
4	3.628	5.472	6.450	11.06	8.044	7.875	13.26	11.06	6.775
5	5.604	8.110	9.537	15.24	13.16	10.41	15.65	15.24	9.135
6	7.326	10.91	12.86	20.06	19.48	13.20	18.67	20.06	12.48
8	13.67	18.06	20.91	30.99	33.16	20.28	25.23	30.99	20.26
10	20.41	26.92	30.75	43.62	47.21	29.27	34.17	43.62	29.18
12.5	31.66	40.41	45.51	61.89	66.65	42.74	47.83	61.89	42.73
15	45.79	56.56	63.00	82.97	88.86	58.73	64.10	82.97	58.73
17.5	62.75	75.35	83.20	106.8	113.9	77.21	82.96	106.8	77.20
20	81.63	96.78	106.1	133.5	141.7	98.18	104.4	133.5	98.18

Legend

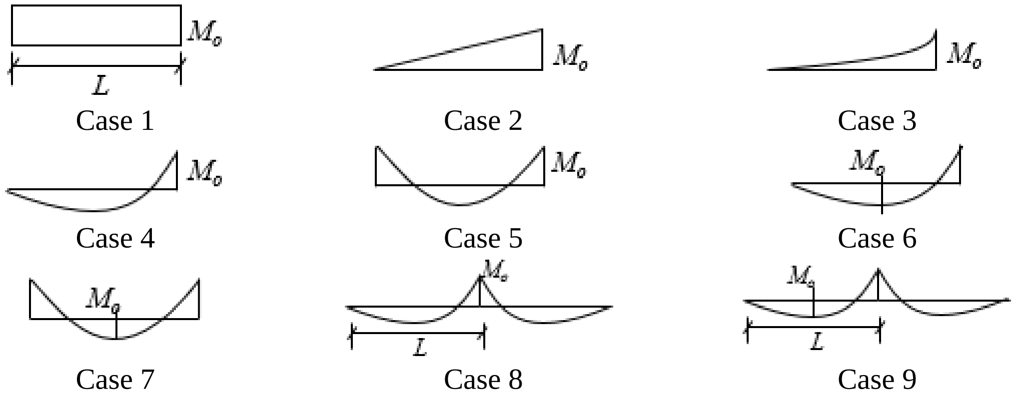

Case 1 Case 2 Case 3

Case 4 Case 5 Case 6

Case 7 Case 8 Case 9

Source: Adapted from Svensson (1985).

Figure 2.8: Model of Williams and Jemah (1987).

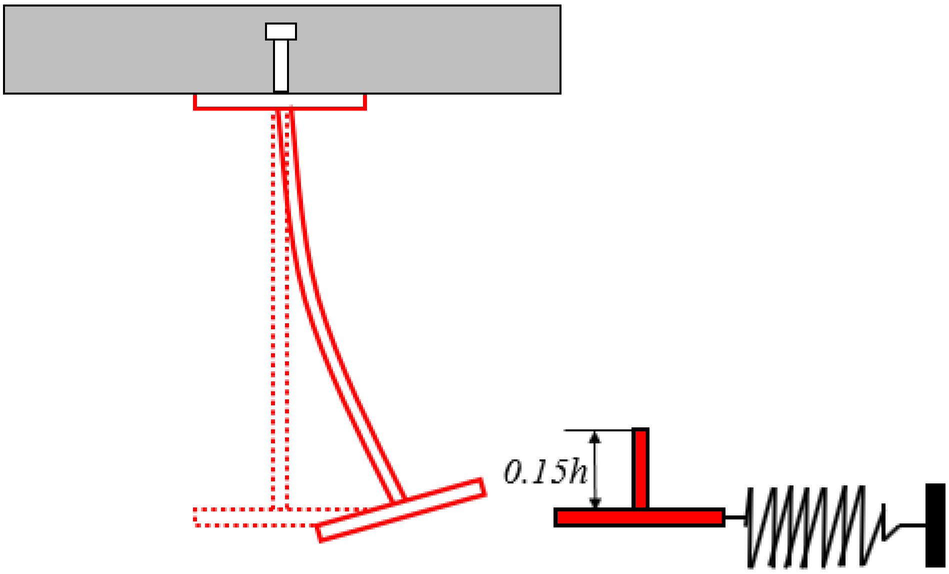

Source: Adapted from Williams and Jemah (1987).

$$M_{cr} = \frac{\dfrac{\pi^2 E}{\lambda_{el}^2} W_x}{\left(1 + 0.15 \dfrac{b_f t_f}{h_0 t_w}\right)} \tag{2.13}$$

The formulation proposed by Roik *et al*. (1990) is presented in **Eqs. 2.14-2.16**, where the parameters are: coefficient referring to the hogging moment distribution (C_{dist}), as described in **Table 2.3-2.4**; I-section shear modulus (G); flange inertia moment about the weak axis ($I_{af,y}$); composite cross-section inertia moment about the strong axis (I_x); I-section inertia moment about the strong axis (I_{ax}); I-section inertia moment about the weak axis (I_{ay}); I-section sectional area (A_a); composite cross-section sectional area (A).

$$M_{cr} = \alpha_g \frac{C_{dist}}{L} \sqrt{\left(GJ + \frac{k_r L^2}{\pi^2}\right) EI_{af,y}} \tag{2.14}$$

$$\alpha_g = \frac{h_0 I_x / I_{ax}}{\dfrac{h_0^2 \Big/ 4 + \dfrac{\left(I_{ax} + I_{ay}\right)}{A_a}}{e} + h_0} \tag{2.15}$$

$$e = \frac{A I_{ax}}{A_a y_c \left(A - A_a\right)} \tag{2.16}$$

In the search for a new strategy for determining the LDB elastic critical moment, Hanswille *et al*. (1998) developed a proposal similar to Roik *et al*. (1990) using the inverted U-frame model to represent the composite beam. However, the authors deduced their procedure through the elastic foundation-beams theory (**Figure 2.9**).

Table 2.3: C_{dist} coefficient for continuous beams with loading on the analyzed span (L).

*Moment distribution	ψ								
	0.50	0.75	1.00	1.25	1.50	1.75	2.00	2.25	2.50
	41.5	30.2	24.5	21.1	19.0	17.5	16.5	15.7	15.2
	33.9	22.7	17.3	14.1	13.0	12.0	11.4	10.9	10.6
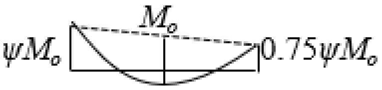	28.2	18.0	13.7	11.7	10.6	10.0	9.5	9.1	8.9
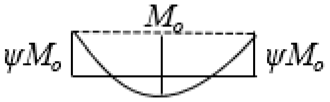	21.9	13.9	11.0	9.6	8.8	8.3	8.0	7.8	7.6
	28.4	21.8	18.6	16.7	15.6	14.8	14.2	13.8	13.5
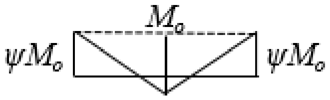	12.7	9.89	8.6	8.0	7.7	7.4	7.2	7.1	7.0

*M_o is the maximum moment, considering the analyzed span as simply supported.

Source: Adapted from ABNT NBR 8800: 2008.

Table 2.4: C_{dist} coefficient for continuous beams without loading on the analyzed span (L).

*Moment distribution	ψ				
	0.00	0.25	0.50	0.75	1.00
	11.1	9.5	8.2	7.1	6.2
	11.1	12.8	14.6	16.3	18.1

*M_o is the higher moment, in modulus, in the analyzed span, in which ψ values higher than 1.00 must be taken as 1.00.

Source: Adapted from ABNT NBR 8800: 2008.

Figure 2.9: Analogy between the compression member on elastic foundation and the lateral torsional buckling problem.

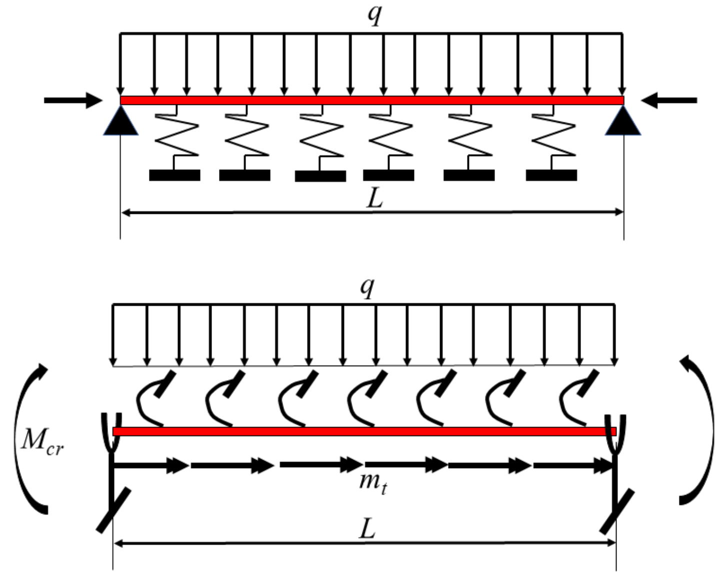

Source: Adapted from Hanswille *et al*. (1998).

The formulation for M_{cr} proposed by Hanswille *et al*. (1998) is presented in **Eq. 2.17**.

$$M_{cr} = \frac{1}{k_z}\left(\frac{\left(\pi^2 E C_{w,d}\right)}{\left(\beta_b L\right)^2} + G J_{ef}\right) \tag{2.17}$$

In which the parameters are the cross-section geometric parameters described by **Eq. 2.18** (k_z, y_f and e) and the distance between the I-section centroid and the composite section (reinforcement bar and I-section) centroid (y^*):

$$k_z = \frac{I_{ax}}{I_x}\left(2y_f - \frac{1}{e}\left(y_f^2 + \frac{I_{ax}+I_{ay}}{A_a}\right)\right) \; ; \; y_f = \frac{d_g - b_f}{2} \; ; \; e = \frac{I_{ax}}{y^* A_a} \tag{2.18}$$

The warping constant calculated with the pole in the center of the profile upper flange is given by **Eq. 2.19** ($C_{w,d}$):

$$C_{w,d} = I_{af,y} h_0^{\,2} \tag{2.19}$$

The effective length factor is determined by **Eq. 2.20** (β_B):

$$\beta_B = \beta_{0B}\left(\frac{1}{1+\left(a\frac{\sqrt{\eta_b}}{\pi}\right)^{n_1}}\right)^{1/n_2} \tag{2.20}$$

The stiffness factor is given by **Eq. 2.21** (η_b), and the effective Saint-Venant torsion stiffness (GJ_{ef}) by **Eq. 2.22**.

$$\eta_b = \sqrt{\frac{k_r L^4}{EC_{w,d}}} \tag{2.21}$$

$$GJ_{ef} = A\left(1.5 - 0.5\psi\right)GJ \tag{2.22}$$

To calculate the parameters B_B and GJ_{ef} is necessary to obtain the coefficients A, a, η_1 and η_2, which are dependent on the hogging moment factors: the relationship between the end moment and the maximum moment (ψ); and the relationship between the smaller end moment and the higher end moment. The parameters A, a, η_1 and η_2 are given according to the load configurations, which are detailed in **Table 2.5** (for members with end moments), **Table 2.6** (for members with concentrated load and end moments) and **Table 2.7** (members with uniformly distributed load and end moments).

Table 2.5: Approximate determination of the elastic critical moment for members with end moments.

***Moment distribution**

$\beta_{0B} = -0.11\psi^2 - 0.37\psi + 0.74$

ψ	a	$\eta 1$	$\eta 2$
1.0	1.48	9.10	9.30
0.5	1.45	8.30	8.80
0.0	1.40	6.40	7.30
–0.5	1.25	4.70	5.70
–1.0	1.00	4.20	5.10

*M_o is the maximum moment, considering the analyzed span as simply supported.

Source: Adapted from Hanswille *et al.* (1998).

Table 2.6: Approximate determination of the elastic critical moment for members with concentrated load and end moments.

***Moment distribution**

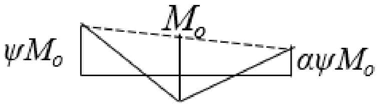

	$\beta_{0B} = 0.320\psi + 0.53$			$\beta_{0B} = 0.075\psi^2 + 0.25\psi + 0.35$			$\beta_{0B} = 0.116\psi^2 + 0.06\psi + 0.21$		
	$\alpha = 1$ A = 1.25			$\alpha = 0.5$ A = 1.5			$\alpha = 0.25$ A = 1.6		
	a	$\eta 1$	$\eta 2$	a	$\eta 1$	$\eta 2$	a	$\eta 1$	$\eta 2$
$\psi = 1.0$	1.46	9.85	9.55	1.35	7.10	6.85	0.95	4.90	4.50
$\psi = 0.5$	1.45	9.00	9.75	1.30	5.75	6.80	0.85	4.50	5.60
$\psi = 0.0$	1.35	5.95	7.75	1.05	4.60	6.30	0.70	4.15	6.10

*M_o is the maximum moment, considering the analyzed span as simply supported.

Source: Adapted from Hanswille *et al.* (1998).

Table 2.7: Approximate determination of the elastic critical moment for members with uniformly distributed load and end moments.

***Moment distribution**

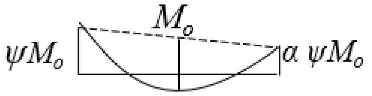

	$\beta_{0B} = 0.037\psi^2 + 0.30\psi + 0.4$			$\beta_{0B} = 0.16\psi^2 + 0.05\psi + 0.24$			$\beta_{0B} = 0.07\psi^2 + 0.01\psi + 0.13$		
	$\alpha = 1$ A = 1.25			$\alpha = 0.5$ A = 1.5			$\alpha = 0.25$ A = 1.75		
	a	$\eta 1$	$\eta 2$	a	$\eta 1$	$\eta 2$	a	$\eta 1$	$\eta 2$
$\psi = 1.0$	1.45	8.80	8.95	1.15	4.90	5.15	0.65	4.05	4.50
$\psi = 0.5$	1.37	5.95	6.70	0.95	4.50	5.90	0.55	4.00	5.70
$\psi = 0.0$	1.13	4.50	5.75	0.77	4.20	5.95	0.48	3.95	6.15

*M_o is the maximum moment, considering the analyzed span as simply supported.

Source: Adapted from Hanswille *et al.* (1998).

The methodology proposed by Dias *et al.* (2019) and Dias (2018) only cover steel-concrete composite beams under uniform hogging moment and are shown in **Eq. 2.23**.

$$M_{cr} = \frac{k_g}{h_0}\left\{GJ + \frac{EC_{w,d}}{L^2}\left[\left(n\pi\right)^2 + \left(\frac{\eta_b}{n\pi}\right)^2\right]\right\} \tag{2.23}$$

The k_g coefficient considers the elastic neutral axis and moment portion absorbed by the reinforcement bars.

$$k_g = \frac{I_x}{I_{ax}}\left(0.31 + 0.69 \cdot 0.05^{y^*/h_0}\right) \tag{2.24}$$

As in the proposition of Hanswille *et al*. (1998), η_b is the stiffness factor (**Eq. 2.25**), and $C_{w,d}$ is the warping constant calculated with the pole in the center of the profile upper flange (**Eq. 2.26**).

$$\eta_b = \sqrt{\frac{k_r L^4}{EC_{w,d}}} \tag{2.25}$$

$$C_{w,d} = I_{af,y} h_0^{\,2} \tag{2.26}$$

According to Dias *et al*. (2019), the number of waves (n) must be an integer to fulfill essential boundary conditions. Thus, one may calculate the M_{cr} value for the two integers n_1 and n_2 nearest to n_{id} (**Eq. 2.27**) and adopt the smallest value of the critical moment obtained.

$$n_{id} = \frac{\sqrt{\eta_b}}{\pi} \tag{2.27}$$

Oliveira (2018) presented an adaptation based on the methodology of Dias (2018) to verify beams subjected to non-uniform moment, according to **Eq. 2.28**.

$$M_{cr} = \frac{k_g}{h_0}\left\{GJ + \frac{EC_{w,d}}{L_{neg}^2}\left[\left(n\pi\right)^2 + \left(\frac{\eta_b}{n\pi}\right)^2\right]\right\}\left\{2.13\beta\left(\frac{L_{neg}}{h_0}\right)^{-0.1}\right\} \tag{2.28}$$

Oliveira's proposition (2018) imposed a reduction factor equal to 1/4 in the stiffness factor (η_b) determined according to **Eq. 2.29**.

$$\eta_b = \frac{1}{4}\sqrt{\frac{k_r L_{neg}^4}{EC_{w,d}}} \tag{2.29}$$

Eq. 2.30 describes the conditions to determine the β coefficient related to the positions of supports for different hogging moment diagrams. The parameters of **Eq. 2.30** are the smallest length of the hogging moment stretch (L_1); and the critical length of the composite beam (L_{cr})

had by **Eq. 2.31**, in which h_w is the web depth. The lengths L_{neg} and L_1 are determined as shown in **Figure 2.10**.

$$\beta = \begin{cases} \beta = 1.0,\ if\ \dfrac{L_1}{L_{cr}} \geq 1.0 \\ \beta = -0.16\left(\dfrac{L_1}{L_{cr}}\right) + 1.15, if\ \dfrac{L_1}{L_{cr}} < 1.0 \end{cases} \tag{2.30}$$

$$L_{cr} = 2.4 h_w \left[\frac{b_f^{\,3} t_f \left(1 - v^2\right)}{t_w^{\,3} h_w}\right]^{0.25} \tag{2.31}$$

Figure 2.10: Possible positions of supports for different hogging moment diagrams.

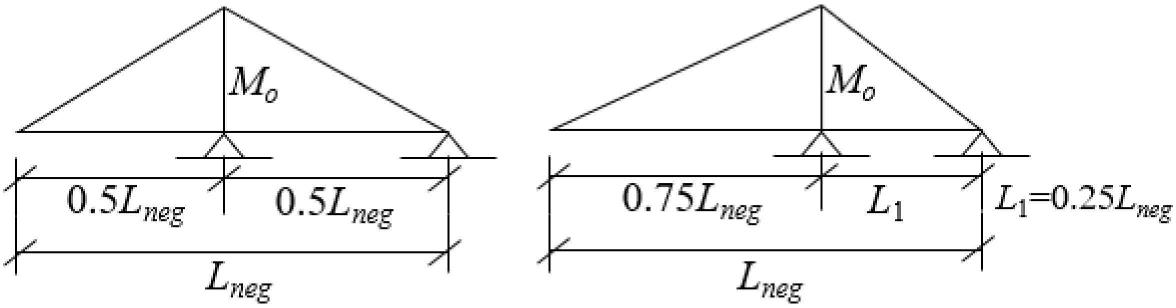

Source: Adapted from Oliveira (2018).

Posteriorly, Nery *et al*. (2023) proposed the coefficient referring to the hogging moment distribution (C_{dist}) for the **Eq. 2.23** developed by Dias (2018) and Dias *et al*. (2019). This way, Nery *et al*. (2023) present **Eq. 2.32** as an adaptation of the method proposed by Dias (2018) and Dias *et al*. (2019), addressing other load conditions. **Eq. 2.32** is the M_{cr} formulation presented in the new version of the Brazilian code (ABNT NBR 8800:2024), in which the C_{dist} coefficient is given by **Tables 2.8-2.9**.

$$M_{cr} = C_{dist} \frac{k_g}{h_0} \left\{ GJ + \frac{EC_{w,d}}{L^2} \left[\left(n\pi\right)^2 + \left(\frac{\eta_b}{n\pi}\right)^2 \right] \right\} \tag{2.32}$$

Finally, the European (prEN 1994-1-1) and Brazilian codes (ABNT NBR 8800:2024) also recommends determining the M_{cr} via Linear Buckling Analysis (LBA) using numerical models.

Table 2.8: C_{dist} coefficient for continuous beams with loading on the analyzed span (L).

***Moment distribution**	ψ								
	0.50	0.75	1.00	1.25	1.50	1.75	2.00	2.25	2.50
	2.00	1.78	1.65	1.56	1.50	1.47	1.43	1.36	1.35
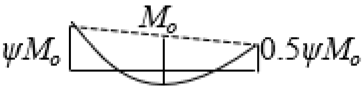	1.96	1.73	1.59	1.50	1.44	1.40	1.37	1.34	1.32
	1.94	1.70	1.56	1.47	1.41	1.37	1.34	1.31	1.29
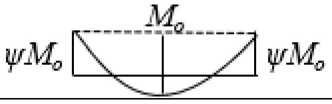	1.92	1.67	1.53	1.44	1.38	1.33	1.30	1.27	1.24

*M_o is the maximum moment, considering the analyzed span as simply supported.

Source: Adapted from ABNT NBR 8800: 2024.

Table 2.9: C_{dist} coefficient for continuous beams without loading on the analyzed span (L).

***Moment distribution**	ψ				
	0.00	0.25	0.50	0.75	1.00
	1.19	1.15	1.11	1.06	1.00
	1.19	1.23	1.26	1.30	1.33

*M_o is the higher moment, in modulus, in the analyzed span, in which ψ values higher than 1.00 must be taken as 1.00.

Source: Adapted from ABNT NBR 8800: 2024.

2.1.2.2 LDB ultimate moment

The standards address the LDB in continuous composite beams by applying a reduction factor in the plastic moment (M_{pl}) of the analyzed section under hogging moment. For this, these standards use curves expressed in terms of the slenderness ratio and the reduction factor determined by full-scale tests of steel elements with initial geometric imperfections and residual stress.

European (EN 1994-1-1: 2004 / prEN 1994-1-1) and Brazilian codes (ABNT NBR 8800: 2008 / ABNT NBR 8800: 2024) present analogous formulations to determine the cross-section plastic moment ($M_{pl\text{-}C.beam}$), which are composed of steel I-beam and reinforcement bars (composite section). According to the codes in question, the plastic theory (full plastic rectangular distribution stress) must be used, and $M_{pl\text{-}C.beam}$ is obtained with **Eq. 2.33**, where the parameters are: longitudinal reinforcement area (A_{bar}); reinforcement bars yield strength ($f_{y,bar}$); I-section tensioned area (A_{at}); I-section compressed area (A_{ac}); steel I-section yield strength (f_y); distance between the geometric centers of the composite cross-section and reinforcement bars (d_3); distance between the geometric centers of the composite cross-section and I-section tensioned area (d_4); and distance between the geometric centers of the composite cross-section and I-section compressed area (d_5).

$$M_{pl-C.beam} = T_{ds} d_3 + A_{at} f_y d_4 + A_{ac} f_y d_5 \tag{2.33}$$

$$T_{ds} = A_{bar} f_{y,bar} \tag{2.34}$$

The parameters that compose **Eq. 2.33** depend on the composite section geometry, materials yield strength, and plastic neutral axis (PNA) position. This way, two cases of PNA position usually occur in steel-concrete composite beams in hogging moment regions: PNA on the I-section web and PNA on the I-section upper flange. In the present study, the $M_{pl\text{-}C.beam}$ formulations are developed considering the composite section in the center region of the opening. Thus, to calculate $M_{pl\text{-}C.beam}$ in the region with solid web, D_o equal to zero must be adopted. The cases in question are detailed below:

I - PNA on the I-section web is true if "$(A_a - A_f)*f_y \geq A_f*f_y + T_{ds}$" which can have PNA position (y_{PNA}) defined in relation to the I-section upper face, as shown in **Figure 2.11**. The parameters A_f is the flange area, A_a is the I-section area at the opening center, and T_{ds} is the calculation tensile strength of the reinforcement bars ($A_{bar}*f_{y,bar}$).

Figure 2.11: PNA on the I-section web.

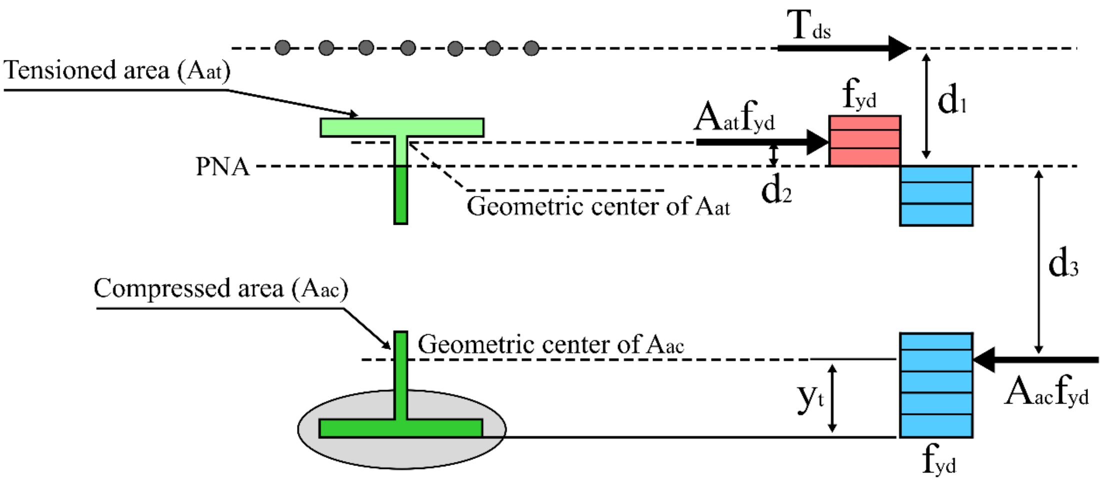

Source: Oliveira *et al*. (2023a).

As the PNA position is on the web, the steel I-section's tensioned area (A_{at}) and compressed area (A_{ac}) are defined as presented in **Eqs. 2.35-2.36**, respectively.

$$A_{at} = b_f t_f + \left(y_{PNA} - t_f\right) t_w \tag{2.35}$$

$$A_{ac} = A_a - A_{at} \tag{2.36}$$

This way, the PNA position is obtained with the equilibrium of resulting forces. These resulting forces are equivalent to full plastic rectangular distribution stress on reinforcement bars and I-section's tensioned and compressed area. Thus, the PNA position in relation to the I-section upper face is determined by **Eq. 2.37**.

$$y_{PNA} = t_f + \frac{-A_{bar} f_{y,bar} + f_y \left(A_a - 2 b_f t_f\right) - D_o t_w}{2 f_y t_w} \tag{2.37}$$

To calculate the distances d_2 and d_3 of **Eq. 2.33**, the geometric center positions of the I-section's tensioned (y^*_{at}) and compressed area (y^*_{ac}) are necessary. **Eq. 2.38** shows the formulation for the tensioned area with the origin on the I-section upper face. On the other hand, **Eq. 2.39** presents the calculus for the compressed area with the origin on the I-section lower face.

$$y^*_{at} = \frac{0.5 b_f t_f^2 + t_w \left(y_{PNA} - t_f\right)\left[0.5\left(y_{PNA} - t_f\right) + t_f\right]}{A_{at}} \tag{2.38}$$

$$y^*_{ac} = \frac{0.5 b_f t_f^2 + t_w \left[0.5\left(d_g - y_{PNA} - t_f - D_o\right)^2 + t_f\right]}{A_{ac}} \tag{2.39}$$

Finally, the distances d_1, d_2 and d_3 are obtained according to **Eqs. 2.40-2.42**, in which c is the distance between the geometric center of the reinforcement bars and the I-section upper face.

$$d_1 = y_{PNA} + c \tag{2.40}$$

$$d_2 = y_{PNA} - y^*_{at} \tag{2.41}$$

$$d_3 = d_g - y_{PNA} - y^*_{ac} \tag{2.42}$$

II - PNA on the I-section upper flange is true if "($A_a - A_f$)*$f_y < A_f$*$f_y + T_{ds}$" and "A_a*$f_y \geq T_{ds}$" which also can have PNA position (y_{PNA}) defined in relation to the I-section upper face. **Figure 2.12** illustrates this case.

Figure 2.12: PNA on the I-section upper flange.

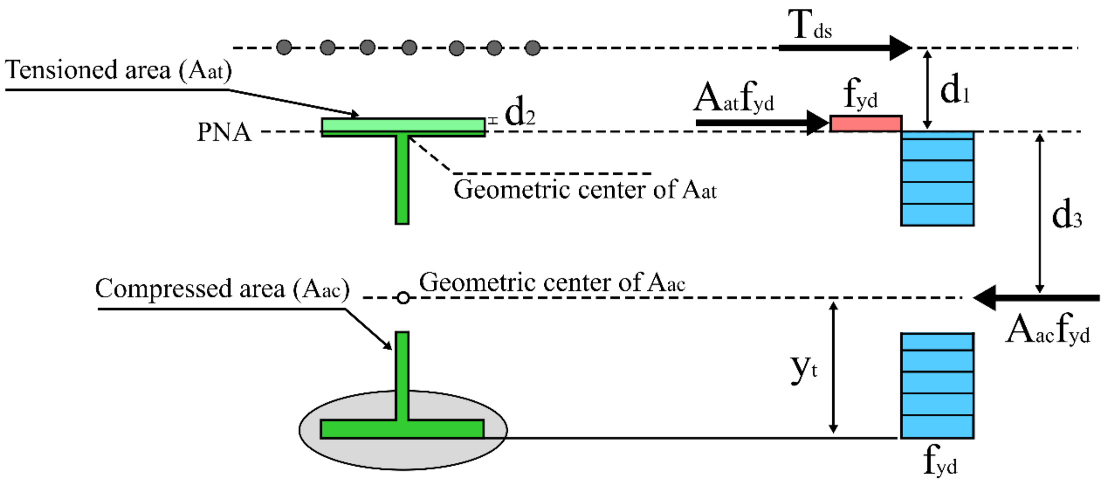

Source: Oliveira *et al*. (2023a).

As the PNA position is on the upper flange, the steel I-section's tensioned area (A_{at}) and compressed area (A_{ac}) are obtained by **Eqs 2.43-2.44**, respectively.

$$A_{at} = b_f y_{PNA} \tag{2.43}$$

$$A_{ac} = b_f t_f + t_w \left(d_g - 2t_f - D_o\right) + b_f \left(t_f - y_{PNA}\right) \tag{2.44}$$

Thus, the PNA position in relation to the I-section upper face is determined by **Eq. 2.45**.

$$y_{PNA} = \frac{-A_{bar} f_{y,bar} + f_y \left[2b_f t_f + t_w \left(d_g - 2t_f - D_o\right)\right]}{2 f_y b_f} \tag{2.45}$$

Like the case I, the formulation for the center position of the tensioned area is developed with the origin on the I-section upper face, and for the compressed area, the origin is on the I-section lower face. **Eqs. 2.46-2.47** describe the calculus of the center positions y^*_{at} and y^*_{ac}. **Eqs. 2.40-2.42** must be used to obtain the distances d_1, d_2 and d_3.

$$\bar{y}_{at} = \frac{y_{PNA}}{2} \tag{2.46}$$

$$\bar{y}_{ac} = \frac{0.5b_f t_f{}^2 + t_w\left(d_g - D_o - 2t_f\right)0.5d_g + b_f\left(t_f - y_{PNA}\right)\left[d_g - y_{PNA} - 0.5\left(t_f - y_{PNA}\right)\right]}{A_{ac}} \tag{2.47}$$

The North American (AISC 360-22 / AASHTO 2017) and Australian standards (AS4100:2020 and AS / NZS2327-2017) provide adaptations of the classic lateral-torsional buckling theories of partially constrained beams. These methodologies consider only the steel I-beam as a resistant cross-section against LDB. **Eq. 2.48** determines the I-section plastic moment ($M_{pl.I\text{-}beam}$), which is used in these formulations.

$$M_{pl_{I-beam}} = 2b_f t_f\left(\frac{t_f + h_w}{2}\right) + \frac{t_w\left(h_w^2 - D_0^2\right)}{4} \tag{2.48}$$

AASHTO 2017 proposes modifications to the LTB formulation of steel I-beams present in AISC 360-22. On the other hand, the Australian standards (AS4100:2020 and AS / NZS2327-2017) present a method that evaluates the so-called critical flange that is not restricted against instability phenomena (ROSSI *et al.*, 2020a). This formulation is shown in **Table 2.10**, in which l_e is the effective length according to the codes AS4100:2020 and AS / NZS2327-2017. In the present study, the North American standards (AISC 360-22 and AASHTO 2017) will not be covered. Therefore, **Table 2.10** shows the formulations for determining the LDB ultimate moment present in Australian (AS4100:2020 and AS / NZS2327-2017), European (EN 1994-1-1: 2004 / prEN 1994-1-1) and Brazilian codes (ABNT NBR 8800: 2008 / ABNT NBR 8800: 2024).

The current version of the Eurocode 4 (EN 1994-1-1: 2004) cites the design curves presented in the previous version of the Eurocode 3 (ENV 1993-1-1: 2005), which adopts multiple Perry-Robertson design curves from ECCS (European Convention for Constructional Steelwork) (ZHOU; YAN, 2017). The Eurocode design curves (EN 1994-1-1: 2004 / ENV 1993-1-1: 2005) are described by the formulation shown in **Table 2.10**, in which α_{LT} is an imperfection factor given by ENV 1993-1-1: 2005 according **Table 2.11.** Meanwhile, the draft version of the Eurocode 4 (prEN 1994-1-1) cites the approach described in the current version of the Eurocode 3 (EN 1993-1-1: 2022), which uses the same α_{LT} provisions given by **Table 2.11** for monosymmetric sections, considering the lowest flange width (b_{min}) in the h/b ratio.

On the other hand, EN 1993-1-1: 2022 provides the α_{LT} proposed Taras and Greiner (2010) for doubly symmetric sections, given by **Table 2.12**.

Table 2.10: Procedures for determining the LDB resistance of steel-concrete composite beams.

Source	**LDB ultimate moment (M_u)**	**LDB elastic critical moment (M_{cr})**
Australian Standards	$M_{u,dist} = \alpha_m \alpha_s M_{pl_{I-beam}} \leq M_{pl_{I-beam}}$ $\alpha_m = \frac{1.7 M_{m\wedge x}}{\sqrt{\left[(M_2)^2 + (M_3)^2 + (M_4)^2\right]}} \leq 2.5$ $\alpha_s = 0.6\left\{\sqrt{\left[\left(\frac{M_{pl_{I-beam}}}{M_{cr}}\right)^2 + 3\right]} - \left(\frac{M_{pl_{I-beam}}}{M_{cr}}\right)\right\}$	$M_{cr} = \sqrt{\left\{\left(\frac{\pi^2 EI_y}{l_e^2}\right)\left[GJ + \left(\frac{\pi^2 EC_w}{l_e^2}\right)\right]\right\}}$
EN 1994-1-1: 2004 / prEN 1994-1-1	$M_{u,dist} = \chi_{LT} M_{pl-C.beam}$ $\chi_{LT} = \left[\phi_{LT} + \sqrt{\phi_{LT}^2 - \bar{\lambda}_{LT}^2}\right]^{-1} \leq 1$ $\phi_{LT} = 0.5\left[1 + \alpha_{LT}\left(\bar{\lambda}_{LT} - 0.2\right) + \bar{\lambda}_{LT}^2\right]$ $\bar{\lambda}_{LT} = \sqrt{\frac{M_{pl-C.beam}}{M_{cr}}}$	• Formulations developed based on the U-frame model
NBR 8800: 2008 / NBR 8800: 2024	$M_{u,dist} = \chi M_{pl-C.beam}$ $\lambda_0 \leq 1.5 : \chi = 0.658^{\lambda_0^2}$ $\lambda_0 > 1.5 : \chi = 0.877 / \lambda_0^2$ $\bar{\lambda}_0 = \sqrt{\frac{M_{pl-C.beam}}{M_{cr}}}$	• NBR 8800: 2008 uses the formulation of Roik *et al*. (1990). • NBR 8800: 2024 uses the proposition of Dias *et al*. (2019) and Nery *et al*. (2023).

Source: Adapted from Rossi *et al*. (2021b).

Table 2.11: Imperfection factor *α* for design curves.

I-section type	**^{a}Limits**	**Design curve**	**Imperfection factor *α***
Rolled I- or H-sections	$h/b \leq 2.0$	a	0.21
	$h/b > 2.0$	b	0.34
Welded I-sections	$h/b \leq 2.0$	c	0.49
	$h/b > 2.0$	d	0.76

^{a}*h* is heigh and *b* is flange width of the cross-section

Source: Adapted from ENV 1993-1-1: 2005 and EN 1993-1-1: 2022.

Table 2.12: Imperfection factor α_{LT} proposed by Taras and Greiner (2010).

I-section type	[a]Limits	[b]Imperfection factor α_{LT}
Rolled I- or H-sections	$h/b > 1.2$	$0.12\sqrt{\frac{W_x}{W_y}} \leq 0.34$
	$h/b \leq 1.2$	$0.16\sqrt{\frac{W_x}{W_y}} \leq 0.49$
Welded I-sections	-	$0.21\sqrt{\frac{W_x}{W_y}} \leq 0.64$

[a] h is heigh and b is flange width of the cross-section; [b] W_x and W_y are elastic section modulus taken about the strong and weak axis, respectively

Source: Adapted from Taras and Greiner (2010) and EN 1993-1-1: 2022.

The previous and current versions of the Brazilian code (ABNT NBR 8800:2008 / ABNT NBR 8800:2024) use the 2P design curve (**Table 2.10**) provided by the SSRC (Structural Stability Research Council) (ROSSI *et al.*, 2020a). The only change between both versions is the M_{cr} formulation, as described in **section 2.1.2.1**.

Rossi *et al.* (2020a) state that the Perry-Robertson curves are based on steel elements under bending, which can be inappropriate for determining the LDB resistance in steel-concrete composite beams. On the other hand, the 2P curve by SSRC is the result of experimental tests of steel elements under compression.

Salah (2009) performed experimental tests on twelve composite beams with web openings under hogging bending. The author also numerically investigated the behavior of the models tested using the ABAQUS software. Salah (2009) used the results of these investigations to validate the direct strength equation developed to verify the M_u to LDB. According to Gizejowski and Salah (2010b), calculations were performed to predict the relative slenderness λ in terms of the elastic buckling load factor Λ_{cr} and the limit load factor Λ_{pl}. For each tested beam, the dimensionless distortion buckling load $\Lambda_{b,exp}/\Lambda_{pl}$ was calculated, where $\Lambda_{b,exp}$ is the experimentally obtained distortional buckling load factor. The results were compared with the predictions of the $\Lambda_{b,dsm}/\Lambda_{pl}$ direct strength method, according to **Eqs. 2.49-2.50**.

$$\frac{\Lambda_{b,dsm}}{\Lambda_{pl}} = \left(\alpha_1 - \alpha_2 \frac{1}{\bar{\lambda}^k}\right)\frac{1}{\bar{\lambda}^k} \tag{2.49}$$

$$\bar{\lambda} = \sqrt{\frac{\Lambda_{pl}}{\Lambda_{cr}}} \tag{2.50}$$

From the parametric study of Salah (2009), the author obtained the following constants for **Eq. 2.49**: $\alpha_1 = 0.75$, $\alpha_2 = 0.11$ and $k = 1$. The proposed methodology was compared with the results of the experimental tests. The authors concluded that the proposed method provides safe results of the LDB resistant capacity of composite beams with web openings.

As described in this section, there to many possibilities to calculate the ultimate moment to LDB of steel-concrete composite alveolar beams. Most of these approaches still need to have their precision measured for the beams in question, mainly for composite castellated beams, in which no assessment present in the bibliography. This way, **section 3.1** deals with the accuracy verification of all approaches shown in this section for composite castellated and cellular beams.

2.1.3 WPB resistance predictions

This section covers the procedures from design guides to calculate the WPB resistance of cellular and castellated beams. The review paper by Ferreira, Martins and Nardin (2020a) presented different predictions found in the literature for cellular I-beams, and those related to design guides are addressed in the present study (**section 2.1.3.1**). For castellated beams, the formulations from Steel Design Guide 31 (FARES; COULSON; DINEHART, 2016) are brought into this research (**section 2.1.3.2**). In addition, Eurocode 3 (EN 1993-1-13: 2024) has been updated and now covers the verification of steel alveolar beams, with the WPB resistant of these beams being addressed. The formulation procedures for castellated and cellular beams presented in EN 1993-1-13: 2024 are described in **section 2.1.3.3**.

2.1.3.1 Formulations for cellular beams

Ward (1990) proposed a formulation limited to composite and non-composite beams with symmetrical cellular I-sections. In the recommendations from Steel Design Guide 31 (FARES; COULSON; DINEHART, 2016), the Ward's proposition (1990) is adapted to asymmetrical cellular I-sections considering the most critical case between the upper and lower tees. The methodology addresses the horizontal shear force (V_h) in the web-post between the openings i and i+1, as shown in **Figure 2.13**. In this figure, the parameters are: the length between the opening diameter centers (p), the bending moment (M_i), the axial force in concrete of a composite section (C_i), the axial force in bottom tee (T_i), the effective depth of composite cellular beam ($d_{ef,comp}$), the opening diameter (D_o), the web-post width (b_w), and the distance from the geometric center of the tee to its welded edge (y_o). For composite cellular beams with normal concrete slabs in hogging moment regions, the parameters C_i and T_i become the axial force in bottom tee and the axial force in reinforcement bars of a composite section, respectively. This model is illustrated in **Figure 2.14**.

Figure 2.13: Ward's model (1990).

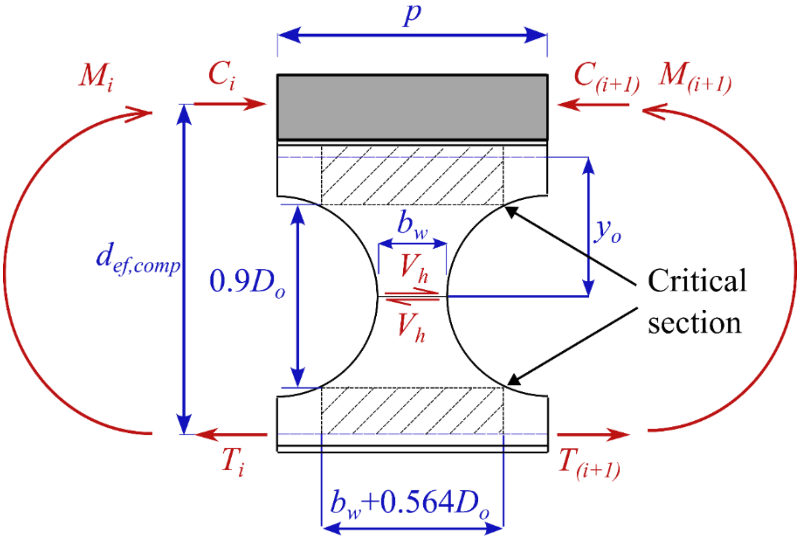

Source: Adapted from Ferreira, Martins e Nardin (2021).

Figure 2.14: Ward's model (1990) for composite cellular beams in hogging moment regions.

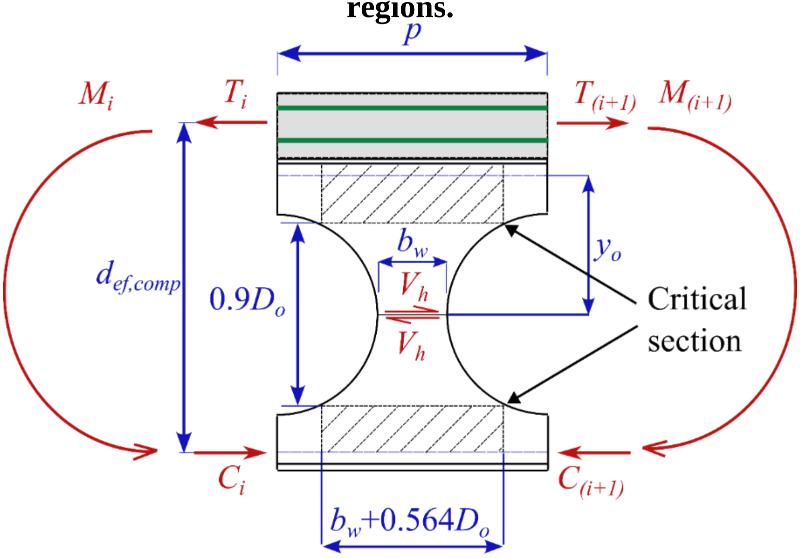

Source: Adapted from Ferreira, Martins e Nardin (2021).

The horizontal shear force (V_h) and the bending moment regarding the yielding in the critical section (M_{vh}) are calculated via **Eqs. 2.51-2.52**.

$$V_h = \left| \frac{M_{i+1} - M_i}{d_{ef,comp}} \right| \tag{2.51}$$

$$M_{Vh} = 0.9\left(\frac{D_o}{2}\right)V_h \tag{2.52}$$

Ward's proposition (1990) considers the parameters C_1, C_2 and C_3 to concern the geometric properties of the web-post. However, this formulation is limited for the $1.08 \leq p/D_o \leq 1.50$ and $1.25 \leq d_g/D_o \leq 1.75$. Therefore, the WPB resistance is determined by **Eqs. 2.53-2.54**.

$$M_{W,Rk} = M_{W,e}\left[C_1\left(\frac{p}{D_o}\right) - C_2\left(\frac{p}{D_o}\right)^2 - C_3\right] \tag{2.53}$$

$$M_{W,e} = \frac{t_w\left(p - D_o + 0.564D_o\right)^2}{6} f_y \tag{2.54}$$

An alternative method of calculation involves determining the resistance against the horizontal shear force, given by **Eq. 2.55**.

$$V_{Wh,Rk} = \frac{M_{W,e}}{0.45D_o}\left[C_1\left(\frac{p}{D_o}\right) - C_2\left(\frac{p}{D_o}\right)^2 - C_3\right] \tag{2.55}$$

Finally, the parameters C_1, C_2 and C_3 are calculated via **Eqs. 2.56-2.58**.

$$C_1 = 5.097 + 0.1464\left(\frac{D_o}{t_w}\right) - 0.00174\left(\frac{D_o}{t_w}\right)^2 \tag{2.56}$$

$$C_2 = 1.441 + 0.0625\left(\frac{D_o}{t_w}\right) - 0.000683\left(\frac{D_o}{t_w}\right)^2 \tag{2.57}$$

$$C_3 = 3.645 + 0.0853\left(\frac{D_o}{t_w}\right) - 0.00108\left(\frac{D_o}{t_w}\right)^2 \tag{2.58}$$

Lawson *et al*. (2006) and Lawson and Hicks (2011) developed a methodology based on the theory of compressed bar, as the horizontal shear force in the web welded region generates tension and compression stresses due to the bending of both tees (**Figure 2.15**). This analytical model is adopted by the Steel Construction Institute SCI P355.

Figure 2.15: Strut model.

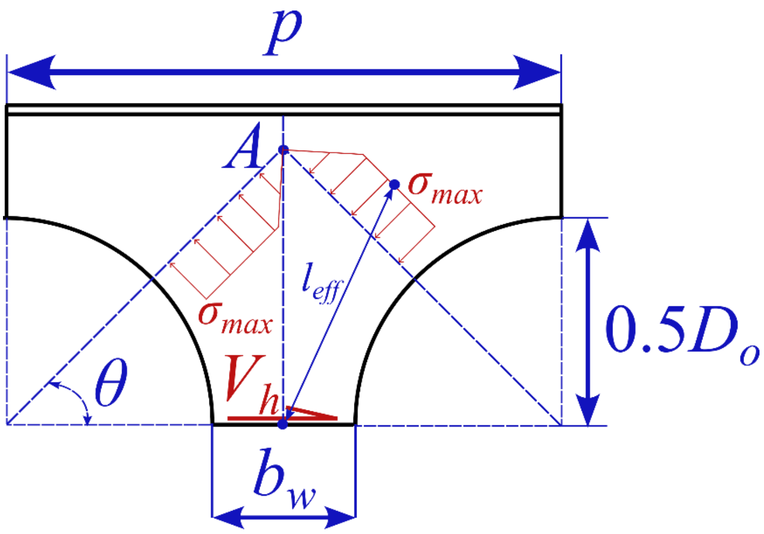

Source: Adapted from Ferreira, Martins e Nardin (2021).

Based on ENV 1993-1-1:2005, the compressed bar theory is employed considering the slenderness of the web-post length and adopting the curve "c" from this code, as described by **Eqs. 2.59-2.64**.

$$\sigma_{Rk} = \chi f_y \tag{2.59}$$

$$\chi = \frac{1}{\varphi + \sqrt{\varphi^2 - \bar{\lambda}^2}} \leq 1.0 \tag{2.60}$$

$$\varphi = 0.5\left[1 + 0.49\left(\bar{\lambda} - 0.2\right) + \bar{\lambda}^2\right] \tag{2.61}$$

$$\bar{\lambda} = \sqrt{\frac{f_y}{f_{cr,w}}} \tag{2.62}$$

$$f_{cr,w} = \frac{\pi^2 E}{\lambda_w^2} \tag{2.63}$$

$$\lambda_w = \frac{l_{eff}\sqrt{12}}{t_w} \tag{2.64}$$

The model of Lawson *et al*. (2006) and Lawson and Hicks (2011) consider the effective length as:

$$l_{eff} = 0.5\sqrt{b_w^2 + D_o^2} \leq 0.7D_o \tag{2.65}$$

Finally, the vertical shear resistance can be taken as:

$$V_{Lv,Rk} = \sigma_{Rk} t_w b_w \tag{2.66}$$

Panedpojaman, Thepchatri and Limkatanyu (2014) proposed an adaptation of the model from SCI P355 (LAWSON; HICKS, 2011; LAWSON *et al*., 2006), which considers the partial constraint of the web-post (**Figure 2.16**), adopting a factor k in the calculus of the effective length.

Figure 2.16: Model proposed by Panedpojaman, Thepchatri and Limkatanyu (2014).

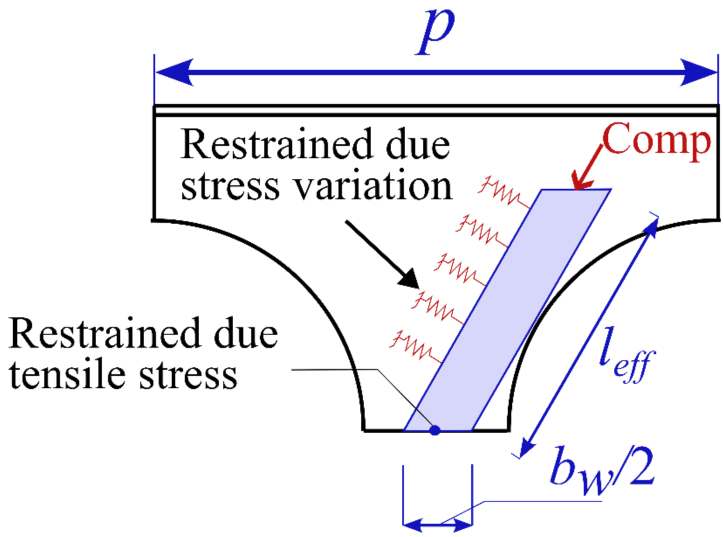

Source: Adapted from Ferreira, Martins e Nardin (2021).

This methodology regards the influence of the tees' height variation. According to the author, the effective length of the web-post is determined via **Eqs. 2.67-2.68**.

$$l_{eff} = k\left(0.5\sqrt{p^2 - D_o^2}\right) \tag{2.67}$$

$$k = 0.9\left(\frac{p}{D_o}\right)\left(\frac{D_o}{d}\right)^2 \leq \min\left(1.15\frac{D_o}{d}, 1.15\right) \tag{2.68}$$

2.1.3.2 Formulations for castellated beams

The Steel Design Guide 31 (FARES; COULSON; DINEHART, 2016) adopts the proposition by Aglan and Redwood (1974) to determine the WPB resistance, in which the same adaptation presented in **Figure 2.14** is applied for castellated beams, only changing the parameters of circular to hexagonal web opening, as shown in **Figure 2.17**.

Figure 2.17: Adaptation for composite castellated beams of the model presented in Steel Design Guide 31 regarding the case of hogging bending.

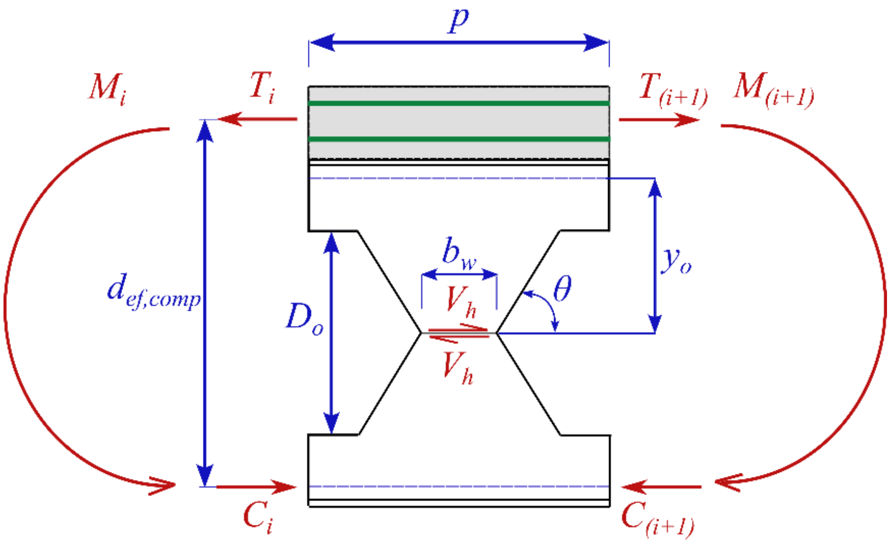

Source: Adapted from Ferreira, Martins e Nardin (2021).

This way, the horizontal shear force (V_h) and the bending moment regarding the yielding in the critical section (M_{vh}) are calculated via **Eqs. 2.69-2.70**, respectively.

$$V_h = \left| \frac{M_{i+1} - M_i}{d_{ef,comp}} \right| \tag{2.69}$$

$$M_{Vh} = \left(\frac{D_o}{2} \right) V_h \tag{2.70}$$

It is worth mentioning that the proposition of Aglan and Redwood (1974) is limited for the $45^0 \leq \theta \leq 60^0$, $10 \leq b_w/t_w \leq 30$ and $D_o/b_w \leq 8$. In this method, the plastic bending moment is calculated via **Eq. 2.71**.

$$M_{W,p} = 0.25 t_w \left(b_w + 2s \right)^2 f_y \tag{2.71}$$

For $\theta = 45°$, where θ is the angle of the hexagonal cut, the WPB resistance is obtained according to the cases presented in **Eqs. 2.72-2.74**. The value of $M_{W,Rk}/M_{W,p}$ is limited to 0.26, which is $M_{W,Rk}/M_{W,p}$ at b_w/t_w=10 with D_o/b_w =2. It can be made the interpolation between **Eqs. 2.72-2.74** based on actual b_w/t_w for $M_{W,Rk}/M_{W,p}$ at $\theta = 45°$.

$$\text{If } b_w/t_w = 10,\ M_{W,Rk} = M_{W,p}\left[0.351 - 0.051\left(\frac{D_o}{b_w}\right) + 0.0026\left(\frac{D_o}{b_w}\right)^2\right] \leq 0.26 M_{W,p} \tag{2.72}$$

$$\text{If } b_w/t_w = 20,\ M_{W,Rk} = M_{W,p}\left[3.276 - 1.208\left(\frac{D_o}{b_w}\right) + 0.154\left(\frac{D_o}{b_w}\right)^2 - 0.0067\left(\frac{D_o}{b_w}\right)^3\right] \tag{2.73}$$

$$\text{If } b_w/t_w = 30,\ M_{W,Rk} = M_{W,p}\left[0.952 - 0.30\left(\frac{D_o}{b_w}\right) + 0.0319\left(\frac{D_o}{b_w}\right)^2 - 0.0011\left(\frac{D_o}{b_w}\right)^3\right] \tag{2.74}$$

For $\theta = 60°$, the WPB resistance is obtained according to the cases presented in **Eqs. 2.75-2.77**. The value of $M_{W,Rk}/M_{W,p}$ is limited to 0.493, which is $M_{W,Rk}/M_{W,p}$ at b_w/t_w=10 with D_o/b_w =2. It can be made the interpolation between **Eqs. 2.73-2.75** based on actual b_w/t_w for $M_{W,Rk}/M_{W,p}$ at $\theta = 60°$.

$$\text{If } b_w/t_w = 10,\ M_{W,Rk} = M_{W,p}\left[0.587(0.917)^{\frac{D_o}{b_w}}\right] \leq 0.493 M_{W,p} \tag{2.75}$$

$$\text{If } b_w/t_w = 20,\ M_{W,Rk} = M_{W,p}\left[1.96(0.699)^{\frac{D_o}{b_w}}\right] \tag{2.76}$$

$$\text{If } b_w/t_w = 30,\ M_{W,Rk} = M_{W,p}\left[2.55(0.574)^{\frac{D_o}{b_w}}\right] \tag{2.77}$$

An alternative method of calculation involves determining the resistance against the horizontal shear force, given by **Eq. 2.78**.

$$V_{Wh,Rk} = \frac{M_{W,Rk}}{0.5 D_o} \tag{2.78}$$

2.1.3.3 Formulation provided by EN 1993-1-13:2024 /prEN 1994-1-1

The draft version of the updates in Eurocode 4 (prEN 1994-1-1) defines the horizontal shear force in web-post ($V_{wp,Ed}$) as shown in **Figure 2.18**. $V_{wp,Ed}$ is given by **Eq. 2.79**.

Figure 2.18: Forces in the web-post between web openings according to prEN 1994-1-1.

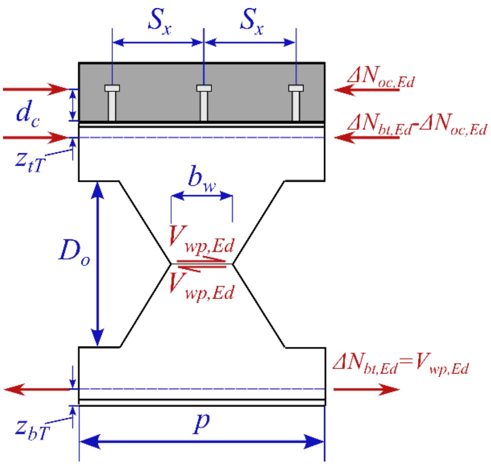

Source: Adapted from prEN 1994-1-1.

$$V_{wp,Ed} = \frac{V_{av,Ed}\, p}{d_g - z_{bT} + d_c} \tag{2.79}$$

It is noteworthy that the horizontal shear force defined by **Eq. 2.79** from prEN 1994-1-1 provides values very close to those given by **Eq. 2.69** from Steel Design Guide 31, and both formulations provide equal values in the case of uniform vertical shear force along the analyzed span. This way, for an approach of hogging moment regions, the same adaptation for the procedure from Steel Design Guide 31 (**Figure 2.16**) is suggested to also adapt the procedure from prEN 1994-1-1. For this adaptation, d_c becomes the distance between the reinforcement bars' geometric center and the steel profile's top face.

To determine the WPB resistance of steel alveolar I-beams, EN 1993-1-13:2024 presents a formulation based on an effective length of the compressed web-post, which is dependent on the opening geometry. According to this code, the axial force in the web-post ($N_{wp,Ed}$) must satisfy:

$$\frac{N_{wp,Ed}}{N_{wp,Rd}} \leq 1.0 \tag{2.80}$$

in which $N_{wp,Rd}$ is the web-post buckling resistance. For this verification, the EN 1993-1-13:2024 states that the compressive force acting on the web-post ($N_{wp,Ed}$) must be taken equal to the horizontal shear force ($V_{wp,Ed}$), given by:

$$N_{wp,Ed} = V_{wp,Ed} \tag{2.81}$$

The web-post buckling resistance ($N_{wp,Ed}$) should be taken as:

$$N_{wp,Rd} = \frac{\chi_{wp} b_w t_w f_y}{\gamma_V} \tag{2.82}$$

in which the minimum value of the multiple of the web thickness (t_w) and yield strength (f_y) of the top and bottom tees considered separately must be taken. In addition, χ_{wp} should be determined using the buckling curve "a" from EN 1993-1-1:2022 for all steel grades, considering the relative slenderness of the web-post (λ_{wp}).

For alveolar I-beams with hexagonal openings (castellated I-beams), λ_{wp} is given by:

$$\lambda_{wp} = \frac{1.75\sqrt{2b_w^{\,2} + D_o^{\,2}}}{t_w}\frac{1}{\lambda_1} \le \frac{2.7D_o}{t_w}\frac{1}{\lambda_1} \tag{2.83}$$

$$\lambda_1 = \pi\sqrt{\frac{E}{f_y}} = 93.9\varepsilon \rightarrow \varepsilon = \sqrt{\frac{235}{f_y}} \tag{2.84}$$

Meanwhile, for alveolar I-beams with circular openings (cellular I-beams), λ_{wp} is given by:

$$\lambda_{wp} = \frac{1.75\sqrt{b_w^{\,2} + D_o^{\,2}}}{t_w}\frac{1}{\lambda_1} \le \frac{2.4D_o}{t_w}\frac{1}{\lambda_1} \tag{2.85}$$

$$\lambda_1 = \pi\sqrt{\frac{E}{f_y}} = 93.9\varepsilon \rightarrow \varepsilon = \sqrt{\frac{235}{f_y}} \tag{2.86}$$

2.2 HIGH-PERFORMANCE MATERIALS IN STEEL-CONCRETE COMPOSITE BEAMS

The adoption of advanced high-performance materials, such as High-Strength Steel (HSS) and Ultra-High-Performance Concrete (UHPC), contributes to innovative concepts of structural designs (LIU *et al*., 2023a). The UHPC is a new type of cement-based composite with elevated strength, durability, and fatigue resistance, and the HSS concerns the steel with yield strength above 460 MPa (HE *et al*., 2023).

Recently, the slab cracking of steel-concrete composite beams under hogging moment has been improved using high-performance materials (ZHAO *et al.*, 2023). Among the studies that addressed this issue, Hamoda *et al.* (2017) assessed the influence of High-Performance Concrete (HPC), which is a steel fiber reinforced concrete. The authors observed that the elastic stiffness of the composite beam with the HPC slab was 23% above that with the Normal-Concrete (NC) slab. Fan *et al.* (2020) performed experimental and analytical research on the flexural behavior of composite beams with steel I-section and Engineered Cementitious Composite (ECC) slab, in which a significant enhancement in stiffness and crack resistance for the steel-ECC composite beams was noted. Regarding the use of Carbon Fiber Reinforced Polymers (CFRP) in hogging moment regions, Sharif *et al.* (2016) conducted experimental studies in continuous composite girders, and Liu *et al.* (2022) four-point bending tests in composite beams. Sharif *et al.* (2016) stated that CFRP sheets can effectively prevent slab cracking, and Liu *et al.* (2022) verified a significant effect on the structural performance in terms of ultimate capacity, load-deflection and load-slip responses, crack propagation, ductility, and failure mode. Another option is the adoption of UHPC slabs, in which their investigations are described in **section 2.2.2.2**.

HSS elements, such as I-sections and shear connectors, have also been implemented in steel-concrete composite beams. Additionally to the better flexural performance, the use of HSS also provides a significant improvement in the behavior of steel and steel-concrete composite beams in seismic performance, under dynamic loads, and at low temperatures (BADALASSI *et al.*, 2017; CHEN *et al.*, 2023, 2016; GUO *et al.*, 2023; YAN *et al.*, 2016). According to the study by Badalassi *et al.* (2017), structures with HSS, compared to conventional steels, had an apparent decrease in the probability of failure due to the estimated seismic effects. Chen *et al.* (2023) observed that HSS can significantly increase the impact load resistance of steel castellated beams. Yan *et al.* (2016) developed numerical analyses of push-out tests focusing on the resistant capacity of connectors embedded in different concretes under Arctic conditions (low temperatures). The results showed a significant gain in the capacity of connectors with HSS. Further to conventional steel-concrete composite beams (concrete slab on steel I-beam), HSS I-sections have also been assessed in encased composite beams with Engineered Cementitious Composites and Lightweight Concrete (ECC-LWC) (KABIR *et al.*, 2020; KABIR; LEE; ZHANG, 2021).

The present study addresses the flexural behavior of steel-concrete composite beams with conventional and high-performance materials (HSS and UHPC), focusing on elements subjected to hogging moment. However, there is still no research on HSS-UHPC composite beams under hogging moment. This way, **sections 2.2.1.2** and **2.2.2.2** present the investigations on HSS-concrete and steel-UHPC composite beams under hogging moment, respectively. The studies on HSS-UHPC composite beams submitted to sagging moment is described in **section 2.2.2.1**.

2.2.1 The use of high-strength steel I-sections

With the development of manufacturing processes and material technology, there was an increase in the strength of available steels (MELA; HEINISUO, 2014). Therefore, steels considered high-performance are called High-Strength Steels (HSS). For example, more than 400 tons of HSS Q460, which has a nominal yield strength ($f_{y,nom}$) of 460 MPa, were used at the Chinese National Stadium, where the opening ceremony of the 2008 Olympic Games was held (WANG *et al.*, 2018).

According to Günther (2005), steels in this category reduce the cross-section of the elements and, consequently, material consumption, lighter structures, lower costs, greater durability (corrosion resistance), and less welding work. The same author also states that the reduction in weight can reach up to 20% for bridges with medium and long spans. HSS profiles have also been adopted in steel-concrete composite beams (YAN; LI; XIE, 2017). Another possibility for more optimization of these structures is using hybrid beams. These are made of welded profiles in which the flanges are made of HSS, and the web is made of low or mild-strength steel (VELJKOVIC; JOHANSSON, 2004).

Regarding the definition of HSS, there is no universally accepted answer to this question, and some authors also describe the classification of Very or Ultra-High-Strength steel (VHSS or UHSS). **Table 2.13** brings the definitions of HSS and VHSS/UHSS found in review papers and research articles related to the present study.

Table 2.13: Definitions of HSS and VHSS/UHSS from review papers and research articles.

Source	Classification (MPa)	
	High-strength steel (HSS)	Very or Ultra-high-strength steel (VHSS or UHSS)
Ban *et al*. (2011)	420 – 690	690 – 1100
Shi, Hu and Shi (2014) Xiong *et al*. (2016) Ban and Shi (2018) Kang *et al*. (2018) Yang *et al*. (2019) Kang, Meng and Lin (2020) Shao, Zhang and Hassanein (2020) Hassanein *et al*. (2021) Huang and Zhang (2022) Xiong *et al*. (2021) Tong *et al*. (2022) He *et al*. (2023a)	≥ 460	–
Odesskii *et al*. (2017)	400 – 450	–
Meng and Kang (2017)	≥ 420	–
Hradil *et al*. (2017)	500 – 700	–
Liew, Yan and Huang (2017)	≥ 700	–
Lee and Choi (2021)	400 – 690	> 690
Tümer, Schneider-Bröskamp and Enzinger (2022)	290 – 700	> 700
Bärnkopf, Jáger and Kövesdi (2022)	420 – 960	–
Le *et al*. (2020a)	460 – 1000	–

Source: The author (2023).

Most research defines HSS as those with yield strength equal to or higher than 460 MPa. In addition, Eurocode 3 (EN 1993-1-12:2007) addresses HSS with nominal yield strengths from 460 MPa to 700 MPa, briefly presenting a few extra design guidelines specifically for HSS. The North American standard (AISC 360-22) cites various specifications from the American Society for Testing and Materials (ASTM) regarding steel members of High-Strength Low-Alloy (HSLA) without definitions of high-strength steel. In this code, the acronym HSS refers to Hollow Structural Sections. According to AISC 360-22: "*The grades of steel approved for* *use under this Specification, covered by ASTM Specifications, extend to a yield stress of 80 ksi (550 MPa) for rolled shapes and 100 ksi (690 MPa) for plates*". The nominal yield strengths of structural steels described in British (BS 4360: 1990), Australian (AS/NZS3678-2016), and Brazilian (ABNT NBR 8800: 2008) standards are up to 450 MPa and 460 MPa in new Chinese steel structure design code (GB50017-2017).

As mentioned above, the covered steel yield strengths are up to 690 MPa in AISC 360-22 and 700 MPa in Eurocode (EN 1993-1-12:2007). However, these design methodologies are based on test data of Normal-Strength Steel (NSS) members with a nominal yield strength of less than 460 MPa (YAN *et al.*, 2020). Moreover, specific design guidelines for HSS implementation are not provided. These guidelines are primarily founded on NSS research, making their reliability and accuracy uncertain due to the limited scope of experimental and analytical research data (BAN *et al.*, 2012; SHI; HU; SHI, 2014). According to the review research by Ban and Shi (2018), applying standard design methods directly to HSS structures is impractical in most cases, as these advanced steels demonstrate distinct material characteristics compared to traditional steels.

The composition of microalloyed steels presents low carbon (C) contents in the range of 0.05% to 0.25% and a manganese (Mn) percentage of up to 2.0% (VILLALOBOS *et al.*, 2018). Additionally, combining other elements in small contents, such as chromium (Cr), nickel (Ni), molybdenum (Mo), copper (Cu), nitrogen (N), vanadium (V), niobium (Nb), titanium (Ti), and zirconium (Zr), can enhance mechanical and durability properties (BAKER, 2016). According to Benedito *et al*. (2024), Nb addition enhances the steel strength and toughness due to the precipitate-strengthening effect, which provides grain refinement at the microstructural level. Khaple *et al*. (2020) assessed the effect of niobium addition on the mechanical properties of low-density steel. The authors observed that the hardness, yield strength, and tensile strength increase with the increase in Nb content (**Figure 2.19a**). Khaple *et al*. (2020) attributed this occurrence to the cumulative contribution from the increase in the volume fraction of the fine NbC carbides and the resulting grain refinement. Despite the decrease in the elongation with the increase in Nb content, Khaple *et al*. (2020) noted that all the compositions exhibit significant (higher than 20%) tensile elongation (**Figure 2.19a**). Regarding high-strength steels, Ban and Shi (2018) cite that HSS have lower ductility (acceptable performance-based design), higher yield-to-tensile strength ratios, higher impact energy, different fracture toughness, and lower ratios between residual compressive stresses and steel yield strengths. The authors stated that there is no apparent yield plateau for steels of nominal yield strength higher than 500 MPa (**Figure 2.19b**).

Figure 2.19: Stress-strain relationship for different steel grades and Nb content.

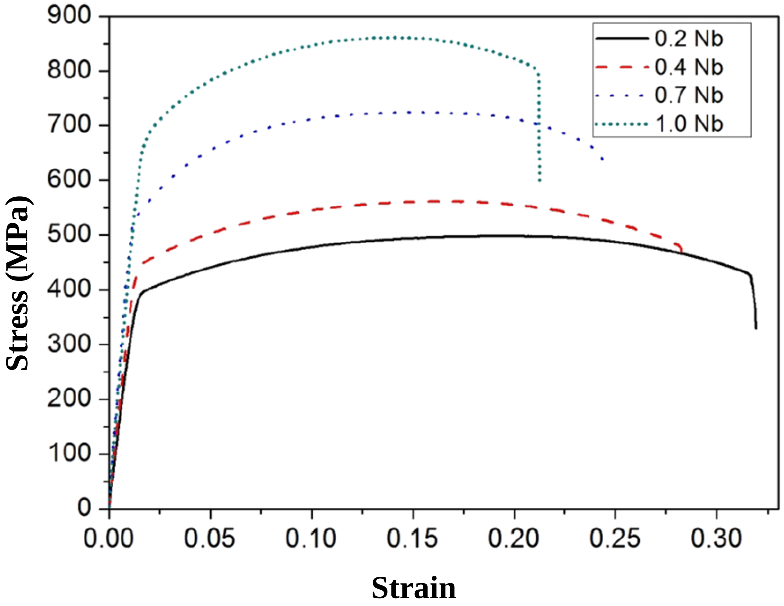

(a) Varying the Nb content

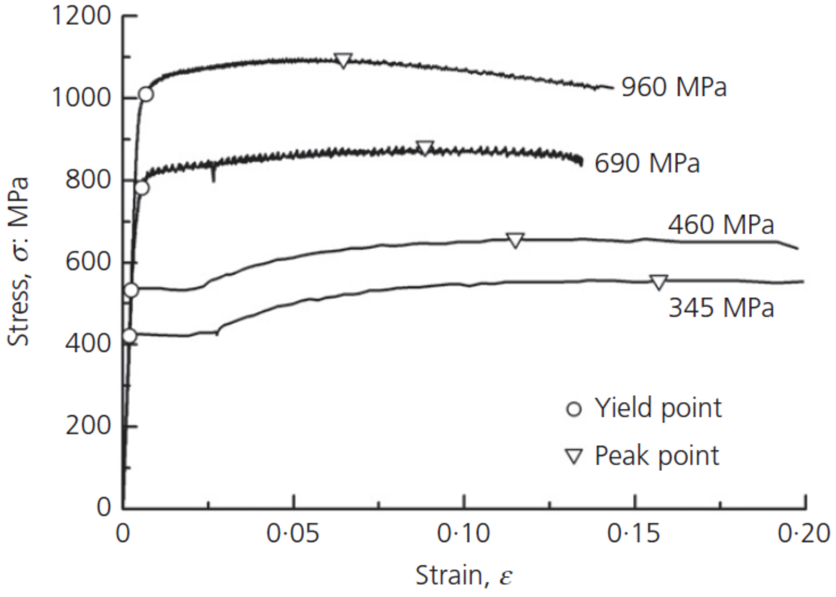

(b) Varying steel grade

Source: Khaple *et al*. (2020) and Ban and Shi (2018).

As there are few investigations on the behavior of conventional composite beams with HSS I-sections, **section 2.2.1.1** brings an overview of HSS I-beams, focusing on their stability behavior. Finally, **section 2.2.1.2** describes the studies on the flexural behavior of HSS-concrete composite beams, as those with UHPC slabs are addressed by section **2.2.2.2**.

2.2.1.1 Overview of high-strength steel I-beams

Varol and Cashell (2017) stated that, although HSS provides greater strength than NSS if the beams do not achieve plastic behavior (cross-section yielding), the gains with HSS will be limited. The capacity for instability often governs the design of steel structures. This problem is an obstacle to using HSS, as the capacity for instability increases less with the increase in yield strength or, in the worst case, does not increase (GÜNTHER, 2005). It is known that beams with greater slenderness can fail due to instability rather than obtaining the ultimate strength of the materials, and, commonly, steel structures are significantly slender. As the modulus of elasticity is the same for HSS and conventional steels, beams with greater slenderness require a more in-depth assessment, especially at high temperatures (VAROL; CASHELL, 2017). In a fire situation, the time to failure of steel structures is referred to as fire resistance, and the HSS structure has a fire resistance similar to that of the NSS structure (WANG *et al*., 2018). For this reason, the stability behavior of HSS H and I-sections have been investigated in beams, composite beams, columns, and beam-columns. This section presents an overview of the stability behavior of HSS I-beams, which supports the investigation of this study.

Ito *et al*. (2005) conducted tests focusing on the moment-plastic rotation of continuous steel girders with homogeneous and hybrid sections. The hybrid beams consisted in web of SM400 steel ($f_{y,nom}$ = 400 MPa) and flanges of SM570 ($f_{y,nom}$ = 570 MPa). The authors observed that the hybrid beams did not obtain a sudden decrease in the moment-plastic rotation curves after reaching the peak load, and the hybrid beams had more deformation capacity than the homogeneous beams. Lee *et al*. (2013) experimental analyzed the flexural and rotation capacity of HSB800 and HSA800 steel beams ($f_{y,nom}$ = 800 MPa), a noted a high flexural resistance and low rotation capacity. The author stated that this can be attributed to the lack of a clear yield plateau and the high steel yield ratio.

Shokouhian and Shi (2015) , Xiong *et al*. (2016), Yang *et al*. (2017, 2019), Kang *et al*. (2018), and Kang, Meng and Lin (2020) performed three and four-point bending tests of I-beams with Q460 steel ($f_{y,nom}$ = 460 MPa), focusing on the global stability behavior to LTB. These investigations showed that the North American (AISC 360-16) and Chinese (GB50017-2017) codes had results against safety, whereas Eurocode 3 (ENV 1993-1-1: 2005) is more conservative. Le *et al*, (2020a), Tankova *et al*. (2021), Xiong *et al*. (2021, 2022) and Le, Bradford e Valipour (2021) experimental assessed the global stability of steel I-beams with yield strengths significant higher than 460 MPa, such as 690 and 890 MPa. The authors also observed divergence between their results and those from the standard procedures. Eurocode 3 (ENV 1993-1-1: 2005) and Australian code (AS4100:1998 R2016) provided conservative results, and the North American (AISC 360-16) and Chinese (GB50017-2017) standard are non-conservative. This way, these standard procedures cannot be appropriated for LTB resistance prediction for these categories of HSS I-beams.

There is still no experimental investigation on HSS alveolar I-beams, having only numerical analyses. Regarding the local stability of these beams, Oliveira, Cardoso e Sotelino (2019) evaluated TLB in Litzka castellated beams, observing that TLB becomes relevant using HSS above 760 MPa of yield strength. Shamass and Guarracino (2020) analyzed the WPB behavior of cellular beams with steels S355, S460, S690, and S960. A WPB resistance prediction was proposed, which obtained better agreement with the numerical results than the methodologies proposed by Lawson *et al*. (2006) and Panedpojaman, Thepchatri and Limkatanyu (2014). According to the authors, their proposition had higher accuracy for the entire range of addressed geometries and steels due to its ability to adapt the width and inclination of the compressed ideal strut to the case geometry. Ferreira *et al*. (2023) developed an extensive parametric study on the WPB resistance of HSS I-beams with elliptically-based web openings and steels S460, S690 and S960. The author presented a formulation to predict WPB capacity of these beams on the truss model according to Eurocode 3 (EN 1993-1-1: 2005). Ferreira *et al*. (2023) stated that the steel yield strength was influential, as increasing it, the WPB resistance also enhances. In addition, the proposed equation obtained high similarity to the numerical results ($R^2 = 0{,}9816$).

Regarding the global stability of HSS alveolar I-beams, Weidlich, Sotelino and Cardoso (2021) analyzed the coupling of LTB and TLB in Litzka castellated beams with steel yield strength equal to 345, 460, 690, 965, 1210, 1600, 2000 and 2300 MPa. According to the authors, although TLB is a failure mode rarely mentioned in the literature, it can govern the capacity of beams with a high local slenderness ratio, resulting from the combination of large flange width/thickness ratios and steels with higher yield strength. Hosseinpour and Sharifi (2021) assessed castellated beams with steel yield strength of 275, 345, 460, 550, and 690 MPa. The authors observed instability modes by LTB, Web-Distortional Buckling (WDB) and LDB. Most models characterized failure by LDB, as expected by the authors due to the I-sections with thick flanges and slender webs. Reducing the global slenderness of the beam, local slenderness of the flanges, and steel yield strength and increasing the local slenderness of the web increased the probability of WDB. On the other hand, LTB was shown to be present in beams with greater global slenderness, greater local slenderness of the flange, greater steel yield strength, and lower local slenderness of the web. Hosseinpour and Sharifi (2021) also verified the accuracy of code procedures for verifying the resistant capacity of the beams, which provided results against safety, with AISC 360-16, ENV 1993-1-1:2005, and AS4100: 1998 R2016 in order from the most to the least non-conservative among the methods. Salah (2022) brings the only study of hybrid alveolar beams using HSS, in which the study consists in homogeneous and hybrid castellated sections of steels S275, S355, S420, and S460. As castellated beams are normally formed by two parts of laminated profiles, for the hybrid sections, steels with higher yield strength were adopted in the upper tee (compressed flange). The study focused on the LTB and LDB behavior of these beams, and an analytical formulation was also presented to predict the LTB and LDB resistant capacity of homogeneous and hybrid castellated beams, which obtained a good approximation in relation to the numerical results. Salah (2022) noted that applying a higher grade of steel to the upper half of the castellated beam is more significant when considering a relatively compact flange. Another point is that whenever lateral instability is expected, it is recommended to use hybrid castellated beams to increase the load capacity by up to 25%, depending on the geometry of the beam and the transverse restrictions applied.

2.2.1.2 Flexural behavior of HSS-concrete composite beams with NC slab

Few investigations addressed the flexural behavior of HSS-concrete composite beams. Yan, Li and Xie (2017) carried out numerical analyses of push-out and four-point bending tests on steel-elastic concrete composite (SECC) beams. H-sections with different steel grades were adopted, such as S275, S355, S460 and S690. According to the authors, increasing the steel yield strength from 275 MPa to 355 MPa, 460 MPa, and 690 MPa, the ultimate capacity of SECC beams with 0%, 5%, and 10% rubber content were all increased by 21%, 46 % and 94%, respectively.

Shin and Kim (2019) also developed numerical models, in which the behavior of composite girders with HSB690 steel subjected to hogging moment was analyzed. The authors observed that using I-sections with compact web and flanges, the composite beams reached the plastic moment before WLB and FLB. However, the sections with non-compact flange and web were significantly affected by the initial imperfections in the flexural resistance, since the initial imperfections promote the appearance of local buckling, resulting in subsequent redistribution of stresses. Finally, regarding the upper limit of yield strength equal to 485 MPa as one of the three main prerequisites for using the Appendix A6 of AASHTO, Shin and Kim (2019) concluded that this limit can be removed from the provisions.

Bui *et al*. (2020) performed numerical analyses of composite girders with symmetric and asymmetric profiles of HPS70W ($f_{y,nom}$ = 480 MPa) under sagging bending. The authors observed that WLB notably reduces the capacity, stiffness and ductility of both steel beams and steel-concrete composite beams with non-compact sections.

Skoglund, Leander and Karoumi (2020) evaluated the optimization of composite girders with hybrid and homogeneous I-sections using Genetic Algorithms (GA). The authors approached a case study of a continuous bridge, in which the computational routine was implemented to evaluate different steels (S275ML, S355ML, S420ML, S460ML, S500QL, S550QL, S620QL and S690QL. In the analyses, in addition to the load limits obtained by static loads, the authors evaluated the performance due to fatigue. Skoglund, Leander and Karoumi (2020) concluded that hybrid beam solutions provided the best utilization ratio and therefore also the most economical solutions; where the steel grade higher should be placed on the lower flange. Furthermore, the steel grade of the web plate and upper flange may be of equal importance.

Nguyen and Lee (2021) conducted test and numerical analyses of HSS-ECC composite beams under four-point sagging bending. The authors noted that the flexural capacity of HSS-ECC beams had a slight improvement concerning HSS-NC composite beam. However, the ductility was significantly enhanced with HSS-ECC composite beams.

2.2.2 The use of ultra-high-performance concrete slabs in composite beams

The development of construction materials has led to the incorporation of fiber-reinforced cementitious composites in steel-concrete composite structures, providing enhanced toughness, ductility, and durability (BENEDETTY *et al*., 2023). Owing to the outstanding mechanical characteristics of UHPC, such as high tensile and compressive strength and exceptional durability, there has been a recent suggestion to use UHPC slabs instead of normal concrete (NC) slabs in composite beams (HU *et al*., 2020). According to Naaman and Chandrangsu (2004), using UHPC slabs increases the flexural stiffness of beams, decreases their self-weight, and improves the durability of the beam. Huang *et al*. (2022) and Wen *et al*.

(2022) stated that the compressive strength of UHPC generally exceeds 150 MPa. On the other hand, standards like ASTM C1856/C1856M-17 define it as being above 120 MPa.

Due to the elevated compressive strength of UPHC slabs, the adoption of HSS shear connectors is required in some cases. Recent research performed push-out tests with HSS perfobond connectors embedded in UHPC slabs (LIU *et al*., 2023b, 2023a; MA *et al*., 2023). Benedetty *et al*. (2023) provided a detailed database of 246 push-out test models with headed connectors embedded in UHPC slabs, in which only 14 models have connector yield strength above 460 MPa from the investigations by Xu *et al*. (2021, 2022b, 2022c). Regarding bending tests of steel-UHPC composite beams, the use of HSS headed connectors is found in the assessments by Zhang *et al*. (2020), Zhu *et al*. (2020b), Fang *et al*. (2022), and Shi *et al*. (2022). In addition, HSS perfobond connectors were addressed in the experimental analyses by He *et al*. (2023a).

When UHPC precast slabs are used in composite beams, these slabs are manufactured with shear pockets. In sequence, the slab is allocated on the steel beam, having grouped shear connectors inside the shear pockets. In the final step, according to Benedetty *et al*. (2023), the pockets are commonly filled on the site with high-strength mortar or UHPC. Hu *et al*. (2020) stated that in the case of steel-UHPC composite beams, it is common to adopt shear pockets (**Figure 2.20b**) with headed studs for the connection between the UHPC precast slab (**Figure 2.20a**) and the steel profile. **Figure 2.20c** shows the shear pocket filling.

Figure 2.20: Manufacturing process of the specimens tested by Hu *et al*. (2020).

(a) Manufacturing of slab with shear pockets

(b) Shear pockets

(c) Filling the shear pockets

Source: Adapted from Hu *et al*. (2020).

Three-point bending tests have been predominantly adopted by investigations on the UHPC contribution in hogging moment regions since applying a single concentrated load simulates the action of a support reaction in a continuous composite beam (BENEDETTY *et al*., 2023). The superior performance of UHPC leads to a better solution for enhancing the flexural behavior of composite beams under hogging moment (ZHAO *et al*., 2023). According to Fang *et al*. (2022), the enhanced tensile strength of UHPC, combined with the fibers' bridging action, serves to reduce the opening and propagation of cracks for this case of hogging bending. Compared to NC, this superior characteristic potentially extends structures' service life.

Wang *et al*. (2019) proposed a fully dry-connected prefabricated steel-UHPC composite beam searching for accelerated bridge construction. The authors conducted bending tests and numerical analyses of this beam under hogging moment. The study examined how dividing UHPC panels and arranging the bolts affected their performance. It was found that changing the panel division did not significantly alter their load-deflection behavior. However, using fewer panels could lead to improved crack resistance. Additionally, increasing the distance between the bolts reduced the global stiffness and crack resistance. Zhang *et al*. (2020) experimentally analyzed the flexural responses of steel-UHPC composite beams with headed studs and bolted connectors at the interface, which showed excellent cracking and flexural performance under the hogging moment (**Figure 2.21**). In **Figure 2.21**, the abbreviations are steel-NC composite beam with studs (SC-S), steel-UHPC composite beam with studs (SU-S) and bolts (SU-B). Compared to the use of NC slabs, the authors noted an increase in the cracking load and flexural capacity by around 340% and 26%, respectively. In addition, the employ of bolted connectors resulted in a reduction of the tensile stress in the UHPC slab due to the bolts' slip, which had an enhanced crack resistance and rotation capacity, and a slight decrease of flexural stiffness and ultimate load concerning the adoption of headed studs.

Figure 2.21: Three-point bending tests by Zhang *et al*. (2020).

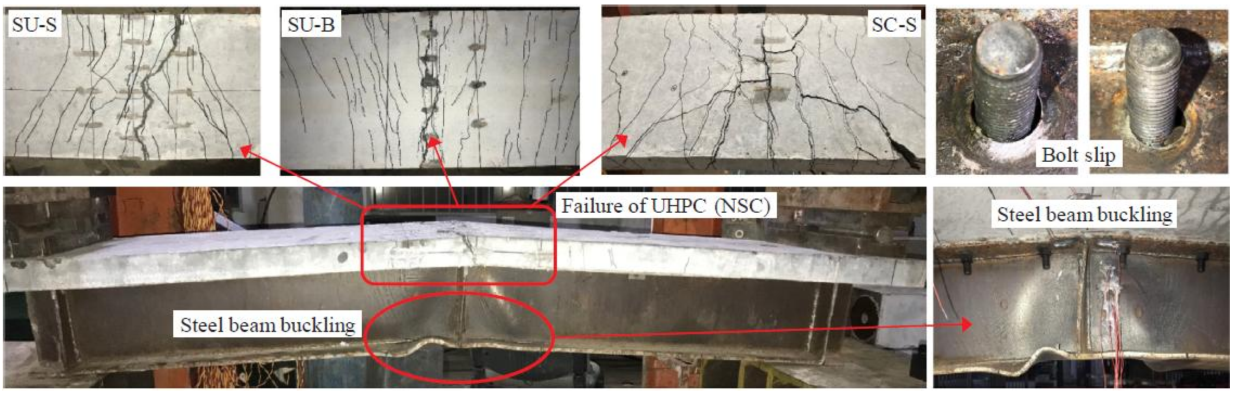

Source: Zhang *et al*. (2020).

Qi *et al*. (2020) performed experimental and numerical studies of composite beams with NC and UHPC precast slab and shear pockets. The test results indicated that employing UHPC slabs enhanced the composite beam's flexural stiffness and crack control (**Figure 2.22**).

Figure 2.22: Three-point bending tests by Qi *et al*. (2020).

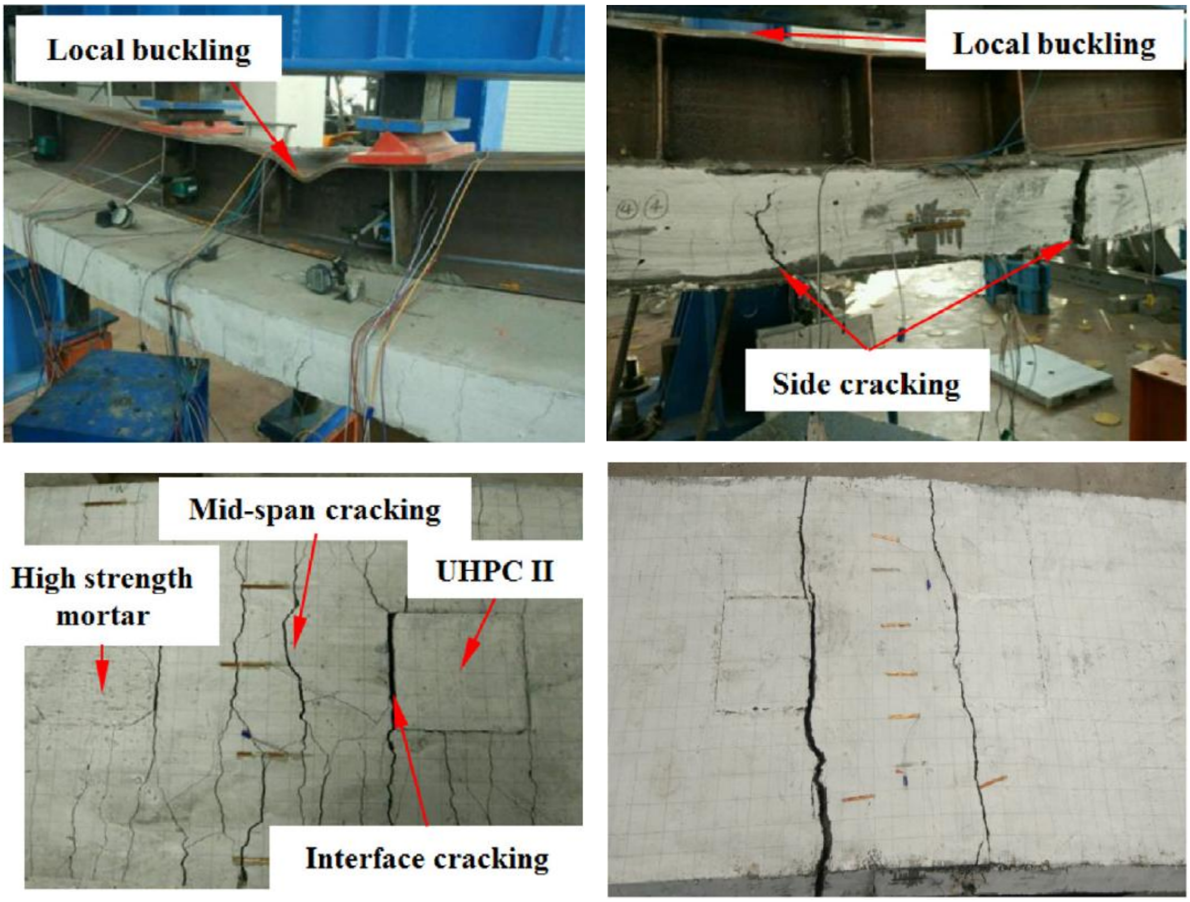

(a) Steel-NC composite beam (b) Steel-UHPC composite beam

Source: Qi *et al*. (2020).

The experimental and numerical results of Liu *et al*. (2021) also showed a better cracking performance with UHPC slabs in composite beams. Regarding composite beams with NC slabs, the authors proposed a reasonable joint form with the UHPC layer in the hogging moment region, in which its longitudinal length might be 10% of the span length. Other studies also investigated the partial replacement from NC by UHPC layers in the joint region. Zhu *et al*. (2020c) reported that UHPC materials offer a solution to mitigate deck slab cracking and suggested that altering joint configurations can improve the connection performance. Lu *et al*. (2022), Wan *et al*. (2022), Xu *et al*. (2022a), and Cai *et al*. (2023) the structural behavior of steel-UHPC-NC composite beams by replacing the upper layer of NC deck slabs with a thin

UHPC coating. The studies revealed that by employing a thin UHPC layer, the issue of concrete slab cracking can be effectively solved.

Zhu *et al*. (2022) conducted experimental and numerical investigations of steel-UHPC composite beams with waffle slab. The results indicated that increasing the reinforcement ratio and incorporating partially filled UHPC into the compressive flange of the steel beam can enhance crack resistance and increase the flexural capacity of these beams subjected to hogging moment. Zhao *et al*. (2023) carried out bending tests and numerical analyses. The findings demonstrated that incorporating a UHPC slab effectively improves the crack resistance of the composite beam, with a slight improvement in its flexural capacity. Furthermore, when determining the ultimate flexural capacity of a steel-UHPC composite beam, it is essential to consider the tensile stress contribution of the UHPC.

2.3 INITIAL STRUCTURAL IMPERFECTIONS OF STEEL I-SECTIONS

Steel profiles have detrimental imperfections developed from their manufacturing process concerning hot-rolled, welded, or cold-formed elements (ROSSI *et al*., 2021d). In the field of steel construction research, there has been a significant interest in the imperfections of structural members. In research concerning the stability design of structures, including the lateral and lateral-torsional buckling in columns, beams, and beam-columns, a recurring observation is the considerable variability in the geometrical and material imperfections (FERREIRA FILHO *et al*., 2022; TANKOVA *et al*., 2018a, 2018b, 2019, 2021).

2.3.1 Structural imperfections' influence on post-buckling analyses

As stated by previous numerical investigations, the stability behavior and resistant capacity of thin-walled structures are sensitive to structural imperfections, such as out-of-flatness, named initial geometric imperfection, and residual stresses of the steel elements (CHACÓN; MIRAMBELL; REAL, 2009; CHEN; JIA, 2010; COUTO; VILA REAL, 2019; FERREIRA; MARTINS; NARDIN, 2021; GRACIANO; CASANOVA; MARTÍNEZ, 2011; KALA; VALEŠ, 2017a, 2017b; KALA; VALEŠ; MARTINÁSEK, 2017; KÖVESDI; MECSÉRI; DUNAI, 2018; LI *et al*., 2023, 2022; LI; BOISSONNADE, 2023; ROSSI *et al*., 2021d, 2021e; SONG; TENG; ROTTER, 2004). For I-section members, this initial stress state has a major detrimental effect on the global instability resistance (SONCK, 2014). Moreover, the residual stresses are more influential when the instability resistance is obtained in an inelastic regime after the compressed flange reaches the steel yield strength (ROSSI *et al.*, 2021d, 2021e; SUBRAMANIAN; WHITE, 2017). The association of loads and residual stresses leads to steel beams' inelastic response reaching stresses values lower than their yield strength (**Figure 2.23**) (GALAMBOS, 1963; SPOORENBERG; SNIJDER; HOENDERKAMP, 2011; YOUNG, 1975).

Figure 2.23: The effect of residual stresses on the steel stress-strain relationship.

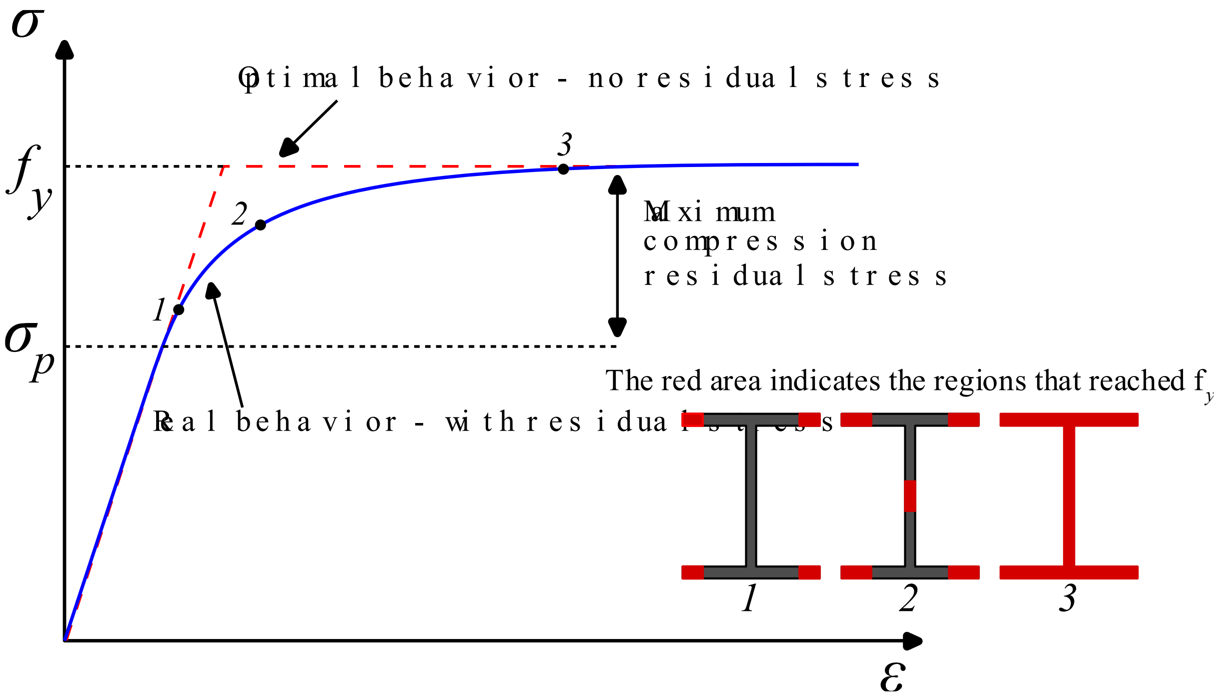

Source: Adapted from Rossi *et al.* (2021c).

As the actual residual stress determination in alveolar I-beams is hard to do, to cover its influence, some numerical assessments of LTB in these beams adopted a higher amplitude of initial geometric imperfection (NSEIR *et al.*, 2012; PANEDPOJAMAN; SAE-LONG; CHUB-UPPAKARN, 2016). Another strategy is using the patterns from full web I-sections, implementing only the residual stresses of the flanges (SONCK; BOISSONNADE; VAN IMPE, 2012). According to Ellobody (2012a, 2012b), presuming that the cutting process is carefully conducted, the residual stress distribution in an alveolar beam can be considered as that of doubly symmetric I-sections. There is only one residual stress pattern for steel alveolar members (SONCK, 2014; SONCK; IMPE; BELIS, 2014). This model was obtained by experimental measurement, and it has already been inserted in nonlinear finite element analyses of composite (OLIVEIRA, 2022; OLIVEIRA *et al.*, 2022) and non-composite beams (BRAGA *et al.*, 2021; DE CARVALHO *et al.*, 2022; DE CARVALHO; ROSSI; MARTINS, 2022;

FERREIRA *et al*., 2022b; FERREIRA; MARTINS, 2020; FERREIRA; ROSSI; MARTINS, 2019; SONCK; BELIS, 2015, 2017).

For nonlinear post-buckling analyses of steel-concrete composite beams submitted to hogging moment, the consideration of the mentioned structural imperfections and material nonlinearity is primordial to LDB assessment (BRADFORD, 2000; BRADFORD; JOHNSON, 1987; CHEN; JIA, 2010; OLIVEIRA *et al*., 2021, 2022; ROSSI *et al*., 2020b, 2021c, 2021b, 2023; VRCELJ; BRADFORD, 2009). On the other hand, the residual stresses can be disregarded for composite beams subjected only to the sagging moment since these are not influential in their structural behavior (FERREIRA; MARTINS; NARDIN, 2020b). Through numerical analyses, Chen and Jia (2010) observed that a little difference in the LDB ultimate moment occurred in varying the residual stress patterns. In contrast, initial geometric imperfections were more influential. Rossi *et al*. (2021c) analyzed the influence of structural imperfections on the LDB resistance, addressing four composite beams tested by Tong *et al*. (2014). As these beams reached instability in an inelastic regime, the authors stated that the LDB ultimate moment was more sensitive to residual stress distribution than the geometric imperfection amplitudes. Rossi *et al*. (2020b, 2021b, 2021c, 2023) and Hosseinpour *et al*. (2022) validated their numerical models by adopting the residual stress pattern by Galambos and Ketter (1959) and a ratio of $L/1000$ as the geometric imperfection value, also concerning the experimental results by Tong *et al*. (2014). Zhou and Yan (2017) also validated their finite element models with these tests using a geometric imperfection value of $L/1000$ and another residual stress pattern for hot-rolled I-sections. Regarding composite alveolar beams under hogging bending, Salah (2009) and Oliveira *et al*. (2022) presented a calibration study comparing their numerical results with tests performed by Salah (2009). This author validated its finite element models by implementing a geometric imperfection value equal to the web thickness, and the material imperfection was inserted using an equivalent stress-strain diagram proposed by Murzewski (1976). This steel constitutive model considers the material nonlinearity caused by the residual stresses. On the other hand, Oliveira *et al*. (2022) validated their numerical models with the residual stress pattern by Beg and Hladnik (1996) and the geometric imperfection value of $d_g/100$, as the authors adopted the condition: $d_g/100$ if $L/d_g<10$ and $L/1000$ if $L/d_g\geq10$, which was also used in LTB assessments of steel cellular I-beams (FERREIRA *et al*., 2022b; FERREIRA; MARTINS, 2020; FERREIRA; ROSSI; MARTINS, 2019).

2.3.2 Measurements and propositions of geometrical and structural imperfections

The initial stress state in a steel element without loading is referred to as residual stresses (CHACÓN; SERRAT; REAL, 2012). The residual stress distribution in actual steel members can be determined only from tests, which are recognized as tasks that are quite challenging and time-intensive with limited precision (ABAMBRES; QUACH, 2016; CLARIN, 2004). Different measurement techniques, classified as destructive, semi-destructive, and non-destructive methods, have been used in experimental investigations of H and I-sections. The sectioning method, a destructive technique introduced by Kalakoutsky in 1888, has gained widespread popularity among researchers for measuring residual stresses in structural steel components (WANG; LI; CHEN, 2012). The studies that adopted this technique can be cited Tebedge, Alpsten and Tall (1973), Spoorenberg, Snijder and Hoenderkamp (2010), Wang, Li and Chen (2012), Spoorenberg *et al*. (2013), Ban *et al*. (2013), Li, Li and Wang (2015), Yang *et al*. (2016, 2021), Tankova *et al*. (2018b, 2018a, 2019, 2021), Unsworth, Driver and Li (2020), Ferreira Filho *et al*. (2022), Schaper *et al*. (2022), Guo *et al*. (2022), Tong *et al*. (2023), Chen, Liu and Chan (2023), Lebastard *et al*. (2023). Regarding semi-destructive methods, researchers have used the hole-drilling method, such as Wang, Li and Chen (2012) and Guo *et al*. (2022). Some non-destructive procedures are the instrumented indentation method adopted by Lee *et al*. (2013) and Kim *et al*. (2014), and the neutron diffraction method utilized by Le *et al*. (2020).

As noted, the sectioning method is the most adopted technique. Wang, Li and Chen (2012) presented the measurement tests of residual stress distribution in three different welded H-sections with Q460 high-strength steel plates. The test results obtained by both sectioning and hole-drilling methods were compared. Wang, Li and Chen (2012) observed that the average of compressive residual stress values from both methods are similar, but the distribution from the sectioning method is more practical for use in numerical analysis. Few residual stress measurements of steel alveolar I-sections were performed (SONCK, 2014; SONCK; IMPE; BELIS, 2014; XUHONG ZHOU *et al*., 2019) and these tests were carried out with the sectioning method. This procedure cuts the steel profile into different longitudinal sections by a series of transverse and longitudinal cuts. Considering that the residual stresses are in an elastic regime, the longitudinal stress in each cross-section can be calculated by measuring the strain difference before and after the cut and using Hooke's law (SONCK, 2014). **Figure 2.24** shows the sectioning method tests performed by Sonck (2014).

Figure 2.24: Residual stress measurements via sectioning method in steel I-sections.

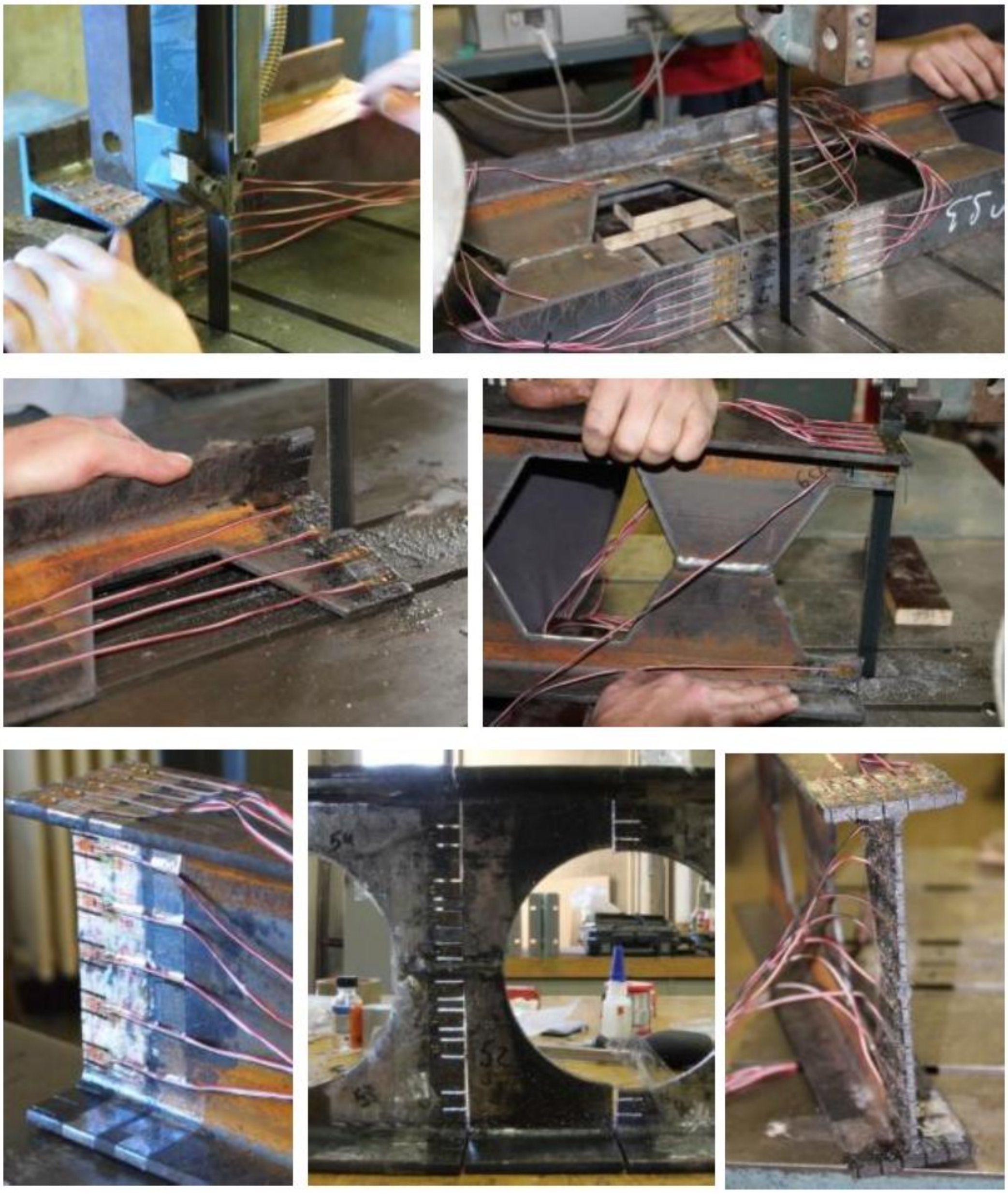

Fonte: Sonck (2014).

Geometrical imperfections are initial curvatures of the plates' axis (KALA; VALEŠ, 2017a), which play a crucial role in defining the global stability behavior of beams and columns, and it is relatively easy to measure despite the absence of systematic measurements (TANKOVA *et al*., 2018b, 2019). Different techniques have been adopted to determine the geometrical imperfection of steel I-sections. A series of full-scale tests were recently conducted at the University of Coimbra. Tankova *et al*. (2018a) performed a procedure involving a "low mass" nylon string attached to two nuts at the ends of the member and stretched to its limit. The string's distance from the member was measured at intervals of 0.50m, and the height of the nuts was subtracted to determine the imperfection's magnitude. This measurement was made along three lines on the member's web and one on each flange. The average of these measurements was taken as the amplitude of the geometrical imperfection. In other studies, the tests were conducted with advanced measurement systems. Tankova *et al*. (2018b) used the *ROBOT Romer F-41800 Montoire*, which provides a map showing the local variations from the nominal geometry. The tests of Tankova *et al*. (2021) and Ferreira Filho *et al*. (2022) were executed via the MetraSCAN 3D^{TM} system. Recently, Lebastard *et al*. (2023) also presented the results of geometrical imperfections measurement tests using manual tools. The actual I-section dimensions and local imperfections in the web were measured on four transverse cross-sections along the beam. The local imperfections in the web were obtained with a steel ruler connected to five calipers. Angles at the compression flange-to-web junctions were also measured. Moreover, the global geometrical imperfections were assessed on the compression flange concerning a reference straight laser line. All these studies also verified the residual stress distribution via the sectioning method and conducted global buckling tests and post-buckling analyses via ABAQUS software. This way, their nonlinear finite element models were validated using the geometrical and material imperfections obtained by the tests. However, most research on the stability behavior of steel structures cannot carry out investigations as complete as those mentioned, often due to funding limitations. A common strategy to cover these limitations is the development of post-buckling analyses with standard values for amplitudes of geometrical imperfections and residual stress distribution patterns found in the literature.

2.3.2.1 Geometric imperfection amplitudes

Geometric imperfections, like initial bending, transform the buckling issue into one of nonlinear geometric analysis, contrasting with the bifurcation issue common in classic stability. The actual shape of steel elements' initial curvature tends to be complex, frequently manifesting as concurrent curvatures along the two main cross-section axes (ROSSI *et al.*, 2021c). Fractions of the beams' geometric parameters are usually used as the geometric imperfection amplitude. The Structural Stability Research Council (SSRC), considering the study by Bjorhovde *et al.* (1972), initially suggested the incorporation of initial curvature values equivalent to $L/1000$. Nevertheless, it was observed that utilizing $L/1470$ values is a more suitable choice for practical profile applications. According to Bjorhovde (1988), the value of L/1470 was adopted to develop the 2P curve proposed by SSRC, the design curve used in the current version of the Brazilian code (ABNT NBR 8800: 2008).

Regarding global imperfections, Galambos (1988) noted that available data indicates the maximum values typical approach around $L/1500$. Lebastard *et al*. (2023) observed the magnitudes range between $L/1911$ and $L/1263$, all lower than $L/1000$, which is the manufacturing tolerance defined by EN 1090-2: 2018. It is commonly presumed that the initial geometric imperfection follows the global buckling mode shape of the examined phenomenon, with a magnitude of $L/1000$ of the member length (TANKOVA *et al*., 2018a). For steel castellated I-sections, in the experimental investigation by Vieira (2015), it was noted that the local geometric imperfection amplitude of $d_g/100$ was similar to the specimens, which were stocky I-sections with L/d_g ratio lower than 10. The limit values of alveolar sections' geometric imperfection on the web-post should not exceed 4mm for those with d_g<600mm, and the limit of $d_g/100$ for I-sections with d_g≥600mm, according to the ArcelorMittal catalog (ARCELORMITTAL, 2020). In addition, EN 1993-1-5:2006 recommends the initial geometric imperfections for post-buckling analysis equal to 80% of the expected manufacturing tolerance.

When instability phenomena arise in an inelastic regime, the impact of global geometric imperfections becomes highly complex (BATTERMAN; JOHNSTON, 1967). Under these circumstances, one cannot merely sum up the isolated effects of geometric imperfection and residual stresses to assess the combined influence on the resistant capacity of steel elements (BATTERMAN; JOHNSTON, 1967). According to Rossi *et al*. (ROSSI *et al*., 2021c), for an accurate representation of steel-concrete composite beams' behavior under hogging moment using numerical simulations, it is essential to regard both residual stresses and geometric imperfection.

2.3.2.2 Residual stress patterns

In the manufacture of hot-rolled steel I-beams, the material is cooled into its final shape, leading to the development of residual stresses mainly due to non-uniform cooling. These stresses' magnitude and spread are influenced by factors like the beam's shape, rolling temperature, cooling methods, straightening processes, and other features (KALA; VALEŠ, 2017b). Experimental studies show that for hot-rolled I-profiles, the level of residual stress does not depend on the steel yield strength, whether it's mild steel or high-strength steel (JÖNSSON; STAN, 2017). On the other hand, the residual stress greatness are higher for heavier and larger cross-sections (ALPSTEN, 1972; GALAMBOS, 1963). Some research of residual stresses in hot-rolled I-sections verified and proposed a parabolic distribution in the flanges and web (**Figure 2.25**), in which its intensity is dependent of the cross-section dimensions, such as

Young (1975), Schulz (1968), Beer and Schulz (1970), Tebedge, Alpsten and Tall (1973), and Szalai and Papp (2005). There are also patterns of residual stress with linear distribution in the flanges (**Table 2.14**), such as those proposed by Huber and Beedle (1954), Galambos and Ketter (1959), Galambos (1963), and *European Convention for Constructional Steelwork* (ECCS, 1984). The models of Huber and Beedle (1954) and ECCS (1984) present a linear configuration along the web depth, whereas those of Galambos and Ketter (1959) and Galambos (1963) have a uniform distribution. Some of these models are described in **Table 2.9**.

Regarding the residual stress distribution of steel alveolar I-sections, only one proposition is found in the literature, presented in the research of Sonck (2014) and Sonck, Impe and Belis (2014). The authors carried out experimental measurements via the sectioning method, and the tests addressed castellated and cellular sections and their respective parent hot-rolled profiles with S275 steel. The authors recommend further investigations with higher-strength steels to assess their effect on the residual stress distribution of steel alveolar I-profiles. The model proposed by Sonck (2014) and Sonck, Impe and Belis (2014) is shown in **Table 2.15**.

Figure 2.25: Parabolic distribution of residual stresses in hot-rolled I-sections.

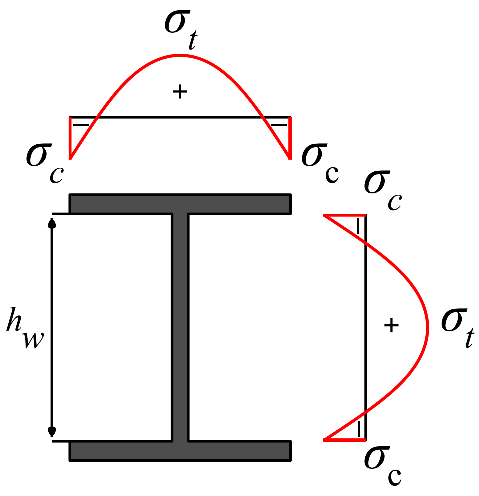

Source: The author (2023).

Table 2.14: Residual stress models with linear distribution for hot-rolled I-section.

Residual stress distribution	Proposed by	Intensity
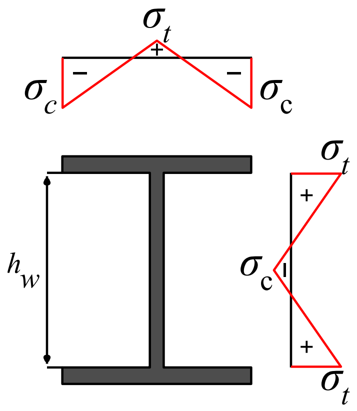	ECCS (1984)	If $d/b_f \le 1.2 \rightarrow \lvert\sigma_t\rvert = \lvert\sigma_c\rvert = 0.5 f_y$ If $d/b_f > 1.2 \rightarrow \lvert\sigma_t\rvert = \lvert\sigma_c\rvert = 0.3 f_y$
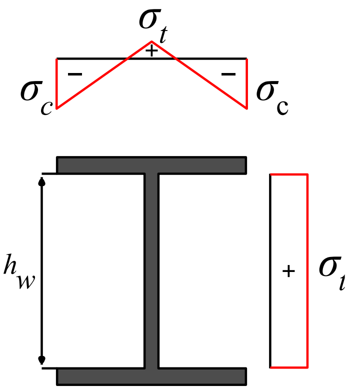	Galambos and Ketter (1959)	$\sigma_t = \left[\frac{b_f t_f}{b_f + t_w\left(d - 2t_f\right)}\right] 0.3 f_y$ $\sigma_c = 0.3 f_y$

Source: Adapted from Rossi *et al.* (2021c).

Table 2.15: Residual stress model for alveolar I-sections proposed by Sonck (2014) and Sonck, Impe and Belis (2014).

Residual stress distribution	Intensity
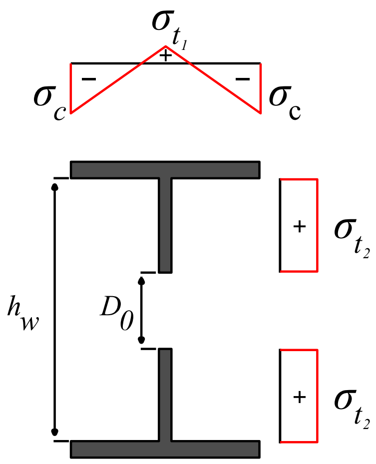	If $d/b_f \le 1.2 \begin{cases} \sigma_c = -150 MPa \\ \sigma_{t1} = +100 MPa \end{cases}$ If $d/b_f > 1.2 \begin{cases} \sigma_c = -100 MPa \\ \sigma_{t1} = +50 MPa \end{cases}$ $\sigma_{t2} = \left[\frac{b_f t_f}{\left(d_g - t_f - D_o\right) t_w}\right] 50$

Source: The author (2023).

For welded I-sections, the residual stress' magnitude and spread are more affected by the welding procedure than the cross-section dimensions (ALPSTEN, 1972; BJORHOVDE *et al.*, 1972; MCFALLS, 1967; TEBEDGE; ALPSTEN; TALL, 1973). According to the investigations by Nagarajo Rao *et al*. (1964) and Alpsten and Tall (1970), the welding type does not influence the residual stress intensity, except if there is a significant variation in the temperatures employed in different welding methods. Dwight and White (1977) stated that the maximum residual stress greatness can be adopted equal to the steel yield strength value. ECCS (1984) provides a residual stress pattern for welded I-sections, in which the weld regions have tensile stresses equal to the steel yield strength, with a linear distribution in the transition region from tensile to compressive stresses. Beg and Hladnik (1996) and Taras (2010) proposed residual stress models similar to ECCS (1984). However, these models present an abrupt transition from tensile to compressive stresses. On the other hand, Barth and White (1998) suggested a new model with residual stress intensity lower than the patterns of ECCS (1984), Beg and Hladnik (1996) and Taras (2010), as the authors asserted that the ECCS model (1984) slightly tends to overestimate the stress values concerning experimental measurements. **Table 2.16** details these residual stress patterns for welded I-sections.

It is evident that various patterns exist for the residual stress distribution in I-sections, attempting to depict the randomness in their shapes and magnitudes. Nevertheless, deciding on the specific residual stress pattern to employ in numerical simulations lacks a straightforward answer.

Table 2.16: Residual stress models for welded I-section.

Distribution	Proposed by	Intensity
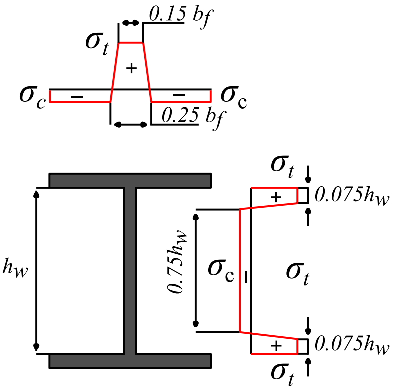	ECCS (1984)	$\sigma_c = 0.25 f_y$ $\sigma_t = f_y$
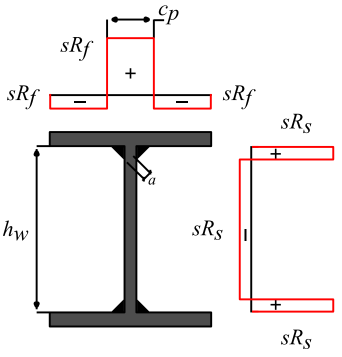	Beg and Hladnik (1996)	$If\ f_y \le 420MPa \begin{cases} \sigma_{cf} = (0.2-0.3) f_{yf} \\ \sigma_{tf} = f_{yf} \\ \sigma_{cw} = (0.2-0.3) f_{yw} \\ \sigma_{tw} = f_{yw} \end{cases}$ $If\ f_y > 420MPa \begin{cases} \sigma_{cf} = (0.1-0.2) f_{yf} \\ \sigma_{tf} = 400-500MPa < f_{yw} \\ \sigma_{cw} = (0.1-0.2) f_{yw} \\ \sigma_{tw} = 400-500MPa < f_{yw} \end{cases}$ $c_p = h_w + 2a\sqrt{2}$
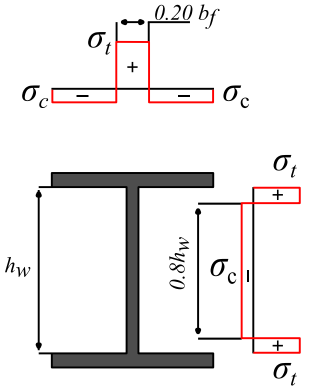	Taras (2010)	$\sigma_c = 0.25 f_y$ $\sigma_t = f_y$
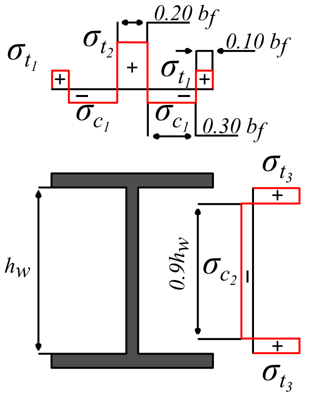	Barth and White (1998)	$\sigma_{c1} = 0.17 f_y$ $\sigma_{c2} = 0.07 f_y$ $\sigma_{t1} = 0.33 f_y$ $\sigma_{t2} = 0.18 f_y$ $\sigma_{t3} = 0.63 f_y$

Source: The author (2023).

2.4 SUMMARY AND CONCLUSIONS OF THE CHAPTER

This chapter discussed the bibliographical review of the main themes involving the development of this thesis. A systematic review of the LDB resistance of composite alveolar beams can be found in the article Oliveira *et al*. (2023a). As a summary and conclusion of the chapter, it can be stated that:

- The main instability modes of composite alveolar beams in hogging moment regions are LDB, WPB, FLB and TLB;
- For composite alveolar beams with lower global slenderness and subjected to linear hogging moment (with shear forces), the ultimate moment to LDB can reach values above the plastic moment of the composite section. In addition, these beams can present VM and the formation of plastic mechanism in the web-post or compressed tee;
- The standard procedures presented in this chapter do not address the LDB verification on continuous steel-concrete composite beams with web openings. However, some authors give adaptations of these standards;
- There are design guides for composite alveolar beams, such as SCI P355 (LAWSON; HICKS, 2011), Steel Design Guide 31 (FARES; COULSON; DINEHART, 2016), and Eurocode (EN 1993-1-13: 2024 / prEN 1994-1-1), which provide methodologies to evaluate the resistance to WPB and VM. However, do not present approaches for LDB;
- The slab cracking of steel-concrete composite beams under hogging moment has been improved using high-performance materials, such as UHPC;
- HSS elements, such as I-sections and shear connectors, have also been implemented in steel-concrete composite beams;
- Studies show an outstanding cooperative performance in the ultimate state between the HSS I-beam and UHPC slab;
- There are still no investigations that have addressed HSS-UHPC composite beams under hogging moment, and there are also no studies that have evaluated the flexural performance of steel-UHPC alveolar composite beams;
- For I-section members, the residual stresses have a major detrimental effect on the global instability resistance, being more influential when the instability resistance is obtained in an inelastic regime;

- The initial geometric imperfection of steel sections can also reduce their resistant capacity in cases of instability.

CHAPTER 3

ANALYTICAL METHODS VERIFICATION

This chapter presents an assessment on the accuracy of formulation predictions of LDB and WPB resistance of composite alveolar beams. The accuracy is verified considering hogging bending tests of these structures that had LDB and WPB in the failure mode. The analysis of the accuracy of the LDB resistance predictions was published in the review article by Oliveira *et al*. (2023a).

3.1 ACCURACY OBTAINED BY LDB RESISTANCE FORMULATIONS

LDB resistance predictions provided by standard codes do not comprehend composite alveolar beams, having only formulations for composite beams with full webs. This way, it is necessary to use adaptation approaches for beams with web openings. Another critical point is that calculation propositions directly developed to verify the M_{cr} to LDB of composite alveolar beams were not found in the literature. Only adaptations made by authors who proposed changes to methodologies that consider the verification of the M_{cr} of composite beams without web openings were found. From these adaptations, it is possible to obtain the M_u to LDB by the methodologies presented by Salah (2009), the European standard (EN 1994-1-1: 2004) and the Brazilian code (ABNT NBR 8800: 2008). As noted, this theoretical study addresses the previous version of the Brazilian code (ABNT NBR 8800: 2008), as Oliveira *et al*. (2023a) performed this assessment before the publication of the current version (ABNT NBR 8800: 2024).

In addition to these methodologies, using the geometric properties of alveolar sections presented by Sonck and Belis (2015, 2017) and Carvalho, Rossi and Martins (2022), it is also possible to verify the M_u to LDB using the Australian standards procedure (AS4100:2020 and AS / NZS2327-2017).

To verify the accuracy of the calculation procedures presented in **section 2.1.2**, the results obtained by these procedures were compared to the experimental results of Salah (2009). Four composite alveolar beams which reached the failure by LDB were used, two with cellular I-section (C4S355 and C4S420) and two with castellated I-section (H4S355 and H4S420), as illustrated in **Figure 3.1**. **Table 3.1** describes the geometric parameters of the specimens, and **Table 3.2** presents their mechanical properties and ultimate load (P_u). As these specimens are the only ones in the literature with the instability mode characterized by LDB, there are no experimental results of other composite alveolar beams to use in this study for verifying the accuracy of analytical formulations from **section 2.1.2**.

The used methodologies are adaptations of procedures developed to verify the LDB in composite beams without web openings, so it was necessary to adopt geometric properties adapted to sections of alveolar beams, as presented in **section 2.1.2**. The approaches presented by Sonck and Belis (2015, 2017) ($J_{2T,Average}$) and Carvalho, Rossi and Martins (2022) (*solid, double T*, *average*, *superficial*, *and linear weighting section*) were utilized. To determine the flexural stiffness of the web (k_2), the adaptation proposed by Müller *et al*. (2006) and Silva *et al*. (2020) adopted for cellular and castellated beams, respectively.

Figure 3.1: Analyzed beams.

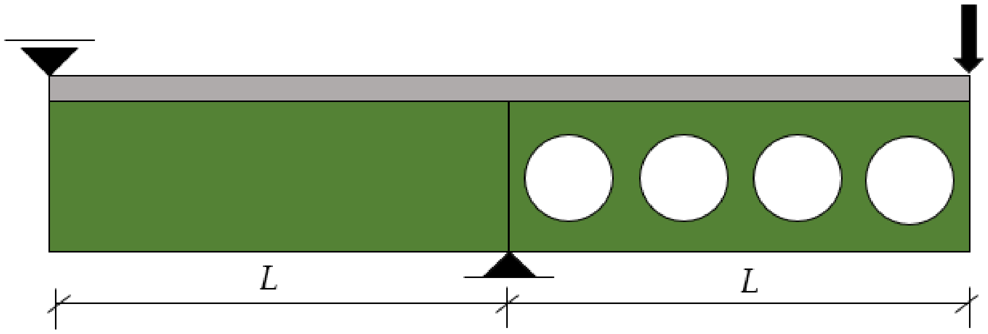

(a) C4S355 and C4S420

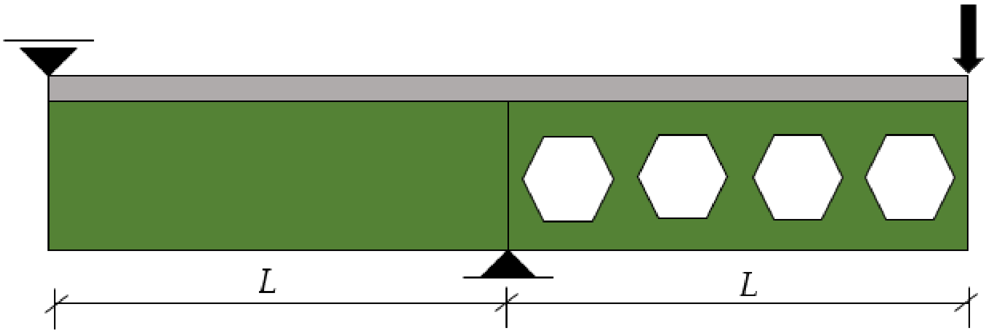

(b) H4S355 and H4S420
Source: Adapted from Salah (2009).

Table 3.1: Geometric parameters of the specimens.

Specimen	L (mm)	d_g (mm)	b_f (mm)	t_f (mm)	t_w (mm)	Do (mm)	b_w (mm)	s (mm)	p (mm)	$*n$ (mm)	A_{bar} (mm^2)	c (mm)
C4S355	2116	480	100	6	4	336	193	-	529	4	1256.64	50
C4S420	2116	480	100	6	4	336	193	-	529	4	1256.64	50
H4S355	2116	480	100	6	4	321	160	92	529	4	1256.64	50
H4S420	2116	480	100	6	4	321	160	92	529	4	1256.64	50

* *n* is the number of openings.

Source: The author (2023).

Table 3.2: Mechanical properties and ultimate load of the specimens.

Specimen	E (GPa)	f_y (MPa)	$f_{y,bar}$ (MPa)	P_u (kN)
C4S355	200	355	459.6	59.56
C4S420	200	420	459.6	62.26
H4S355	200	355	459.6	62.03
H4S420	200	420	459.6	62.55

Source: The author (2023).

3.1.1 Results

The following graphs show the comparison of the experimental results of Salah (2009) with the following calculation procedures for determining the $M_{u,dist}$ to the LDB: AS4100:2020 and AS / NZS2327-2017, EN 1994- 1-1: 2004, ABNT NBR 8800: 2008 and Salah (2009). The proposition of Roik *et al*. (1990) is described in the Brazilian code (ABNT NBR 8800: 2008) to calculate the M_{cr}. On the other hand, Eurocode 4 (EN 1994- 1-1: 2004) does not specify a formulation to obtain the M_{cr}. However, this code proposes calculation methodologies based on the inverted-U frame model. The equations of Roik *et al*. (1990), Hanswille *et al*. (1998) and Dias *et al*. (2019) are based on the model in question. These methodologies and those proposed by Svensson (1985) and Williams and Jemah (1987) to determine M_{cr} were also used in the calculation of Salah's proposition (2009) for the determination of $M_{u,dist}$. The proposition by Dias *et al*. (2019) considers only the uniform hogging moment configuration. However, the procedure by Oliveira (2018) was used, which adopted the proposal by Dias *et al*. (2019) for other loading settings. In the graphs below, the capital letters S, W, R, H and O mean that the procedure for determining the $M_{u,dist}$ is the calculation of the M_{cr} from the propositions of Svensson (1985), Williams and Jemah (1987), Roik *et al*. (1990), Hanswille *et al*. (1998) and Oliveira (2018), respectively. The ratio between the ultimate moment theoretical and the ultimate moment of the tests ($M_{u\text{-}Theoretical}$ /$M_{u\text{-}test}$) with values above 1 represent non-conservative results.

From **Figure 3.2** and **Figure 3.3**, it is noted that most code's adaptation methods overestimated the M_u. The procedures that had conservative results were: ABNT NBR 8800: 2008 for all geometric properties approaches (**Figure 3.2b** and **Figure 3.3b**); and EN 1994-1-1: 2004, from M_{cr} determination by Roik *et al*. (1990) for all approaches, and M_{cr} by Oliveira (2018) for $J_{2T,Average}$ and *double T* (**Figure 3.2c** and **Figure 3.3c**). Among these formulations, EN 1994-1-1: 2004 with M_{cr} by Oliveira (2018) and $J_{2T,Average}$ was the formulation that had the highest mean of the ratio ($M_{u\text{-}Theoretical}/M_{u\text{-}test}$ = 0.951), followed by the same equations with *double T* geometric properties ($M_{u\text{-}Theoretical}/M_{u\text{-}test}$ = 0.949). For ABNT NBR 8800: 2008, the highest $M_{u\text{-}Theoretical}/M_{u\text{-}test}$ value (0.83) was obtained with the *solid section* (**Figure 3.2b**). The methods that had non-conservative results were: AS4100:2020 for all geometric properties approaches (**Figure 3.2a** and **Figure 3.3a**); EN 1994-1-1: 2004 with M_{cr} by Hanswille *et al*. (1998) for all geometric properties approaches; and EN 1994-1-1: 2004 with M_{cr} by Oliveira (2018) for *solid, average, superficial*, and *linear weighting section* (**Figure 3.2c** and **Figure 3.3c**). EN 1994-1-1: 2004 with M_{cr} by Hanswille *et al*. (1998) and *solid section* obtained the most M_u overestimation within code's adaptations, having the highest $M_{u\text{-}Theoretical}/M_{u\text{-}test}$ value equal to 1.97. For EN 1994-1-1: 2004 with M_{cr} by Hanswille *et al*. (1998), the *solid, average, superficial,* and *linear weighting section* provided $M_{u\text{-}Theoretical}/M_{u\text{-}test}$ values above 1.5, which shows the significant non-conservatism of then. Within the other combinations of M_u and M_{cr} equations with non-conservative results, the $M_{u\text{-}Theoretical}/M_{u\text{-}test}$ values were: AS4100:2020 for *solid section* (1.42); and EN 1994-1-1: 2004 with M_{cr} by Oliveira (2018) for *solid section* (1.32). Another issue is that no significant differences were observed between the accuracies obtained for the models with circular and hexagonal openings considering the same calculation method. For the Australian code (AS4100:2020), the geometric properties considering $J_{2T,Average}$, *double*

T and *average section* had similar values of $M_{u\text{-}Theoretical}/M_{u\text{-}test}$ (**Figure 3.2a** and **Figure 3.3a**), which also occurred with *superficial and linear weighting sections* in the composite cellular beams (**Figure 3.2a**). On the other hand, *superficial and linear weighting section* provided lower values of $M_{u\text{-}Theoretical}/M_{u\text{-}test}$ than $J_{2T,Average}$, *double T* and *average section* in the composite castellated beams (**Figure 3.3a**). In addition, these geometric properties approach presented a trend for the other procedures shown in **Figure 3.2** and **Figure 3.3**. This trend is *double T*, $J_{2T,Average}$, *linear weighting, average, superficial weighting* and *solid section* from smallest to highest values of $M_{u\text{-}Theoretical}/M_{u\text{-}test}$ (**Figure 3.2** and **Figure 3.3**). Finally, the only methodologies that obtained safe results for all section approaches were EN 1994-1-1: 2004 and ABNT NBR 8800: 2008 with M_{cr} by Roik *et al*. (1990).

Figure 3.4 and **Figure 3.5** show that most approaches with Salah's M_u proposition (2009) overestimated the M_u. This M_u formulation with M_{cr} by Roik *et al*. (1990) for $J_{2T,Average}$, *double T*, *average section, superficial and linear weighting section* were the procedures that had conservative results (**Figure 3.4a** and **Figure 3.5a**). Among these calculation methodologies, the one with the *superficial weighting section* had the highest mean of the ratio ($M_{u\text{-}Theoretical}/M_{u\text{-}test} = 0.902$), followed by the *average section* ($M_{u\text{-}Theoretical}/M_{u\text{-}test} = 0.863$). The use of M_{cr} proposed by Roik *et al*. (1990) with *solid section* and M_{cr} by Oliveira (2018) with the $J_{2T,Averange}$, and *double T section* provided the most similar results against the tests. However, the results of the models C4S420 and H4S420 were non-conservative (**Figure 3.4a** and **Figure 3.5a**). The methods that obtained non-conservative results were: M_{cr} by Roik *et al*. (1990) with *solid section*; and M_{cr} by Hanswille *et al*. (1998), Oliveira (2018), Svensson (1985), and Williams and Jemah (1987) for all geometric properties approaches. Some methodologies fall into a high level of non-conservatism with $M_{u\text{-}Theoretical}/M_{u\text{-}test}$ values above 2, such as M_{cr} by Hanswille *et al*. (1998) with *solid section*; M_{cr} by Svensson (1985) and Williams and Jemah (1987) with *solid, average*, *superficial*, and *linear weighting section*. Within these methods, M_{cr} by Svensson (1985) and Williams and Jemah (1987), with *solid section* presented $M_{u\text{-}Theoretical}/M_{u\text{-}test}$ values above 2.5. The most M_u overestimation was observed in M_{cr} by Svensson (1985) and *solid section*, having $M_{u\text{-}Theoretical}/M_{u\text{-}test}$ value equal to 2.65 for the specimen C4S420 (**Figure 3.4b**). Other formulations with significant non-conservatism provided $M_{u\text{-}Theoretical}/M_{u\text{-}test}$ values above 1.5, such as M_{cr} by Hanswille *et al*. (1998) with $J_{2T,Average}$, *double T, superficial,* and *linear weighting*; and M_{cr} by Svensson (1985) and Williams and Jemah (1987), with *double T section*. As well as for the code's adaptation methods (**Figure 3.2** and **Figure 3.3**), significant differences were not observed between the accuracies obtained for the models with circular and hexagonal openings considering the same calculation method (**Figure 3.4a** and **Figure 3.5a**). Finally, the same trend of the geometric section approaches in **Figure 3.2** and **Figure 3.3** are noted in **Figure 3.4** and **Figure 3.5**, in which, from smallest to highest values of $M_{u\text{-}Theoretical}/M_{u\text{-}test}$, is *double T*, $J_{2T,Average}$, *linear weighting*, *average*, *superficial weighting* and *solid section*.

Figure 3.2: Accuracy obtained by the codes' adaptation approaches for composite cellular beams.

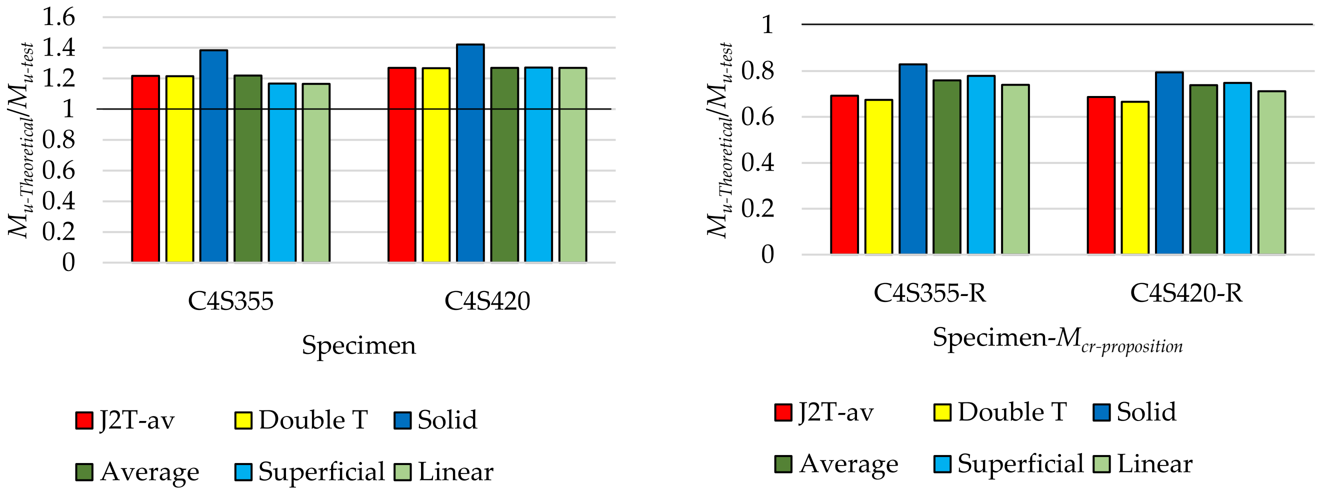

(a) AS4100:2020

(b) ABNT NBR 8800: 2008

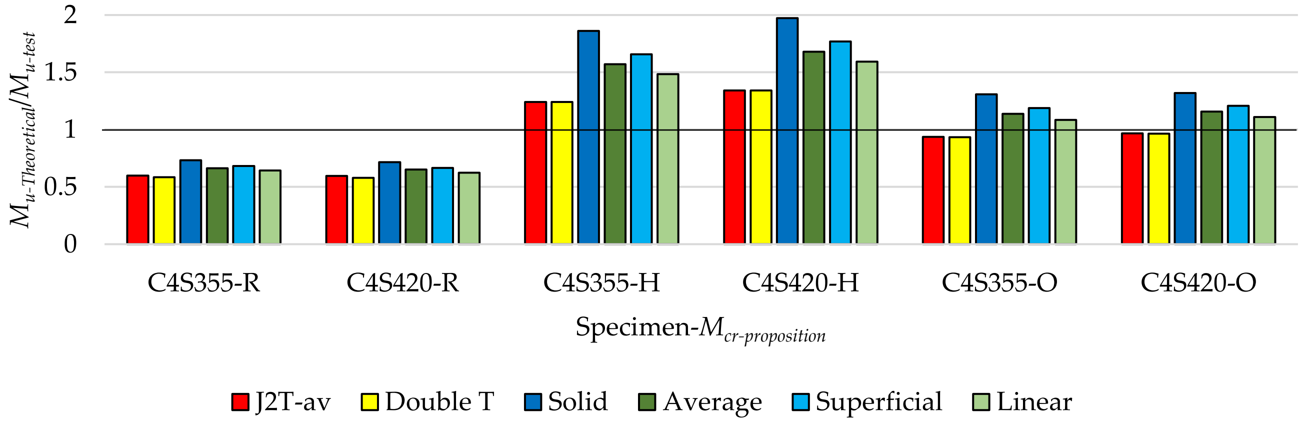

(c) EN 1994- 1-1: 2004

Source: Oliveira *et al*. (2023a).

Figure 3.3: Accuracy obtained by the codes' adaptation approaches for composite castellated beams.

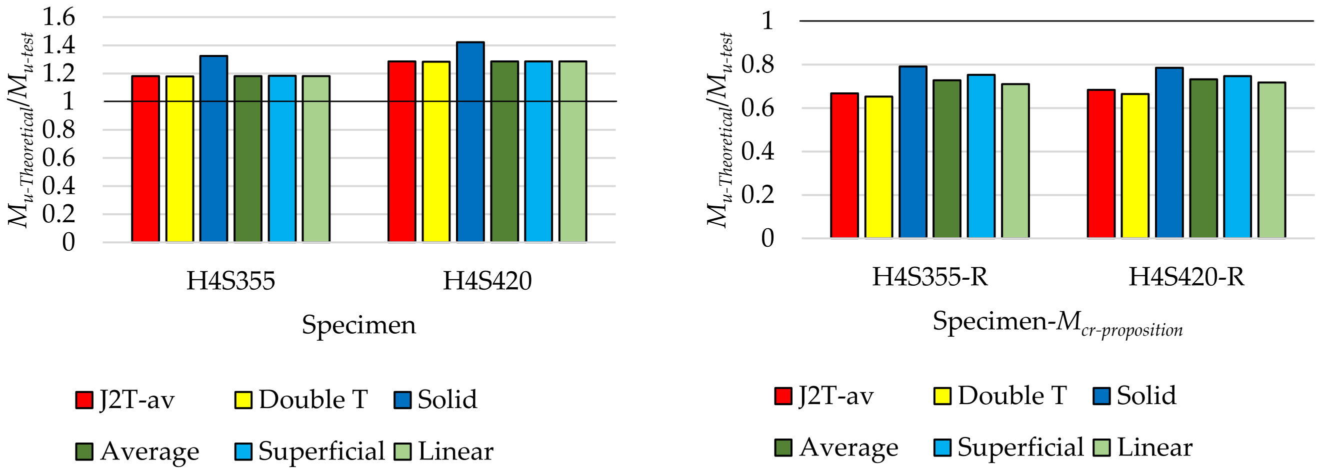

(a) AS4100:2020

(b) ABNT NBR 8800: 2008

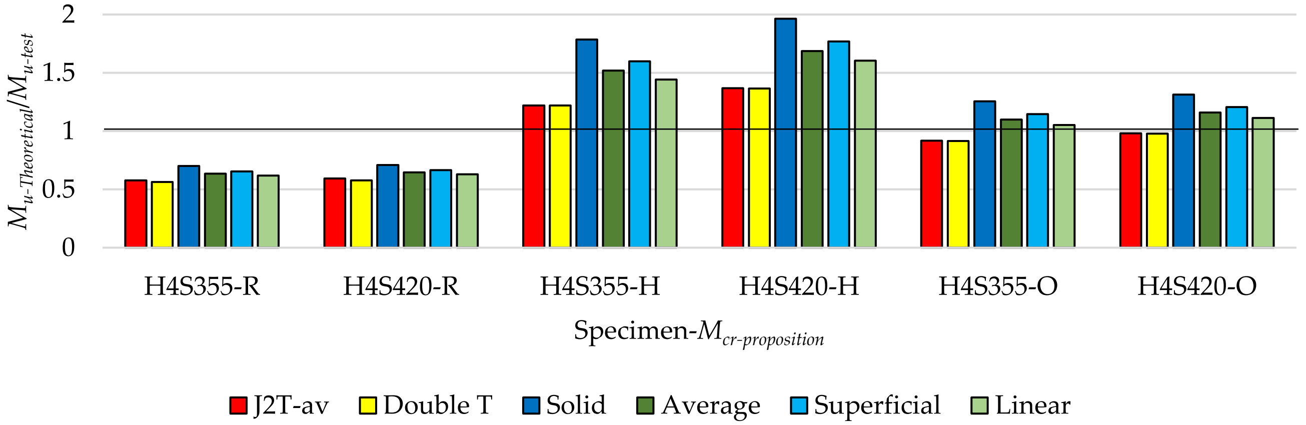

(c) EN 1994- 1-1: 2004

Source: Oliveira *et al*. (2023a).

Figure 3.4: Accuracy obtained by the proposition of Salah (2009) for composite cellular beams.

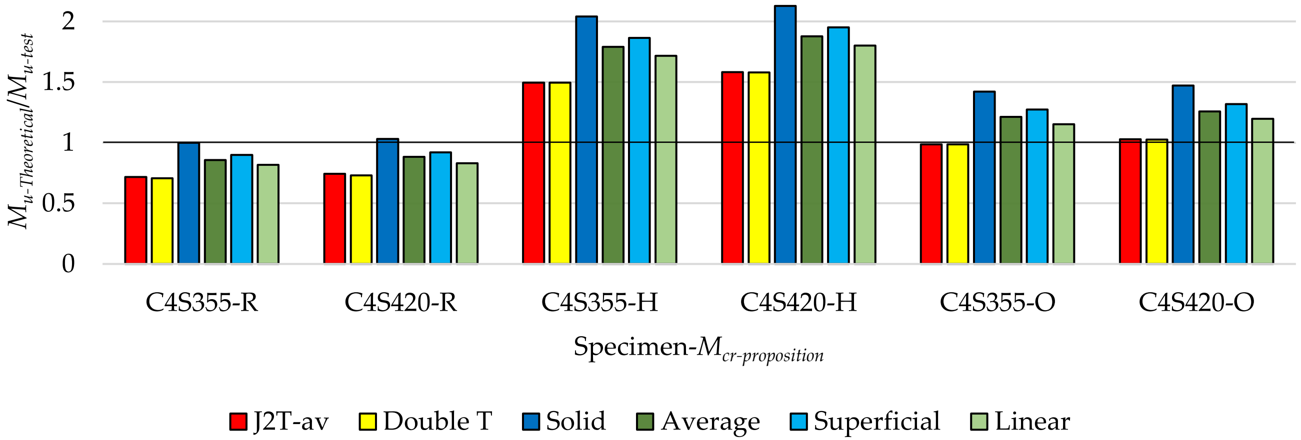

(a) M_{cr} calculation based on the U-frame model

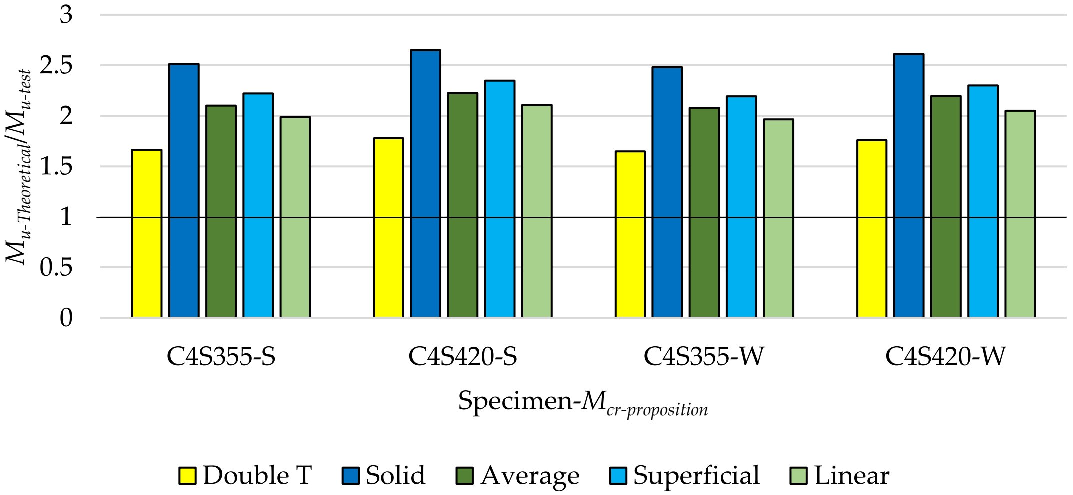

(b) M_{cr} calculation proposed by Svensson (1985) and Williams and Jemah (1987)
Source: Oliveira *et al*. (2023a).

Figure 3.5: Accuracy obtained by the proposition of Salah (2009) for composite castellated beams.

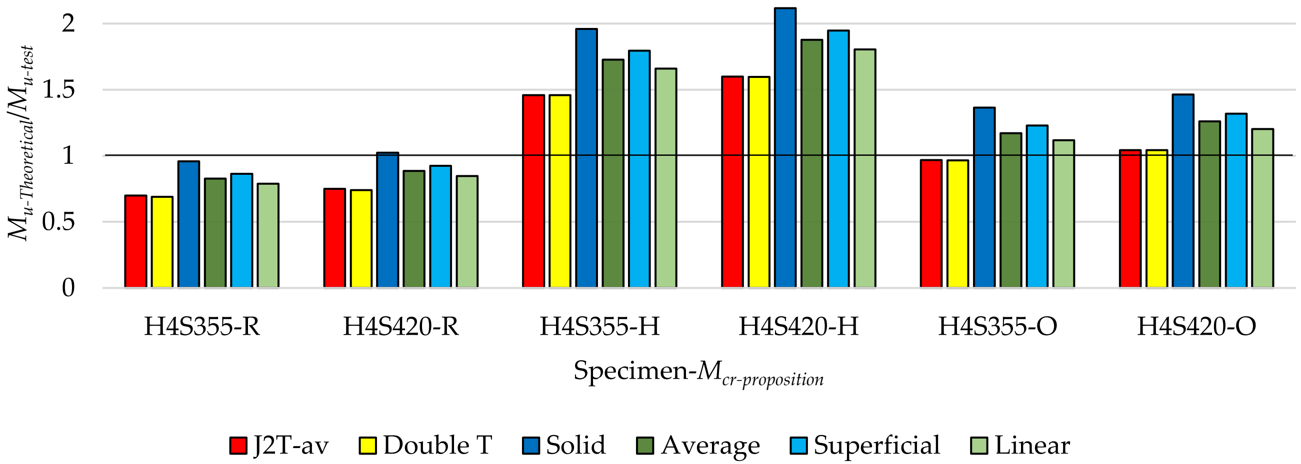

(a) M_{cr} calculation based on the U-frame model

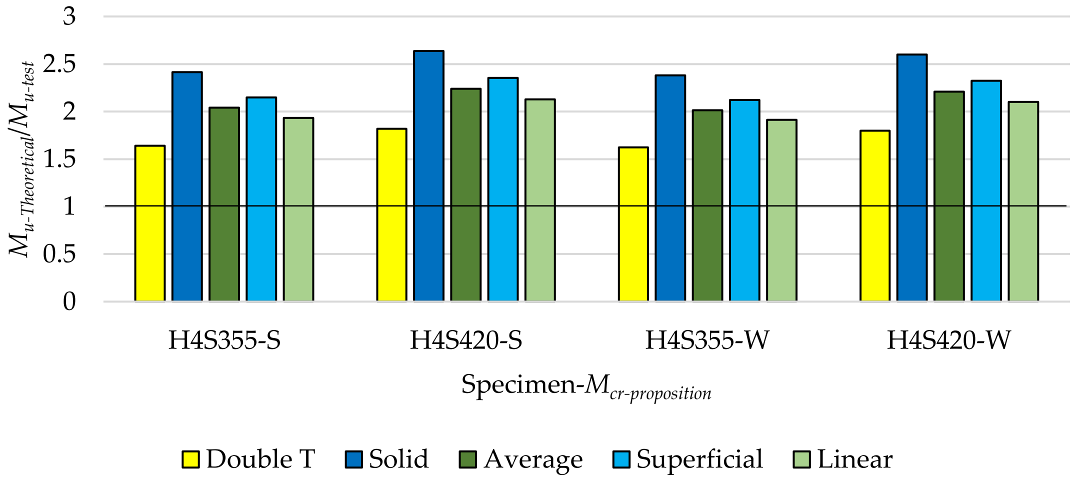

(b) M_{cr} calculation proposed by Svensson (1985) and Williams and Jemah (1987)
Source: Oliveira *et al*. (2023a).

Table 3.3 shows the $M_{u\text{-}Theoretical}/M_{u\text{-}test}$ values obtained by the calculation procedure of AS4100:2020. As noted, all geometric property approaches provide significant M_u overestimation, with $M_{u\text{-}Theoretical}/M_{u\text{-}test}$ values above 1.23. This may occur because the code disregards some factors that occurred in the specimens, such as the web distortion and the interaction with local failure modes (WPB). On the other hand, ABNT NBR 8800: 2008 provides only safe results as described in **Table 3.4**, in which the highest mean of the ratio ($M_{u\text{-}Theoretical}/M_{u\text{-}test}$ = 0.80) was obtained with the *solid section* approach. In addition, the *double T section* had the most conservative result ($M_{u\text{-}Theoretical}/M_{u\text{-}test}$ mean = 0.66).

Table 3.3: $M_{u\text{-}Theoretical}/M_{u\text{-}test}$ obtained by the calculation procedure of AS4100:2020.

Model	Geometric properties approach					
	$J_{2T\text{-}Average}$	*Double T*	*Solid*	*Average*	*Superficial*	*Linear*
C4S355	1.22	1.22	1.38	1.22	1.17	1.17
C4S420	1.27	1.27	1.42	1.27	1.27	1.27
H4S355	1.18	1.18	1.32	1.18	1.18	1.18
H4S420	1.28	1.28	1.42	1.29	1.29	1.28
Mean	1.24	1.24	1.39	1.24	1.23	1.23
SD. (10^2)	4.77	4.75	4.52	4.78	6.09	6.07
Var. (%)	0.23	0.23	0.20	0.23	0.37	0.37

Source: Oliveira *et al*. (2023a).

Table 3.4: $M_{u\text{-}Theoretical}/M_{u\text{-}test}$ obtained by the calculation procedure of ABNT NBR 8800: 2008.

Model	Geometric properties approach					
	$J_{2T\text{-}Average}$	*Double T*	*Solid*	*Average*	*Superficial*	*Linear*
C4S355	0.69	0.67	0.83	0.76	0.78	0.74
C4S420	0.69	0.67	0.79	0.74	0.75	0.71
H4S355	0.67	0.65	0.79	0.73	0.75	0.71
H4S420	0.68	0.67	0.79	0.73	0.75	0.72
Mean	0.68	0.66	0.80	0.74	0.76	0.72
SD. (10^2)	1.05	0.92	2.01	1.42	1.51	1.36
Var. (%)	0.01	0.01	0.04	0.02	0.02	0.02

Source: Oliveira *et al*. (2023a).

Table 3.5 presents the $M_{u\text{-}Theoretical}/M_{u\text{-}test}$ values provided by the standard recommendation of EN 1994- 1-1: 2004. As observed, utilizing the M_{cr} calculation proposed by Roik *et al*. (1990), this code obtained safe results for all geometric property approaches, with the highest mean of the ratio ($M_{u\text{-}Theoretical}/M_{u\text{-}test}$ = 0.71) obtained with the *solid section* approach. In addition, considering all results in **Table 3.5**, the M_{cr} proposition by Hanswille *et al*. (1998) with the *solid section* had the most non-conservative $M_{u\text{-}Theoretical}/M_{u\text{-}test}$ values, having a mean equal to 1.90. As previously stated, using M_{cr} by Oliveira (2018) and $J_{2T,Average}$, EN 1994- 1-1: 2004 formulation had the highest mean of the ratio ($M_{u\text{-}Theoretical}/M_{u\text{-}test} = 0.951$) considering only safe values, followed by *double T section* approach ($M_{u\text{-}Theoretical}/M_{u\text{-}test} = 0.949$). Finally, within all methods analyzed in this study, the most conservative results were obtained by EN 1994- 1-1: 2004 recommendation with M_{cr} by Roik *et al*. (1990) and *double T section* ($M_{u\text{-}Theoretical}/M_{u\text{-}test}$ mean = 0.58).

Within all formulations analyzed in this work, the Salah's M_u proposition (2009) with M_{cr} by Roik *et al*. (1990) and *solid section*, as well as with Oliveira (2018) and *double T section*, had the better mean of the ratio ($M_{u\text{-}Theoretical}/M_{u\text{-}test} = 1.00$), as shown in **Table 3.6**. However, these formulations overestimated the M_u for the specimens C4S420 and H4S420. On the other hand, among the results presented in Table 14, the most M_u overestimation were obtained using M_{cr} by Hanswille *et al*. (1998) and *solid section* ($M_{u\text{-}Theoretical}/M_{u\text{-}test}$ mean = 2.06).

As noted, all results presented in **Table 3.7** were significantly non-conservative. Within all formulations analyzed in this study, Salah's M_u proposition (2009) with M_{cr} by Svensson (1985) and the *solid section* provided the most M_u overestimation, in which the mean of $M_{u\text{-}Theoretical}/M_{u\text{-}test}$ ratio was 2.55 (**Table 3.7**). This way, one must have a critical eye when adopting the propositions of Svensson (1985) and Williams and Jemah (1987) to determine the M_{cr}.

It is noted that the assessment presented in this section is limited, as it addresses only four specimens (C4S355, C4S420, H4S355 and H4S420). Furthermore, when verifying the same formulations addressed in this study for beams with other geometries and materials, the calculation procedures can obtain different precisions from those presented in this section. Salah (2009) tested the other four composite cellular and castellated beams with short spans (C2S355, C2S420, H2S355 and H2S420). However, these beams reach the failure by WPB predominance. This way, formulations for WPB resistance must be verified.

Table 3.5: $M_{u\text{-}Theoretical}/M_{u\text{-}test}$ obtained by the calculation procedure of EN 1994- 1-1: 2004.

Model	M_{cr} proposition / *Geometric properties approach																	
	Roik *et al*. (1990)						Hanswille *et al*. (1998)						Oliveira (2018)					
	$J_{2T\text{-}Avg}$	*Db. T*	*Solid*	*Avg.*	*Sup.*	*Lin.*	$J_{2T\text{-}Avg}$	*Db. T*	*Solid*	*Avg.*	*Sup.*	*Lin.*	$J_{2T\text{-}Avg}$	*Db. T*	*Solid*	*Avg.*	*Sup.*	*Lin.*
C4S355	0.60	0.58	0.73	0.66	0.68	0.64	1.24	1.24	1.86	1.57	1.66	1.48	0.94	0.93	1.31	1.14	1.19	1.09
C4S420	0.59	0.58	0.72	0.65	0.67	0.62	1.34	1.34	1.97	1.68	1.77	1.59	0.97	0.97	1.32	1.16	1.21	1.11
H4S355	0.58	0.56	0.70	0.64	0.65	0.62	1.22	1.22	1.79	1.52	1.60	1.44	0.92	0.91	1.26	1.10	1.15	1.05
H4S420	0.59	0.58	0.71	0.65	0.67	0.63	1.37	1.37	1.96	1.69	1.77	1.60	0.98	0.98	1.31	1.16	1.21	1.11
Mean	0.59	0.58	0.71	0.65	0.67	0.63	1.29	1.29	1.90	1.61	1.70	1.53	0.95	0.95	1.30	1.14	1.19	1.09
SD. (10^2)	0.94	0.83	1.39	1.11	1.19	1.09	7.35	7.35	8.89	8.30	8.51	8.07	2.93	2.91	2.96	2.88	2.89	2.87
Var.(%)	0.01	0.01	0.02	0.01	0.01	0.01	0.54	0.54	0.79	0.69	0.72	0.65	0.09	0.08	0.09	0.08	0.08	0.08

**Db. T* is the *double T*, *Avg.* is the *Average*, *Sup*. is the *Superficial*, and *Lin*. is the *Linear* weighting section approaches.

Source: Oliveira *et al*. (2023a).

Table 3.6: $M_{u\text{-}Theoretical}/M_{u\text{-}test}$ obtained by the calculation procedure of Salah's M_u proposition (2009) with M_{cr} calculation based on the U-frame model.

Model	M_{cr} proposition / Geometric properties approach																	
	Roik *et al*. (1990)						Hanswille *et al*. (1998)						Oliveira (2018)					
	$J_{2T\text{-}Avg}$	*Db. T*	*Solid*	*Avg.*	*Sup.*	*Lin.*	$J_{2T\text{-}Avg}$	*Db. T*	*Solid*	*Avg.*	*Sup.*	*Lin.*	$J_{2T\text{-}Avg}$	*Db. T*	*Solid*	*Avg.*	*Sup.*	*Lin.*
C4S355	0.72	0.71	1.00	0.86	0.90	0.82	1.50	1.49	2.04	1.79	1.86	1.72	0.99	0.99	1.42	1.21	1.27	1.15
C4S420	0.74	0.73	1.03	0.88	0.92	0.83	1.58	1.58	2.13	1.88	1.95	1.80	1.03	1.03	1.47	1.26	1.32	1.20
H4S355	0.70	0.69	0.96	0.83	0.86	0.79	1.46	1.46	1.96	1.73	1.80	1.66	0.97	0.97	1.36	1.17	1.23	1.12
H4S420	0.75	0.74	1.02	0.88	0.92	0.85	1.60	1.60	2.12	1.88	1.95	1.80	1.04	1.04	1.46	1.26	1.32	1.20
Mean	0.73	0.72	1.00	0.86	0.90	0.82	1.53	1.53	2.06	1.82	1.89	1.74	1.01	1.00	1.43	1.23	1.28	1.17
SD. (10^2)	2.39	2.34	3.28	2.78	2.75	2.40	6.67	6.66	7.84	7.25	7.42	7.08	3.54	3.53	4.86	4.16	4.36	3.98
Var.(%)	0.06	0.05	0.11	0.08	0.08	0.06	0.44	0.44	0.61	0.52	0.55	0.50	0.13	0.12	0.24	0.17	0.19	0.16

**Db. T* is the *double T*, *Avg.* is the *Average*, *Sup*. is the *Superficial*, and *Lin*. is the *Linear* weighting section approaches.

Source: Oliveira *et al*. (2023a)

Table 3.7: $M_{u\text{-}Theoretical}/M_{u\text{-}test}$ obtained by the calculation procedure of Salah's M_u proposition (2009) with M_{cr} calculation proposed by Svensson (1985) and Williams and Jemah (1987).

Model	**M_{cr} proposition / Geometric properties approach**									
	Svensson (1985)					Williams and Jemah (1987)				
	Double T	*Solid*	*Average*	*Superficial*	*Linear*	*Double T*	*Solid*	*Average*	*Superficial*	*Linear*
C4S355	1.66	2.51	2.10	2.22	1.99	1.65	2.48	2.08	2.19	1.96
C4S420	1.78	2.65	2.23	2.35	2.11	1.76	2.61	2.20	2.30	2.05
H4S355	1.64	2.41	2.04	2.15	1.93	1.62	2.38	2.02	2.12	1.91
H4S420	1.82	2.64	2.24	2.35	2.13	1.80	2.60	2.21	2.32	2.10
Mean	1.72	2.55	2.15	2.27	2.04	1.71	2.52	2.12	2.23	2.01
SD. (10^2)	8.57	11.06	9.68	10.05	9.34	8.34	10.78	9.43	9.36	8.45
Var. (%)	0.73	1.22	0.94	1.01	0.87	0.70	1.16	0.89	0.88	0.71

**Db. T* is the *double T*, *Avg.* is the *Average*, *Sup.* is the *Superficial*, and *Lin.* is the *Linear* weighting section approaches.

Source: Oliveira *et al*. (2023a).

3.1.2 Final remarks and discussion

The accuracy of the procedures in question was verified by comparing their results with the experimental results of Salah (2009). Through this analysis, it was observed that many analyzed approaches overestimated the M_u. Among the formulations that had only safe results, the combination of EN 1994-1-1: 2004 with M_{cr} by Oliveira (2018) and $J_{2T,Average}$ obtained the highest mean of the ratio ($M_{u\text{-}Theoretical}/M_{u\text{-}test}$ = 0.951). Additionally, EN 1994-1-1: 2004 and ABNT NBR 8800: 2008 with M_{cr} by Roik *et al*. (1990) were the only methodologies that provided conservative results for all section approaches.

As discussed, the procedures assessed in the present study are adaptations of methodologies for checking the LDB in steel-concrete composite beams without web openings. Therefore, specific development design calculation for composite alveolar beams is necessary to consider the possibility of WPB. However, it is a complex study to be carried out due to the significant influence of many parameters. This way, some authors have been using artificial intelligence algorithms, in which a reliable database with information on the behavior of alveolar beams are adopted to generate mathematical formulations for the beams resistance prediction (ABAMBRES *et al*., 2019; AMAYREH; SAKA, 2005; DE CARVALHO *et al*., 2022; DEGTYAREV; TSAVDARIDIS, 2022; FERREIRA *et al*., 2022b; GHOLIZADEH; PIRMOZ; ATTARNEJAD, 2011; HOSSEINPOUR; SHARIFI; SHARIFI, 2020; LIMBACHIYA; SHAMASS, 2021; MOGHBELI; SHARIFI, 2021; NGUYEN; LY; TRAN, 2021; RAJANA; TSAVDARIDIS; KOLTSAKIS, 2020; SEGHIER *et al*., 2023; SHAMASS *et al*., 2022; SHARIFI *et al*., 2020; SHARIFI; TOHIDI, 2014). These techniques also were used for LDB resistance prediction of beams without web openings (COUTO, 2022; HOSSEINPOUR *et al*., 2022; ROSSI *et al*., 2022; TOHIDI; SHARIFI, 2015).

3.2 ACCURACY OBTAINED BY WPB RESISTANCE FORMULATIONS

To verify the accuracy of the calculation procedures presented in **section 2.1.3**, the results obtained by these WPB resistance predictions were compared to the experimental results of Salah (2009) and Geng *et al*. (2023). Two composite cellular beams (C2S355 and C2S420) and two composite castellated beams (H2S355 and H2S420) tested by Salah (2009) reached failure by WPB. Additionally, two composite castellated beams (CBS-2 and CBS-4) tested by Geng *et al*. (2023) also had the ultimate capacity limited by WPB. These specimens are adopted for the present theoretical analyses. However, some methodologies cannot be applied to the specimens tested by Salah (2009), which, for this reason, were not verified. The method proposed by Ward (1990) is limited for the $1.08 \leq p/D_o \leq 1.50$ and $1.25 \leq d_g/D_o \leq 1.75$, and the C2S355 and C2S420 specimens of Salah (2009) have $p/D_o=1.57$. Moreover, the H2S355 and H2S420 specimens have $b_w/t_w=40$, and the proposition of Aglan and Redwood (1974) is limited for the $45^0 \leq \theta \leq 60^0$, $10 \leq b_w/t_w \leq 30$ and $D_o/b_w \leq 8$. The methodology of Panedpojaman, Thepchatri and Limkatanyu (2014) was also not verified, as the calculation procedure needs the parent I-section depth (d), and the cellular I-profiles of Salah (2009) were manufactured directly cutting the web. This way, the cellular I-sections of Salah (2009) were not manufactured by the height expansion process of the parent profile.

Table 3.8 and **Table 3.9** present the parameters and properties of the specimens used in the analyses. In **Table 3.9**, V_v is the ultimate vertical shear force, and V_h is the ultimate horizontal shear force obtained by the tests.

Table 3.8: Geometric parameters of the specimens (in mm).

Specimen	d_g	b_f	t_f	t_w	D_0	$^a b_w$	$^b e$	s	θ	p	c
C2S355	480	100	6	4	336	193	-	-	-	529	50
C2S420	480	100	6	4	336	193	-	-	-	529	50
H2S355	480	100	6	4	321	160	369	92	60.2^0	529	50
H2S420	480	100	6	4	321	160	369	92	60.2^0	529	50
CBS-2	500	250	14	8	236	224	272	68	60^0	496	45
CBS-4	500	250	14	8	300	224	346	86.5	60^0	570	45

$^a b_w$ is the web-post width; $^b e$ is the tee length of the castellated I-section.

Source: The author (2025).

Table 3.9: Mechanical properties and ultimate shear force (horizontal and vertical) of the specimens.

Specimen	E (GPa)	f_y (MPa)	V_v (kN)	V_h (kN)
C2S355	200	355	86.66	89.20
C2S420	200	420	89.39	92.01
H2S355	200	355	-	90.14
H2S420	200	420	-	91.51
CBS-2	200	355	-	363.68
CBS-4	200	355	-	304.05

Source: The author (2025).

Table 3.10 and **Table 3.11** show the accuracy obtained by the WPB resistance predictions for composite cellular and castellated beams, respectively. As noted in **Table 3.10**, the methodology of Lawson *et al*. (2006) provided conservative results, with differences of around 50% lower than the test results. The EN 1993-1-13: 2024 procedure also obtained conservative results for composite cellular beams, with divergences of 46.1% and 47.2% lower than the experimental results (**Table 3.10**). In contrast, the formulation of Aglan and Redwood (1974) had elevated non-conservative results for the CBS-2 and CBS-4 specimens, with divergences of 21.1% and 84.4% higher than the test results (**Table 3.11**). Meanwhile, the EN 1993-1-13: 2024 procedure for composite castellated beams provided conservative and non-conservative results. This formulation had conservative results for the H2S355 and H4S420 specimens, with deviation around 57% lower than the tests. On the other hand, it had slight non-conservative results for the CBS-2 and CBS-4 specimens, in which the theoretical WPB resistance was 8.1% and 0.8% higher than the tests.

Table 3.10: Results of the procedures for composite cellular beams and the tests of Salah (2009).

Specimen	Test	Lawson *et al*. (2006)		Test	EN 1993-1-13: 2024	
	$V_{v\text{-}tests}$ (kN)	$V_{v\text{-}theoretical}$ (kN)	$V_{v\text{-}theoretical}/V_{v\text{-}tests}$	$V_{h\text{-}tests}$ (kN)	$V_{h\text{-}theoretical}$ (kN)	$V_{h\text{-}theoretical}/V_{h\text{-}tests}$
C2S355	86.66	43.85	0.506	89.20	48.11	0.539
C2S420	89.39	45.39	0.508	92.01	48.57	0.528

Source: The author (2025).

Table 3.11: Results of the procedures for composite castellated beams and the tests of Salah (2009) and Geng *et al*. (2023).

Specimen	Test	Aglan and Redwood (1974)		EN 1993-1-13: 2024	
	$V_{h\text{-}tests}$ (kN)	$V_{h\text{-}theoretical}$ (kN)	$V_{h\text{-}theoretical}/V_{h\text{-}tests}$	$V_{h\text{-}theoretical}$ (kN)	$V_{h\text{-}theoretical}/V_{h\text{-}tests}$
H2S355	90.14	-	-	38.89	0.431
H2S420	91.51	-	-	39.25	0.429
CBS-2	363.68	440.31	1.211	393.13	1.081
CBS-4	304.05	560.83	1.844	306.47	1.008

Source: The author (2025).

All WPB resistance predictions for composite alveolar beams presented in **section 2.1.3** do not consider the contribution of the slab, which can lead to an inappropriate analysis and provide divergence with test results, as shown in this section. Therefore, the contribution of the composite action might be regarded in the WPB resistance, as proposed by Ferreira *et al*. (2021b, 2021c) for composite cellular beams with precast hollow-core slabs.

3.3 SUMMARY AND CONCLUSIONS OF THE CHAPTER

This chapter presented a theoretical study on the accuracy of formulation predictions of LDB and WPB resistance of composite alveolar beams. The results of the analyzed approaches for LDB resistance predictions can be found in the review article by Oliveira *et al*. (2023a). As a summary and conclusion of the chapter, it can be stated that:

- Regarding the LDB formulations, it was observed that many analyzed approaches provided non-conservative results. Among the formulations that had only conservative results, the combination of EN 1994-1-1: 2004 with M_{cr} by Oliveira (2018) and $J_{2T,Average}$ obtained the highest mean of the ratio ($M_{u\text{-}Theoretical}/M_{u\text{-}test}$ = 0.951);
- Among the WPB formulations for composite cellular beams, the proposition of Lawson *et al*. (2006) and the EN 1993-1-13: 2024 procedure provided conservative results;
- The methodology for WPB resistance of composite castellated beams proposed by Aglan and Redwood (1974) had elevated non-conservative results for the analyzed specimens;
- EN 1993-1-13: 2024 procedure provided, at the same time, conservative and slight non-conservative results for WPB resistance of composite castellated beams.
- The analyses presented in this section are limited, and there is a need for further investigations.

CHAPTER 4

EXPERIMENTAL TESTS

This section presents the laboratory tests performed. It describes the geometry of the specimens with their respective dimensions, the instrumentation for measurements, material property characterization, and the flexural response of each model. In addition, the accuracy of formulations for WPB resistance prediction is also verified against experimental results. All this chapter is based on the article by Oliveira *et al*. (2025).

4.1 THREE-POINT BENDING TESTS

Full-scale tests were performed to analyze the WPB behavior of steel-concrete composite castellated beams with precast UHPC slabs in hogging moment regions. This experimental program assesses the local stability behavior of two steel-UHPC composite castellated beams, addressing the Peiner and Anglo-Saxon opening patterns (**Figure 1.2b-c**). This way, short-span alveolar beams in three-point bending tests were adopted in compliance with experimental assessments of WPB in steel alveolar beams (GRILO *et al.*, 2018; TSAVDARIDIS; MELLO, 2011; VIEIRA, 2015). The tests were conducted with the inverted composite beam, in which the slab was allocated in the supports, and the load was applied in the I-section to apply the hogging bending (GENG *et al.*, 2023; QI *et al.*, 2020; QIU *et al.*, 2025). The details and layout of the tests are presented in the following subsection.

4.1.1 Geometry and materials

Both specimens are steel-concrete composite castellated beams with precast UHPC slabs, having shear pockets. The beams were manufactured from a W360x44.6 parent profile and the parameter that varied in this experimental program was the opening pattern of the castellated I-sections. The adopted patterns were Peiner and Anglo-Saxon. Therefore, the experimental models are named CCB-P and CCB-A, respectively. **Figures 4.1-4.2** present the details of the two specimens' design. The design of the UHPC slabs was informed by prior numerical simulations and analytical modeling, offering insights for achieving an optimal configuration suited to laboratory conditions and actuator capacity. Both composite castellated beams were designed to ensure full composite action while minimizing the required connectors. The shear pocket design, including their spacing and the arrangement of head studs within the shear pocket regions, was thoroughly analyzed in advance. Furthermore, the truncated pyramid shape of the shear pockets was selected based on findings from previous studies (FANG *et al*., 2022b; HU *et al*., 2020; QI *et al*., 2020).

Figure 4.1: Elevation view and cross-section detailing of the specimens (in mm).

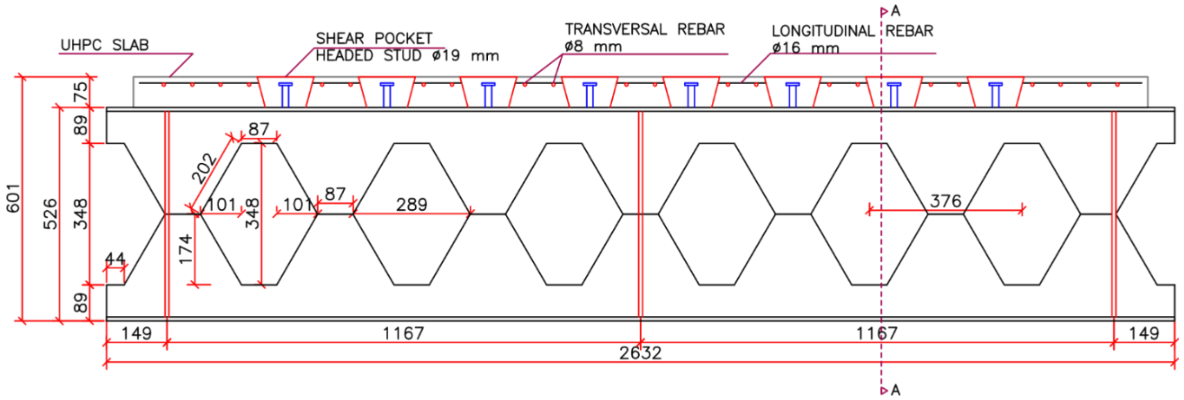

(a) CCB-A specimen

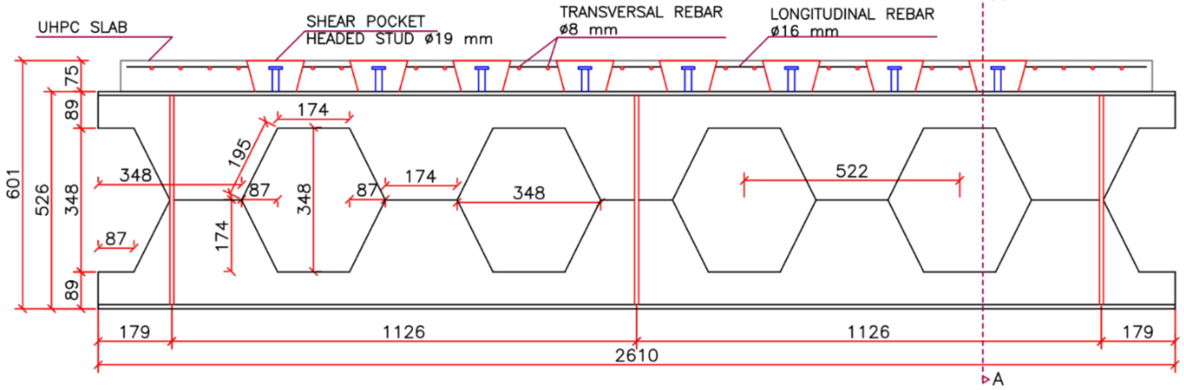

(b) CCB-P specimen

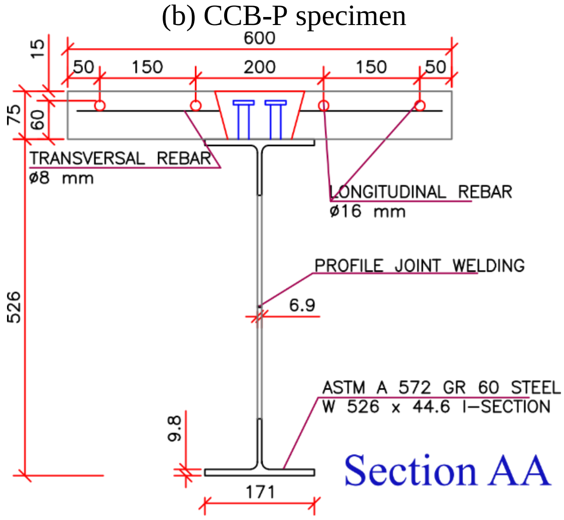

(c) Cross-section

Source: The author (2025).

Figure 4.2: Slab detailing of the specimens (in mm).

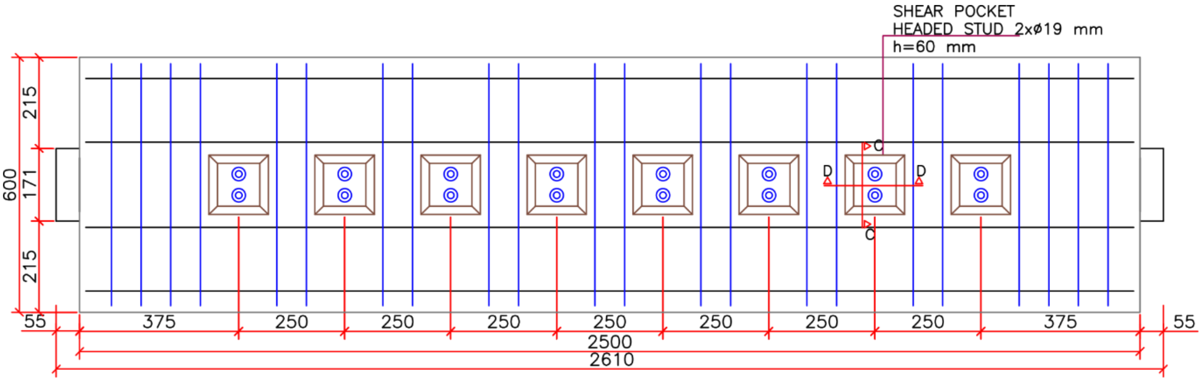

(a) Plan view (shear pockets)

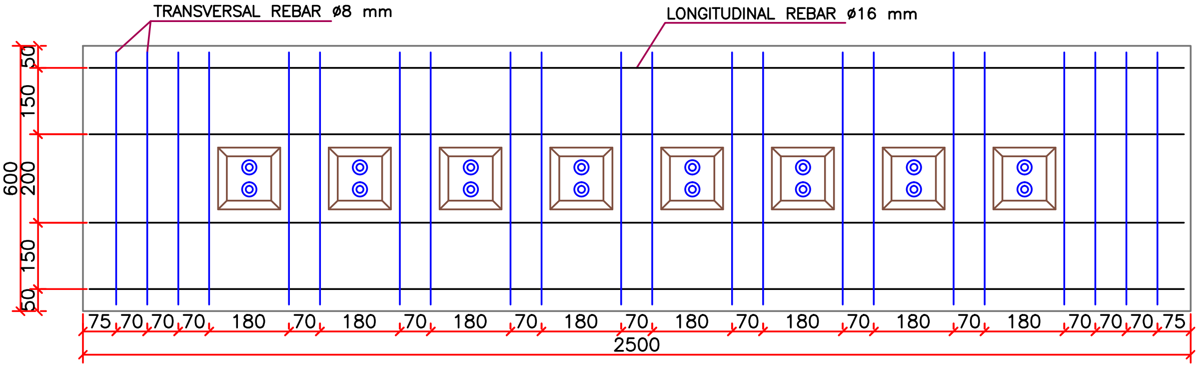

(b) Plan view (reinforcement)

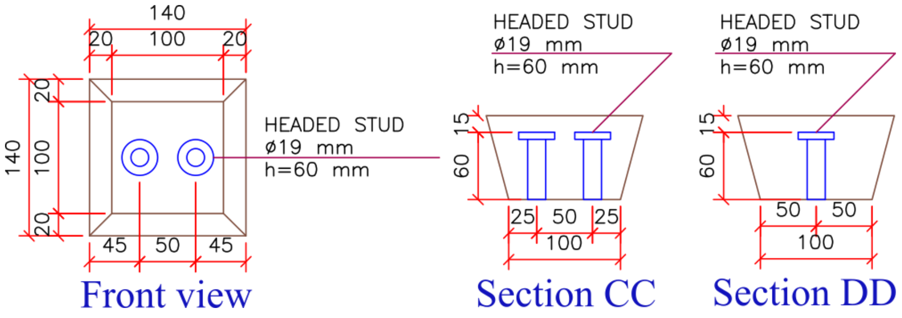

(c) Shear pockets detailing

Source: The author (2025).

Table 4.1 shows the nominal material properties of the adopted steel I-section and reinforcement bars. The castellated I-sections are made of ASTM A572 Gr 60 steel, and the longitudinal and transversal reinforcement bars are deformed steel bars with yield strength of 700 MPa and 500 MPa, respectively. Due to the employment of the UHPC slab, high-strength carbon steel headed studs were utilized. As a reference, steel-UHPC composite beams tested by Tong *et al*. (2022) for sagging bending failed in the stud shear connectors, which had a tensile strength of around 455 MPa. Thus, 19x60mm and high-strength carbon steel headed studs were used to avoid the same happening in this experimental program. **Table 4.2** presents the material properties of the steel I-section and headed studs obtained by the axial tensile tests, which were performed according to ASTM A370-24. The high-strength carbon steel of the headed studs did not show an evident yield plateau. This way, only the tensile strength of the steel headed stud could be determined. Finally, **Table 4.3** presents the composition of UHPC, in which the adopted straight steel fiber is 0.2mm in diameter and 13mm in length with a minimum tensile strength of 2850 MPa and a modulus of elasticity of 200 GPa. **Table 4.4** describes the UHPC characterization test results, which were performed according to Osorio, Bairán and Marí (2013), Krahl, Carrazedo and El Debs (2018), and Pressmair *et al*. (2022). The UHPC was produced according to experimental tests performed by doctoral student Vinicius Brother dos Santos in his thesis (**Table 4.3**), which is in development, with the theme "*Experimental and numerical study of steel and ultra-high performance concrete composite beams under hogging moment*". The author in question also carried out the steel and UHPC characterization tests (**Table 4.2**) and (**Table 4.4**), in which the same materials were used in his and present thesis.

Table 4.1: Steel I-section and reinforcement bars nominal material properties.

Material	E (MPa)	v	f_y (MPa)	f_u (MPa)
Steel I-section	200,000	0.3	415	520
Longitudinal rebars	210,000	0.3	700	770
Transversal rebars	210,000	0.3	500	550

Source: The author (2025).

Table 4.2: Steel axial tensile test results.

Element	Mean f_y (MPa)	SD (MPa)	CoV (%)	Mean f_u (MPa)	SD (MPa)	CoV (%)
I-section	422.54	25.01	5.92	529.19	19.67	3.53
Headed stud	-	-	-	738.63	6.91	0.94

Source: Santos, V.B, Experimental and numerical study of steel and ultra-high performance concrete composite beams under hogging moment (in development).

Table 4.3: Composition of UHPC.

Component	Consumption (kg/m3)
Cement (ASTM type III)	800.00
Quartz sand (max. diameter of 1.2 mm)	846.20
Fly ash	80.00
Quartz powder	200.00
Silica fume	80.00
Water	166.20
Polycarboxylate superplasticizer	20.00
Steel fiber (2% Vol.)	156.00

Source: Santos, V.B, Experimental and numerical study of steel and ultra-high performance concrete composite beams under hogging moment (in development).

Table 4.4: UHPC characterization test results.

Property	Mean (MPa)	SD (MPa)	CoV (%)
Modulus of elasticity	44,936	-	-
Compressive strength	139.84	12.31	8.80
Tensile strength	11.07	1.51	13.64

Source: Santos, V.B, Experimental and numerical study of steel and ultra-high performance concrete composite beams under hogging moment (in development).

4.1.2 Beams manufacturing

For manufacturing the steel castellated I-beams, the computer numerical control (CNC) plasma cutting machine was employed to cut the parent I-sections, as presented in **Figure 4.3a**. Posteriorly, both parts of the I-section were separated, and, in sequence, the chamfering process with an electric angle grinder (**Figure 4.3b**) was carried out to provide better penetration of the weld material. Before the web-posts welding process, the two parts of the castellated I-section and the transversal stiffeners were tack-welded to keep them together during the welding. Finally, the web-posts were welded (**Figure 4.3c**) using gas metal arc welding (GMAW) with metal inert gas (MIG) and a MIG wire electrode with a nominal tensile strength of 760 MPa. In addition, headed studs were welded on the top flange of the castellated I-section, obtaining the final profiles (**Figure 4.3d**) adopted for the steel-UHPC composite castellated beams specimens.

Figure 4.4 presents the precast UHPC slab manufacturing process. The formwork and its reinforcement bar allocation are shown in **Figure 4.4a**, and the formwork casting process and the post-casting result are shown in **Figure 4.4b-c**. As the cement had high initial strength (equivalent to ASTM type III), the slabs were removed from formworks and from wet curing after 15 days for the steel-UHPC composite castellated beams assembly. **Figure 4.5** shows the composite castellated beam assembling and shear pockets casting, in which the same UHPC was used. Before casting, the shear pockets of the precast slab were cleaned to improve the adhesion of both UHPC (of the shear pocket and precast slab) and wet curing was carried out after casting. The flexural tests were performed after at least 28 days of casting the shear pockets.

Figure 4.3: Steel castellated I-beams manufacturing.

(a) Thermal cutting (b) Separation and chamfering process (c) Web-posts welding

(d) Manufactured steel castellated I-beams with headed studs welded in the top flanges

Source: The author (2025).

Figure 4.4: Precast UHPC slab manufacturing.

(a) Formwork and reinforcement bars (b) Casting (c) Post-casting

Source: The author (2025).

Figure 4.5: Composite castellated beam assembling and shear pockets casting.

(a) Pre-assembling

(b) Assembling

(c) Cast shear pocket

Source: The author (2025).

4.1.3 Test setup

Figure 4.6 presents the layout of the three-point bending tests, in which the instrumented and non-instrumented sides are the side A and B, respectively. The non-instrumented side (side B) was used to perform the 3D digital image correlation (DIC) covering the regions of the web posts. For the 3D DIC, two 5-megapixel photo cameras of Correlated Solutions® captured images at intervals of 5 seconds throughout the test. VIC 3D software was used in the analyses. The grid, scale, and calibration were made using the tools provided by the Correlated Solutions® and following its user manual.

The models were supported using appropriate support devices on concrete blocks over the reaction slab. The load was applied at the center of the beam span using a hydraulic actuator fixed to the reaction frame with a capacity of 1000 kN. A ball joint was placed between the load cell and the heavy steel plate, which distributed the load at the I-section flange, and it was properly fixed to the I-section. Firstly, 50 kN was applied to the beams as a preload, eliminating any initial accommodation effect. Posteriorly, the loading program was displacement-controlled, which was conducted with two rates, 0.3 and 1.5 mm/min, for the first and second ranges, respectively. The first range is where the program begins, up to 20 mm of actuator displacement, and the second range is up to 50mm. In addition, the acquisition data were obtained at a rate of 5 Hz.

Figure 4.7 presents the instrumentation adopted on the physical models. For the vertical displacement measurements, four transducers of 100mm (D7, D8, D9 and D10) were adopted. Additionally, twelve transducers of 25mm were adopted for the longitudinal (D2, D3, D4, D5 and D6) and lateral displacements (D1, D11, D12, D13, D14, D15 and D16). The web-posts covered by the 3D DIC are the same ones to which the D15 and D16 displacement transducers were allocated. Regarding the strain measurement, three electrical strain gauges were allocated in the transversal reinforcement bars (S1, S2 and S3), as illustrated in **Figure 4.7c**. In addition, in the composite section of the central region, two electrical strain gauges were used in the lower face of the UHPC slab (S12 and S13), four in the longitudinal reinforcement bars (S6, S7, S8 and S9), and five in the steel I-section (S16, S17, S18, S19 and S20), as shown in **Figure 4.7a-c**.

Displacement transducers were used to measure and monitor the vertical displacements of the composite beam (**Figure 4.7a**), the lateral displacements of the steel profile (**Figure 4.7a-b**), and possible longitudinal slips between the steel section and the UHPC slab (**Figure 4.7a**). Two displacement transducers (D7 and D8) were allocated in both supports to capture the vertical displacements of the accommodation effect. Based on the three-point bending tests by Grilo (2018) and Grilo *et al.* (2018), which analyzed the WPB behavior of steel cellular beams, displacement transducers were adopted in the compressed diagonal of the web-post (**Figure 4.7a-b**), seeking to measure the lateral displacements caused by WPB. Both sides of the beams were instrumented in the web-post.

The D1 and D9 displacement transducers were employed to control the tests' conduction (**Figure 4.7a-b**). D1 was used to verify lateral displacements on the compressed flange, which would be observed if LDB had occurred, and D9 was allocated to evaluate relative vertical displacements between the steel profile and the UHPC slab. The D2, D3, D4, D5 and D6 displacement transducers were fixed to the I-section to measure the relative slip between the UHPC slab and the I-section.

Figure 4.6: Three-point bending tests.

(a) CCB-P specimen (view from side B and DIC's view) (b) CCB-P specimen (DIC's side)

(c) Instrumentation (view from side A)

Source: The author (2025).

Figure 4.7: Instrumentation and measurements.

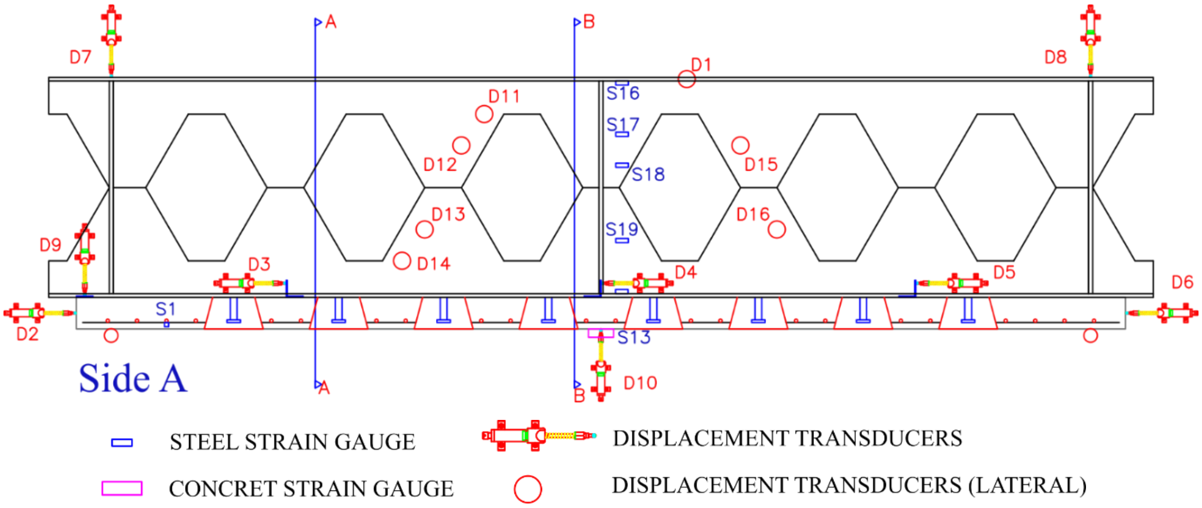

(a) Elevation view from side A

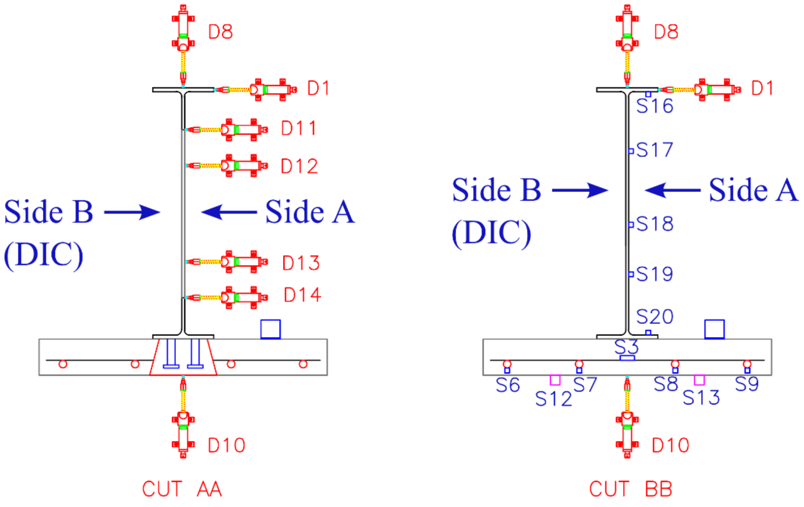

(b) Cuts (AA and BB)

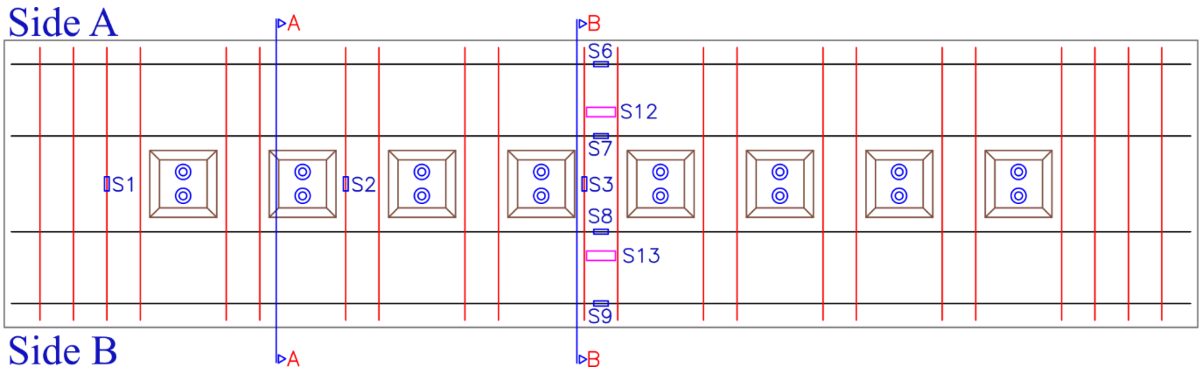

(c) Plan view

Source: The author (2025).

4.2 RESULTS AND DISCUSSION

Figure 4.8a brings the load-deflection curves of the tests. The CCB-A beam had a higher ultimate load ($P_{u\text{-}Exp}$= 535.14kN) and lower respective deflection ($d_{u\text{-}Exp}$= 10.43mm) than the CCB-P beam ($P_{u\text{-}Exp}$= 506.61kN; $d_{u\text{-}Exp}$= 11.37mm). The percentual difference in load capacity was 5.6%, which is not considered significant for experimental tests. Several factors, such as load and support accommodations, concrete and steel mechanical properties variability, geometrical imperfections, and weld production processes, can influence experimental results. In contrast, the CCB-P sustained a higher load than CCB-A after peak, indicating more ductility of the CCB-P beam. However, the loads sustained by both beams are very similar after peak. It is clear from **Figure 4.8c** that the lateral deflection in the web-post measured by D15 displacement transducer started to present higher lateral deflections earlier than the other points, probably resulting from a higher initial imperfection at that point, which explains the stiffness reduction observed in this beam at a load level of 200kN and can be a major reason for the smaller peak. For the other displacement transducers, D15 and 16 for beam CCB-A and D16 for CCB-P (**Figure 4.8b-c**), large displacements started near the peak, indicating the WPB phenomenon. It should be highlighted that D1 and D9 displacement transducers did not measure significant displacements for both specimens. Thus, there was no LDB occurrence (D1) or detachment of the composite beam (D9). **Figure 4.8b-c** show the characteristic behavior of instability in both specimens, which had smaller displacements until close to the ultimate load, and, from 450 kN onwards, the curves present a nonlinear behavior with a significant increase in the displacements. At the end of the tests, the CCB-P specimens reached higher values of lateral displacements on the web-post because it was subjected to loads above the CCB-A beam at most post-peak ranges.

Figure 4.9 presents that both specimens reached instability by WPB, which occurred in only one of the beams' half-spans. Additionally, plastic hinges were observed at some corners of the openings, which characterizes the VM phenomenon. In the CCB-P beam, VM was slightly more accented than in the CCB-A beam, which was also evident in the results obtained by the DIC. The verified results from the 3D DIC analysis include the lateral displacements (LD) in the web-post and the in-plane principal strains (PS).

Figure 4.8: (a) Load-deflection curves of the tests and (b)-(c) Load-lateral displacement on the web-post of the tests.

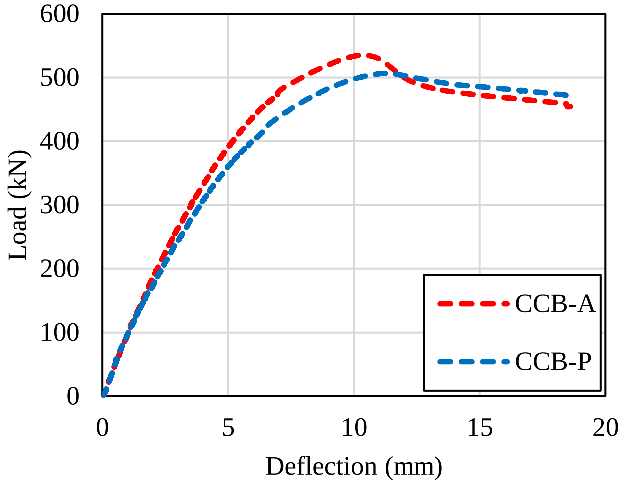

(a) CCB-A and CCB-P

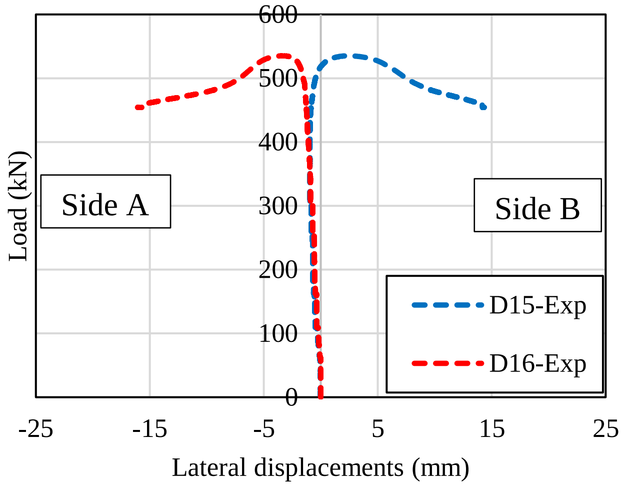

(b) CCB-A

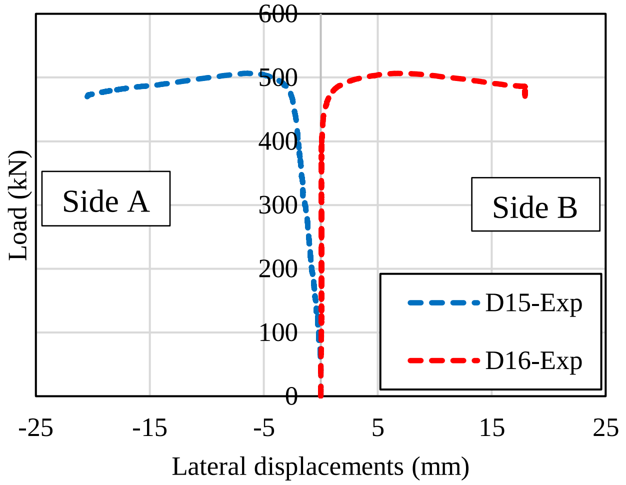

(c) CCB-P

Source: The author (2025).

Figure 4.9: Deformed configuration of the castellated I-sections.

(View from side B) (View from side B)

(View from side A) (View from side B)

(a) CCB-A (b) CCB-P

Source: The author (2025).

Figure 4.10 and **Figure 4.11** show the development of LD (on the left) and PS (on the right) with the evolution of the load-deflection relationship (P–v) for the CCB-A and CCB-P specimens, respectively. The positive values of the LD fields indicate displacements in the DIC's sense.

Figure 4.10: Lateral displacements (LD) on the left and in-plane principal strains (PS) on the right for the CCB-A specimen.

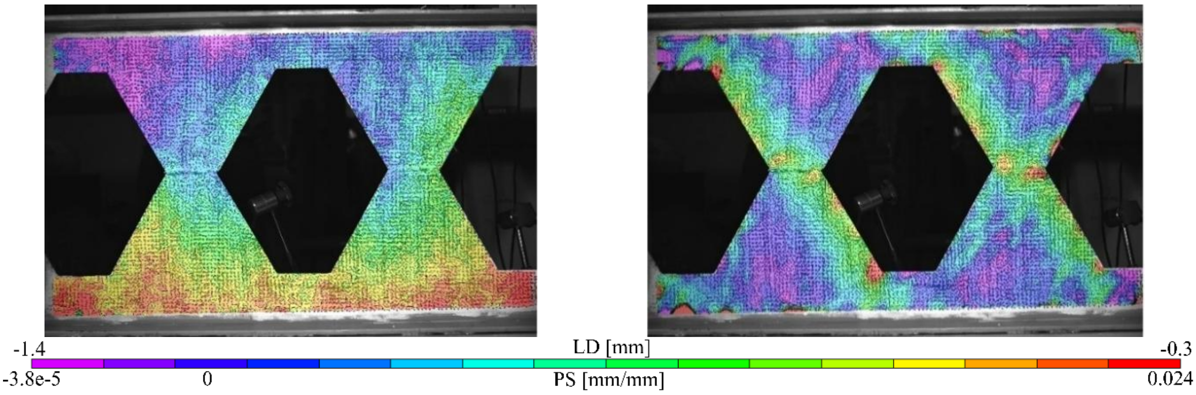

(a) P= 304kN – v= 3.6mm

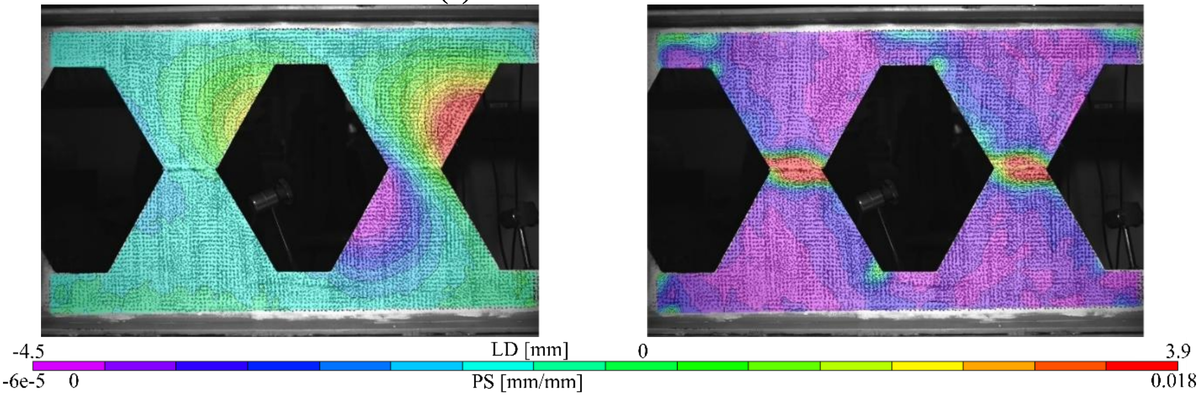

(b) P_u= 535kN – v= 10.4mm

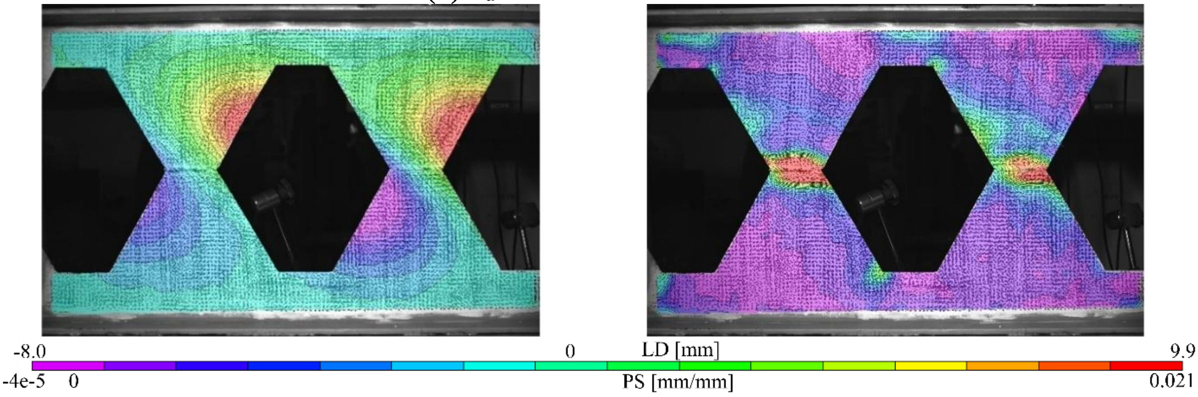

(c) P= 512kN – v= 11.6mm

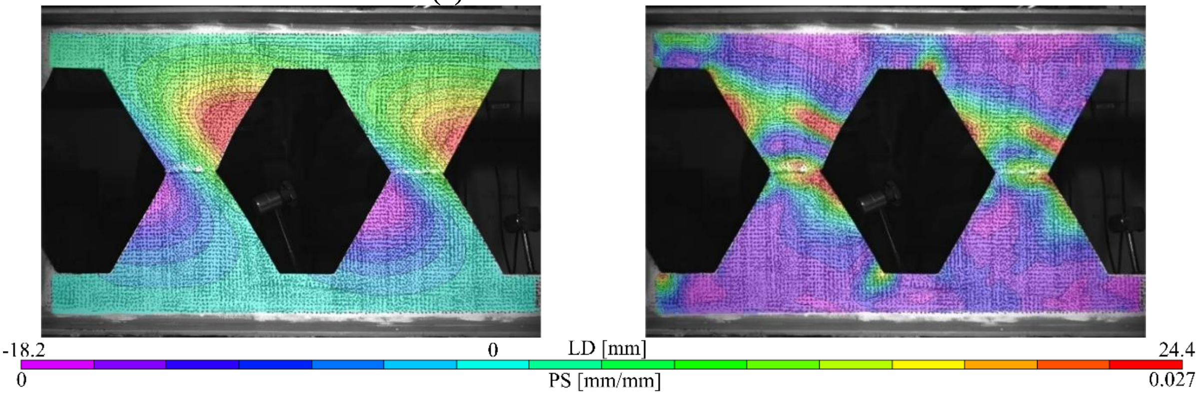

(d) P= 458kN – v= 18.3mm

Source: The author (2025).

Figure 4.11: Lateral displacements (LD) on the left and in-plane principal strains (PS) on the right for the CCB-P specimen.

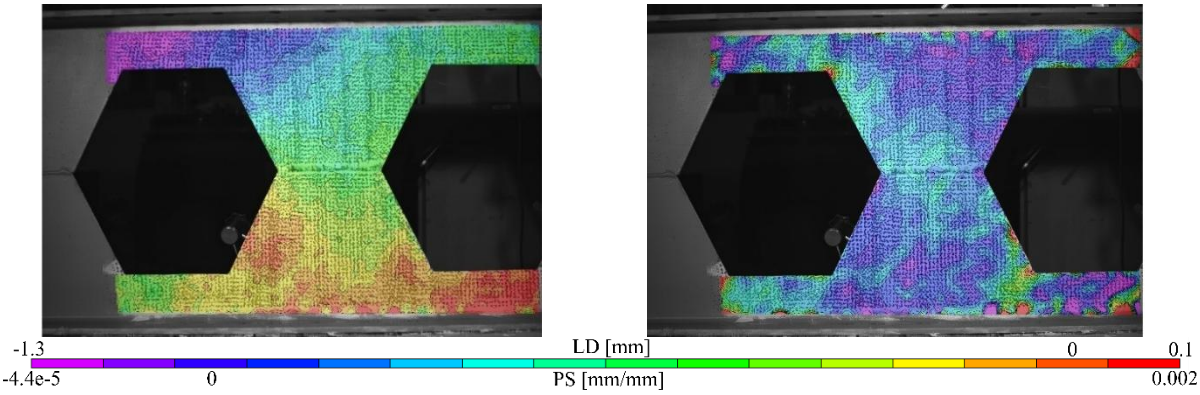

(a) *P*= 149kN – *v*= 1.7mm

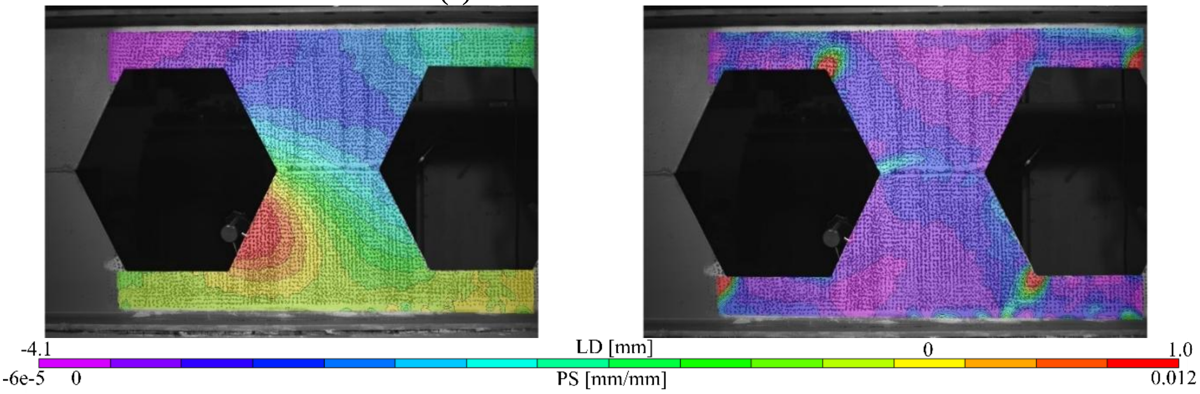

(b) *P*= 472kN – *v*= 8.4mm

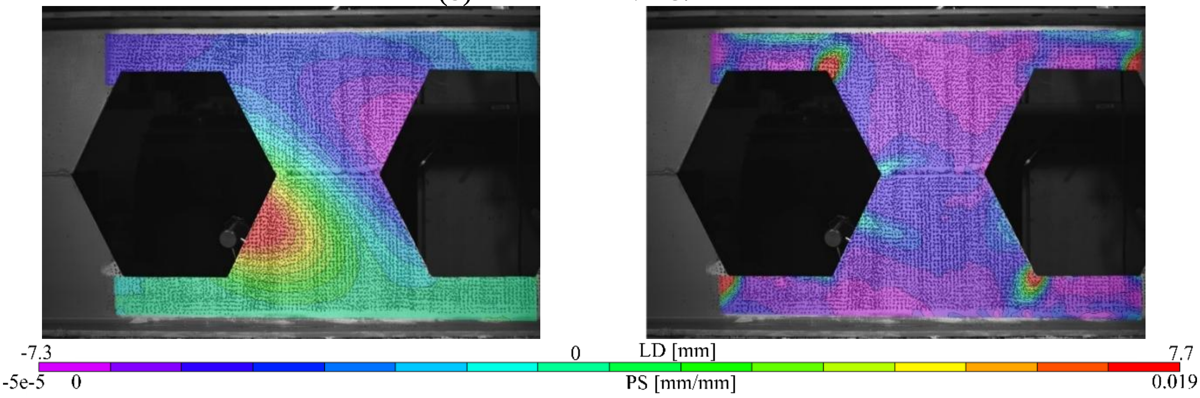

(c) P_u= 506kN – *v*= 11.4mm

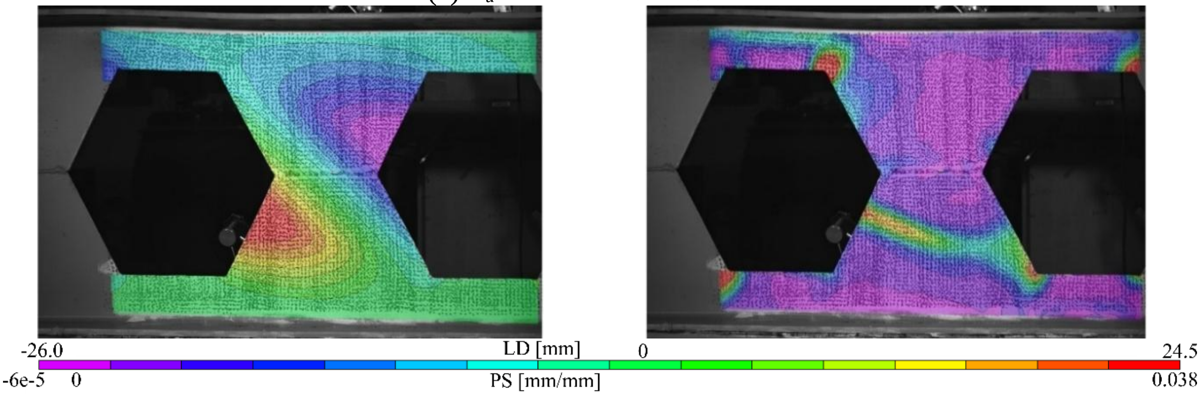

(d) *P*= 470kN – *v*= 18.5mm

Source: The author (2025).

A strain concentration of PS arises at some corners of the hexagonal openings for *P*= 304kN – *v*= 3.6mm in the CCB-A (**Figure 4.10a**) and for *P*= 149kN – *v*= 1.7mm in the CCB-P (**Figure 4.11a**). The CCB-P beam has a higher tee length (length of the hexagon horizontal edge), which makes it more critical to the VM phenomenon (formation of plastic hinges at the corners of the openings) because alveolar I-beams with higher tee length are more susceptible to VM phenomenon (MARTIN *et al.*, 2017; PANEDPOJAMAN; THEPCHATRI; LIMKATANYU, 2015; SHEEHAN *et al.*, 2016; TAŞ *et al.*, 2024; ZEYTINCI *et al.*, 2021). At this point of the test, the WPB phenomenon is not yet apparent (**Figure 4.10a** and **Figure 4.11a**). For the CCB-A beam, the LD fields that characterize the WPB occurrence are notorious, only in the closest web-post to the loading point, for *P*= 522kN – *v*= 9.1mm. When this beam reaches the ultimate load (P_u= 535kN – *v*= 10.4mm), the LD fields are very similar to *P*= 522kN – *v*= 9.1mm, only changing the LD magnitudes (**Figure 4.10b**), as the LD values of *P*= 522kN – *v*= 9.1mm vary from -2.5mm to +1.1mm. Furthermore, the PS fields are also similar in these stages of the *P*–*v* relationship, in which there is a strain concentration in the weld region of the web-posts (**Figure 4.10b**), which the short weld length can have caused due to the lower web-post width of the CCB-A beam. Regarding the CCB-P beam, the LD fields characteristic of the WPB phenomenon arise for *P*= 472kN – *v*= 8.4mm (**Figure 4.11b**) only in the bottom part of the web-post, indicating a lower load than the CCB-A at the beginning of the WPB occurrence. This also shows that the lateral deflections of WPB began only in the region of the D15 displacement transducer of the CCB-P, which may have occurred due to a higher initial imperfection in this region. It is not observed strain concentration in the weld region of the web-posts, as this castellated I-section have a higher web-post width, resulting in a higher weld length (**Figure 2.11b**). When the CCB-P beam reaches the ultimate load (P_u= 506kN – *v*= 11.4mm), the LD fields already present significant magnitudes, with maximum values in modulus of around 7mm (**Figure 4.11c**). On the other hand, when the CCB-A beam reaches the *P*-*v* relationship o *P*= 512kN – *v*= 11.6mm (after peak), the second web-post of this castellated I-section presents the LD fields of the WPB characterization, with maximum values in modulus of around 9mm, and the PS fields are still affected by the strain concentration in the weld region of the web-posts (**Figure 4.10c**). Finally, at the end of both tests (**Figure 4.10d** and **Figure 4.11d**), the LD fields present maximum values in modulus of around 25mm, and the "S" shapes in the compressed diagonal of the web-posts are evident, as shown in **Figure 4.9**. The PS fields present strain concentration at the corners of the openings, being more apparent in the CCB-P beam (**Figure 4.11d**), as this castellated I-section was more critical to the VM occurrence due to the higher tee length. Furthermore, elevated tensile strains are observed in the compressed diagonal ("S" shape region) of the web-posts in both specimens (**Figure 4.10d** and **Figure 4.11d**), caused by the membrane strains from the excessive deformations due to the WPB phenomenon in the region of the LD positive value measured by the DIC.

Figure 4.12 shows the strain diagrams for different load levels in the composite cross-section, composed of strains of both flanges and the longitudinal reinforcement bar. These measures allow an understanding of the overall behavior and the contributions of each material to the structural behavior. The strain in the I-section web was disregarded because the web presented distortion. In **Figure 4.12**, the height equal to zero is the reinforcement bars, followed by the tensioned and compressed flanges, in which the strain in the reinforcement bar is regarding the one with higher strain values in the tests, which is S7 and S8 for the CCB-A and CCB-P, respectively. The tensile cracking strain for UHPC is 246×10^{-6}, so nonlinear behavior due to UHPC multiple cracking started between 100 and 200 kN for both beams and increased faster for the CCB-A beam. However, as can be seen, the gradual cracking was incapable of reducing the stiffness for low load levels as much as the lateral displacement detected in the web of beam CCB-P at 200 kN. UHPC is on the tensioned side in hogging moment composite beams, so it does not restrict flange buckling as in sagging moment regions. However, as shear stresses influences WPB, the UHPC slab is expected to absorb shear until near the peak as the material has significant residual capacity for strains up to 2000×10^{-6} (HUNG; EL-TAWIL; CHAO, 2021). In this stage, the material presents strain localization and a significant reduction in capacity not contributing significantly to the composite beam behavior after peak. The roles of UHPC are controlling cracking for the service limit stage and absorbing part of the shear stresses at the ultimate load because of its residual capacity. The cracking pattern at the end of the test is shown in **Figure 4.13**, which evidenced the cracking localization after multiple cracking in UHPC, a typical behavior, and the cracking formation from the shear pocket corners (stress concentration) and interface (typically a region of weakness). In **Figure 4.13**, the cracks in purple color are the main cracks.

Figure 4.12: Strain diagram in the composite cross-section of the tests.

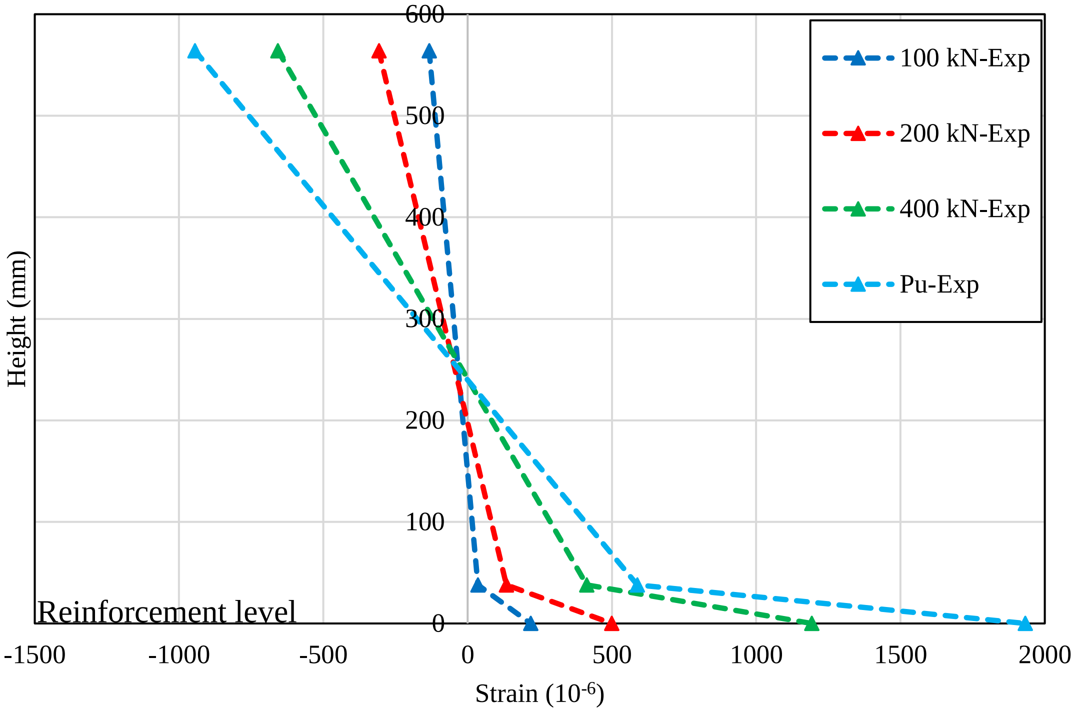

(a) CCB-A

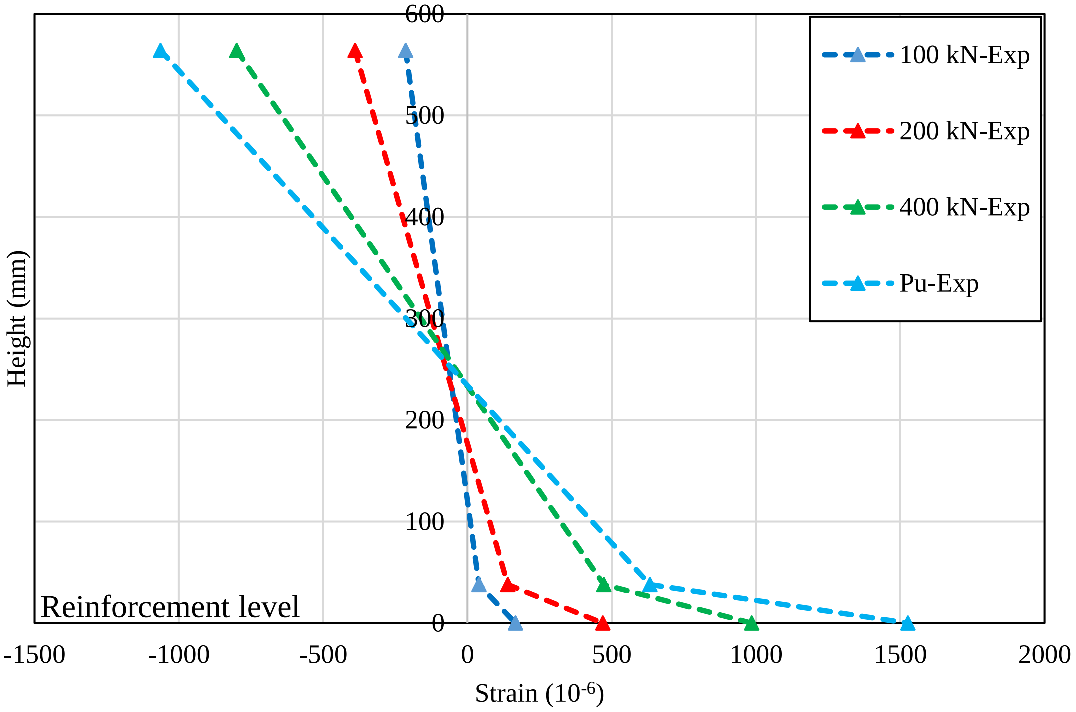

(b) CCB-P

Source: The author (2025).

Figure 4.13: Crack distribution on the UHPC slabs.

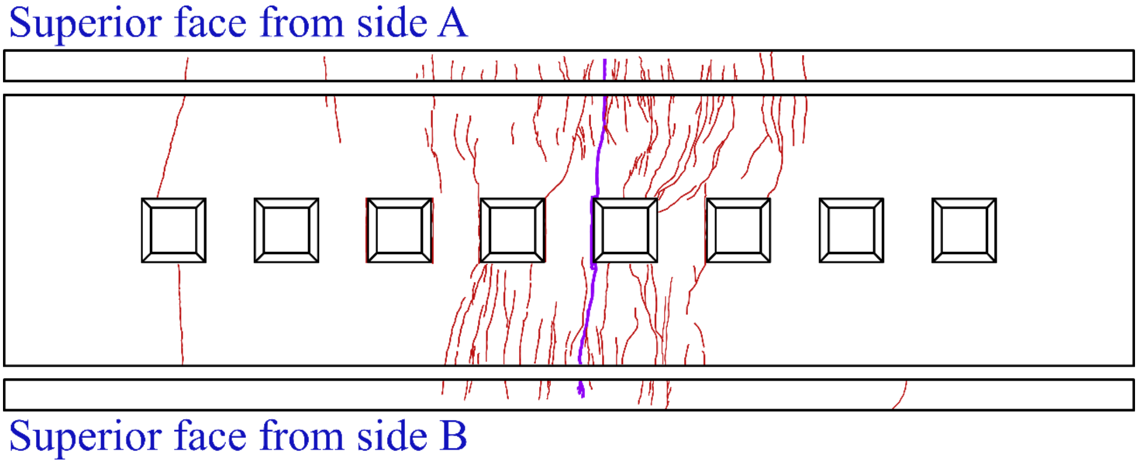

(a) CCB-A

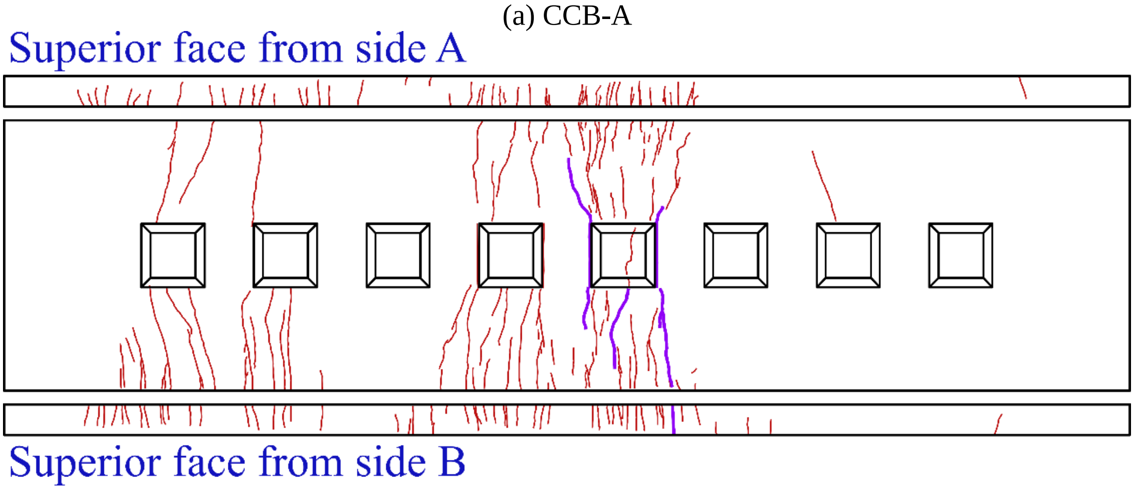

(b) CCB-P

Source: The author (2025).

Figure 4.14 presents the development of the relative slip (in modulus) along the composite beam with the load evolution. In these graphs, the measurements from the left end to the right are those measured by D2 to D6 displacement transducers according to **Figure 4.7a**. The CCB-A specimen had a slip diagram characterized by an "N" shape, in which a half-span showed the highest slip values in its central region, while the other had the highest values in its extremity. On the other hand, the CCB-P specimen presented a diagram with a "U" shape, and the highest slip values were obtained in both extremities of the beam. The differences in slip patterns are associated with the intrinsic variability of experimental tests (imperfections, material variability, construction process, etc.). It is because the static scheme's horizontal shear forces are constant along the span for a simply supported beam with a concentrated load at midspan, which would generate a constant slip. It should be emphasized that the level of relative displacement between steel and UHPC is very small, considering that the designed shear pockets effectively guarantee load transfer between steel and concrete.

Regarding the strain gauges employed in the tests, those named S1, S2 and S3 measured the strain in the transversal reinforcement bars (**Figure 4.7**). For both specimens, the S1 strain gauge measured the highest values of strain, significantly higher than those measured by S2 and S3. Thus, the transversal reinforcement bars closer to the extremities had higher strain values than those from the central region of the composite beam. In addition, only the S1 strain gauge of the CCB-P measured strain values above the yield limit before the composite beam reached the ultimate load, which may have occurred by the significantly higher slip measured at this extremity of the composite beam, as shown in the left end from **Figure 4.14b**. Despite the static scheme presenting constant shear throughout the span, cracking and buckling promote redistribution, combined with test variability can be reasons for such a behavior.

Figure 4.14: Relative slip (in modulus) along the composite castellated beams of the tests.

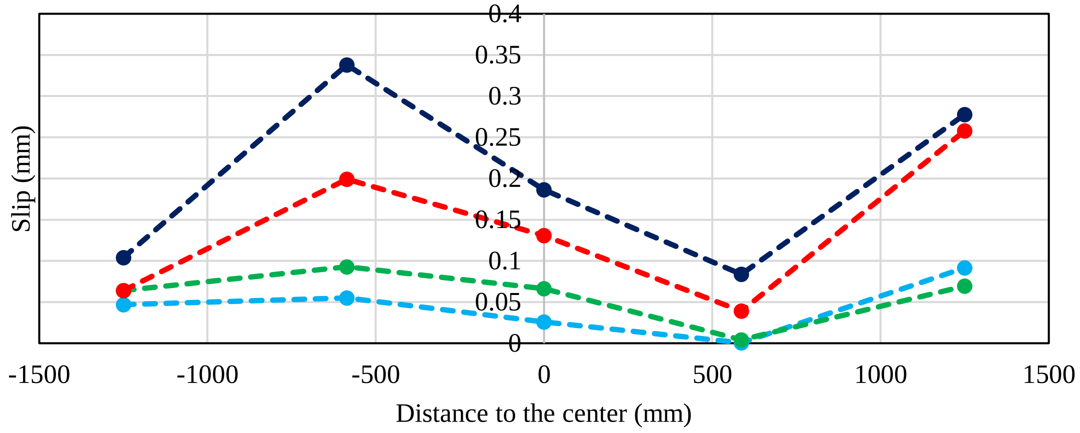

(a) CCB-A

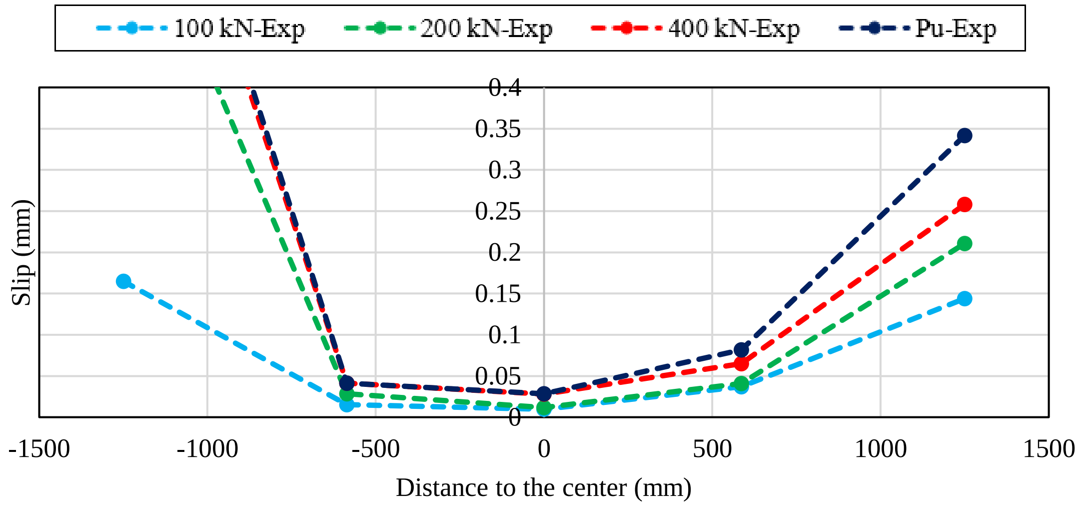

(b) CCB-P

Source: The author (2025).

4.3 ACCURACY OBTAINED BY WPB RESISTANCE FORMULATIONS

This section covers the accuracy of the procedures for WPB resistance prediction described in **sections 2.1.3.2-2.1.3.3** against the test results of this study (**section 4.2**) and other experimental results obtained by Salah (2009) (H2S355 and H2S420 specimens) and Geng *et al*. (2023) (CBS-2 and CBS-4 specimens). As all these specimens were subjected to three-point bending tests, their spans were submitted to uniform vertical shear forces. This way, the ultimate horizontal shear force ($V_{h,exp}$) given by **Eq. 2.69** from Steel Design Guide 31 (FARES; COULSON; DINEHART, 2016) and **Eq. 2.79** from prEN 1994-1-1 provided equal values for each specimen.

Figure 4.15 shows the accuracy obtained by WPB resistance formulations regarding experimental results, in which $V_{h,R}$ is the horizontal shear force resistance given by each procedure. Notably, as described in **section 2.1.3.2**, the procedure from Steel Design Guide 31 does not address castellated beams with $\theta > 60^0$ or $b_w/t_w > 30$. The Peiner castellated pattern has θ approximately equal to 63.4^0 (**Figure 1.2b**). This way, for the present analyses, the formulation from Steel Design Guide 31 for the WPB resistance of the CCB-P specimen was calculated considering θ equal to 60^0. In addition, H2S355 and H2S420 specimens tested by Salah (2009) have $b_w/t_w = 40$, which were not analyzed for the procedure from Steel Design Guide 31 because their b_w/t_w ratios are significantly higher than the limit of $b_w/t_w \leq 30$. The values of $V_{h,R}/V_{h,exp}$ ratios higher than 1.0 in **Figure 4.15** are non-conservative results of the procedures, and vice-versa. As noted, the formulation from Steel Design Guide 31 had only one conservative result (CCB-A specimen). This way, Steel Design Guide 31 overestimated the WPB resistance of most specimens, in which the $V_{h,R}/V_{h,exp}$ ratio of 1.933 for the CCB-P specimen was the highest value. The CCB-P beam was more susceptible to VM due to its higher tee length than the CCB-A beam. In addition, the CBS-4 beam has a lower tee height and higher tee length than the CBS-2 beam, which makes the CBS-4 more critical to the VM phenomenon. Therefore, Steel Design Guide 31 considerably overestimated the WPB resistance of the CCB-P and CBS-4, which showed that this procedure provides highly non-conservative results for castellated beams significantly affected by the VM phenomenon. In contrast, EN 1993-1-13:2024 provided only one non-conservative result (**Figure 4.15**), in which the CBS-2 had a $V_{h,R}/V_{h,exp}$ ratio slightly higher than 1.0 ($V_{h,R}/V_{h,exp} = 1.081$). These observations show that, in most cases, the method from EN 1993-1-13:2024 does not overestimate the WPB resistance of composite castellated beams, even occurring the WPB and VM interaction. However, this formulation considerably underestimated the WPB resistance of the H2S355 and H2S420 specimens (**Figure 4.15**), which may have happened due to their thinner web thickness, in which both beams have t_w= 4mm that is significantly lower than the other addressed I-sections.

Figure 4.15: Comparison of the accuracy obtained by WPB resistance formulations regarding experimental results.

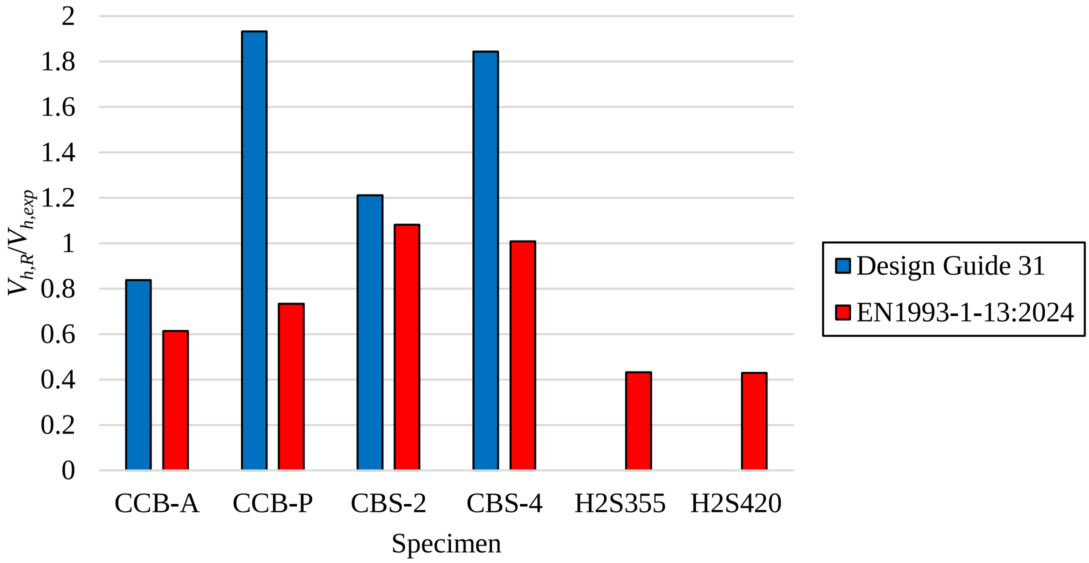

Source: The author (2025).

4.4 SUMMARY AND CONCLUSIONS OF THE CHAPTER

In this chapter, the geometry of the specimens with their respective dimensions, the instrumentation for measurements, material property characterization, and the flexural response of each model were discussed. All these discussions can be found in the research paper published by Oliveira *et al*. (2025). As a summary and conclusion of the chapter, it can be stated that:

- Three-point bending tests were performed in two specimens with Peiner (CCB-P) and Anglo-Saxon (CCB-A) castellated opening patterns, in which the deflection, out-plane-beam lateral displacements, relative slip, and strain in the composite section and transversal reinforcement bars were measured;
- Both composite castellated beams reached failure by WPB coupled with VM. In addition, the opening pattern influenced the ultimate load of the specimens, and that with a higher tee length had a lower bearing capacity because the VM occurrence was more critical in this castellated beam;

- The UHPC slab presented cracking localization after multiple cracking, a typical behavior of UHPC;
- The accuracy of the procedures for WPB resistance prediction from Steel Design Guide 31 and EN 1993-1-13:2024 were verified with the experimental results obtained in the present study and other test results from the literature;
- Steel Design Guide 31 provided non-conservative results in most cases and overestimated the WPB resistance of castellated beams considerably affected by VM;
- The procedure from EN 1993-1-13:2024 had conservative results in most cases and slightly overestimated in some cases. At the same time, underestimated the WPB resistance of castellated beams with thinner web thickness.

CHAPTER 5
NUMERICAL MODELING

This section describes the development of the preliminary and final numerical models with ABAQUS software. It details the methodological approach and all phases of the numerical models' implementation. The preliminary numerical model was developed before the experimental tests, and the final numerical model was developed after them, in which only minor adjustments were needed. This way, the preliminary numerical model was validated against experimental studies found in the literature, and the final numerical model was calibrated against the test results of the present study (**section 4**). A comparative analysis of geometric imperfections and residual stresses on the global stability behavior of cantilever composite alveolar beams was performed using the preliminary numerical model and the specimens tested by Salah (2009), and these analyses were published by Oliveira *et al*. (2024).

5.1 THE PRELIMINARY NUMERICAL MODEL

According to the review presented in **section 2**, some experimental studies addressed the flexural behavior of steel-concrete composite alveolar beams under hogging moment. However, all these bending tests investigated composite alveolar beams with Normal-Concrete (NC) slabs. Therefore, the development of the preliminary numerical model, which is the same as that used by Oliveira (2022) and Oliveira *et al*. (2022), is based on the experimental model of Salah (2009) performed with alveolar I-sections and NC slab. Additionally, the experimental results by Qi *et al*. (2020) are also used, which assessed composite beams without web openings and precast ultra-high-performance concrete (UHPC) slabs with shear pockets.

The same numerical model developed by Oliveira *et al*. (2022) and Oliveira (2022) for steel-NC composite alveolar beams is used in the present study. The beams are analyzed assuming linear buckling analysis (LBA) and geometrically and materially nonlinear analyses with imperfections (GMNIA), considering two methods: linear perturbation and Static Riks, respectively.

The linear perturbation method provides eigenvalues regarding the critical buckling loads and eigenvectors to their respective buckling mode shape. As an initial geometric imperfection, the eigenvector considering the first positive eigenvalue is implemented in the post-buckling analysis. Therefore, the "IMPERFECTION" command is used to insert this structural imperfection, and the effect of different initial geometric imperfection values on the composite alveolar beam behavior is evaluated. The values in question are used to normalize the deformed configuration obtained by the buckling analysis as the structure shape at the beginning of the post-buckling assessment.

Another structural imperfection addressed in the sensitivity analyses is the I-section residual stresses, implemented with the command INITIAL CONDITIONS, TYPE=STRESS. For this structural imperfection, the intensity and distribution configuration of the residual stresses are varied according to models present in the literature. As this study aims to investigate the behavior of continuous and cantilever composite alveolar beams, which are subjected to hogging moment, the I-section residual stress is an important parameter for nonlinear finite element models. Residual stresses favor the occurrence of the I-section lateral instability by LDB.

The Static Riks method is employed to tackle the geometric nonlinearity problem. With the arc-length methodology, the response of the load-displacement relationship presents a decrease in stiffness, and the structure must release the strain energy to maintain equilibrium, solving the problem of geometric nonlinearity. Thus, the Static Riks can represent the negative part of the equilibrium trajectory. All information about the numerical modeling and the specimens adopted for the validation are presented in the subsections below.

5.1.1 Specimens addressed in the validation study

5.1.1.1 Steel-NC composite alveolar beams tested by Salah (2009)

Four composite beams tested by Salah (2009) with sequential circular (C4S355 and C4S420) and hexagonal web openings (H4S355 and H4S420) were adopted for the sensitivity analyses. Salah (2009) performed three-point bending tests in continuous beams with two unbraced lengths, one cantilever with web openings (analyzed span), and another simply supported with full web. The loading is applied on the free extremity of the cantilever span. These beams are detailed in **Figures 5.1-5.2**. Their material properties and geometric parameters are presented in **Table 5.1-4.2**. In **Table 5.2**, 4.0 mm to t_w is the nominal web thickness of the I-section, but the test measurements by Salah (2009) obtained smaller web thickness dimensions than the nominal value. According to the author, as the behavior of the tested specimens is sensitive to any small variation in the web plate thickness, five measurement readings were taken from different positions in the web plate. Salah (2009) also presents a finite element calibration analysis with the obtained experimental results and validates his numerical models using t_w equal to 3.8 mm, a value from the test measurement readings. This value of t_w is also used for the numerical model validation.

Figure 5.1: Continuous composite beams with web openings tested by Salah (2009).

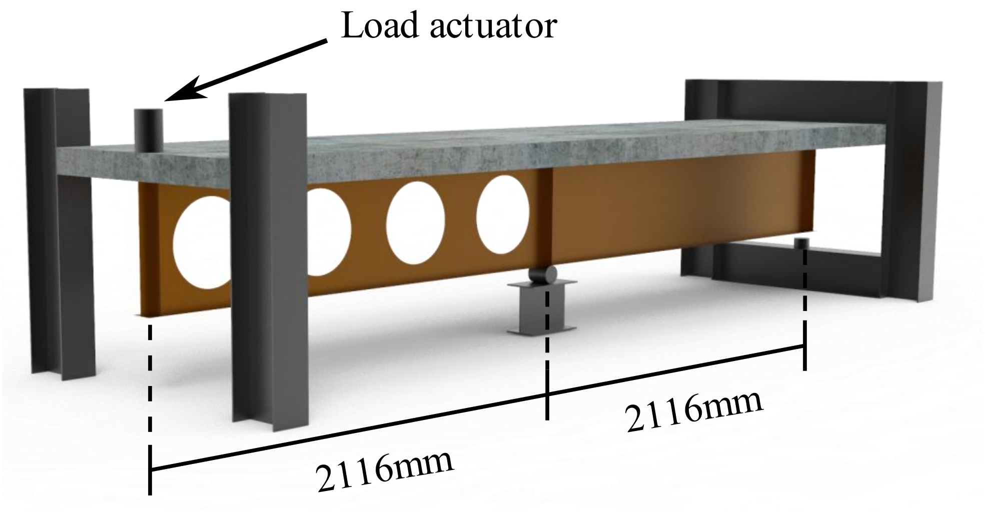

(a) C4S355 and C4S420

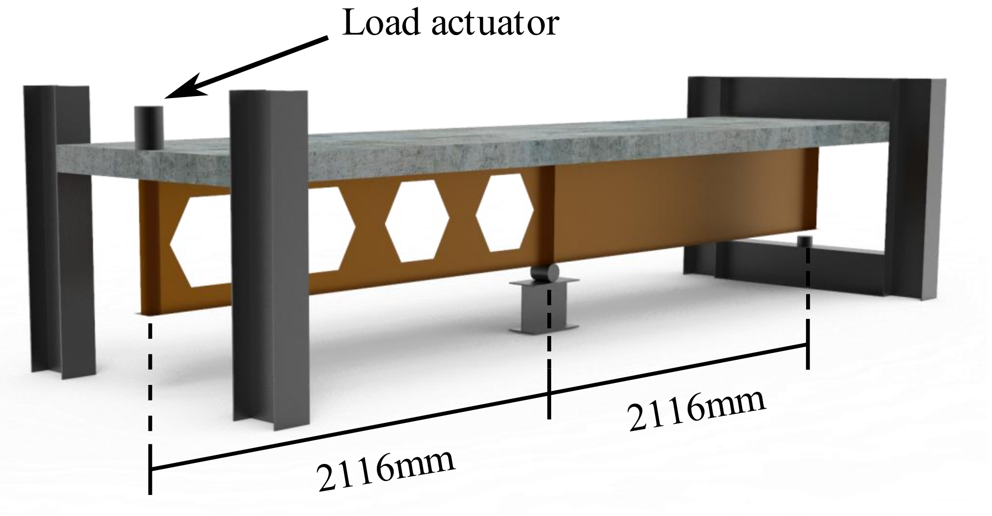

(b) H4S355 and H4S420

Source: The author (2023).

Figure 5.2: Specimen cross-section detailing (in mm).

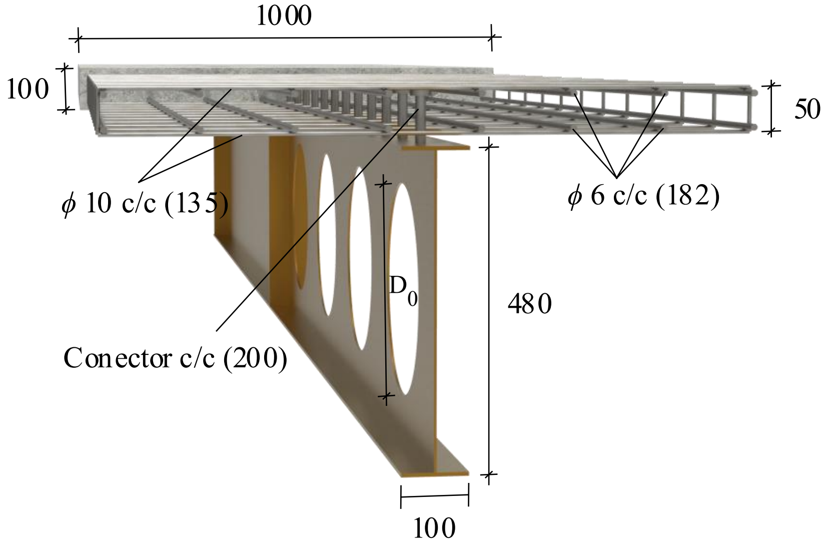

Source: The author (2023).

Table 5.1: Material properties.

Material	E (MPa)	v	f_{ck} (MPa)	f_y (MPa)	f_u (MPa)
Concrete	29,962	0.2	30	-	-
Steel S355	200,000	0.3	-	355	490
Steel S420	200,000	0.3	-	420	520
Reinforcement bars	200,000	0.3	-	459.6	608
Stud M12	200,000	0.3	-	611.35	-

Source: The author (2023).

Table 5.2: Geometric parameters.

Specimen	d_g (mm)	b_f (mm)	t_f (mm)	t_w (mm)	n	D_0 (mm)	p (mm)
C4S355	480	100	6	4	4	336	529
C4S420	480	100	6	4	4	336	529
H4S355	480	100	6	4	4	321	529
H4S420	480	100	6	4	4	321	529

Source: The author (2023).

5.1.1.2 Steel-UHPC composite beams tested by Qi *et al.* (2020)

Qi *et al*. (2020) performed a four-point bending test in a steel-UHPC composite beam. This way, the supports are located in the slab, and the loads are applied in the steel section. The detailing of the specimen is illustrated in **Figure 5.3**. The diameter of the reinforcement bars is 12mm, and the diameter and height of the studs are 30 mm and 120 mm, respectively. In each shear pocket, the stud's spacing is 150mm in the longitudinal direction and 120mm in the transverse, with 630mm spacing between the shear connector groups. According to the numerical model developed and validated by Qi *et al*. (2020), the shear pockets can be disregarded in the numerical analyses. **Table 5.3** shows the material properties of the specimen.

Figure 5.3: Dimensions and cross-section of the specimen tested by Qi *et al*. (2020) (in mm).

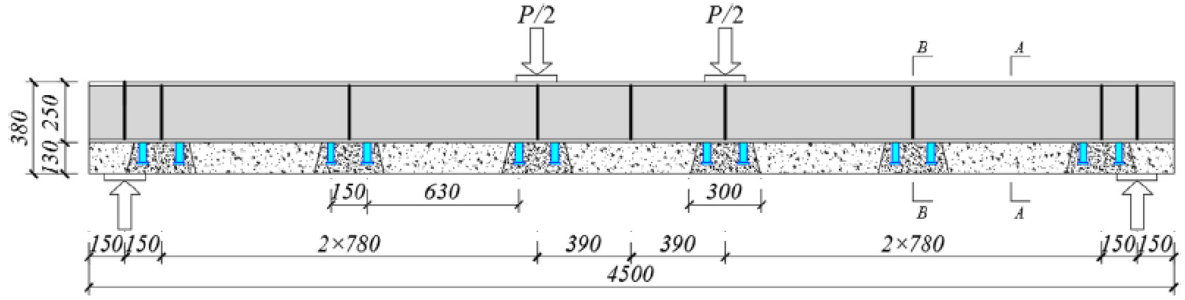

(a) Elevation view

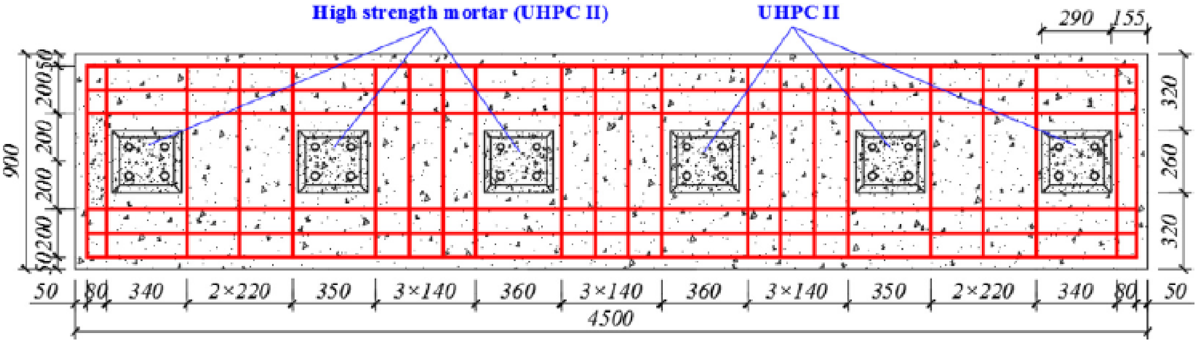

(b) Plan view

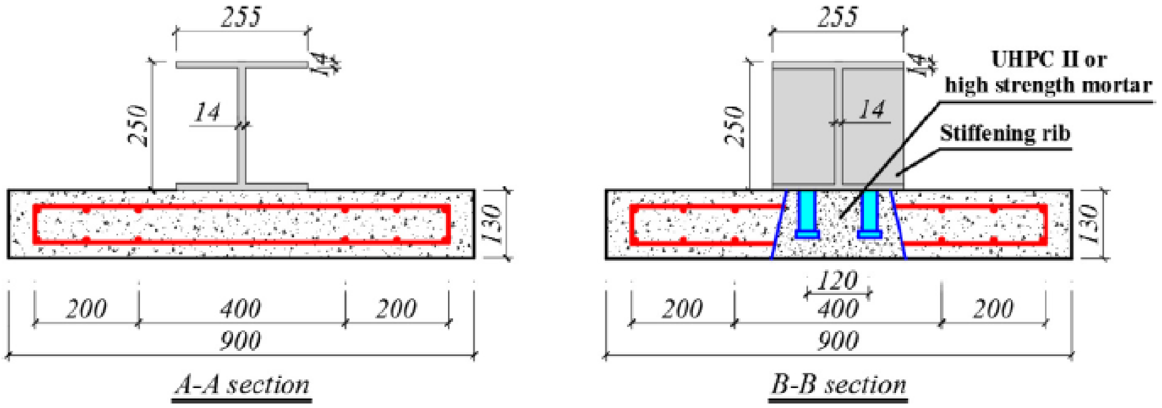

(c) Cross-section

Source: Qi *et al*. (2020).

Table 5.3: Material properties.

Material	E (MPa)	ν	$f_{cm\text{-}cubic}$ (MPa)	f_y (MPa)	f_u (MPa)
Concrete	48,000	0.2	124	-	-
Steel section	200,000	0.3	-	360	505
Reinforcement bars	200,000	0.3	-	567.1	673.1
Headed stud	200,000	0.3	-	390.4	-

Source: The author (2023).

5.1.2 Considerations for implementation

5.1.2.1 Materials

Figure 5.4 shows the constitutive models for steel. In the cellular profile, the quadrilinear model proposed by Earls (1999) was used (**Figure 5.4a**). For the reinforcement, the bilinear with hardening (**Figure 5.4b**) models were used. To the shear connectors, the elastic-perfectly plastic (**Figure 5.4c**). The stress-strain relationship implementation must be done with the true values, according to **Eqs. 5.1-5.2**.

Figure 5.4: Constitutive models of steel elements.

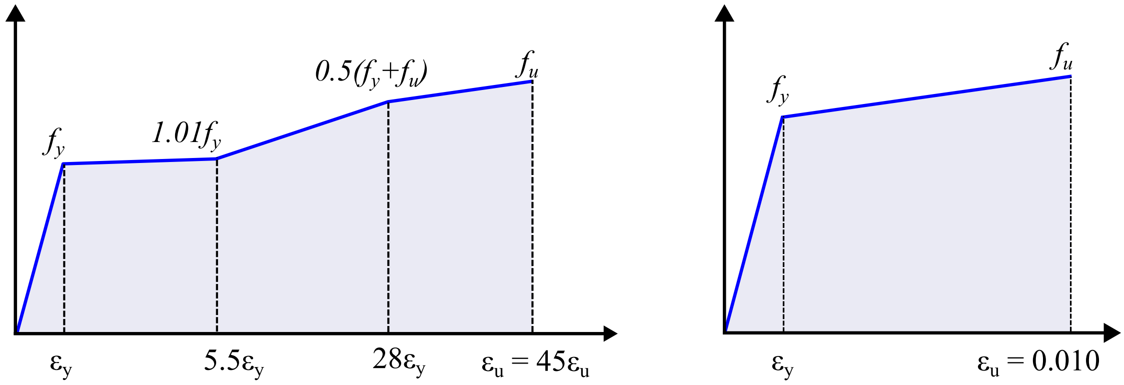

(a) Quadrilinear model by Earls (1999)

(b) bilinear with hardening

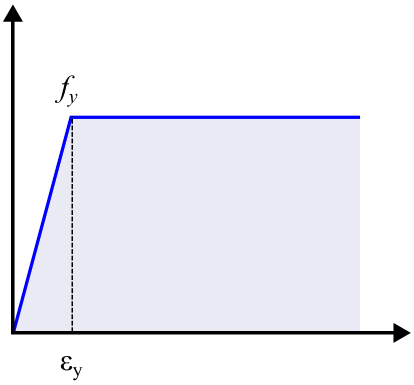

(c) elastic-perfectly plastic

Source: The author (2023).

$$\sigma^{true} = \sigma^{nom}\left(1+\varepsilon^{nom}\right) \tag{5.1}$$

$$\varepsilon^{true} = \ln\left(1+\varepsilon^{nom}\right) \tag{5.2}$$

The concrete damaged plasticity model (CDP) available in ABAQUS was used. As per ABAQUS Analysis User's Guide (SIMULIA, 2016). The CDP is a criterion adopted to represent the behavior of fragile materials, such as concrete (HILLERBORG; MODÉER; PETERSSON, 1976; LEE; FENVES, 1998; LUBLINER *et al.*, 1989). The input parameters that characterize the plasticity are dilation angle (Ψ), flow potential eccentricity (ξ), the ratio of the compressive strength under biaxial loading to uniaxial compressive strength (f_{b0}/f_{c0}), the ratio of the second stress invariant on the tensile meridian to that on the compressive meridian (K_c), and the viscosity parameter that represents the relaxation (μ). **Table 5.4** presents the input parameters of CDP used for the numerical model. The input parameters for the UHPC behavior are adopted based on Sousa *et al.* (2021).

Table 5.4: CDP input parameters.

Parameter	Value	
	In-situ NC	UHPC
Ψ(°)	36	54
ξ	0.1	0.1
f_{b0}/f_{c0}	1.16	1.07
K_c	2/3	2/3
μ	0.001	0.00001

Source: The author (2023).

For the behavior of NC in tension and compression, the model of Carreira and Chu (1985, 1986) is adopted **Eqs. 5.3-5.5**.

$$\frac{\sigma}{f_c} = \frac{\beta_c\left(\varepsilon/\varepsilon_c\right)}{\beta_c - 1 + \left(\varepsilon/\varepsilon_c\right)^{\beta_c}} \tag{5.3}$$

$$\frac{\sigma}{f_t} = \frac{\beta_c\left(\varepsilon/\varepsilon_t\right)}{\beta_c - 1 + \left(\varepsilon/\varepsilon_t\right)^{\beta_c}} \tag{5.4}$$

$$\beta_c = \left(\frac{f_c}{32.4}\right)^3 + 1.55 \quad \left(MPa\right) \tag{5.5}$$

The mechanical proprieties of concrete materials were defined using f_{ck} (characteristic strength after 28 days) through the EC2 (EN 1992-1-1:2023), according to the **Eqs. 5.6-5.10**:

$$f_{cm} = f_{ck} + 8 \quad (MPa) \tag{5.6}$$

$$f_{tm} = 0.3 f_{ck}^{2/3} \quad (MPa) \tag{5.7}$$

$$E_{cm} = 22\left(\frac{f_{cm}}{10}\right)^{0.3} \quad (MPa) \tag{5.8}$$

$$\varepsilon_{c1} = 0.7 f_{cm}^{0.31} \leq 2.8 \quad (‰) \tag{5.9}$$

$$\varepsilon_{cu1} = 3.5 \quad (‰) \tag{5.10}$$

For the UHPC, the compression behavior was inserted considering the model of Carreira and Chu (1985) modified by Mansur, Chin and Wee (1999). As described by **Eqs. 5.11-5.14**.

$$\frac{\sigma_c(\varepsilon_c)}{f_{cm}} = \frac{k_1\beta_{cc}(\varepsilon_c/\varepsilon_{c1})}{k_1\beta_{cc} - 1 + (\varepsilon_c/\varepsilon_{c1})^{k_2\beta_{cc}}} \tag{5.11}$$

$$\beta_{cc} = \frac{1}{1 - \dfrac{f_{cm}}{\varepsilon_{c1}E_c}} \tag{5.12}$$

$$k_1 = \left(\frac{50}{f_{cm}}\right)^3 \left[1 + 2.5\left(\frac{\rho_f l_f}{d_f}\right)^{2.5}\right] \tag{5.13}$$

$$k_2 = \left(\frac{50}{f_{cm}}\right)^{1.3} \left[1 - 0.11\left(\frac{\rho_f l_f}{d_f}\right)^{-1.1}\right] \tag{5.14}$$

Finally, the model proposed by Li and Leung (1993) is adopted for the tension behavior, as shown in **Eqs. 3.15-3.17**. It was considered $\eta = 0.5$ and $\tau_{eq} = 6.13$ MPa according to Krahl *et al*. (2021), in which these values were determined for a similar non-proprietary UHPC.

$$\sigma_t(w) = \begin{cases} \sigma_{f0}\left(2\sqrt{\dfrac{w}{w_0}} - \dfrac{w}{w_0}\right) & for \quad w \leq w_0 \\ \sigma_{f0}\left(1 - \dfrac{4w}{l_f}\right)^2 & for \quad w > w_0 \end{cases} \tag{5.15}$$

$$\sigma_{f0} = \eta \frac{l_f}{d_f} V_f \tau_{eq} \tag{5.16}$$

$$w_0 = \frac{\tau_{eq} l_f^{\,2}}{E_f d_f} \tag{5.17}$$

5.1.2.2 Interactions

The interaction and constraint commands available in the software ABAQUS were used for the interaction between the elements in the numerical models. The headed stud shear connectors are inserted into the concrete volume of the slab (FERREIRA *et al.*, 2021c, 2021e, 2021b, 2021d; FERREIRA; MARTINS; NARDIN, 2020b; HOSSEINPOUR *et al.*, 2022; OLIVEIRA *et al.*, 2022; ROSSI *et al.*, 2020b, 2021e, 2021b; WIJESIRI PATHIRANA *et al.*, 2016). The tie constraint, which allows modeling the perfect bond between the contact surfaces, is applied between the shear connector and the steel profile top flange. This type of contact is also used in the actuator-slab interaction. The interaction between the concrete with the reinforcement is made with the embedded region type. Thus, a perfect connection is made between embedded and host elements. The surface-surface interaction is considered the normal and tangential behavior between the slab-connector and slab-profile contact (**Figure 5.5**). The value of the friction coefficient was defined as 0.4, according to Wijesiri Pathirana *et al.* (2016). **Table 5.5** shows the type of interaction and the master and slave surfaces.

Figure 5.5: Interaction between the elements.

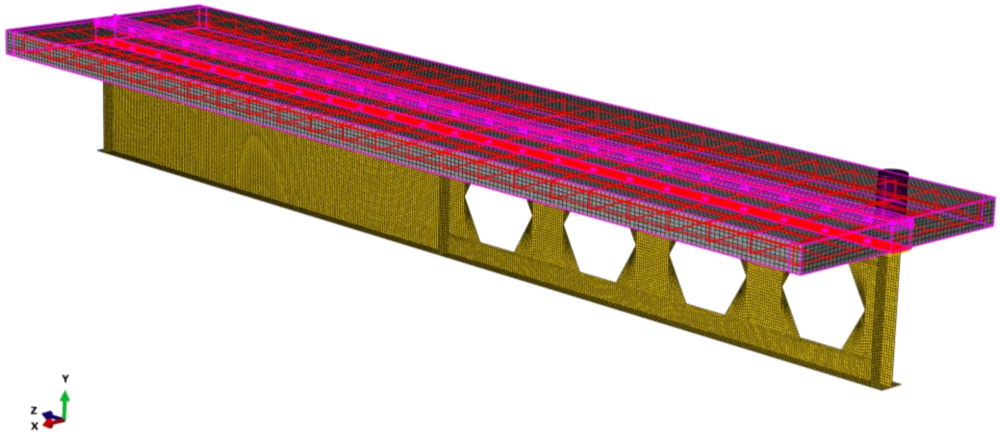

(a) Tie constraint and embedded region

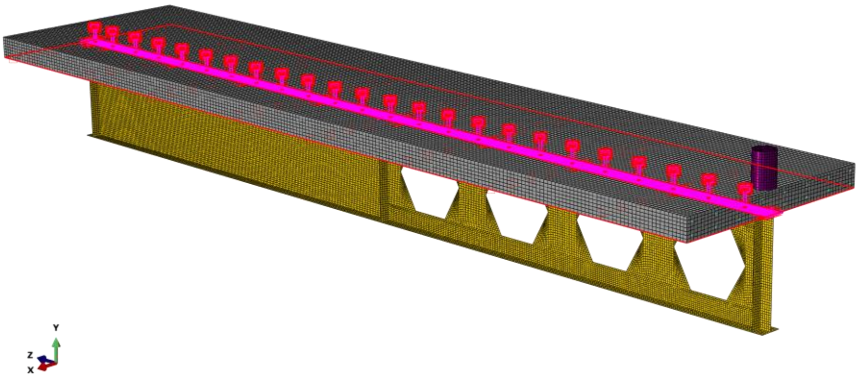

(b) Surface-to-surface interaction
Source: The author (2023).

Table 5.5: Master and slave surfaces.

Interaction	Surfaces		Type
	Master	Slave	
Cellular profile and shear connector	Cellular profile	Shear connector	Tie
Concrete slab and cellular profile	Concrete slab	Cellular profile	Normal/Tangential
Actuator and concrete slab	Concrete slab	Actuator	Tie
Shear connector and concrete slab	Concrete slab	Shear connector	Normal/Tangential
Reinforcement and concrete slab	Concrete slab	Reinforcement	Embedded

Source: The author (2023).

5.1.2.3 Boundary conditions and discretization

The headed stud shear connectors, actuators and concrete slab are discretized with C3D8R solid elements, which have eight nodes, reduced integration, support plastic analysis with high deformations, and allow the visualization of the cracks. The reinforcements are discretized with T3D2 truss elements with two nodes and linear approximation, containing three degrees of freedom per node. The cellular profile is discretized using an S4R element, also used by (FERREIRA; MARTINS, 2020; FERREIRA; ROSSI; MARTINS, 2019; ROSSI *et al.*, 2020c, 2020d). This element is a quadrilateral element with four nodes and reduced integration. Furthermore, the mesh size elements were defined accordingly with the literature review developed. The mesh size for concrete and actuator elements was 20mm, for the headed stud connectors 2mm and 10mm for the reinforcement and cellular profile (FERREIRA *et al.*, 2021a, 2021c, 2021b; FERREIRA; MARTINS; NARDIN, 2021; ROSSI *et al.*, 2020b, 2021e, 2021b). The details of the finite elements employed in discretizing composite cellular beams is presented in **Table 5.6**.

Table 5.6: Finite element details.

Finite element	Element type	Geometry	Number of nodes	Degrees of freedom per node	Integration
S4R	Shell	Quadrilateral	4	3 translations and 3 rotations	Reduced
T3D2	Truss	One-dimensional	2	3 translations	-
C3D8R	Solid	Hexahedral	8	3 translations and 3 rotations	Reduced

Source: The author (2023).

The boundary conditions and discretization regarding the experimental models of Salah (2009) are illustrated in **Figure 5.6**. In the numerical modeling, the boundary conditions were imposed to simulate supported beams with lateral bracing (Uy=Uz=0). According to Rossi *et al.* (2020b), lateral bracing simulates the condition of a composite floor, which has infinite stiffness in the slab plane (Ux=0). The load control is done by displacement (Uy<0) at one or both actuators utilizing the cantilever effect of the continuous composite beam, according to the hogging moment distribution configuration to be analyzed.

The same discretization presented in **Figure 5.6** is adopted for any other model of this study. Regarding the boundary conditions of the numerical models considering the specimen of Qi *et al.* (2020), the symmetry on the Z axis (Uz=URx=URy=0) is implemented. In the support, the vertical and lateral displacements are constrained (**Figure 5.7**).

Figure 5.6: Discretization and boundary condition with the specimens of Salah (2009).

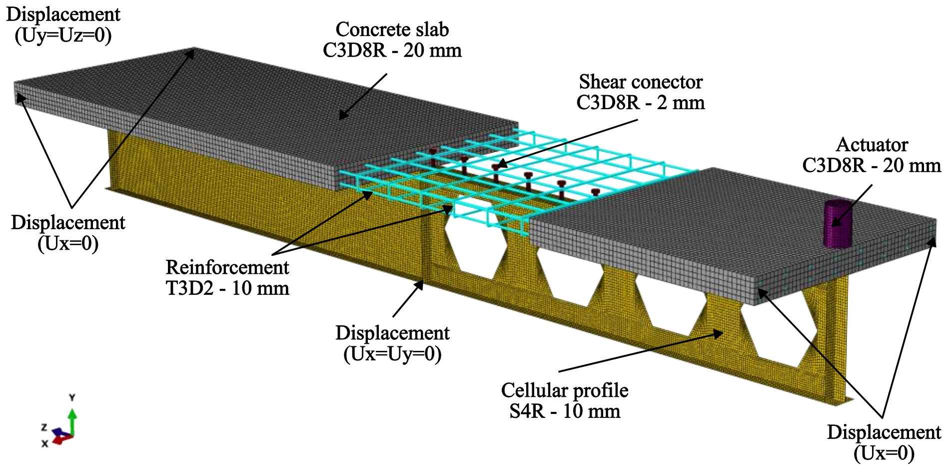

Source: The author (2023).

Figure 5.7: Boundary condition regarding the specimens of Qi *et al*. (2020).

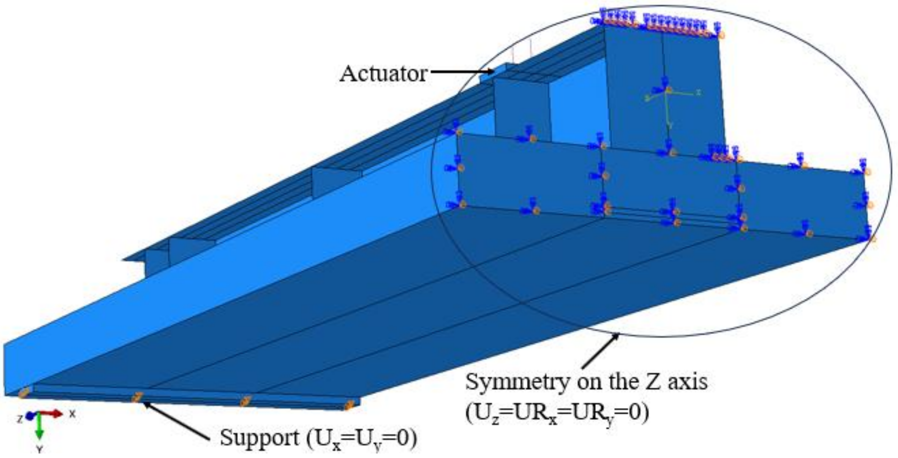

Source: The author (2023).

5.1.2.4 Geometric imperfection and residual stresses

A comparative analysis of geometric imperfections and residual stresses on the global stability behavior of cantilever composite alveolar beams was performed using the specimens tested by Salah (2009), and these analyses were published by Oliveira *et al*. (2024).

As mentioned, the "IMPERFECTION" command implements the initial geometric imperfection of the evaluated beams, adopting values for the amplitude of this imperfection, which normalizes the eigenvector (deformed configuration) from the buckling analysis as the initial structure shape for the GMNIA analyses. From the stability elastic investigations, the obtained eigenvector for the first positive eigenvalue is the initial structure configuration for the nonlinear inelastic analyses. Four ratios for the initial geometric imperfection amplitude were addressed in the comparative study, such as $d_g/100$, $d_g/200$, $L/1000$, and $L/2000$. In addition, a small value of an out-of-straightness is also adopted, equal to 0.01mm.

The command INITIAL CONDITIONS, TYPE=STRESS is used to implement the I-section residual stresses. This way, an initial condition of stresses is inserted in sets of finite elements, which compose the discretized steel I-section, considering the respective mean value of residual stress for such finite elements set. These sets are several longitudinal partitions of the I-section geometry. Each division is defined according to the respective adopted residual stress pattern, focusing on determining a set of finite elements with similar residual stress amplitude. The residual stress distribution is constant along the longitudinal direction, disregarding the effects of the transverse stiffeners and shear studs welding, which might affect the I-section initial stresses locally. In the comparative study, six residual stress distribution models were adopted for the analyses: three patterns for hot-rolled (**Figure 5.8a-c**) and three for welded I-sections (**Figure 5.8d-f**). It is noteworthy that only the pattern proposed by Sonck (2014) and Sonck, Impe and Belis (2014) (**Figure 5.8a**) was developed for steel alveolar I-profile. The other patterns were obtained from steel sections without web openings. It is debatable whether the residual stress distribution in the web of models referring to sections without web openings can be used in alveolar sections. In addition, it is well-known that the residual stresses in the flanges are dominant for the considered behavior, which is the LDB occurrence. Therefore, only the distribution of residual stresses in the flanges is implemented to adapt the residual stress models from full-web I-sections to those with web openings. It is the same strategy that Sonck, Boissonnade and Van impe (2012) used in their numerical modeling, which simulated the behavior of steel cellular beams.

Figure 5.8: Residual stress distribution models addressed in the comparative study.

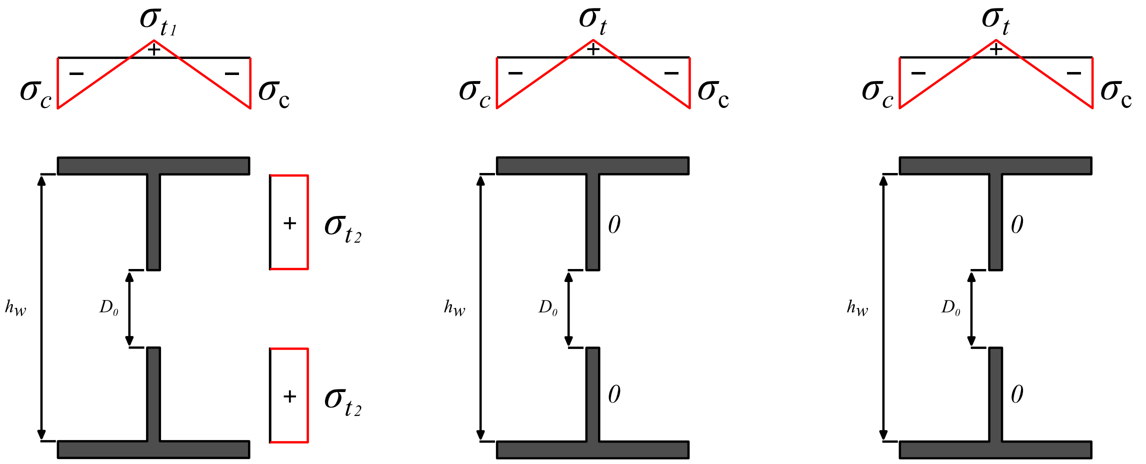

(a) Sonck (2014)

(b) ECCS (1984) for hot-rolled sections

(c) Galambos and Ketter (1959)

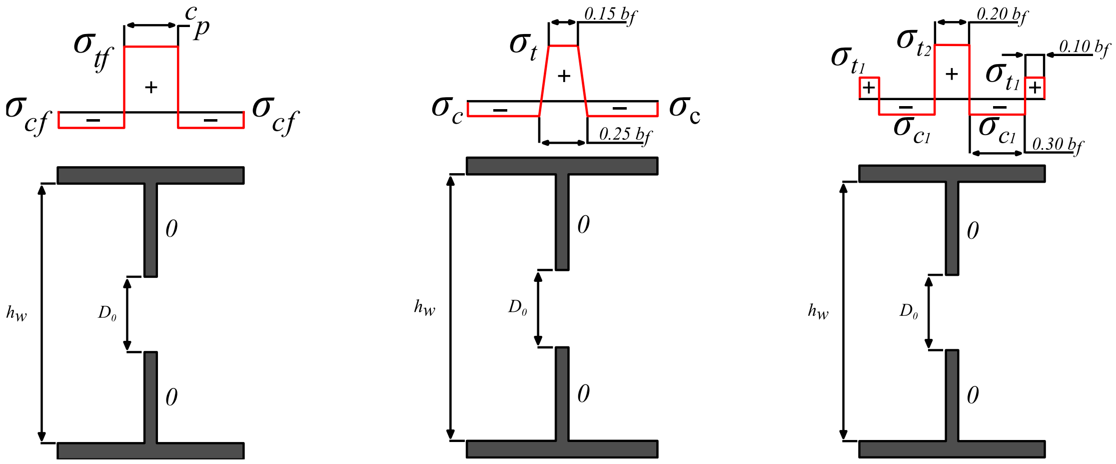

(d) Beg and Hladnik (1996)

(e) ECCS (1984) for welded I-section

(f) Barth and White Barth and White (1998)

Source: The author (2023).

The comparative analysis is separated into two steps. Firstly, the nonlinear finite element models were simulated, disregarding the residual stresses, considering only the initial geometric imperfection, with values for normalization equal to $d_g/100$, $d_g/200$, $L/1000$, and $L/2000$. Finally, the analyses are performed by varying the six residual stress distribution models from **Figure 5.8** and the initial geometric imperfection values of 0.01mm, $d_g/100$, and L/1000. This way, 88 nonlinear analyses are assessed in the comparative study. **Figure 5.9** presents the residual stress patterns implemented in the numerical model as an initial stress state.

Figure 5.9: The implemented residual stresses as an initial stress state.

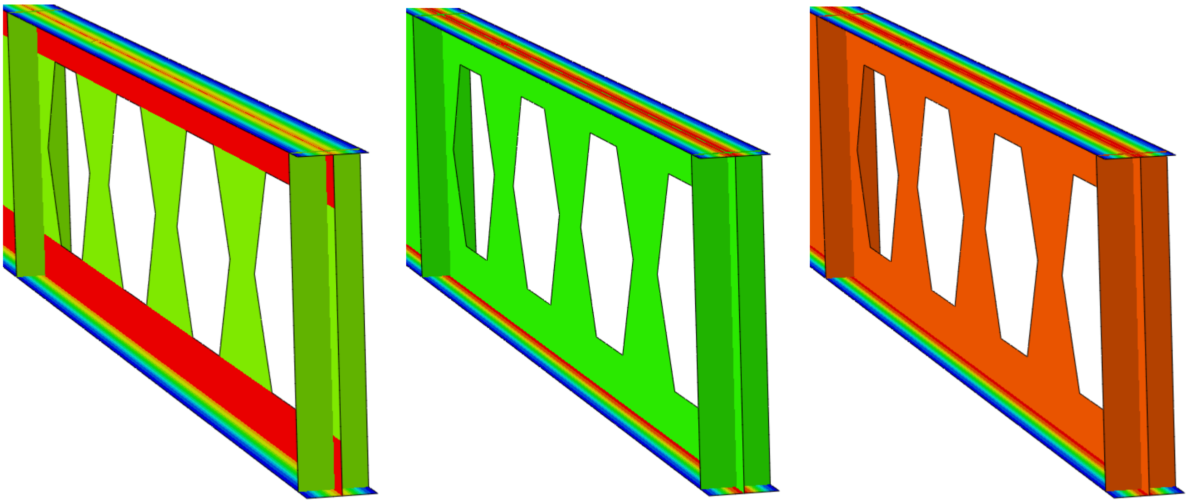

(a) Sonck (2014) (b) ECCS (1984) for hot-rolled sections (c) Galambos and Ketter (1959)

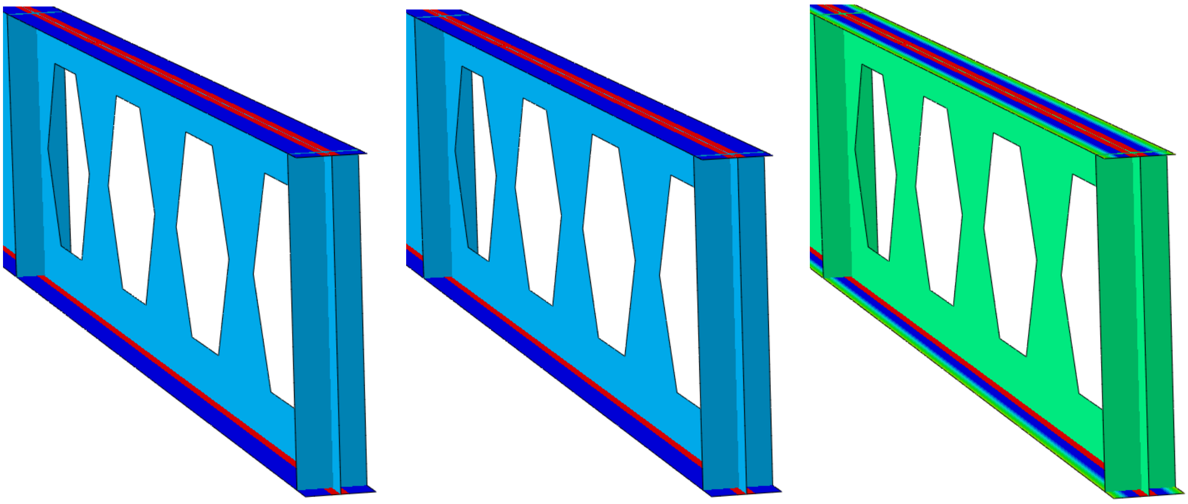

(d) Beg and Hladnik (1996) (e) ECCS (1984) for welded I-section (f) Barth and White Barth and White (1998)

Source: The author (2023).

Regarding the first positive eigenvalue from LBA analyses, the eigenvectors presented Web-Post Buckling (WPB) with a slight compressed flange lateral curvature, inserted as the initial geometric imperfection in the GMNIA analyses. However, when the residual stresses were implemented in the GMNIA analyses, some finite element models had different failure modes regarding the deformed configurations from LBA analyses, in which the failure modes were characterized by Lateral- Distortional Buckling (LDB), which was in agreement with the test results. As the beams reached LDB in an inelastic regime, residual stresses significantly affected their resistant capacity. This way, the distribution of compressive residual stresses in the flanges had the most critical influence on the global stability behavior of the analyzed beams, as these residual stresses favor the LDB occurrence. Finally, higher geometric imperfection amplitudes did not provide only lower ultimate loads, as when the instability phenomena are reached in an inelastic regime, the effect of global geometric imperfections becomes highly complex. More information on the described comparative analysis can be found in Oliveira *et al*. (2024).

As **section 5.1.3** will show, the best agreement with the specimens tested by Salah (2009) was obtained using the combination of the initial geometric imperfection equal to $d_g/100$ and the residual stress pattern proposed by Beg and Hladnik (1996), as the profiles used by Salah (2009) are welded I-sections with web openings.

For the validation against the test result of Qi *et al*. (2020), the geometric imperfection value of $d/100$ and the residual stress model of Beg and Hladnik (1996) were adopted.

5.1.3 Validation of the preliminary numerical model

5.1.3.1 Tests of Salah (2009)

As described in **section 5.1.2.4**, the residual stress distribution for welded I-sections proposed by Beg and Hladnik (1996) was adopted, as Salah's composite beams have welded profiles. The initial imperfection of $d_g/100$ was applied as a normalization value in the eigenvector related to the first positive eigenvalue from the linear buckling analysis of this member. The initial imperfection and residual stress distribution were obtained from sensitivity analyses, in which Oliveira *et al*. (2024) present more details.

The selected beams have the highest unrestrained length and hexagonal and circular web openings. These members presented failure by LDB, as shown in **Figure 5.10**. Therefore, the experimental and numerical results were compared. **Figure 5.10**, **Table 5.7** and **Figure 5.11** establish the relationship between these analyses. It was noted that there was a good agreement of the results. **Figure 5.10** shows that experimental and numerical models had the same deformed shape related to the LDB failure mode. **Table 5.7** and **Figure 5.11** show that the difference between the ultimate load and the displacement in the peak load was less than 4%, showing that the present numerical model can represent the behavior of the members related to this work, and therefore, the numerical model can be considered validated.

Figure 5.10: Comparison between the failure modes considering the tests of Salah (2009).

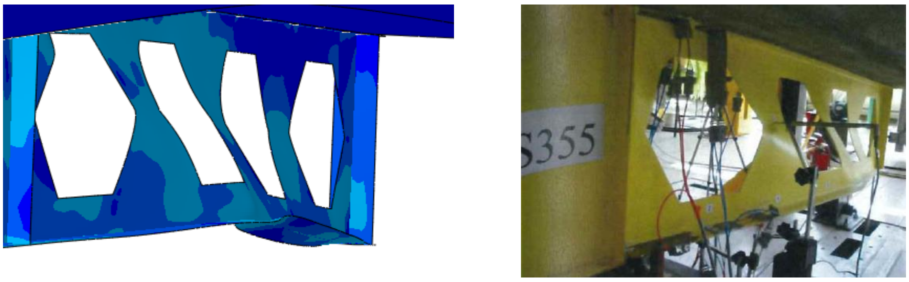

(a) H4S355

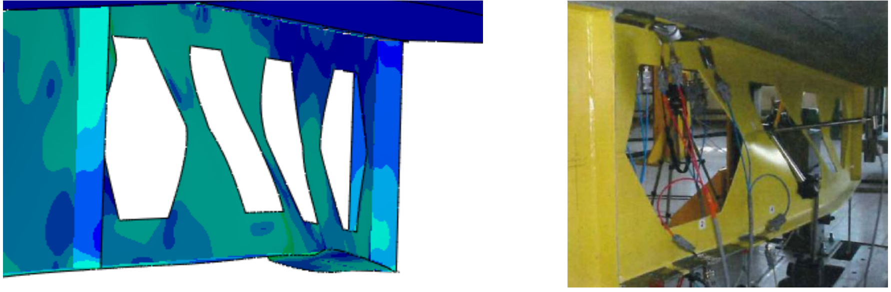

(b) H4S420

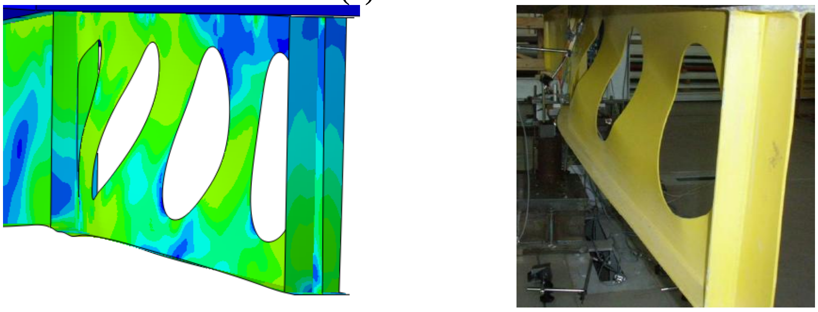

(c) C4S355

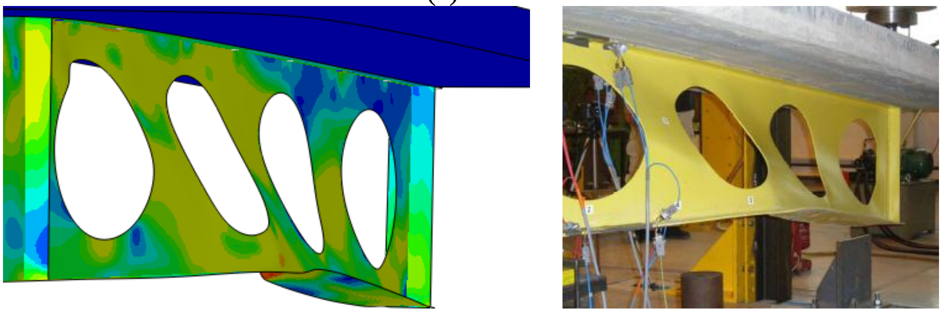

(d) C4S420

Source: Adapted from Oliveira *et al*. (2022), Oliveira (2022) and Oliveira *et al*. (2024).

Table 5.7: Validation results with the specimens of Salah (2009).

Model	Experimental (kN)	Numerical (kN)	P_{Num}/P_{Exp}
H4S355	62.03	59.95	0.966
H4S420	62.55	64.44	1.030
C4S355	59.56	58.55	0.983
C4S420	62.26	63.89	1.026

Source: Adapted from Oliveira *et al*. (2022) and Oliveira (2022).

Figure 5.11: Validation results with the specimens of Salah (2009).

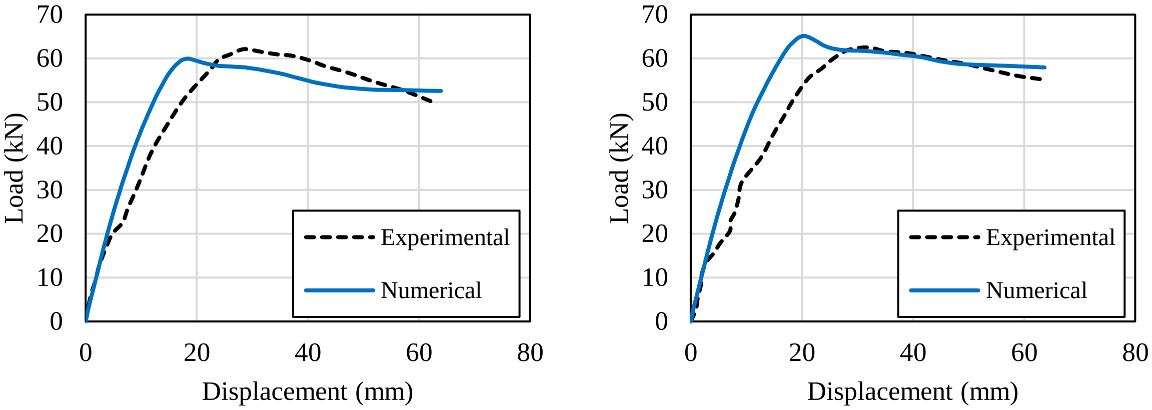

(a) H4S355 (b) H4S420

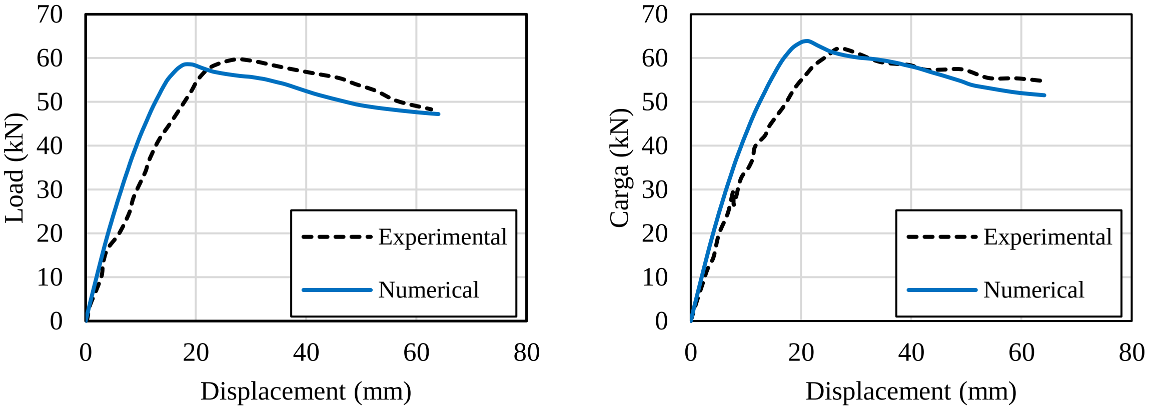

(c) C4S355 (d) C4S420

Source: Adapted from Oliveira *et al*. (2022) and Oliveira (2022).

5.1.3.2 Test of Qi *et al*. (2020)

The residual stress pattern by Beg and Hladnik (1996) and the geometric imperfection value of *d*/100 were also adopted for this validation. **Figure 5.12** shows the validation results regarding the load-displacement curves, and **Figure 5.13** addresses the failure modes. Both comparisons show good agreement between the numerical response and experimental tests. The difference was 2.54%, considering the load concerning the ultimate displacement. This way, the preliminary numerical modeling is considered validated.

Figure 5.12: Validation result with the specimen of Qi *et al*. (2020).

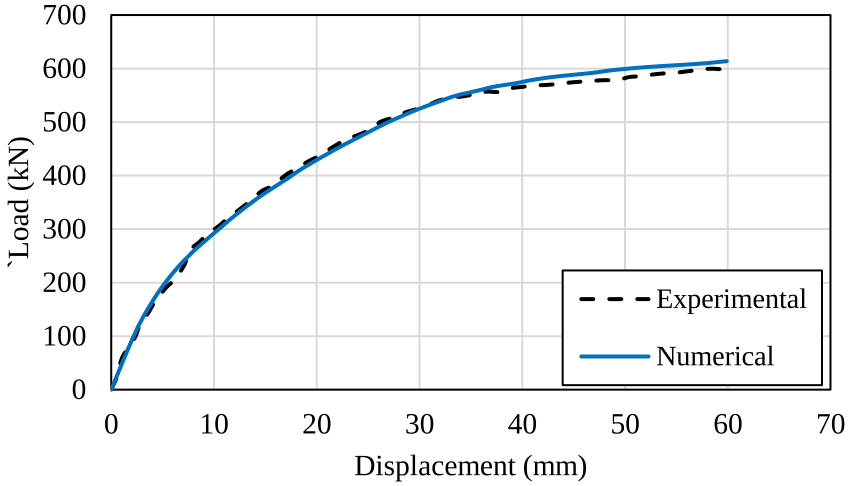

Source: The author (2023).

Figure 5.13: Comparison between the failure modes considering the tests of Qi *et al*. (2020).

(a) Specimen

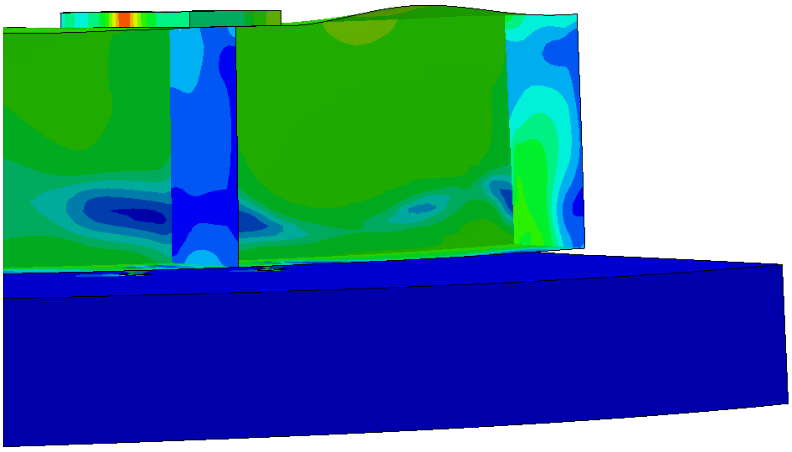

(b) Numerical model

Source: The author (2023).

5.2 THE FINAL NUMERICAL MODEL

The final numerical model is calibrated against the tests performed in this study, which were discussed in **section 4**. Only small adjustments are made to the preliminary numerical model, in which the I-section constitutive relationship, geometric imperfection value, residual stress model, and friction coefficient are changed.

5.2.1 Considerations for implementation

The same discretization presented in **section 5.1.2.3** is used. The discretization and boundary conditions are presented in **Figure 5.14**. The castellated I-sections were modeled using S3R and S4R shell finite elements, while the concrete slab, shear connector, support, and actuator were modeled with C3D8R solid elements. In addition, the T3D2 truss element was employed for the longitudinal and transversal reinforcement bars. Regarding the boundary conditions, one support restricted the vertical displacement (Uy = 0) and longitudinal displacement (Uz = 0), and the other only restricted the vertical one (Uy = 0). Finally, lateral displacements (Ux = 0) were restrained at the lateral of the supports and actuator.

Figure 5.14: Boundary conditions and discretization.

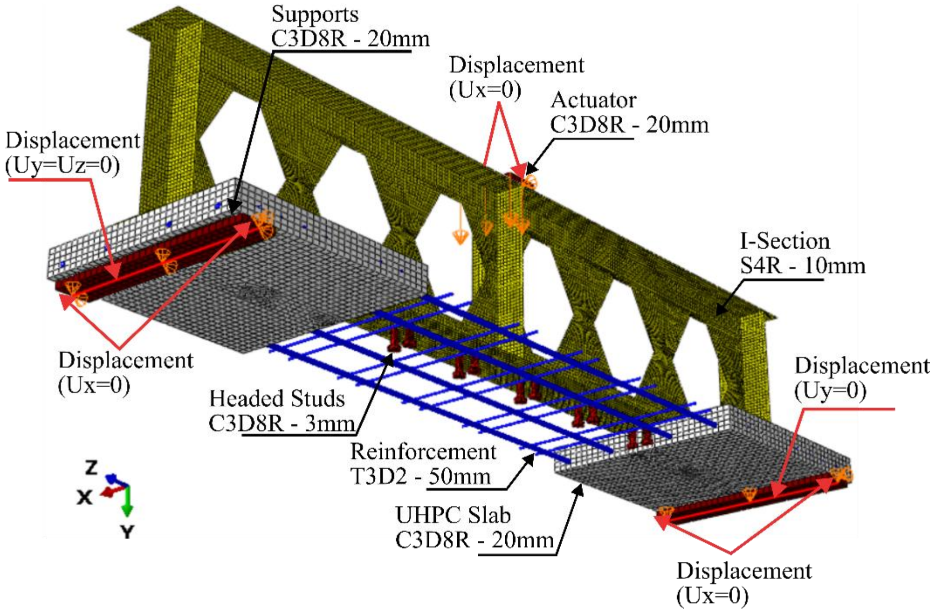

Source: The author (2025).

The friction coefficient values addressed for the calibration were 0.3, 0.4 and 0.6 based on Ebrahimi, Zahrai and Mirghaderi (2019), Guezouli and Lachal (2012), Liu *et al*. (2016), Sjaarda *et al*. (2017), and Wijesiri Pathirana *et al*. (2016), in which the friction coefficient of 0.3 was defined by the calibration study discussed in **section 5.2.2**.

The stress-strain models for the steel I-section addressed in the calibration for the sensibility analysis are presented in **Figure 5.15a-c**, which are the quadrilinear models with hardening proposed by Earls (1999) (**Figure 5.15a**) and Yun and Gardner (2017) (**Figure 5.15b**), and the elastic-perfectly plastic model (**Figure 5.15c**). **Eqs. 5.18-5.22** define the parameters of Yun and Gardner's model (YUN; GARDNER, 2017). For the castellated I-section, the elastic-perfectly plastic model was used based on the calibration study (**section 5.2.2**). The constitutive models for the other steel elements and UHPC are the same as in **section 5.1.2.1**. The specimens' material properties adopted in the implementation are summarized in **Table 5.8**.

Figure 5.15: Constitutive relationships of steel elements.

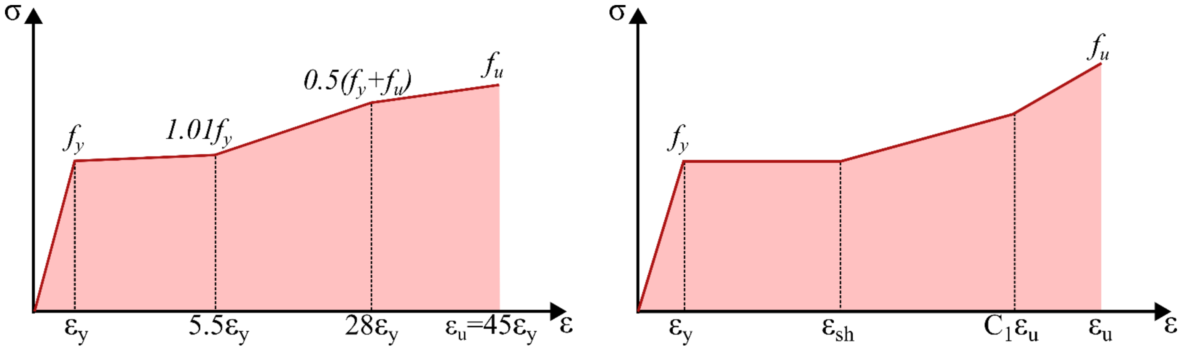

(a) Earls' quadrilinear model

(b) Yun and Gardner's quadrilinear model

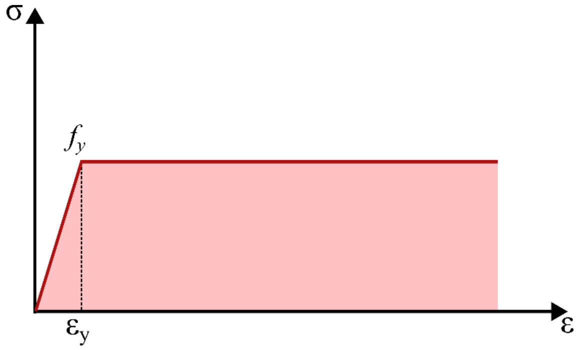

(c) Elastic-perfectly plastic

Source: The author (2025).

$$f(\varepsilon)=\begin{cases} E\varepsilon,\ \varepsilon \le \varepsilon_y \\ f_y,\ \varepsilon_y < \varepsilon \le \varepsilon_{sh} \\ f_y + E_{sh}\left(\varepsilon - \varepsilon_{sh}\right),\ \ \varepsilon_{sh} < \varepsilon \le C_1\varepsilon_u \\ f_{C_1\varepsilon_u} + \left(\dfrac{f_u + f_{C_1\varepsilon_u}}{\varepsilon_u - C_1\varepsilon_u}\right),\ C_1\varepsilon_u < \varepsilon \le \varepsilon_u \end{cases} \tag{5.18}$$

$$\varepsilon_u = 0.6\left(1-\frac{f_y}{f_u}\right),\ \varepsilon_u \ge 0.06 \tag{5.19}$$

$$\varepsilon_{sh} = 0.1\frac{f_y}{f_u} - 0.055,\ 0.015 < \varepsilon_{sh} \le 0.03 \tag{5.20}$$

$$C_1 = \frac{\varepsilon_{sh} + 0.25\left(\varepsilon_u - \varepsilon_{sh}\right)}{\varepsilon_u} \tag{5.21}$$

$$E_{sh} = \frac{f_u - f_y}{0.4\left(\varepsilon_u - \varepsilon_{sh}\right)} \tag{5.22}$$

Table 5.8: Material properties.

Material	E (MPa)	v	f_{cm} (MPa)	f_{cmt} (MPa)	f_y (MPa)	f_u (MPa)
Concrete	44,936	0.2	139.84	11.07	-	-
Steel section	200,000	0.3	-	-	422.54	529.19
Longitudinal rebars	200,000	0.3	-	-	700	770
Transversal rebars	200,000	0.3	-	-	500	550
Headed stud	200,000	0.3	-	-	738.63	-

Source: The author (2025).

The calibration study (**section 5.2.2**) defined the initial geometric imperfection amplitude of $d_g/500$, in which the values of $d_g/100$, $d_g/500$, and $d_g/1000$ were analyzed according to Ferreira, Martins and Nardin (2021). The residual stress model proposed by the ECCS (1984) for hot-rolled profiles (**Figure 5.16**) was also determined in the calibration analyses, in which it was checked whether it was necessary to insert this structural imperfection. This residual stress model was adopted for the calibration study according to the numerical models developed by Ellobody (2012a, 2012b), which addressed steel castellated and cellular beams that failed by Lateral-Torsional Buckling (LTB), Web-Distortional Buckling (WDB), WPB, or their coupling. According to Ellobody (2012a, 2012b), presuming that the cutting process is carefully conducted, the residual stress distribution in an alveolar beam can be considered as that of doubly symmetric I-sections.

Figure 5.16: Residual stress model proposed by ECCS (1984) for hot-rolled I-sections.

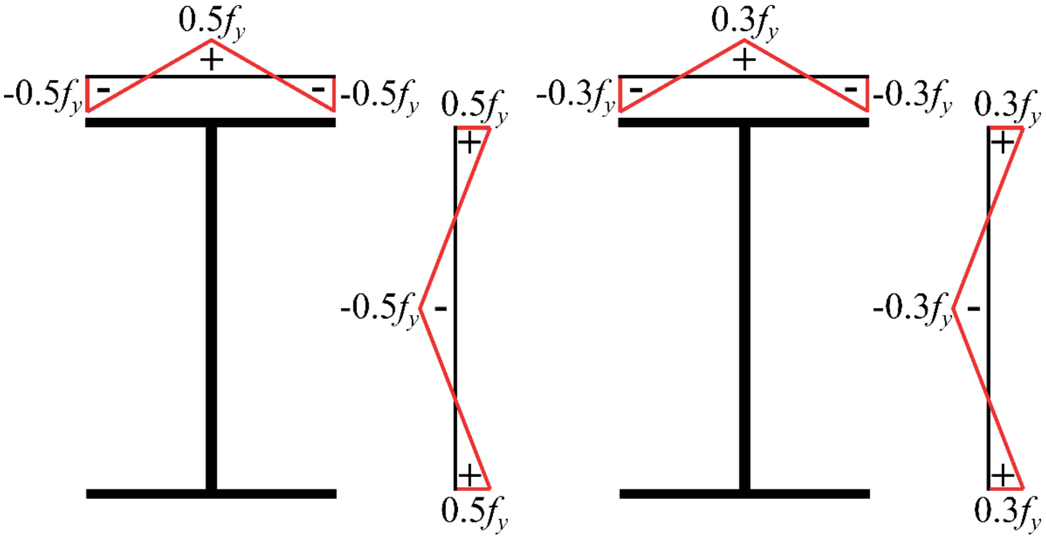

(a) $d/b_f \leq 1.2$ (b) $d/b_f > 1.2$

Source: The author (2025).

Regarding other numerical studies on the stability behavior of steel and composite alveolar beams, there is no consensus on which residual stress pattern must be considered. Some studies on the global stability of these elements used the residual stress model for alveolar profiles proposed by Sonck (2014) and Sonck, Impe, and Belis (2014), which was developed based on experimental measurements. However, this model was elaborated by simplifying the residual stresses in the web, considering stresses only in the double tee section (cross-section at the central region of the openings) and propagating them along the member's length, disregarding the stresses in the web region besides the openings. This way, Sonck (2014) states that the proposed residual stress cannot be applied in analyses of structures where the web residual stresses have a significant role, which is the case of the WPB phenomenon.

Another strategy is inserting only the residual stress distribution in the flanges (DA SILVA; MESQUITA, 2024; OLIVEIRA *et al*., 2022, 2024; ORIBI *et al*., 2023; SILVA; DALCANAL; MESQUITA, 2020; SONCK; BOISSONNADE; VAN IMPE, 2012). However, Oliveira *et al*. (2024) showed that considering only the residual stresses in the flanges does not significantly influences the WPB behavior of cantilever composite alveolar beams (hogging moment). Finally, the numerical model of this study had better agreement with the experimental results when the residual stresses in the web and flanges were implemented (**section 5.2.2**), as considered by Ellobody (2012a, 2012b).

5.2.2 Calibration against the test results

In the first step of the calibration study, the eigenmodes obtained from the LBA were analyzed. In total, five eigenmodes of the five lower eigenvalues were assessed. All these eigenmodes characterized WPB for both specimens (CCB-A and CCB-P). Thus, in the first analysis, it was observed that using the different eigenmodes, or the coupling between them, as an initial geometric imperfection in the GMNIA did not significantly affect the load-displacement curves and the failure modes of the numerical models. This way, the eigenmode from the first positive eigenvalue (lower energy) was defined as the initial geometric configuration for the calibration study, which are shown in **Figure 5.17**.

Figure 5.17: Eigenmodes regarding the first positive eigenvalue.

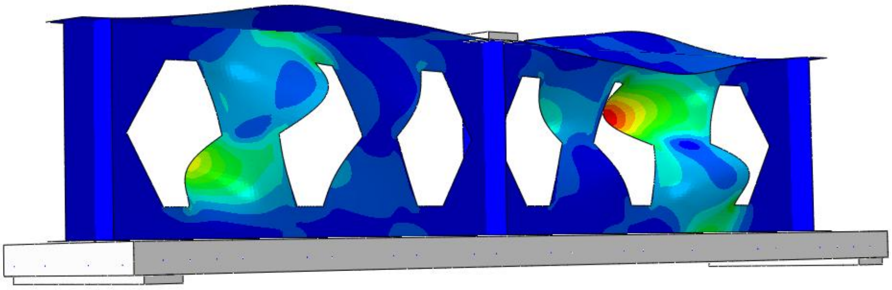

(a) CCB-A

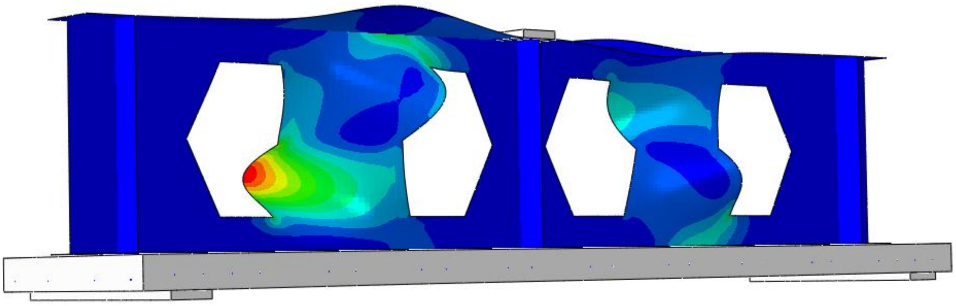

(a) CCB-P

Source: The author (2025).

The numerical model calibration began by evaluating the initial geometrical imperfection value variation, disregarding residual stresses. As described in **section 5.2.1**, the steel constitutive model and the value of the friction coefficient were varied in the calibration study. However, Yun and Gardner's model (YUN; GARDNER, 2017) for the steel stress-strain relationship and the friction coefficient of 0.4 were adopted for these analyses, focusing on the initial imperfections.

Figure 5.18a (CCB-A specimen) and **Figure 5.19a** (CCB-P specimen) compare the load-displacement curves obtained by the tests with the numerical models without residual stresses, varying the initial geometrical imperfection value. It is noted that, for both specimens, the values of $d_g/1000$ and $d_g/100$ provided the highest and lowest ultimate loads, respectively. For the CCB-A specimen (**Figure 5.18a**), the value of $d_g/500$ had the closest ultimate load regarding the tests. On the other hand, the numerical results for the CCB-P specimen (**Figure 5.19a**) had the closest results using $d_g/100$, even though the load-displacement curve of this model significantly diverges regarding the test. Subsequently, the same geometric imperfection values were adopted for the models with the residual stress pattern proposed by ECCS (1984) for hot-rolled I-section (**Figure 5.18b** and **Figure 5.19b**). The best agreement with the tests for the CCB-A specimen (**Figure 5.18b**) was obtained with $d_g/1000$, while the CCB-P specimen (**Figure 5.19b**) was with $d_g/100$.

Comparing the models with and without residual stresses, it was noted that the residual stresses caused a slight decrease in the ultimate load regarding the models with the same geometric imperfection amplitude. In addition, it was observed that no combination of initial imperfections resulted in the best approximation to the tests considering both specimens. This way, the combination of $d_g/500$ for the geometric imperfection value and the residual stress proposed by ECCS (1984) was defined to proceed with the calibration. This combination was adopted because it was the intermediate case for both specimens regarding the agreement with the tests.

Proceeding with the calibration, the effect of the steel constitutive models was analyzed (**Figure 5.20**). In these analyses, it was noted that the elastic-perfectly plastic model provided the highest agreement with the tests for both specimens. This way, this stress-strain relationship was adopted to proceed with the validation. Finally, the value of the friction coefficient was assessed in the calibration (**Figure 5.21**). In the CCB-A specimen, this parameter did not significantly influence its behavior. In contrast, it influenced the CCB-P specimen behavior in the post-peak range, having the best agreement with the tests using the value of 0.3. This way, considering the ultimate loads and the load-displacement curves (**Figures 4.18-5.21**), the numerical models adopted for the validation have the following parameters:

- Geometric imperfection value of $d_g/500$;
- Residual stress pattern proposed by ECCS (1984) for hot-rolled profiles;
- Elastic-perfectly plastic model for the steel constitutive relationship of the I-section;
- Friction coefficient of 0.3.

Figure 5.18: Numerical model calibration regarding geometric and structural imperfections for the CCB-A specimen.

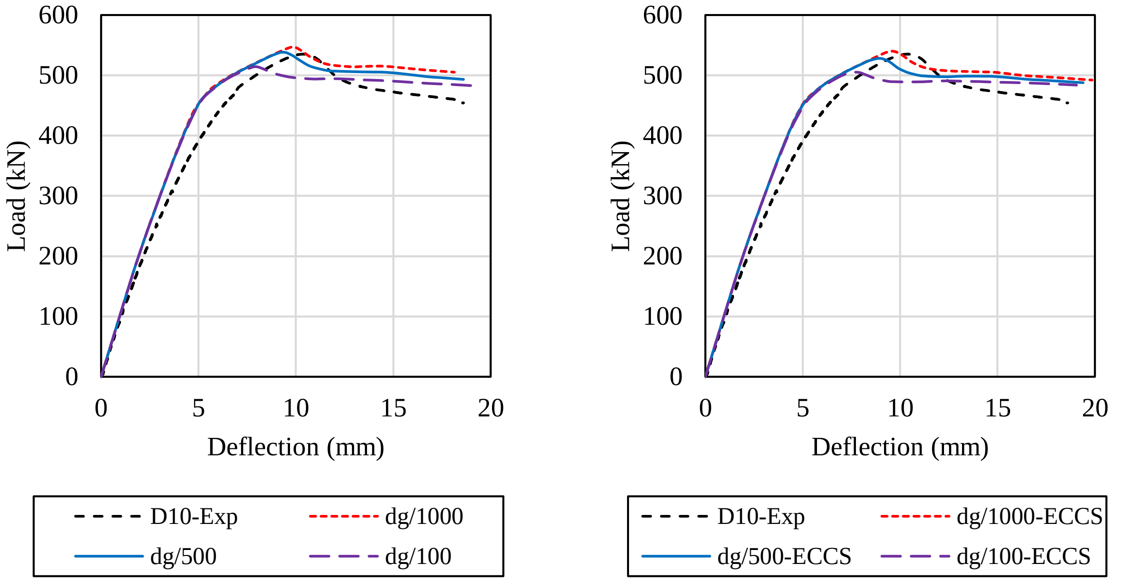

(a) Without residual stresses (b) With ECCS model for hot-rolled I-section

Source: The author (2025).

Figure 5.19: Numerical model calibration regarding geometric and structural imperfections for the CCB-A specimen.

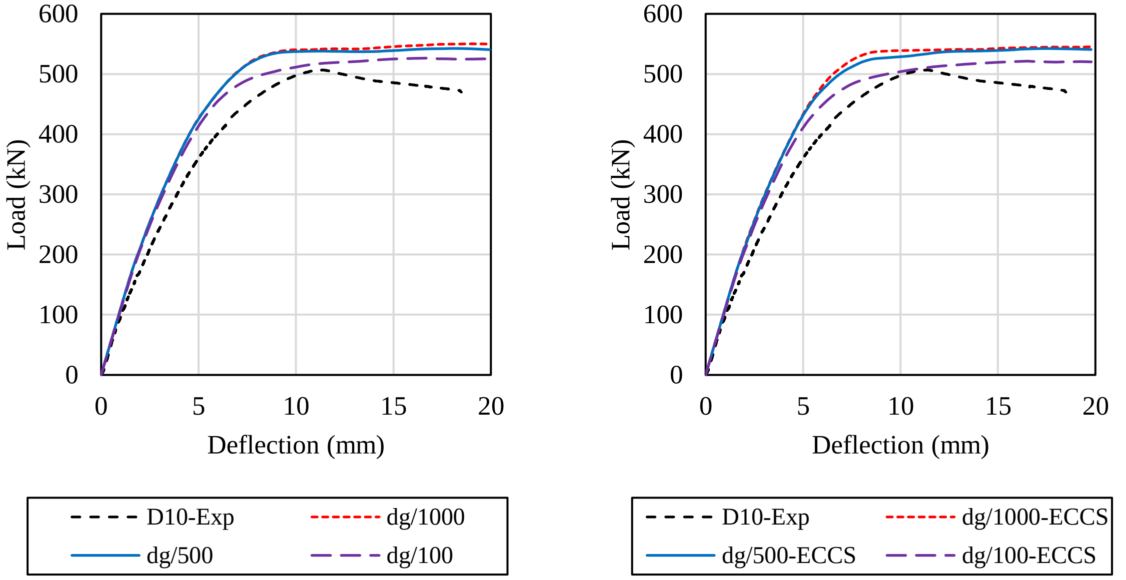

(a) Without residual stresses (b) With ECCS model for hot-rolled I-section

Source: The author (2025).

Figure 5.20: Numerical model calibration regarding the I-section steel constitutive model.

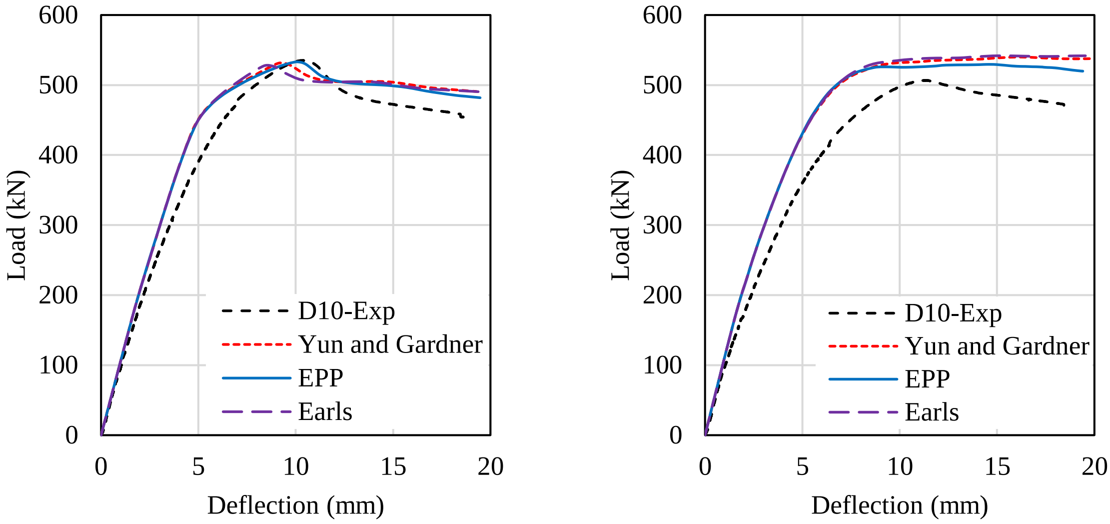

(a) CCB-A

(b) CCB-P

Source: The author (2025).

Figure 5.21: Numerical model calibration regarding the friction coefficient value.

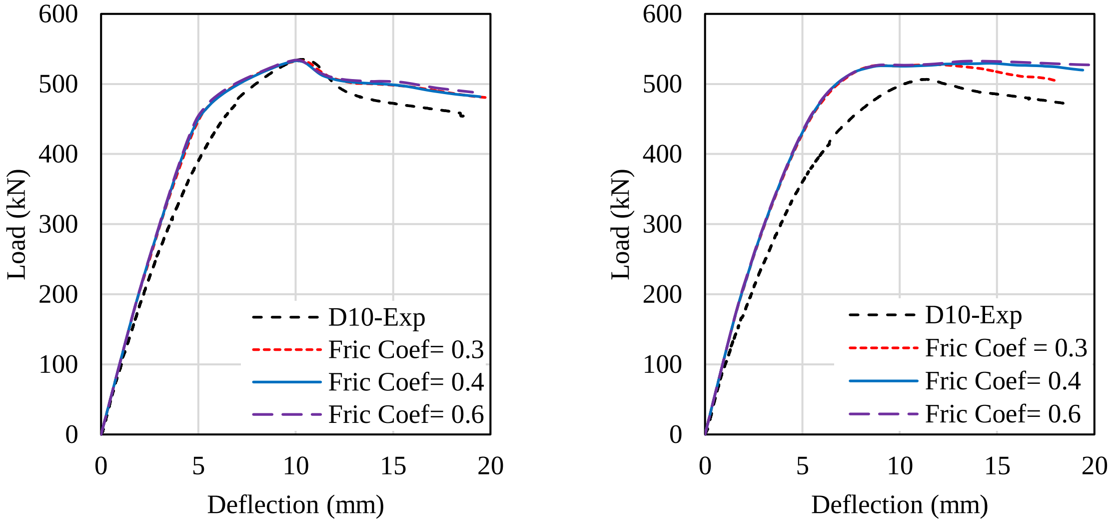

(a) CCB-A

(b) CCB-P

Source: The author (2025).

Table 5.9 compares the ultimate loads (P_u) and their respective deflection (d_u) obtained by the numerical models adopted for the validation and the tests. The divergences between the numerical and experimental P_u are below 4.1%, and the CCB-A model had the highest P_u and the lowest d_u for both analyses.

Table 5.9: Comparison between experimental and numerical ultimate loads.

Specimen	$P_{u\text{-}Num}$ (kN)	$P_{u\text{-}Exp}$ (kN)	$P_{u\text{-}Num}/P_{u\text{-}Exp}$	$d_{u\text{-}Num}$ (mm)	$d_{u\text{-}Exp}$ (mm)	$d_{u\text{-}Num}/P_{u\text{-}Exp}$
CCB-A	533.21	535.14	0.996	10.23	10.43	0.981
CCB-P	527.20	506.61	1.041	12.26	11.37	1.078

Source: The author (2025).

For all analyses (**Figures 4.18-5.21**), the numerical model's bending stiffness begins to diverge from the experimental one at 200 kN of load for CCB-A and 150 kN for CCB-P. This stiffness divergence can be attributed to the initiation of cracking in the UHPC slab, an effect that the numerical model did not capture well. However, it is worth mentioning that the initial stiffness had elevated agreement between the numerical and experimental analyses. **Table 5.10** compares the failure modes obtained by the numerical models adopted for the validation and the tests. The failure modes were characterized by WPB, presenting a high agreement between the numerical and experimental results.

Proceeding with the validation, **Figure 5.22** presents the lateral displacements caused by WPB, measured by the D15 and D16 displacement transducers in the tests. The same trend is noted between the numerical and experimental results for both specimens. In addition, the displacement transducers in the tests presented the effect of accommodation, and it is not guaranteed that the experimental and numerical results refer to the same point throughout the test. This is because the initial and final points of displacement transducer measurement are not the same regarding the specimen. The point of measurement in the specimen changes during the test due to the deflection and deformation caused by WPB. In contrast, the displacements obtained by the numerical analyses are nodal displacements from the adopted mesh. This way, these factors contribute to some divergences between the numerical and experimental results observed in **Figure 5.22**.

Table 5.10: Comparison between experimental and numerical deformed shapes.

Model	**Experimental**	**Numerical**
CCB-A		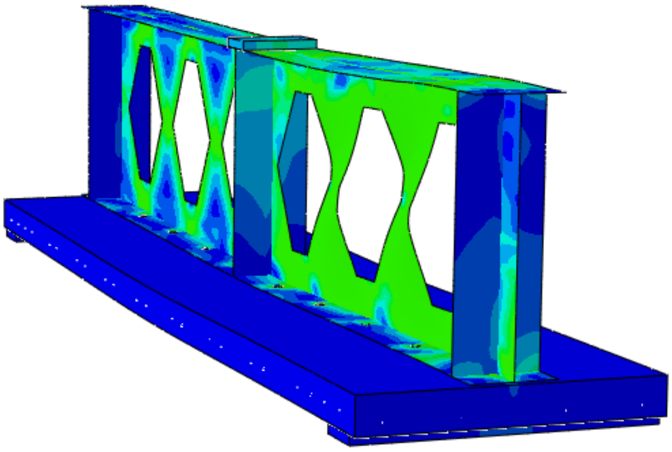
CCB-P		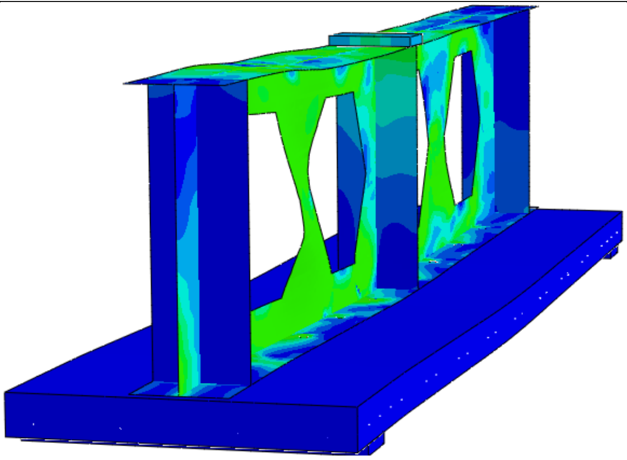

Source: The author (2025).

Figure 5.22: Comparison between experimental and numerical results of lateral displacements in the web-post.

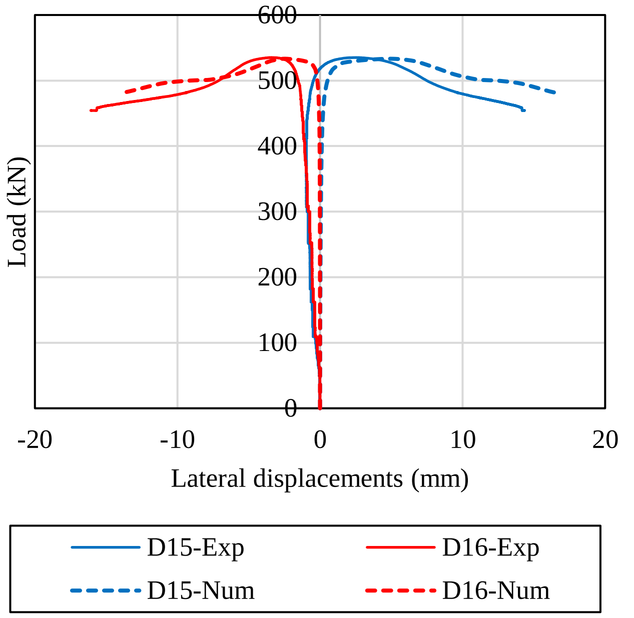

(a) CCB-A

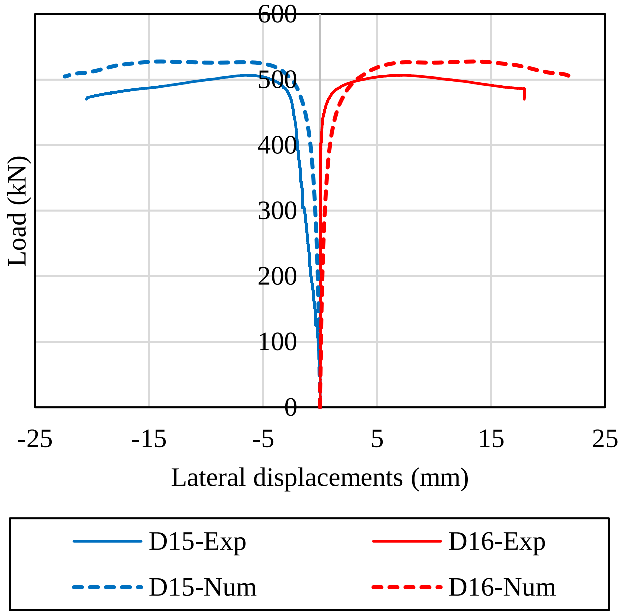

(b) CCB-P

Source: The author (2025).

Figure 5.23 shows the relative slip measured in the 1/4 and 3/4 span obtained by the numerical analyses and the tests. As these are very small displacements, the measurements are too sensitive, as is observed regarding the experimental results. Even so, the same trend was obtained in both models between the numerical and experimental results, with the numerical results presenting an intermediate behavior regarding the test response. Finally, **Figure 5.24**

presents the strain diagram in the composite cross-section, which is composite by the longitudinal reinforcement and both flanges. It is observed in **Figure 5.24** that the strain evolution in the analyzed composite section had good agreement between the numerical and experimental results, mainly for the CCB-P specimen, which presented elevated similarity. This way, all these results contribute to considering the numerical model validated against the tests.

Figure 5.23: Comparison between experimental and numerical results of relative slip measured in the 1/4 and 3/4 of span.

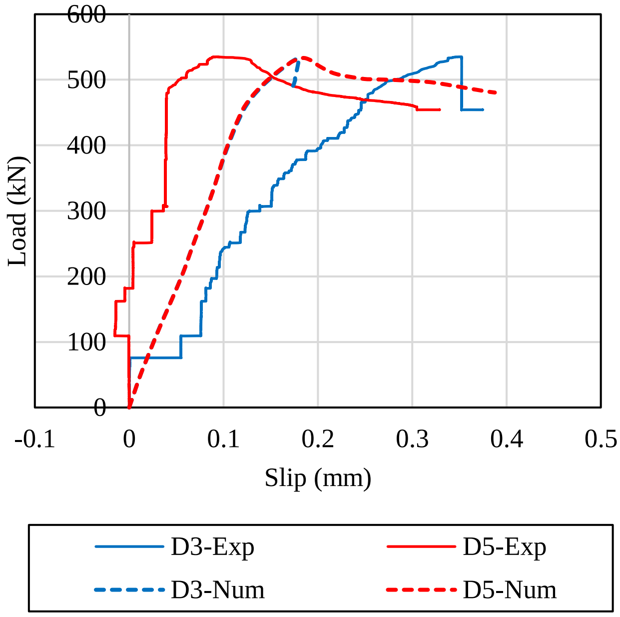

(a) CCB-A

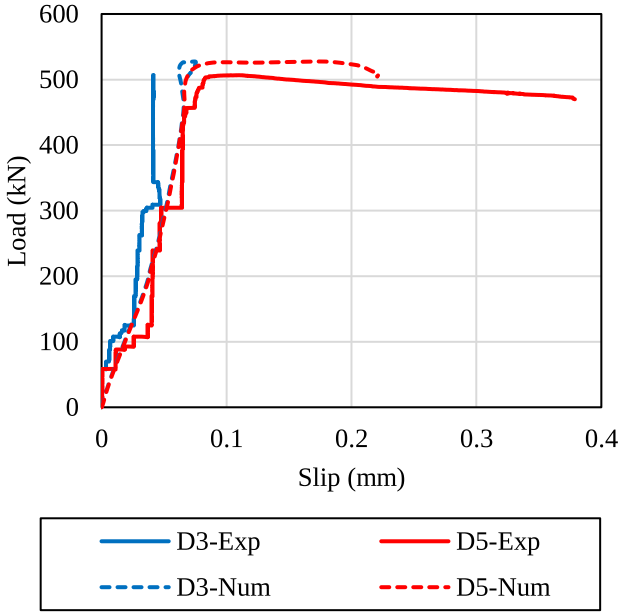

(b) CCB-P

Source: The author (2025).

Figure 5.24: Comparison between experimental and numerical results of strain diagram in the composite cross-section.

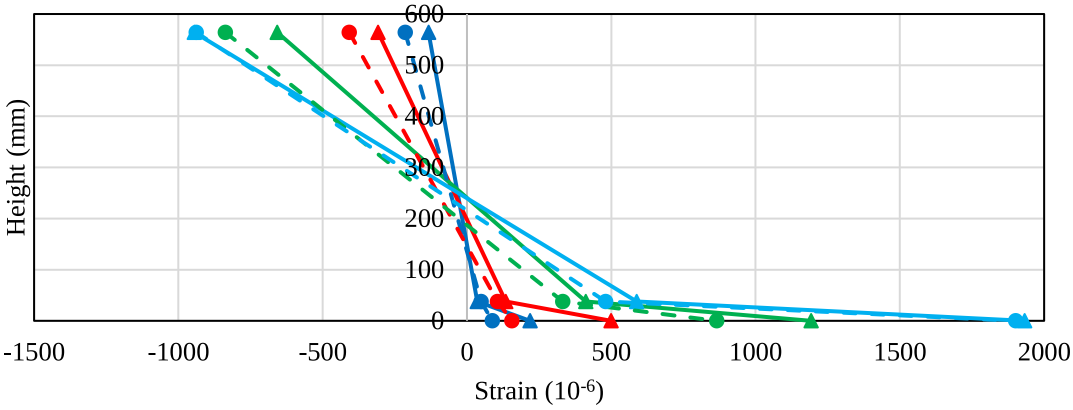

(a) CCB-A

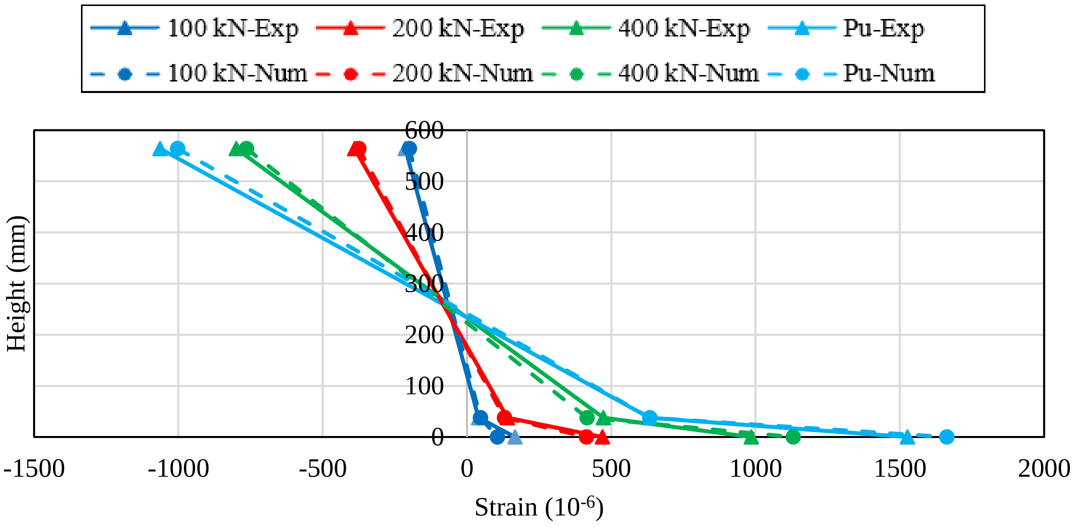

(b) CCB-P

Source: The author (2025).

5.3 SUMMARY AND CONCLUSIONS OF THE CHAPTER

This chapter presents the development of numerical modeling and its validation. As a summary and conclusion of the chapter, it can be stated that:

- The numerical analysis of this study consists of two steps. The first is a linear buckling analysis (LBA), which provides eigenvalues and eigenvectors for the elastic critical load and deformed configuration, respectively. In this one, the structure imperfections and plasticity are disregarded. Subsequently, the deformed shape linked to the first positive eigenvalue is selected in the LBA analysis and used as an initial imperfection for the nonlinear post-buckling analysis. For this, an initial curvature is inserted to simulate the imperfection geometry of the I-beam;

- It described the various components utilized in the numerical model, including its geometric characteristics, the types of finite elements employed, the mesh size, properties of contact, models of residual stress, and the geometric imperfections incorporated. Additionally, it outlines the constitutive relationships that will characterize the behavior of each material within the model;
- Considering both tests performed by Salah (2009) and Qi *et al*. (2020), the preliminary numerical models were validated with the imperfection value of d_g/100 (or d/100) and the residual stress distribution proposed by Beg and Hladnik (1996), as these composite beams have welded I-sections;
- In the preliminary numerical model, the constitutive model of Earls (1999) was inserted for the steel I-section, and a friction coefficient of 0.4 was adopted for the contact tangential behavior;
- The final numerical model was calibrated against the tests performed in this study, and only small adjustments are made to the preliminary numerical model;
- The I-section constitutive relationship, geometric imperfection value, residual stress model, and friction coefficient were changed from the preliminary to the final numerical model;
- The final numerical model, validated against the tests, have the following parameters: geometric imperfection value of d_g/500; residual stress pattern proposed by ECCS (1984) for hot-rolled profiles; elastic-perfectly plastic model for the steel constitutive relationship of the I-section; and friction coefficient of 0.3.

CHAPTER 6

PARAMETRIC STUDY

This chapter presents three parametric studies conducted using numerical models. **Section 6.1** presents the investigations on the elastic stability of composite cellular beams with slabs of Normal Concrete (NC) in hogging moment regions. **Section 6.2** addresses the study on the WPB resistance of composite castellated beams with slabs of Ultra-High-Performance Concrete (UHPC) under hogging bending. Finally, **section 6.3** discusses the assessment of the stability and dematerialization of continuous composite beams using HSS castellated I-sections and UHPC slabs. The parametric studies regarding sections 6.1-6.2 were published by Oliveira *et al*. (2023b, 2025), respectively. The research article regarding the parametric study described in **section 6.3** is under development.

6.1 ELASTIC STABILITY OF STEEL-NC COMPOSITE CELLULAR BEAMS IN HOGGING MOMENT REGIONS

This parametric study is a continuity of the master's dissertation of the present author (OLIVEIRA, 2022). As described in **section 2.1.1**, Oliveira *et al*. (2022) and Oliveira (2022) conducted nonlinear analyses to investigate the effect of geometric parameters and hogging moment distribution on the ultimate moment of steel-NC composite cellular beam. Meanwhile, the present parametric study analyzes the elastic buckling behavior of the same composite cellular beams addressed by Oliveira *et al*. (2022) and Oliveira (2022). This investigation was published by Oliveira *et al*. (2023b).

The boundary conditions of the analyzed models are based on the tests performed by Tong *et al*. (2014), which is shown in **Figure 6.1**. In the slab, lateral displacement (Ux=0) was prevented in three regions: supports and the center of the unrestrained length. The vertical displacement (Uy=0) on both supports and the longitudinal displacement (Uz=0) on one of the supports were restrained. Only material elastic properties (Young's modulus and Poisson ratio) were inserted in the parametric study because it investigates the beams' elastic behavior.

Figure 6.1: Discretization and boundary conditions.

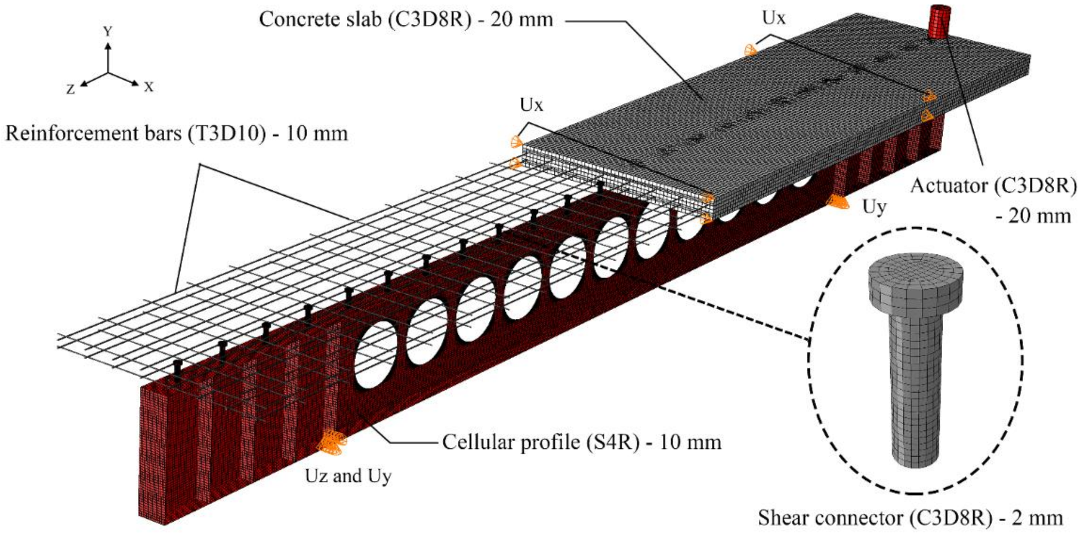

Source: Oliveira *et al*. (2023b).

The parametric study addresses steel-concrete composite cellular beams constituted by hot-rolled parent sections W 360x32.9, W 360x39 and W 360x51. As the study evaluates beams with different values of flange and web slenderness, these I-profiles were selected. In addition, the key parameters variation of the cellular beam openings is extensive, totaling 360 models. As a simplification and to better study the effect of the openings, d_g is kept equal in the parametric study. However, in commercial beams, this value would vary with b_w and D_0 due to the fabrication process. Future assessments should be carried out with different parent section geometries, the depth of cellular beam (d_g), and other parameters of composite cellular beams.

In the present study, the models of composite cellular beams are made by:

- One unrestrained span with web openings and two cantilevers with the presence of transversal stiffeners (**Figure 6.2**);
- Unrestrained length equal to 4 and 6 m;
- Composite cross-section according to the specimens of Salah (2009) as detailed in **Figure 5.2**;
- Height of the cellular I-section (d_g) equal to 520 mm;
- Three different original I-sections as per **Table 6.1**;
- The ranges variation of the ratios D_0/d and p/D_0 are 0.8-1.2 and 1.2-1.5, respectively;
- All cellular I-beams have an opening in the center region of the unrestrained span;
- The width of the end web-post (b_{we}) is greater than the width of the intermediate web-post (b_w);

- Concrete slab according to **Figure 5.2**, and headed studs of 19x80mm with 250 mm spacing;
- For the I-beam and headed studs, the modulus of elasticity is equal to 200 GPa;
- f_{ck}= 30 MPa is adopted for the slab's concrete with a modulus of elasticity equal to 32.8 GPa. The reinforcement bars have a modulus of elasticity equal to 210 GPa;
- Three different hogging moment distributions along the analyzed span (**Figure 6.2**).

Figure 6.2: Beam geometry and hogging moment distribution addressed in the parametric study.

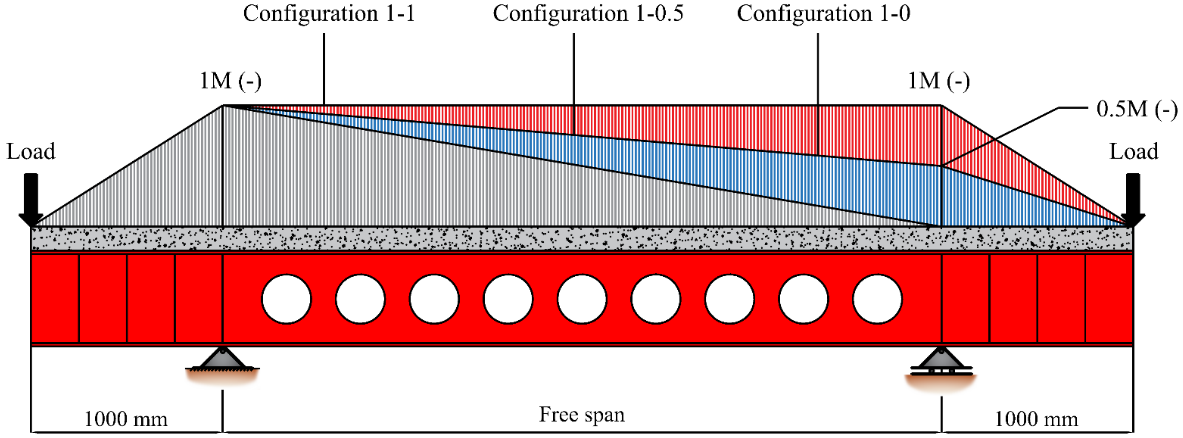

Source: Oliveira *et al*. (2023b).

Table 6.1: Parent I-section dimensions.

Section profile	d (mm)	b_f (mm)	t_w (mm)	t_f (mm)
W 360 x 32,9	350	127	5.8	8.5
W 360 x 39	350	128	6.5	10.7
W 360 x 51	350	171	7.2	11.6

Source: Oliveira *et al*. (2023b).

To avoid an extensive chapter, the main observations and conclusions of this parametric study are summarized in **section 6.4**. This study focused only on the linear buckling analysis, addressing extensive discussions on the buckling modes and the elastic critical moment of these composite cellular beams. More information can be found in the article by Oliveira *et al*. (2023b).

6.2 WPB RESISTANCE OF STEEL-UHPC COMPOSITE CASTELLATED BEAMS UNDER HOGGING BENDING

This investigation was performed using the final numerical model (**section 5.2**) and was published by Oliveira *et al*. (2025). In total, 30 models were analyzed. In addition, all composite castellated beams were designed to ensure full composite action.

The composite castellated beams addressed in the parametric study are equal to the specimens of the tests detailed in **Figures 4.1-4.2** and **Tables 4.1-4.2**. The web-post and opening geometries, I-section web thickness, and concrete strength were varied. In total, 30 numerical models were analyzed. The influence of the web-post and opening geometries was analyzed considering the opening width (a_o), the tee length and web-post width (both given by b_w). The tee length (length of the hexagon horizontal edge) and web-post width are always equal due to the cutting and welding process of castellated I-section manufacturing (**Figure 1.2**). Therefore, when the web-post width varies, a_o also changes because a_o is the sum of b_w and both bases of the hexagon diagonal edges (s). This means that it is not possible to verify separately the effects of web-post width and tee length on the flexural response of castellated beams in practical cases.

Further to Anglo-Saxon and Peiner patterns equal to the specimens (**Figures 4.1-4.2**), three hexagonal opening geometries were adopted. This way, five castellated I-sections were used in the analyzed composite beams, and their geometries are described in **Table 6.2**. Additionally, the influence of the web thickness (t_w) was verified with three values: 5.8mm, 6.9mm and 7.9mm. Finally, two types of concrete were applied to the slab: ultra-high-performance concrete (UHPC) from the tests of the present study (f_{cm}= 139.8MPa) and normal concrete (NC) from the tests of Tong *et al*. (2014) ($f_{cm\text{-}cubic}$= 25.1MPa). The final numerical model (**section 5.2**) was also validated against the tests of Tong *et al*. (2014), as presented by Oliveira *et al*. (2025).

Table 6.2: Castellated I-section parameters.

I-section	D_o (mm)	b_w (mm)	a_o (mm)	s (mm)	θ	*n_{op}	L (mm)
1	348	87	289	101	60°	6	2343
2	348	139	340	100.5	60°	4	2055
3	348	157	358	100.5	60°	4	2217
4	348	174	348	87	63.4°	4	2262
5	348	174	375	100.5	60°	4	2370

*n_{op} is the number of openings

Source: The author (2025).

6.2.1 Results and discussion

Figure 6.3 presents the parametric study results, considering the P_u of the models. Those with t_w of 5.8mm (**Figure 6.3a**) had P_u values in the range of 351kN–437kN, while the ones with t_w of 6.9mm and 7.9mm had values in the ranges of 505kN–558kN and 627kN–696kN (**Figure 6.3b-c**), respectively. This way, the higher the t_w is, the higher the WPB resistance because the local web slenderness (h_w/t_w) decreases with the t_w increase. All models reached failure by WPB coupled with VM, as well as the test specimens. Steel and composite alveolar beams with shorter web-post widths are more susceptible to the WPB occurrence, while those with longer tee lengths are more critical to the VM phenomenon (FERREIRA *et al.*, 2021b; FERREIRA; MARTINS; NARDIN, 2021; MARTIN *et al.*, 2017; OLIVEIRA, 2022; PANEDPOJAMAN; THEPCHATRI; LIMKATANYU, 2015; SHEEHAN *et al.*, 2016; TAŞ *et al.*, 2024; ZEYTINCI *et al.*, 2021). Therefore, the models with b_w= 87mm had the lowest P_u values for both concrete slabs (NC and UHPC) within those of t_w= 5.8mm (**Figure 6.3a**). The castellated beams with t_w= 5.8mm have the highest local web slenderness (h_w/t_w), making them more critical to the WPB phenomenon, and these models of b_w= 87mm had the lowest WPB resistance because the web-post width of 87mm is the shortest one. On the other hand, the castellated I-sections with the second shortest web-post width (b_w= 139mm) had the highest P_u values for both concrete slabs (**Figure 6.3a**). As the models in question have b_w= 139mm, which is considerably higher than b_w= 87mm, their susceptibility to the WPB occurrence is significantly lower than those of b_w= 87mm. In addition, the ones with b_w= 139mm present the second lowest tee length, making them less critical to the VM phenomenon than the other models with higher b_w values, resulting in the highest P_u values due to being the best case regarding the WPB and VM interaction. Still discussing the models with $b_w \geq$ 139mm and t_w= 5.8mm (**Figure 6.3a**), the P_u values decreased with the increase of b_w because the VM phenomenon significantly affected their shear capacities. Therefore, the models with longer tee lengths had lower P_u values. This trend was also observed in the models with t_w= 6.9mm and 7.9mm (**Figure 6.3b-c**) for those of $b_w \geq$ 139mm due to the same facts previously described. This way, the ones with b_w= 139mm also had the highest P_u values for both concrete slabs (**Figure 6.3b-c**). The castellated beams with b_w= 87mm had higher P_u values than those of b_w= 174mm (with a_o= 348mm and 375mm) within the models of t_w= 7.9mm (**Figure 6.3c**) for both slabs because t_w= 7.9mm provides the lowest h_w/t_w ratio and lower sensitivity to WPB. This way, the ones with the highest tee length had lower bearing capacity due to VM. Regarding the models of t_w= 6.9mm, the one with b_w= 87mm had a slightly higher P_u than both models of b_w=

174mm within those with t_w= 6.9mm and NC slab (**Figure 6.3b**). In contrast, the ones with UHPC had higher P_u for b_w= 87mm than b_w= 174mm (**Figure 6.3b**), as these models of t_w= 6.9mm have the intermediate h_w/t_w ratio concerning t_w= 5.8mm and 7.9mm, also presenting an intermediate susceptibility to WPB and VM occurrence. Analyzing only the models with b_w= 174mm, it is noted that the ones with s= 87mm (θ= 63.4° and a_o= 348mm) had a higher P_u than those with s= 100.5mm (θ= 60° and a_o= 375mm) for the beams of t_w= 5.8mm, which are more sensitivity to WPB (**Figure 6.3a**). On the other hand, the P_u values of both castellated beams (θ= 63.4° – a_o= 348mm and θ= 60° – a_o= 375mm) are similar considering those of t_w= 6.9 and 7.9mm for both slabs (**Figure 6.3b-c**) because s and θ parameters are not influential on the VM occurrence.

Figure 6.3: Parametric study results.

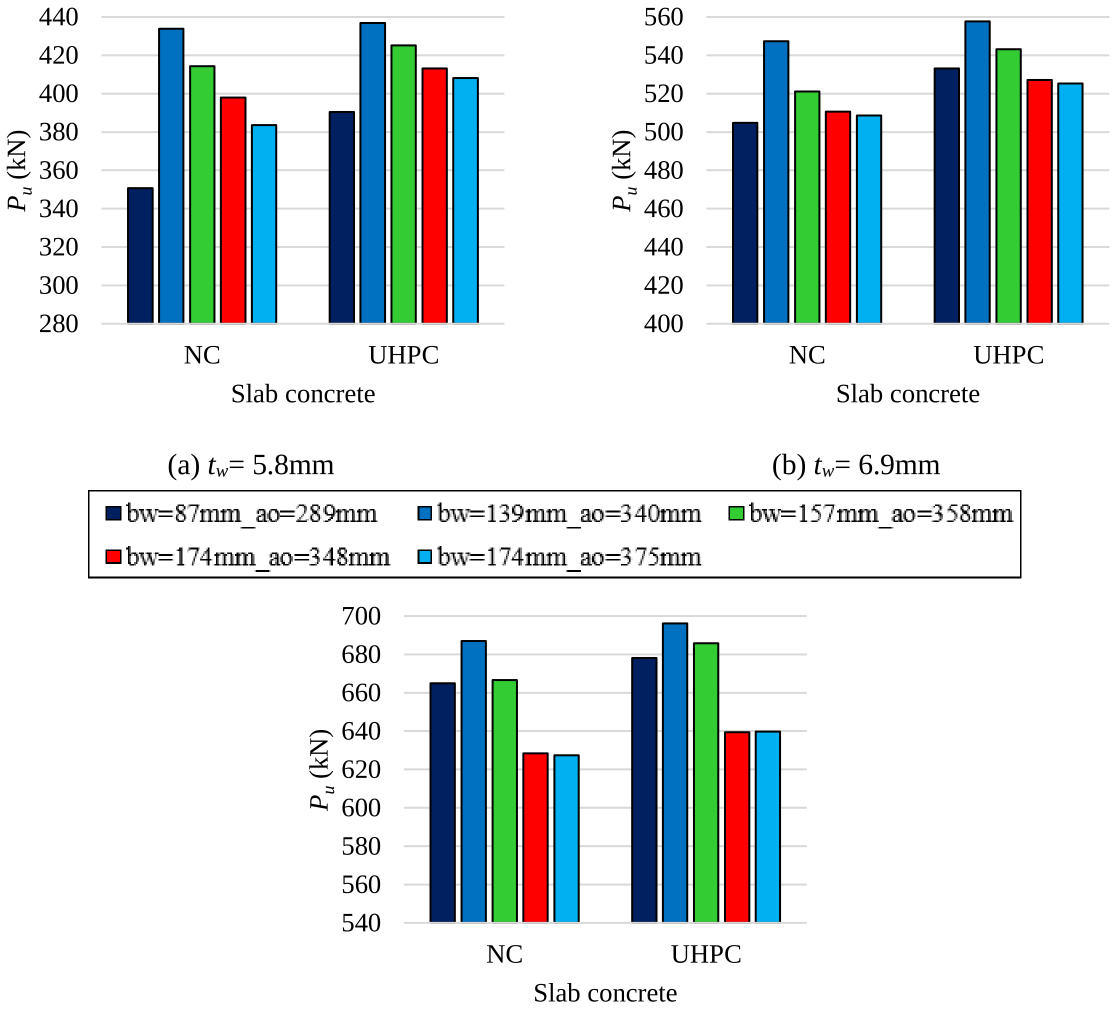

(a) t_w= 5.8mm

(b) t_w= 6.9mm

(c) t_w= 7.9mm

Source: The author (2025).

Figure 6.4 shows the ratio between the P_u values of the models with UHPC slabs and NC slabs ($P_{u\text{-}UHPC}/P_{u\text{-}NC}$). All models present $P_{u\text{-}UHPC}/P_{u\text{-}NC}$ ratios higher than 1.0, demonstrating that using UHPC not only enhances the slab cracking but also contributes to composite castellated beams' bearing capacity, even occurring WPB and VM phenomenon. The initial bending stiffness and the load at the beginning of the load-displacement curve's nonlinear range are considerably higher for the composite beams with UHPC slabs than those with NC slabs. The models with a higher effect of the WPB phenomenon presented an evident peak load, and using UHPC slabs, the peak was also evident in all these composite beams. However, the models with NC slabs significantly influenced by the VM did not present an evident peak load up to a deflection value of $L/100$ ($v \approx$ 20mm). In these cases, the defined $P_{u\text{-}NC}$ value is regarding the deflection of $L/100$ (FERREIRA; MARTINS; NARDIN, 2020c). Because of this, the composite beams highly affected by the VM reached similar values of $P_{u\text{-}UHPC}$ and $P_{u\text{-}NC}$, as the $P_{u\text{-}UHPC}$ was similar to the load for the deflection of $L/100$ in the models with NC slabs. However, the models with NC slabs have a considerably lower initial bending stiffness, and the beginning of the load-displacement curve's nonlinear range occurred for significantly lower loads. The models more affected by the WPB occurrence presented similar behavior of their load-displacement curves for both slabs, in which the UHPC slab elevated their initial bending stiffness and ultimate load simultaneously. Therefore, the UHPC slab substantially influenced the P_u values of the models with WPB predominance in the failure mode. The mean value of $P_{u\text{-}UHPC}/P_{u\text{-}NC}$ ratio regarding all models was 1.035 (**Figure 6.4**), and the maximum and minimum values were 1.113 and 1.007, respectively. The maximum value of 1.113 was obtained by the model with "1" I-section (**Table 6.2**) and t_w= 5.8mm, which is the most critical model regarding the WPB occurrence. In contrast, the model with "2" I-section (**Table 6.2**) and t_w= 5.8mm had the minimum value of 1.007, in which its failure mode was highly affected by VM.

Figure 6.4: $P_{u\text{-}UHPC}/P_{u\text{-}NC}$ ratios of the numerical models.

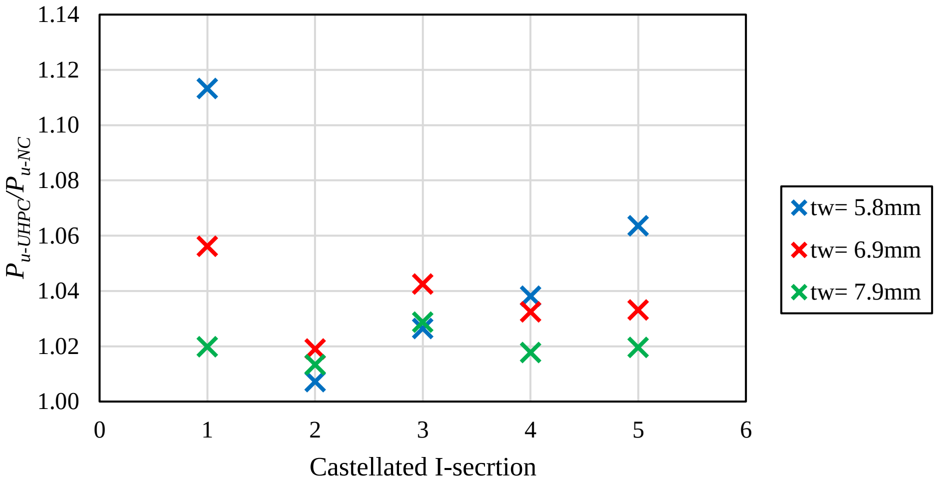

Source: The author (2025).

6.2.2 Accuracy obtained by WPB resistance formulations

This section covers the accuracy of the procedures for WPB resistance prediction described in **sections 2.1.3.2-2.1.3.3** against the numerical results of this study (**section 4.2**). As all models were subjected to three-point bending, their spans were submitted to uniform vertical shear forces. This way, the ultimate horizontal shear force ($V_{h,exp}$) given by **Eq. 2.69** from Steel Design Guide 31 (FARES; COULSON; DINEHART, 2016) and **Eq. 2.79** from the draft version of EC4 (prEN 1994-1-1) provided equal values for each model.

Figure 6.5 shows the accuracy obtained by WPB resistance formulations regarding numerical results, in which $V_{h,R}$ is the horizontal shear force resistance given by each procedure. Notably, as described in **section 2.1.3.2**, the procedure from Steel Design Guide 31 does not address castellated beams with $\theta > 60^0$ or $b_w/t_w > 30$. The castellated I-section "4" (**Table 6.2**) has θ approximately equal to 63.4^0 (**Figure 1.2b**). This way, for the present analyses, the formulation from Steel Design Guide 31 for the WPB resistance of the castellated I-section "4" was calculated considering θ equal to 60^0. The values of $V_{h,R}/V_{h,exp}$ ratios higher than 1.0 in **Figure 6.5** are non-conservative results of the procedures, and vice-versa. As observed, the formulation from Steel Design Guide 31 had non-conservative results in most cases, overestimating the WPB resistance of most models (**Figure 6.5a**). The castellated beams named from "1" to "5" (**Table 6.2**) vary the tee length (b_w) increasingly, also increasing their susceptibility to VM occurrence. Therefore, Steel Design Guide 31 considerably overestimated the WPB resistance of the models with higher tee length (b_w), in which the models with castellated I-section "5" (**Table 6.2**) had the highest $V_{h,R}/V_{h,exp}$ ratio values, showing that this procedure provides highly non-conservative results for castellated beams significantly affected by the VM phenomenon. In contrast, EN 1993-1-13:2024 provided only conservative results (**Figure 6.5b**). This way, the method from EN 1993-1-13:2024 does not overestimate the WPB resistance of composite castellated beams, even occurring the WPB and VM interaction.

Figure 6.5: Comparison of the accuracy obtained by WPB resistance formulations regarding the numerical models.

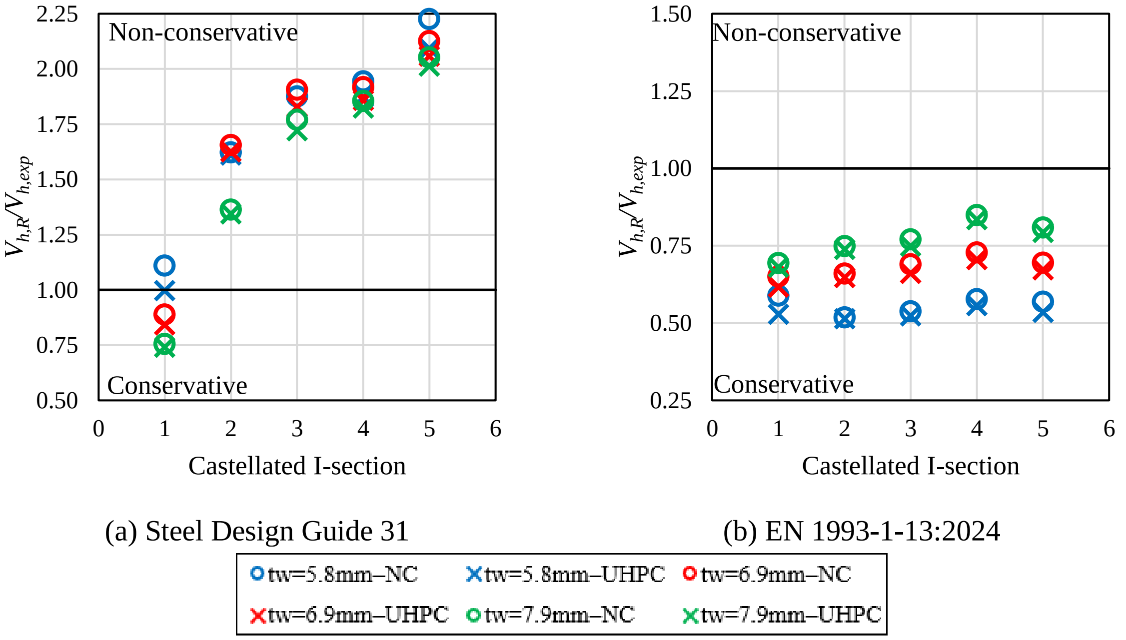

(a) Steel Design Guide 31 (b) EN 1993-1-13:2024

Source: The author (2025).

6.3 STABILITY AND DEMATERIALIZATION OF CONTINUOUS COMPOSITE BEAMS USING HSS CASTELLATED I-SECTIONS AND UHPC SLABS

This investigation was also conducted using the final numerical model (**section 5.2**). The study addresses the stability behavior of composite castellated beams under hogging bending, in which the influence of the opening geometry, parent I-section dimensions, the expansion ratio of the castellated profile (d_g/d), I-section steel yield strength (f_y), longitudinal reinforcement bars' diameter (ϕ) and their steel yield strength ($f_{y\text{-}bar}$), concrete strength, and slab height (h_s) are analyzed. **Figure 6.6** shows the layout and composite section of the numerical models adopted in the analyses. All composite castellated beams were designed to ensure full composite action.

Six parent I-sections are adopted for the castellated beams, as described in **Table 6.3**. **Table 6.4** presents the geometric parameters of the castellated beams. The Litzka, Peiner, and Anglo-Saxon opening patterns (**Figure 1.2**) are addressed, in which three expansion ratios of the castellated profile (d_g/d= 1.4, 1.5, and 1.6) are applied for those with the Litzka pattern. Meanwhile, only d_g/d= 1.5 is assumed for the castellated beams with Peiner and Anglo-Saxon patterns. Four I-section steel yield strengths (f_y) are adopted, which is regarding the S355 normal-strength steel (NSS) and the S460, S690, and S960 high-strength steel (HSS). For the slab, two concrete strengths are used: NC from the tests of Salah (2009) (f_{ck}= 30MPa) and UHPC from the tests of the present study (f_{cm}= 139.8MPa). In addition, two slab heights are utilized: h_s= 75 and 100mm. Three ϕ values and two $f_{y\text{-}bar}$ values are assessed for the longitudinal reinforcement bars: ϕ= 8, 10, and 12.5mm and $f_{y\text{-}bar}$= 500 and 700MPa.

Figure 6.6: Layout of the numerical models.

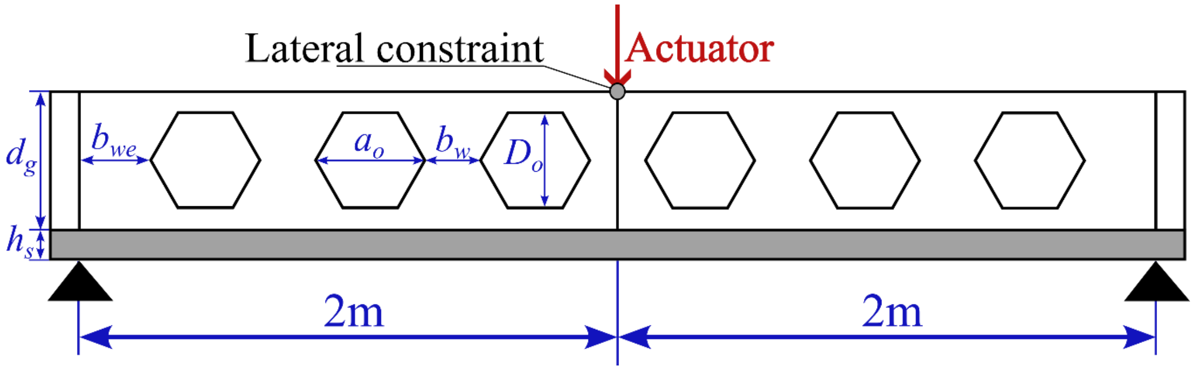

(a) Three-point bending test

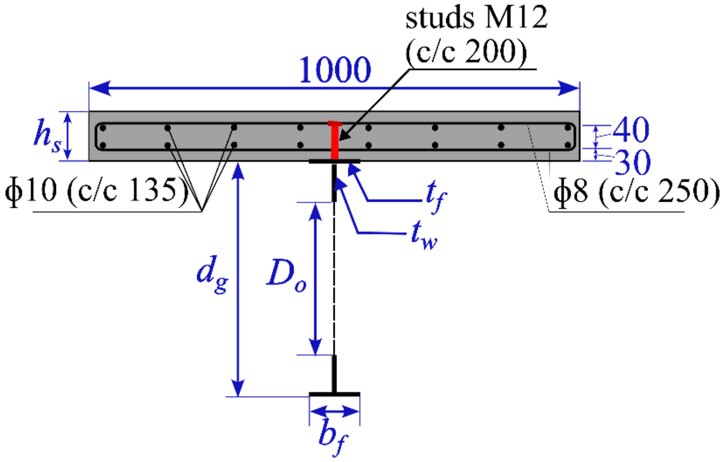

(b) Composite section (in mm)

Source: The author (2025).

Table 6.3: Parent I-sections adopted for the castellated beams.

Profile	I-section	Linear mass (kg/m)	d (mm)	b_f (mm)	t_w (mm)	t_f (mm)
1	W310x21	21.0	303	101	5.1	5.7
2	W310x23.8	23.8	305	101	5.6	6.7
3	W360x32.9	32.9	349	127	5.8	8.5
4	W360x39	39.0	353	128	6.5	10.7
5	W410x38.8	38.8	399	140	6.4	8.8
6	W410x46.1	46.1	403	140	7.0	11.2

Source: The author (2025).

Table 6.4: Geometric parameters of the castellated beams.

Pattern	d_g/d	D_o/d	I-section	d_g (mm)	h_w/t_w	D_o (mm)	b_w (mm)	s (mm)	a_o (mm)	$^*n_{op}$	b_{we} (mm)
Litzka	1.4	0.8	W310x21	424.20	80.94	242.40	139.96	69.98	279.92	8	390.44
			W360x32.9	488.60	81.31	279.20	161.21	80.61	322.42	6	629.71
			W410x38.8	558.60	84.53	319.20	184.31	92.15	368.61	6	433.40
	1.5	1.0	W310x21	454.50	86.88	303.00	174.95	87.48	349.90	6	512.91
			W310x23.8	457.50	79.30	305.00	176.11	88.05	352.21	6	503.09
			W360x32.9	523.50	87.33	349.00	201.51	100.76	403.03	6	287.14
			W360x39	529.50	78.17	353.00	203.82	101.91	407.64	6	267.51
			W410x38.8	598.50	90.77	399.00	230.38	115.19	460.77	4	732.90
			W410x46.1	604.50	83.16	403.00	232.69	116.35	465.38	4	720.19
	1.6	1.2	W310x21	484.80	92.82	363.69	210.00	105.00	419.99	6	215.04
			W360x32.9	558.40	93.34	418.90	241.88	120.94	483.75	4	669.68
			W410x38.8	638.40	97.00	478.92	276.53	138.26	553.06	4	479.09
Peiner	1.5	1.0	W310x21	454.50	86.88	303.00	151.50	75.75	303.00	8	257.75
			W310x23.8	457.50	79.30	305.00	152.50	76.25	305.00	8	246.25
			W360x32.9	523.50	87.33	349.00	174.50	87.25	349.00	6	516.75
			W360x39	529.50	78.17	353.00	176.50	88.25	353.00	6	499.75
			W410x38.8	598.50	90.77	399.00	199.50	99.75	399.00	6	304.25
			W410x46.1	604.50	83.16	403.00	201.50	100.75	403.00	6	287.25
Anglo-Saxon	1.5	1.0	W310x21	454.50	86.88	303.00	75.75	87.87	251.49	10	401.68
			W310x23.8	457.50	79.30	305.00	76.25	88.45	253.15	10	391.13
			W360x32.9	523.50	87.33	349.00	87.25	101.21	289.67	10	159.03
			W360x39	529.50	78.17	353.00	88.25	102.37	292.99	10	137.93
			W410x38.8	598.50	90.77	399.00	99.75	115.71	331.17	8	326.20
			W410x46.1	604.50	83.16	403.00	100.75	116.87	334.49	8	309.42

$^*n_{op}$ is the number of openings

Source: The author (2025).

The parametric study is separated into four parts, which are described below:

- Part 1: assessment of the effect of the d_g/d ratio combined with different parent I-sections and f_y;

- Part 2: analysis of the influence of the opening geometry combined with different parent I-sections and f_y are analyzed;
- Part 3: investigation of the effect of the concrete strength, h_s, ϕ, and $f_{y\text{-}bar}$;
- Part 4: evaluation of the possibilities for dematerialization of conventional composite beams (with NSS solid I-section and NC) using NSS and HSS castellated I-sections and UHPC.

6.3.1 Results and discussion

Parts 1-3 of the parametric study (**sections 6.3.1.1-6.3.1.3**) analyze 130 composite castellated beams. Additionally, more 19 composite beams with solid and castellated I-sections are assessed in **section 6.3.1.4**. Therefore, in total, 149 numerical models were analyzed in this parametric study.

6.3.1.1 Part 1: the influence of the expansion ratio, I-section dimensions and steel yield strength of the castellated beams

All composite castellated beams assessed in this part of the study have the following geometry parameters and material properties:

- Litzka opening pattern;
- Concrete slab with h_s= 100mm and NC (f_{ck}= 30MPa);
- Longitudinal reinforcement bars with ϕ= 10mm and $f_{y\text{-}bar}$= 500 MPa.

Meanwhile, the following parameters were varied in this part:

- d_g/d= 1.4, 1.5, and 1.6;
- Parent I-section: W310x21, W360x32.9, and W410x38.8;
- f_y= 355, 460, 690, and 960MPa (S355, S460, S690, and S960 steels, respectively).

Table 6.5 describes the instability modes characterized by models in the parametric study's part 1, and **Table 6.6** shows the lateral displacement fields regarding the ultimate moment for the castellated beams with f_y= 355 and 960MPa. All models presented lateral displacement at the compressed flange, which characterizes the LDB occurrence. In most models, the "S" shape in the web-post was also characterized by the WPB phenomenon, with some presenting WPB as more accented than others. The coupling between LDB and WPB was expected, as in three-point bending, the composite castellated beams were subjected to hogging moment and shear loads simultaneously. Within the models with d_g/d= 1.4, those with

W310x21 I-section and f_y= 355 and 460MPa did not characterize the WPB in their instability modes, as well as for the one with d_g/d= 1.5, W310x21 I-section and f_y= 355MPa. Only the LDB occurred in their instability modes. Even with the WPB occurrence, all models with the W310x21 parent profile were not significantly affected by the WPB in the LDB-WPB interaction due to their lower bearing capacity, not reaching critical shear loads regarding the WPB phenomenon. In contrast, the castellated beams with the W360x32.9 and W410x38.8 parent profiles had higher ultimate loads, characterizing the WPB in all their instability modes. Considering the same I-section and f_y, those with d_g/d= 1.4 and 1.6 had the lowest and highest effect in the LDB-WPB interaction, respectively. In addition, for the same I-section and d_g/d value, the higher the f_y is, the greater the WPB characterization in the instability mode. This occurrence is due to the models with higher f_y presenting higher bearing capacity, which makes them reach shear loads more critical for the WPB phenomenon. This way, as an example, the castellated beam with the W310x21 I-section, d_g/d= 1.4, and f_y= 355MPa did not characterize the WPB occurrence, only showing LDB in its instability mode. Meanwhile, the one with W410x38.8 I-section, d_g/d= 1.6, and f_y= 960MPa presented the most accentuated "S" shape in the web-post, which characterizes the WPB phenomenon.

Table 6.5: Instability modes obtained in the parametric study's part 1.

d_g/d	I-section	Instability modes			
		f_y= 355 MPa	f_y= 460 MPa	f_y= 690 MPa	f_y= 960 MPa
1.4	W310x21	LDB	LDB	LDB + WPB	LDB + WPB
	W360x32.9	LDB + WPB	LDB + WPB	LDB + WPB	LDB + WPB
	W410x38.8	LDB + WPB	LDB + WPB	LDB + WPB	LDB + WPB
1.5	W310x21	LDB	LDB + WPB	LDB + WPB	LDB + WPB
	W360x32.9	LDB + WPB	LDB + WPB	LDB + WPB	LDB + WPB
	W410x38.8	LDB + WPB	LDB + WPB	LDB + WPB	LDB + WPB
1.6	W310x21	LDB + WPB	LDB + WPB	LDB + WPB	LDB + WPB
	W360x32.9	LDB + WPB	LDB + WPB	LDB + WPB	LDB + WPB
	W410x38.8	LDB + WPB	LDB + WPB	LDB + WPB	LDB + WPB

Source: The author (2025).

Table 6.6: Lateral displacements regarding the ultimate moment (deformation scale factor= 2).

Steel section	Expansion ratio (d_g/d)		
	d_g/d= 1.4	d_g/d= 1.5	d_g/d= 1.6
W310x21-S355	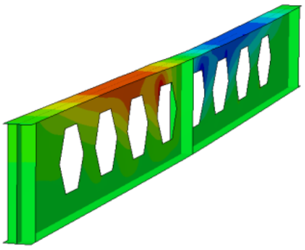	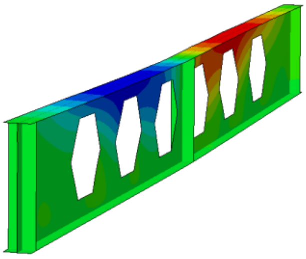	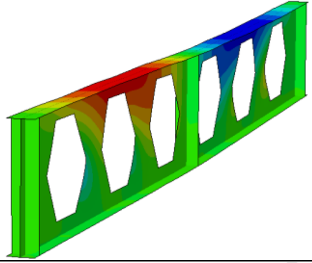
W310x21-S960	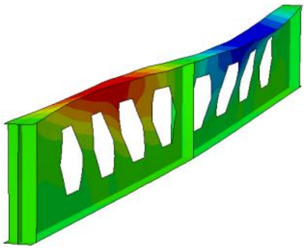	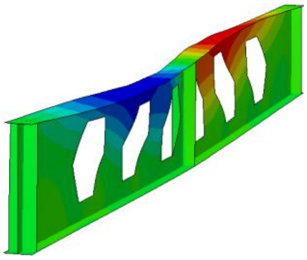	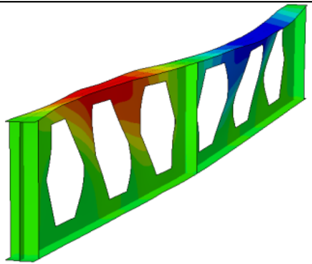
W360x32.9-S355	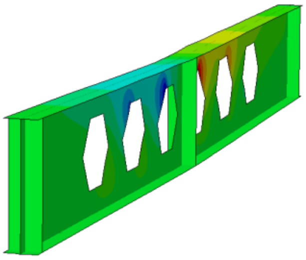	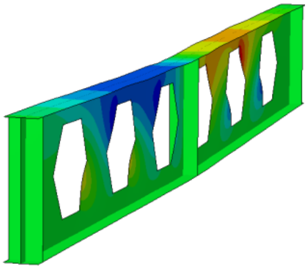	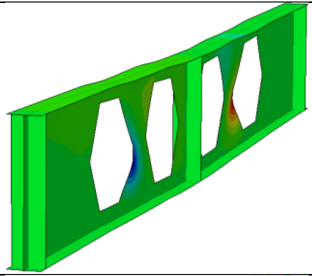
W360x32.9-S960	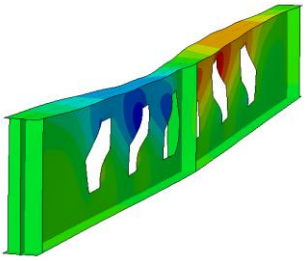	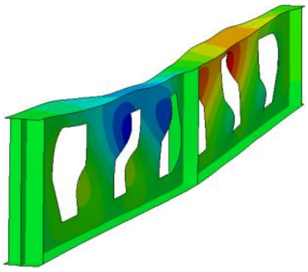	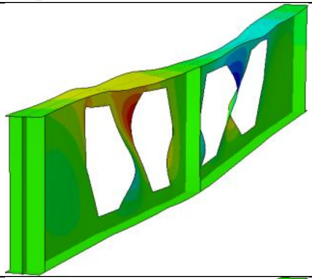
W410x38.8-S355	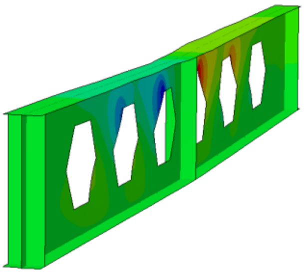	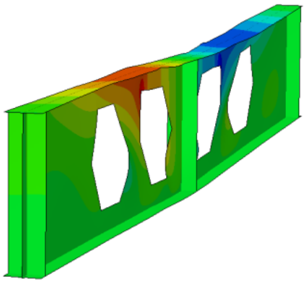	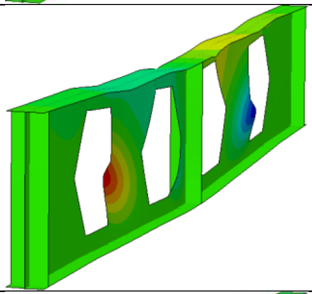
W410x38.8-S960	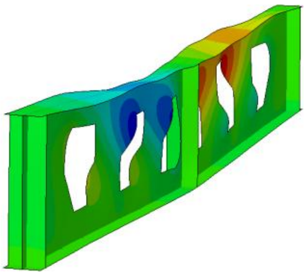	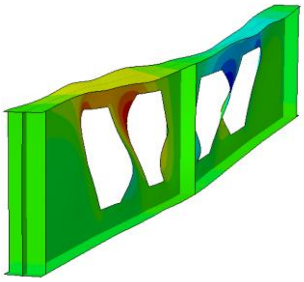	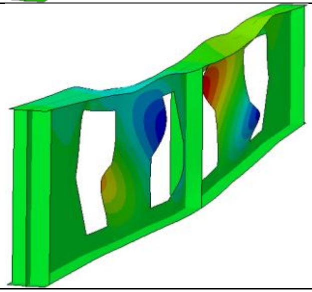

Source: The author (2025).

Figure 6.7 presents the graphs of moment-deflection curves of the models with equal f_y, varying the castellated I-section and its d_g/d ratio. The castellated beams with the W310x21 parent profile were not sensitive to the d_g/d variation for all f_y values. This I-section has the lowest cross-section dimensions, resulting in a considerably lower bearing capacity for these models with the W310x21 parent profile. They did not reach shear loads for a critical WPB, and the LDB was predominant in their failure modes (**Table 6.5** and **Table 6.6**). In addition, the d_g values of these castellated beams present a lower variation for changing the d_g/d ratio, as the W310x21 parent profile has a significantly lower I-section depth (d).

In contrast, the castellated beams with W360x32.9 and W410x38.8 parent profiles were influenced by the d_g/d ratio (**Figure 6.7**), exhibiting a greater effect in those with the W410x38.8 parent I-section due to the highest d value. These models characterized a significant WPB, and this instability mode is more sensitive to the d_g/d variation, as it also varies the castellated beam's local web slenderness (h_w/t_w). A slight influence of the d_g/d ratio on the M_u observed was observed in the models with W360x32.9 profile. However, an elevated effect on these castellated beams' initial bending stiffness and ductility was noted. In general, the ones with d_g/d= 1.4 had a higher initial bending stiffness and a lower ductility, presenting LDB predominance on the LDB-WPB interaction. On the other hand, the models with d_g/d= 1.6 had a lower initial bending stiffness and a higher ductility, exhibiting an intensive deformation by WPB on the LDB-WPB interaction. Those with d_g/d= 1.5 presented an intermediate case regarding initial bending stiffness, ductility, and the deformations caused by the LDB-WPB interaction. This occurrence is due to the variation in the h_w/t_w and D_o/d ratios (**Table 6.4**). The models with higher d_g/d values have higher h_w/t_w and D_o/d ratios, making them more susceptible to the WPB phenomenon. The ones with d_g/d= 1.4, which presented LDB predominance, kept the initial stiffness until close to the ultimate moment, reaching the peak for lower deflections. Meanwhile, those with d_g/d= 1.6, more susceptible to the WPB, lose the initial stiffness considerably earlier and show a more extended nonlinear range until the peak, reaching the ultimate moment for higher deflections.

Figure 6.7: The effect of the I-section and its steel yield strength on the hogging moment-deflection curves.

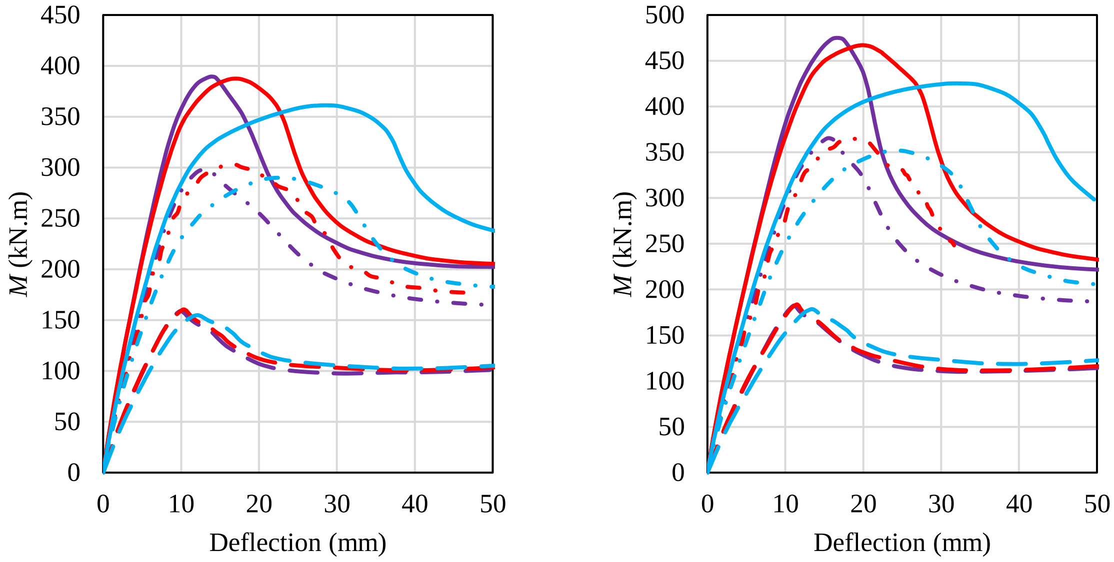

(a) f_y= 355MPa

(b) f_y= 460MPa

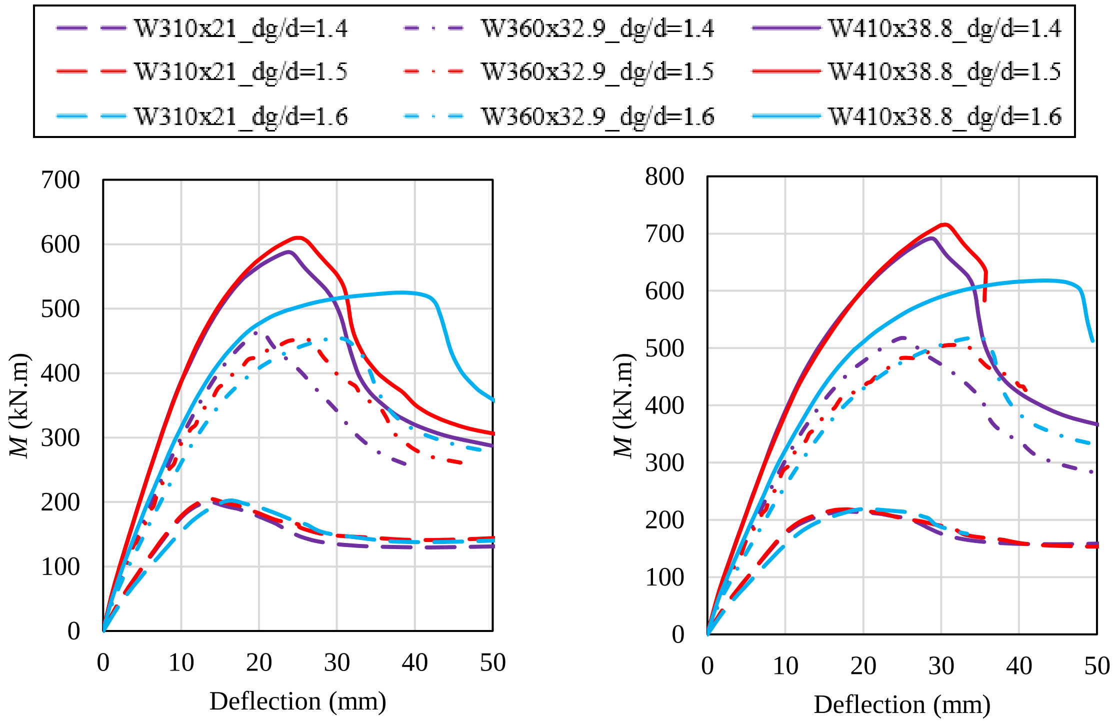

(c) f_y= 690MPa

(d) f_y= 960MPa

Source: The author (2025).

All these trends described for the castellated beams with a W360x32.9 profile were also observed in those with a W410x38.8 I-section (**Figure 6.7**). However, the M_u of the models with a W410x38.8 parent profile was sensitive to the d_g/d variation. **Figure 6.8** shows the effect of the d_g/d ratio and I-section steel yield strength (f_y) on the models' ultimate moment (M_u). The only clear trend in **Figure 6.8** is that all models with W410x38.8 I-section and d_g/d= 1.6 (**Figure 6.8c**) had the lowest M_u values for all f_y due to their h_w/t_w ratio, which is the highest one within all castellated beams (**Table 6.4**). This way, the WPB occurrence was critical in the models with W410x38.8 I-section and d_g/d= 1.6, as shown in **Table 6.6**, decreasing their bearing capacity compared to the other models with the same I-section and f_y. On the other hand, the models with W410x38.8 I-section and d_g/d= 1.4 and 1.5 had different influences of the WPB phenomenon on their failure modes. Those with f_y= 355 and 460MPa had lower deformation due to WPB, which was more intensive for the ones with f_y= 690 and 960MPa. This way, the models with the combinations of W410x38.8 I-section and d_g/d= 1.4-1.5 had similar ultimate loads for f_y= 355 and 460MPa (**Figure 6.7a-b** and **Figure 6.8c**), as the WPB occurrence was not accentuated in the LDB-WPB interaction. In contrast, the coupling of W410x38.8 I-section and d_g/d= 1.4-1.5 had different ultimate loads for f_y= 690 and 960MPa (**Figure 6.7c-d** and **Figure 6.8c**), as the WPB was more accentuated in their failure modes, in which those with d_g/d= 1.5 had the highest M_u for the same f_y, due to their considerably higher b_{we} (**Table 6.4**). The WPB phenomenon in composite alveolar beams is significantly influenced by the b_{we} (FERREIRA *et al.*, 2021b; FERREIRA; MARTINS; NARDIN, 2021; OLIVEIRA *et al.*, 2022, 2023b). This influence of the b_{we} was also observed in the castellated beams with W360x32.9 I-section and f_y= 690 and 960MPa (**Figure 6.7c-d** and **Figure 6.8b**), in which those with d_g=1.5 have the lowest b_{we} value (**Table 6.4**) and obtained the lowest M_u within them. Finally, the steel yield strength significantly influenced the M_u for all d_g/d ratios and I-sections combinations (**Figure 6.8**). All models had higher M_u values due to the increase in f_y.

Figure 6.8: The effect of the d_g/d ratio and I-section steel yield strength on the models' ultimate moment.

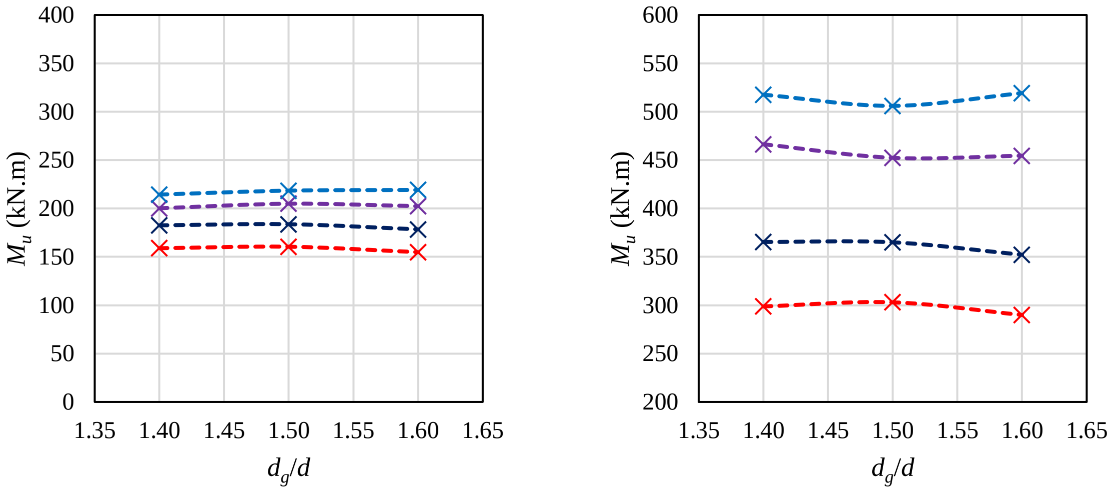

(a) Profile 1 (W310x21) (b) Profile 3 (W360x32.9)

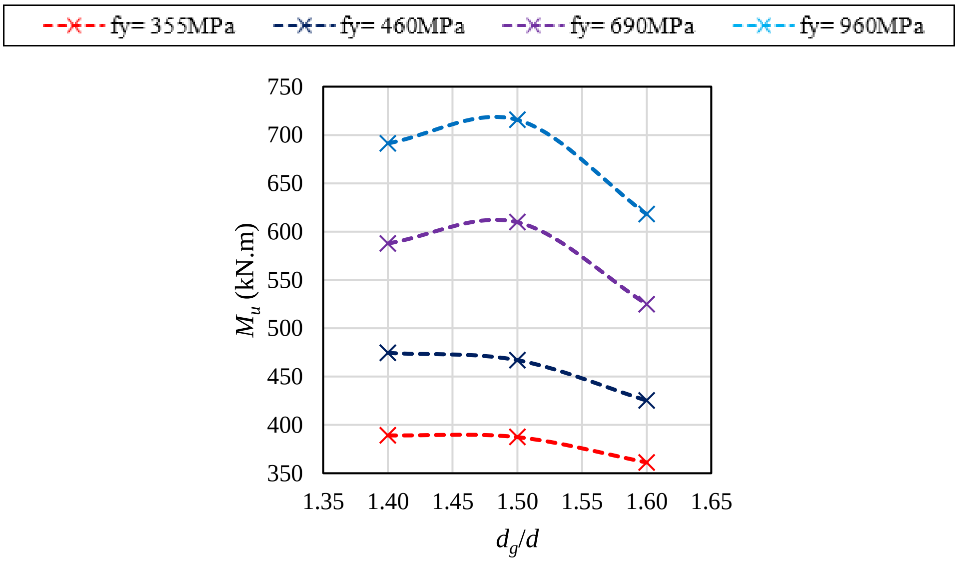

(c) Profile 5 (W410x38.8)
Source: The author (2025).

6.3.1.2 Part 2: the influence of the opening geometry, I-section dimensions and steel yield strength of the castellated beams

All composite castellated beams addressed in this part of the study have the following geometry parameters and material properties:

- d_g/d= 1.5;
- Concrete slab with h_s= 100mm and NC (f_{ck}= 30MPa);
- Longitudinal reinforcement bars with ϕ= 10mm and $f_{y\text{-}bar}$= 500 MPa.

At the same time, the following parameters were varied in this part:

- Opening pattern: Litzka, Peiner and Anglo-Saxon;
- Parent I-section: W310x21, W310x23.8, W360x32.9, W360x39, W410x38.8, and W410x46.1;
- f_y= 355, 460, 690, and 960MPa.

Table 6.7 brings the instability modes characterized by models in the parametric study's part 2, and **Table 6.8** presents the lateral displacement fields at the ultimate moment for the castellated beams with f_y= 460MPa. As noted in **Table 6.7**, all models characterized the LDB in their instability modes due to the compressed flange's lateral displacements. In addition, the WPB was observed in most models, which exhibited the LDB-WPB interaction. For all opening patterns, the models with W310x21 and W310x23.8 I-sections of f_y= 355 and 460MPa reached failure only by LDB. Although WPB occurred in those with f_y= 690 and 960MPa, this instability mode did not significantly impact all models using the W310x21 and W310x23.8 parent profiles. This is because their lower bearing capacity prevented them from reaching the critical shear loads required for the WPB occurrence, as also observed in models of part 1. On the other hand, the models with the W360x32.9, W360x39, W410x38.8, and W410x38.8 parent I-sections showed an evident "S" shape in the web-post due to their higher ultimate loads, which was more accentuated using the W410x38.8 and W410x38.8 profiles by their higher I-section dimensions. Those with the Anglo-Saxon opening pattern presented a higher susceptibility to the WPB occurrence due to their shorter web-post width (b_w), and the shorter the web-post width is, the lower the WPB resistance of the alveolar beams (FERREIRA *et al.*, 2021b; FERREIRA; MARTINS; NARDIN, 2021; OLIVEIRA *et al.*, 2022, 2023b). In contrast, the castellated beams with the Liztka pattern were less susceptible to the WPB phenomenon due to their larger web-post width, and those with the Peiner pattern presented an intermediate case. In addition, it is noted that with the f_y increase, a higher deformation due to WPB was observed, also explained by the higher ultimate loads of the models, reaching critical shear loads for the WPB occurrence. Finally, the models with the combination of W410x38.8 parent profile and Peiner opening patterns showed a significant influence of the f_y variation on their deformed configuration, in which the one with f_y= 355MPa had a lower effect of the WPB phenomenon on the LDB-WPB interaction. Meanwhile, for this same combination, the ones with f_y= 460, 690 and 960MPa had an accentuated "S" shape in the web-post.

Table 6.7: Instability modes obtained in the parametric study's part 2.

Opening pattern	I-section	Instability modes			
		f_y= 355 MPa	f_y= 460 MPa	f_y= 690 MPa	f_y= 960 MPa
Litzka	W310x21	LDB	LDB	LDB + WPB	LDB + WPB
	W310x23.8	LDB	LDB	LDB + WPB	LDB + WPB
	W360x32.9	LDB + WPB	LDB + WPB	LDB + WPB	LDB + WPB
	W360x39	LDB + WPB	LDB + WPB	LDB + WPB	LDB + WPB
	W410x38.8	LDB + WPB	LDB + WPB	LDB + WPB	LDB + WPB
	W410x46.1	LDB + WPB	LDB + WPB	LDB + WPB	LDB + WPB
Peiner	W310x21	LDB	LDB	LDB + WPB	LDB + WPB
	W310x23.8	LDB	LDB	LDB + WPB	LDB + WPB
	W360x32.9	LDB + WPB	LDB + WPB	LDB + WPB	LDB + WPB
	W360x39	LDB + WPB	LDB + WPB	LDB + WPB	LDB + WPB
	W410x38.8	LDB + WPB	LDB + WPB	LDB + WPB	LDB + WPB
	W410x46.1	LDB + WPB	LDB + WPB	LDB + WPB	LDB + WPB
Anglo-Saxon	W310x21	LDB	LDB	LDB + WPB	LDB + WPB
	W310x23.8	LDB	LDB	LDB + WPB	LDB + WPB
	W360x32.9	LDB + WPB	LDB + WPB	LDB + WPB	LDB + WPB
	W360x39	LDB + WPB	LDB + WPB	LDB + WPB	LDB + WPB
	W410x38.8	LDB + WPB	LDB + WPB	LDB + WPB	LDB + WPB
	W410x46.1	LDB + WPB	LDB + WPB	LDB + WPB	LDB + WPB

Source: The author (2025).

Table 6.8: Lateral displacements regarding the ultimate moment (deformation scale factor= 2).

Steel Section	Opening patterns		
	Litzka	Peiner	Anglo-Saxon
W310x23.8-S460	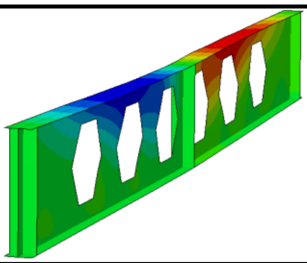	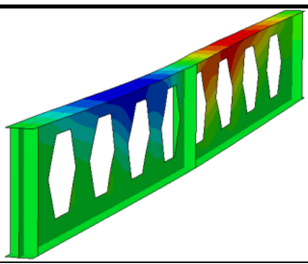	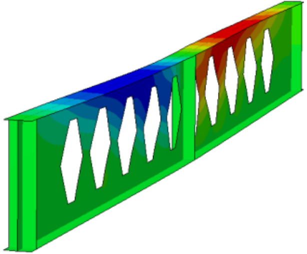
W360x39-S460	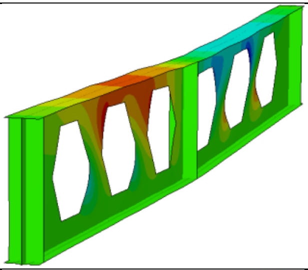	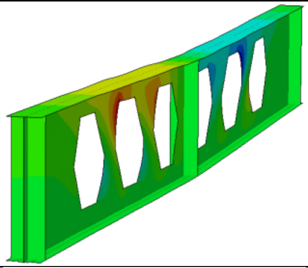	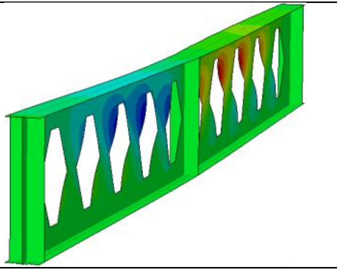
W410x46.1-S460	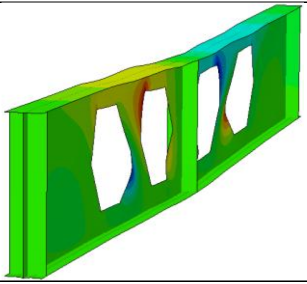	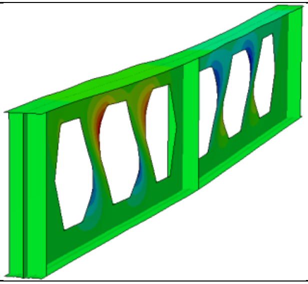	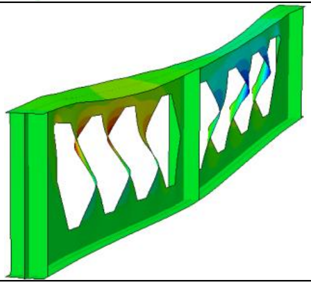

Source: The author (2025).

Figure 6.9 shows the effect of the I-section dimensions (**Table 6.3** and **Table 6.4**) and its steel yield strength (f_y) on the models' ultimate moment (M_u). The nomenclatures of each parent profile varying from "1" to "6" are detailed in **Table 6.3**. For all models, a higher M_u was obtained with the increasing in f_y, regarding the same parent profile and opening patterns of the castellated beams (**Figure 6.9**). In addition, the effect of the f_y variation on the M_u was higher for the castellated beams with greater I-section dimensions for all opening patterns (**Figure 6.9a-c**). Using W310x21 and W310x23.8 I-sections (profiles 1 and 2) in the composite castellated beams, the influence of the f_y variation on the M_u was significantly lower than utilizing the other I-sections. This occurrence is due to the considerably lower cross-section dimensions of the profiles 1 and 2. Despite the f_y varying from 355MPa to 960MPa, the plastic moment of the composite cross-section (M_{pl}) using these profiles varies in a lower proportion than the other parent I-sections. The parent profiles (**Table 6.3**) named from "1" to "6" are also in the sequence from the lowest to the highest moments of inertia about the strong axis (I_x), which is the same sequence for the respective castellated I-sections. In addition, the M_{pl} of the composite castellated beams keeps this same sequence, varying the parent profiles. This way, the M_u increased with the parent profile variation from 1 to 6 in most cases of **Figure 6.9**. The only exception occurred for the models with the combination of profile 5 (W410x38.8), Peiner pattern, and f_y= 460-960MPa (**Figure 6.9b**), which had lower M_u values than those with the profile 4 (W360x39). The castellated beams with parent profile 5 (W410x38.8) present the highest h_w/t_w ratio (**Table 6.4**), which characterized a more critical case to the WPB occurrence in the LDB-WPB interaction. Therefore, despite their higher I_x and M_{pl}, the reached shear loads were critical for the WPB phenomenon in these models with profile 5, and the WPB occurrence was less critical for the ones with profile 4.

Figure 6.9: The effect of the I-section (Table 6.3 and Table 6.4) and its steel yield strength on the models' ultimate moment.

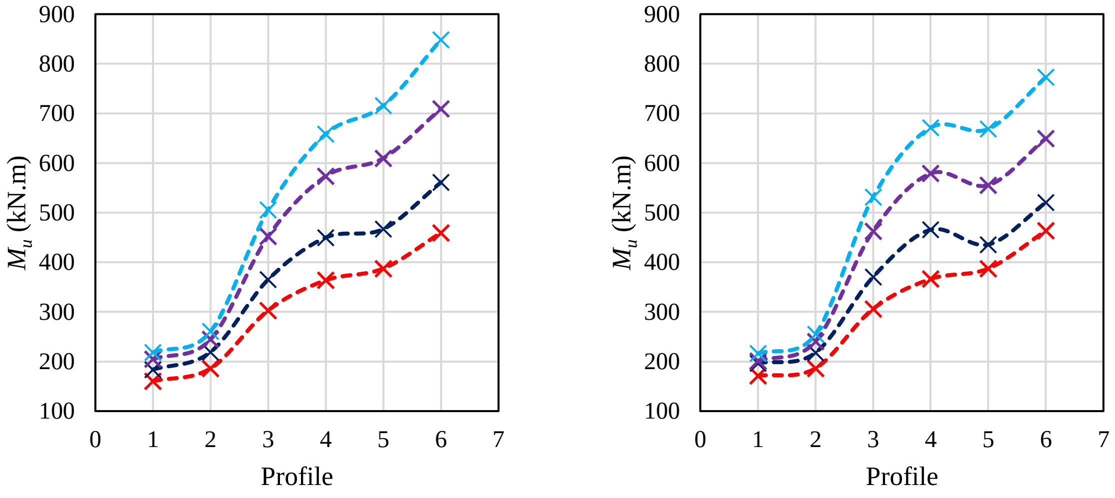

(a) Litzka

(b) Peiner

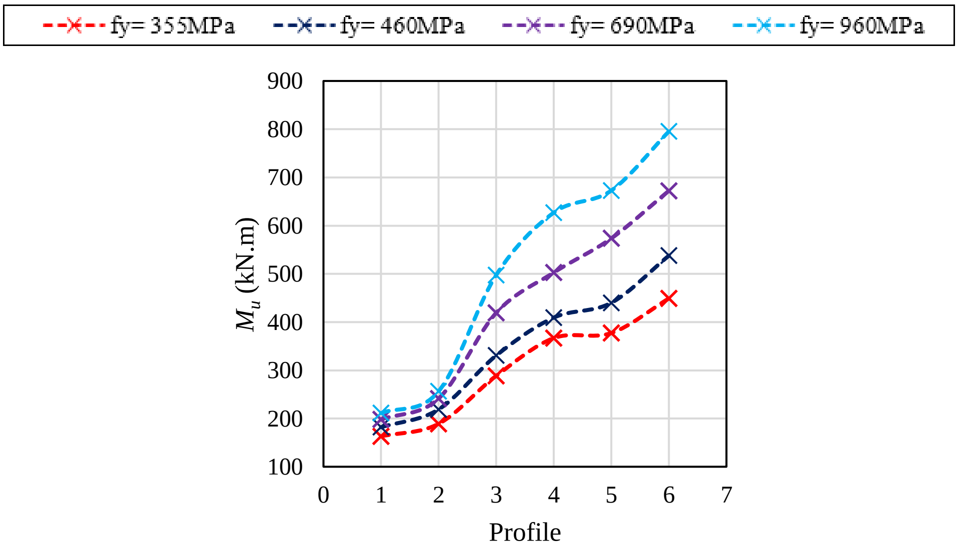

(c) Anglo-Saxon
Source: The author (2025).

Figure 6.10 presents the influence of the castellated beams' opening pattern (**Table 6.4**) on the models' ultimate moment (M_u). A clear trend on the M_u values with the opening pattern variation was not observed. It is noted that the M_u of the models was less sensitive to the opening pattern using f_y= 355MPa (**Figure 6.10a**). At the same time, those with higher f_y values were more sensitive to the opening pattern variation (**Figure 6.10b-d**), except the ones with profiles 1 and 2. This is because the models with profiles 3-6 and HSS reached higher M_u values and, consequently, higher shear loads, which were critical to the WPB occurrence. Therefore, this higher sensitivity for these castellated beams is due to the WPB phenomenon, which is significantly influenced by the opening and web-post geometry. Even though the web-post width (b_w) affects the WPB resistance of alveolar beams, the width of the web-post at the end (b_{we}) also considerably influences this instability mode (FERREIRA *et al.*, 2021b; FERREIRA; MARTINS; NARDIN, 2021; OLIVEIRA *et al.*, 2022, 2023b). This way, the M_u values obtained by the models with profiles 3-6 and HSS (**Figure 6.10b-d**) presented the same trend of the b_{we} variation (**Table 6.4**), in which those with higher b_{we} values had higher M_u.

Figure 6.10: The effect of the castellated beams' opening pattern (Table 6.4) on the models' ultimate moment.

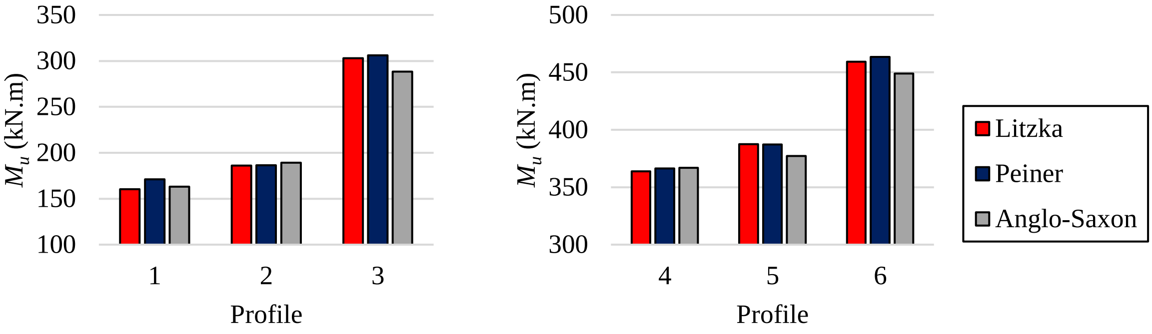

(a) f_y= 355MPa

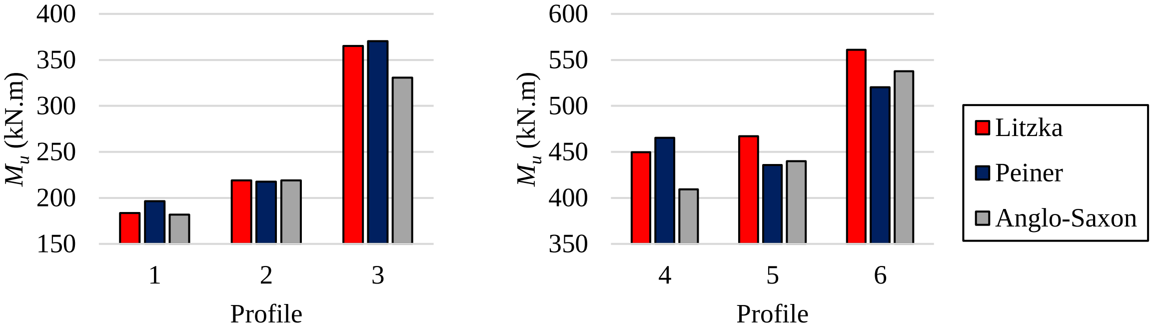

(b) f_y= 460MPa

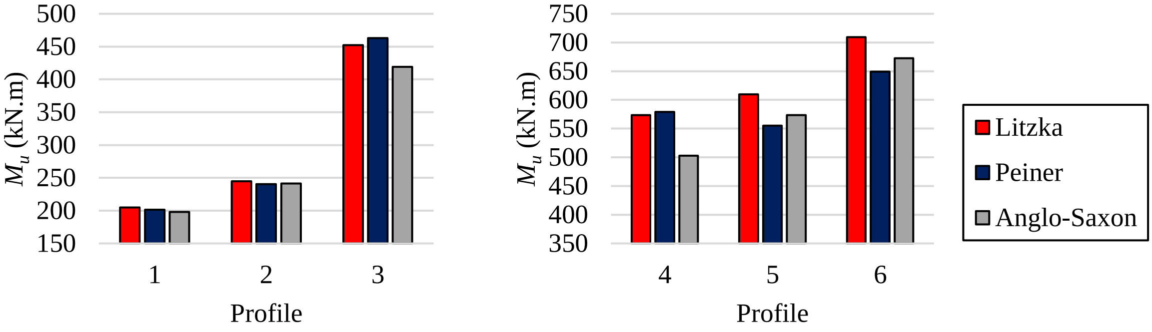

(c) f_y= 690MPa

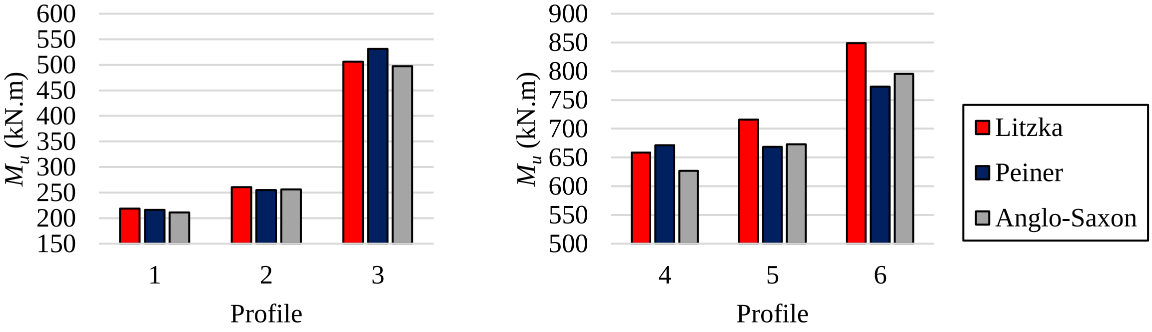

(d) f_y= 960MPa

Source: The author (2025).

6.3.1.3 Part 3: The influence of the concrete slab and longitudinal reinforcement bars

All composite castellated beams assessed in this part of the study have the following geometry parameters and material properties:

- W360x39 parent I-section;
- d_g/d= 1.5;
- Litzka opening pattern.

Meanwhile, the following parameters were varied in this part:

- f_y= 355 and 460MPa;
- ϕ= 8, 10 and 12.5mm;
- $f_{y\text{-}bar}$= 500 and 700Pa;
- h_s= 75 and 100mm;
- For the slab with h_s= 100mm, NC and UHPC were used;
- For the slab with h_s= 75mm, only UHPC was used.

Table 6.9 shows the instability modes characterized by the models in the parametric study's part 3. It is noted that all models characterized the LDB-WPB interaction, in which the deformations by WPB were not accentuated, as can be observed in **Table 6.8** for the model with the Litzka pattern and W360x39-S460 steel I-section. This way, the variation of the slab parameters, such as ϕ, $f_{y\text{-}bar}$, f_{ck}, and h_s, did not affect the failure mode of the models.

Table 6.9: Instability modes obtained in the parametric study's part 3.

f_y (MPa)	$f_{y\text{-}bar}$ (MPa)	Concrete slab	h_s (mm)	Instability modes		
				ϕ= 8mm	ϕ= 10mm	ϕ= 12.5mm
355	500	NC	100	LDB + WPB	LDB + WPB	LDB + WPB
		UHPC	100	LDB + WPB	LDB + WPB	LDB + WPB
			75	LDB + WPB	LDB + WPB	LDB + WPB
	700	NC	100	LDB + WPB	LDB + WPB	LDB + WPB
		UHPC	100	LDB + WPB	LDB + WPB	LDB + WPB
			75	LDB + WPB	LDB + WPB	LDB + WPB
460	500	NC	100	LDB + WPB	LDB + WPB	LDB + WPB
		UHPC	100	LDB + WPB	LDB + WPB	LDB + WPB
			75	LDB + WPB	LDB + WPB	LDB + WPB
	700	NC	100	LDB + WPB	LDB + WPB	LDB + WPB
		UHPC	100	LDB + WPB	LDB + WPB	LDB + WPB
			75	LDB + WPB	LDB + WPB	LDB + WPB

Source: The author (2025).

Figure 6.11 presents the influence of the longitudinal reinforcement bars' diameter (ϕ) and their steel yield strength ($f_{y\text{-}bar}$) on the hogging moment-deflection curves of the models with f_y= 355MPa, in which those with f_y= 460MPa obtained a similar behavior varying the analyzed parameters. For all combinations of concrete strength and slab height, the initial bending stiffness was unaffected by the ϕ and $f_{y\text{-}bar}$ variations (**Figure 6.11a-c**). In addition, the M_u values had a maximum increase of 0.7% with the $f_{y\text{-}bar}$ variation from 500MPa to 700MPa. The M_u of the models with NC and h_s= 100mm had an increase of 1.3% with the ϕ variation from 8mm to 10mm, and the ones with ϕ= 10 and 12.5mm had a lower divergence on the M_u values (**Figure 6.11a**). Meanwhile, the models with UHPC and h_s= 100 and 75mm (**Figure 6.11b-c**) had an increase of around 1.7-2.3% in the M_u with the ϕ variation from 8mm to 10mm and from 10mm to 12.5mm. This way, it is noted that the longitudinal reinforcement bars' ϕ and $f_{y\text{-}bar}$ did not significantly influence the initial bending stiffness and M_u of the models.

Figure 6.11: Influence of the longitudinal reinforcement bars on the moment-deflection curves of the models with f_y= 355MPa.

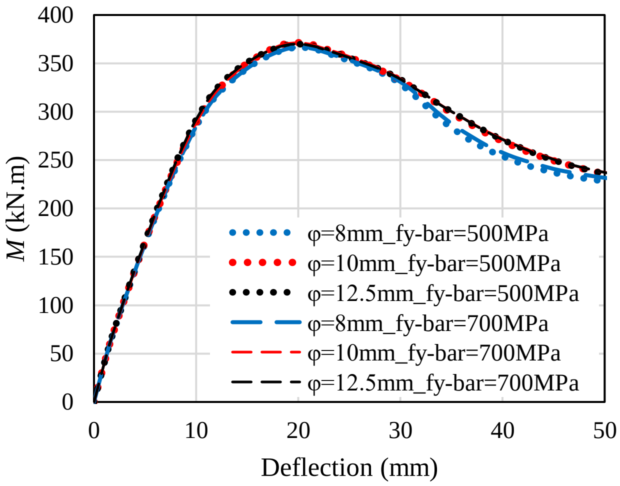

(a) Slab with NC and h_{slab}= 100mm

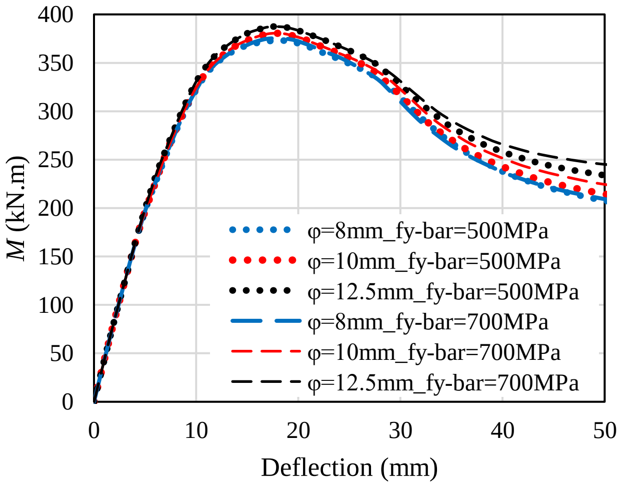

(b) Slab with UHPC and h_{slab}= 100mm

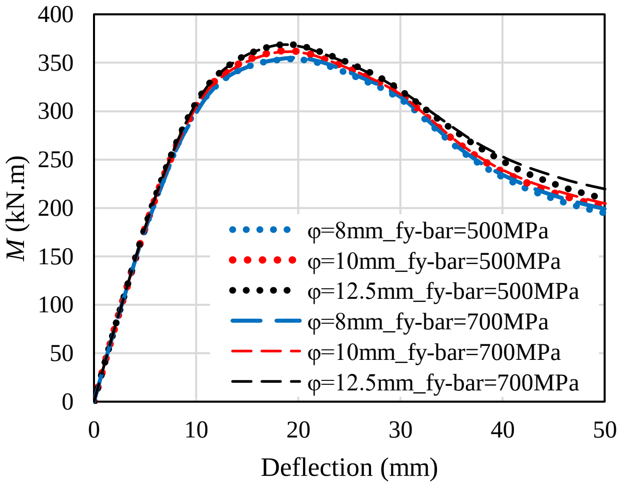

(c) Slab with UHPC and h_{slab}= 75mm
Source: The author (2025).

Figure 6.12 shows the influence of the concrete and slab height (h_s) on the hogging moment-deflection curves of the models with f_y= 355MPa, in which those with f_y= 460MPa presented a similar response varying the analyzed parameters. Comparing the composite castellated beams with h_s= 100mm, those with UHPC obtained gains in the initial bending stiffness and M_u concerning NC for all models (**Figure 6.12a-c**). For the models in question, the gains in the M_u using the UHPC were 1.8%, 2.4%, and 4.8% for the ones with ϕ= 8, 10, and 12.5mm (**Figure 6.12a-c**), respectively. This way, the gains in the M_u adopting UHPC instead of NC were not elevated, and these gains increase with the ϕ increasing. As stated in the discussions of the experimental results (**section 4.2**), the main role of UHPC in composite castellated beams under hogging bending is controlling cracking for the service limit stage, which evidenced the cracking localization after multiple cracking in UHPC. These statements were also observed in studies of steel-UHPC composite beams with solid I-sections, as shown in the literature review (**section 2.2.2**).

Another analysis is regarding a possible dematerialization of the slab cross-section, reducing its h_s by using UHPC instead of NC and seeking to keep a similar bearing capacity of the composite beams. Comparing the combinations NC-h_s= 100mm and UHPC-h_s= 75mm (**Figure 6.12a-c**), the ones with UHPC-h_s= 75mm obtained a slightly higher initial bending stiffness than those with NC-h_s= 100mm, even with the reduction of 33.3% in the h_s. On the other hand, the models with UHPC-h_s= 75mm had slightly lower M_u values than those with NC-h_s= 100mm, in which their divergences decreased with the ϕ increasing. The divergences in the M_u values were 3.6%, 2.5%, and 0.2% for the models with ϕ= 8, 10, and 12.5mm (**Figure 6.12a-c**), respectively. These divergences in the M_u values were not significant. Therefore, continuous composite castellated beams with sagging and hogging moment regions can reduce the concrete consumption of the slab using UHPC, as the composite beams in the sagging moment regions can present considerable gains due to the slab being under compression. At the same time, the hogging moment regions can maintain an appropriate hogging bending performance adopting UHPC, mainly regarding slab cracking.

Figure 6.12: Moment-deflection curves using f_y= 355MPa, slabs of NC with h_s= 100mm and of UHPC with h_s= 75 and 100mm.

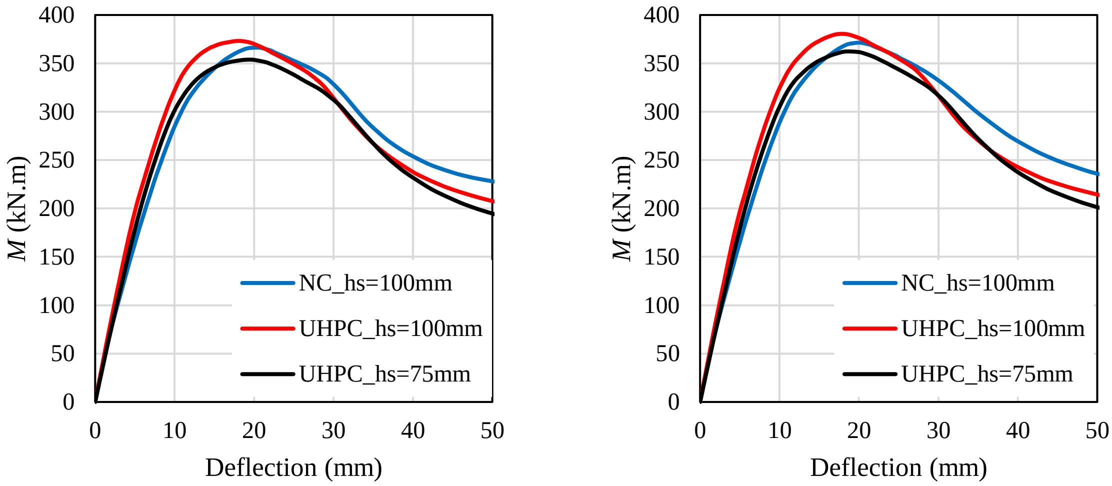

(a) ϕ= 8mm and $f_{y\text{-}bar}$= 500MPa (b) ϕ= 10mm and $f_{y\text{-}bar}$= 500MPa

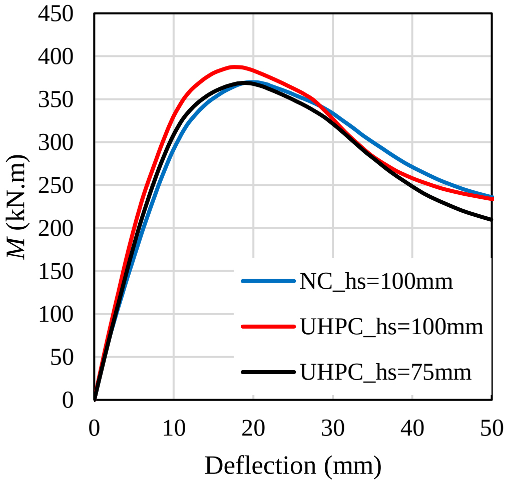

(c) ϕ= 12.5mm and $f_{y\text{-}bar}$= 500MPa
Source: The author (2025).

6.3.1.4 Dematerialization of conventional composite beams

This part of the parametric study assesses some possibilities for dematerializing conventional NSS-NC composite beams of solid I-sections using HSS castellated I-sections and UHPC. Therefore, five conventional composite beams were adopted for this analysis, varying only the solid I-section, in which these composite beams have the following parameters:

- Solid I-sections: W360x32.9, W360x44.6, W360x51, W410x60, and W410x52 (**Table 6.10**);
- f_y= 355MPa (S355 steel);

- Slab with NC (f_{ck}= 30MPa) and h_s= 100mm;
- Longitudinal reinforcement bars with ϕ= 10mm and $f_{y\text{-}bar}$= 500MPa.

Table 6.10: Solid I-sections adopted for the conventional composite beams.

I-section	Linear mass (kg/m)	d (mm)	b_f (mm)	t_w (mm)	t_f (mm)
W360x32.9	32.9	349	127	5.8	8.5
W360x44.6	44.6	352	171	6.9	9.8
W360x51	51.0	355	171	7.2	11.6
W410x60	60.0	407	178	7.7	12.8
W460x52	52.0	450	152	7.6	10.8

Source: The author (2025).

As previously described, the final numerical model (**section 5.2**) was also validated against the tests conducted by Tong *et al*. (2014), which assessed steel-NC composite beams with solid I-sections under hogging moment. This validation is presented by Oliveira *et al*. (2025), in which the residual stress pattern of Galambos and Ketter (1959) and the geometric imperfection value of L/1000 were incorporated, following Rossi *et al*. (2020b, 2021b, 2021c, 2023). These considerations were also applied in the study for conventional composite beams of solid I-sections.

Firstly, the flexural performance of these conventional composite beams was compared with that of the NSS-NC and HSS-NC composite castellated beams addressed in **sections 6.3.1.1–6.3.1.3**. Posteriorly, some composite castellated beams were adopted to apply a thinner slab with UHPC. Only the castellated I-sections with d_g/d= 1.5 (**Table 6.4**) were considered in this part of the study. The criteria determined in sequence for the analyses of the possibilities of dematerialization of conventional composite beams are presented below:

1) For the I-section dematerialization, only the composite castellated beams using parent I-sections with lower linear mass (**Table 6.3**) than the solid I-section of the conventional composite beam under analysis (**Table 6.10**) were considered;
2) The composite castellated beams that exhibited similar initial bending stiffness compared to the conventional beams were analyzed;
3) The composite castellated beams with the lowest f_y value for each analyzed parent I-section (following criteria number 2) and that obtained equal or higher M_u compared to the conventional beams were selected for applying thinner slabs with UHPC. For this criterion, a tolerance in M_u values up to 5% lower than the conventional beam was considered;

4) The composite castellated beams with thinner slabs and UHPC that maintained an appropriated hogging bending performance concerning the conventional composite beam, following the previous criteria, are considered as a possibility for the dematerialization of these structures.

The possibilities explored for dematerializing the conventional composite beams are presented below. As a simplification, the reduction in steel consumption is verified by the ratio between the linear mass of the solid I-section (**Table 6.3**) and the castellated beam's parent profile (**Table 6.10**). Meanwhile, the reduction in concrete consumption is assessed by the slab height (h_s) ratio of NC about UHPC ($h_{s\text{-}NC}/h_{s\text{-}UHPC}$). Finally, general comments on the observed possibilities for the dematerialization are brought.

Figures 6.13-6.14 show the I-section lateral displacements (in mm) regarding the ultimate moment of the conventional composite beams and steel-UHPC composite castellated beams, respectively. As noted in **Figure 6.13**, the conventional composite beam's ultimate moment was limited by LDB coupled with local buckling (LB) in the flange and web, in which the lateral displacements were up to 5mm. Meanwhile, the steel-UHPC composite castellated beams reached the ultimate moment by the LDB-WPB interaction (**Figure 6.14**), in which the lateral displacements were up to 36mm. In some cases, the WPB was slightly characterized, while in others, it was more accentuated by the same reasons previously discussed in **sections 6.3.1.1-6.3.1.2**. This way, the steel-UHPC composite castellated beam presented higher lateral displacements before reaching the peak load than the conventional composite beam. This occurrence is due to higher local web slenderness (h_w/t_w) and lower flange dimensions (b_f and t_f) of the castellated I-section, contributing to its higher susceptibility to LDB occurrence (**Figure 6.14**), also resulting in a higher susceptibility to WPB due to the higher h_w/t_w ratios. In contrast, the solid I-section has lower h_w and higher t_w, resulting in lower local web slenderness (h_w/t_w), which makes it less susceptible to the LDB phenomenon (**Figure 6.13**), as the flexural rigidity of the profile web is an essential parameter of the LDB resistance (ROSSI *et al.*, 2020b). In addition, the solid I-section has higher flange dimensions (b_f and t_f), providing a lower propensity to LDB occurrence than the castellated I-section. As these solid profiles are compact I-sections, according to ABNT NBR 8800:2024, they are also not critical regarding the flange and web local buckling.

Figure 6.13: I-section lateral displacements (in mm) regarding the ultimate moment of the conventional composite beams with solid I-sections (deformation scale factor= 2).

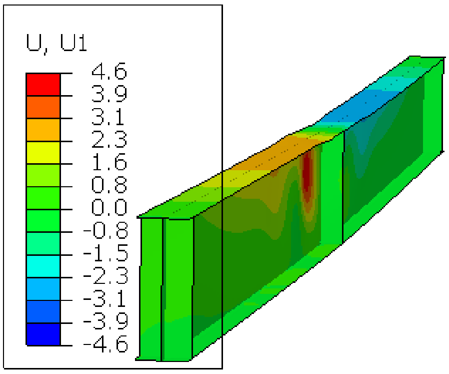

(a) Solid W360x32.9-S335 I-section

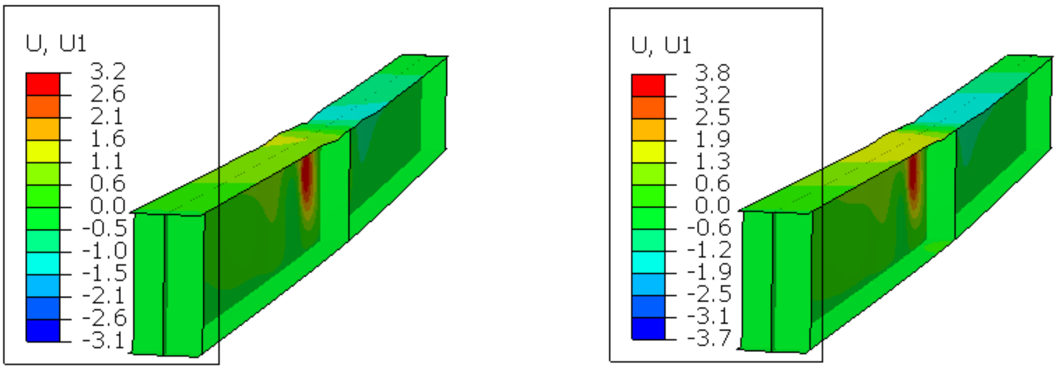

(b) Solid W360x44.6-S335 I-section

(c) Solid W360x51-S335 I-section

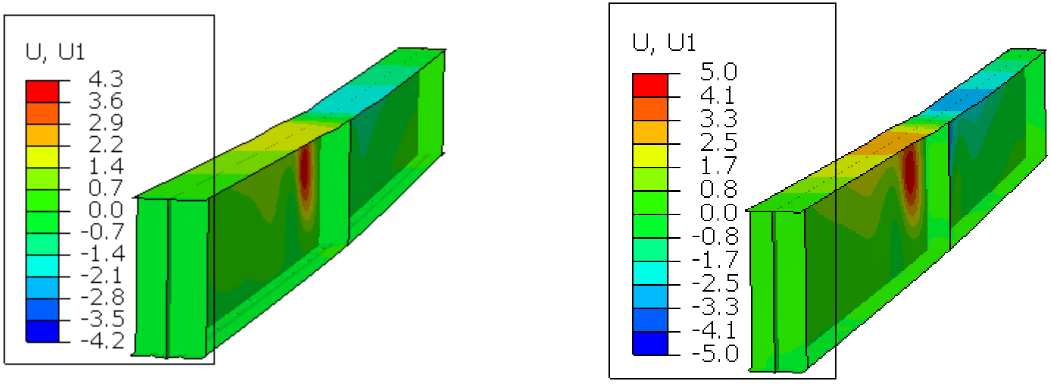

(d) Solid W410x60-S335 I-section

(e) Solid W460x52-S335 I-section

Source: The author (2025).

Figure 6.14: I-section lateral displacements (in mm) regarding the ultimate moment of the steel-UHPC composite castellated beams (deformation scale factor= 2).

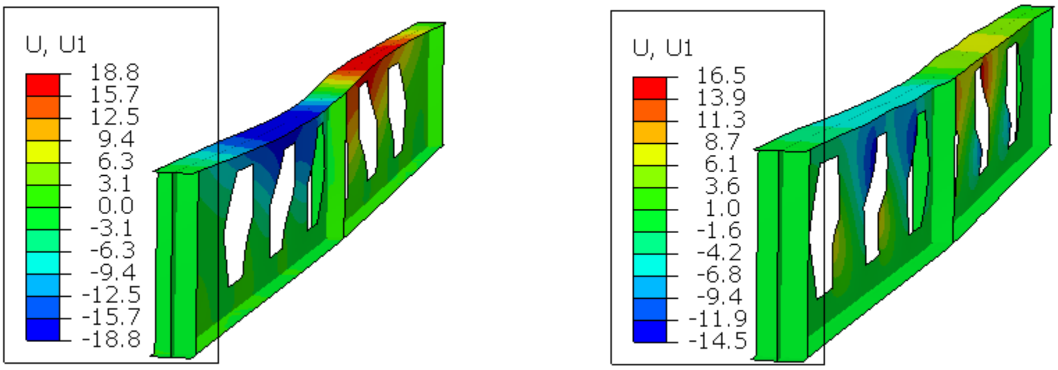

(a) Castellated W310x23.8-S690 I-section with the Litzka pattern

(b) Castellated W360x32.9-S460 I-section with the Litzka pattern

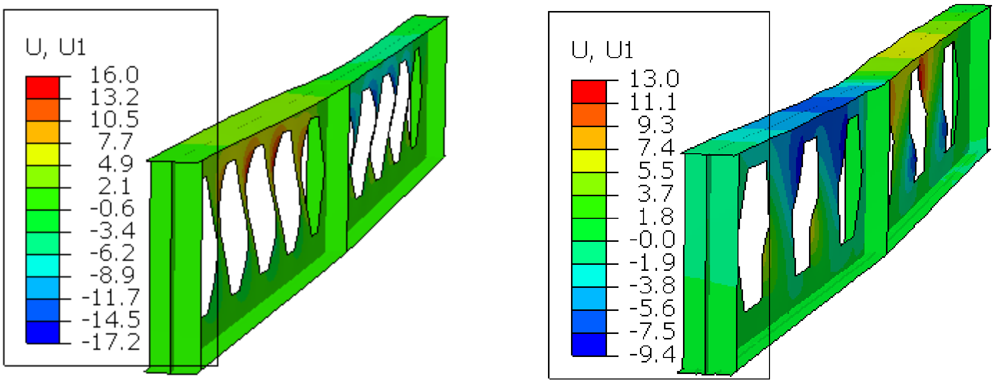

(c) Castellated W360x32.9-S460 I-section with the Anglo-Saxon pattern

(d) Castellated W360x39-460 I-section with the Litzka pattern

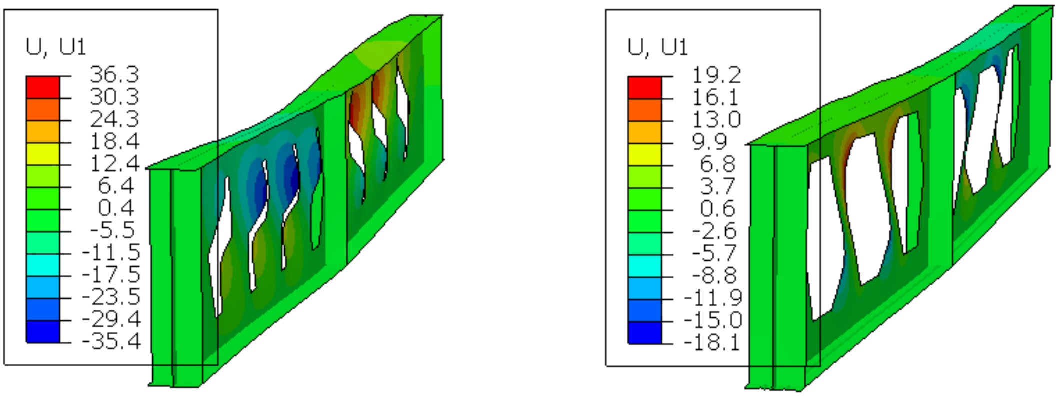

(e) Castellated W410x38.8-S690 I-section with the Anglo-Saxon pattern

(e) Castellated W410x46.1-S460 I-section with the Peiner pattern

Source: The author (2025).

Figures 6.15-6.23 show the moment-deflection curves obtained by the conventional composite beam with solid I-sections and the steel-NC and steel-UHPC composite castellated beams, which had similar initial bending stiffness and slight divergences in the ultimate moments. In **Figures 6.15a-6.23a**, all composite beams have slabs with NC and h_s= 100mm, focusing only on the dematerialization of the steel I-section. Subsequently, some steel-NC composite castellated beams were adopted to apply a thinner slab (h_s= 75mm) with UHPC, as shown in **Figures 6.15b-6.23b**. Following, the discussions on the flexural performance of these beams and the possibilities for dematerialization are presented.

Figure 6.15 compares the moment-deflection curves obtained by the conventional composite beam with solid W360x32.9-S355 I-section and the composite castellated beams with W310x23.8-S690 parent I-section. As noted in **Figure 6.15a**, all HSS-NC composite castellated beams (Litzka, Peiner, and Anglo-Saxon) presented similar initial bending stiffness and M_u concerning the conventional NSS-NC composite beam, in which the composite castellated beams obtained a slightly lower initial stiffness and higher M_u. Given this, it is possible to reduce the steel consumption while the initial stiffness and bearing capacity are maintained regarding the composite beam analyzed. This approach diminishes the steel consumption of the solid W360x32.9-S355 I-section using a castellated beam with a W310x23.8-S690 parent I-section by 38.2%. In addition, the castellated beams begin to support less load than the solid beam only after reaching a deflection of 20 mm, which concerns the L/200 ratio, as the span length of the composite beams is equal to 4m (**Figure 6.6**). This way, even with the I-section dematerialization, the composite castellated beams maintained the ductility until a deflection of 20mm (L/200 ratio), not showing elevated divergences in the supported loads for deflections higher than 20mm. **Figure 6.15a** shows that the HSS-NC composite castellated beam with the Litzka pattern had a slightly higher ductility than the ones with Peiner and Anglo-Saxon patterns. Given this, the model with the Litzka pattern was adopted to apply a thinner slab (h_s= 75mm) with UHPC, as shown in **Figure 6.15b**. Regarding the conventional NSS-NC composite beam, the HSS-UHPC composite castellated beam (**Figure 6.15b**) had a higher agreement in the initial bending stiffness than the HSS-NC composite castellated beams (**Figure 6.15a**). Therefore, even with the concrete slab dematerialization, reducing the concrete consumption by 33.3%, the initial stiffness was slightly enhanced using UHPC. In addition, the bearing capacity and significant ductility were maintained.

Figure 6.15: Conventional composite beam with solid W360x32.9-S355 I-section, HSS-NC and HSS-UHPC composite beams with castellated W310x23.8-S690 I-section.

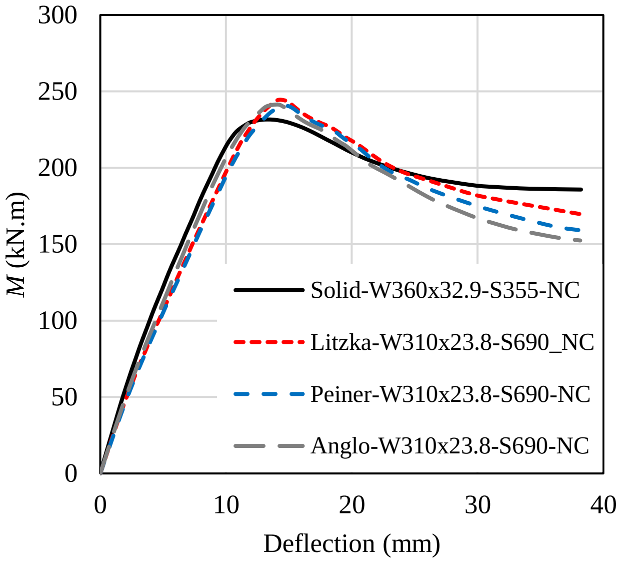

(a) NC slab with h_s= 100mm

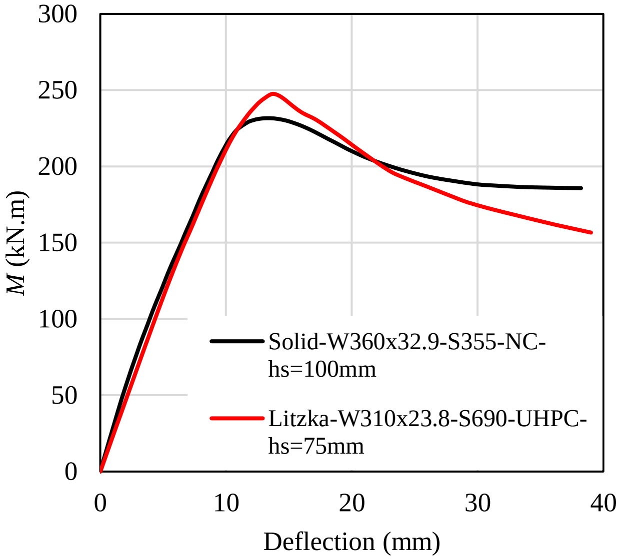

(b) NC slab with h_s= 100mm and UHPC slab with h_s= 75mm
Source: The author (2025).

Figures 6.16-6.17 compare the moment-deflection curves of the conventional composite beam with solid W360x44.6-S355 I-section and the composite castellated beams with W360x32.9-S460 and W360x39-S355 parent I-sections. Regarding the composite castellated beams with W360x32.9-S460 parent I-sections addressed in **Figure 6.16a**, all beams (Litzka, Peiner, and Anglo-Saxon) presented similar initial bending stiffness compared to the conventional NSS-NC composite beam (**Figure 6.16a**). The models with Litzka and Peiner patterns had M_u values of 9.5% and 11.1%, respectively, higher than the conventional composite beam. In contrast, the castellated beam with the Anglo-Saxon pattern had a M_u value of 0.8% lower than the conventional one, which is not a significant divergence. Among the castellated beams addressed in **Figure 6.16a**, the one with the Anglo-Saxon pattern presented a critical WPB occurrence due to its considerably lower web-post width (b_w), resulting in a lower M_u value concerning the other opening patterns. As noted in **Figure 6.16a**, after the conventional composite beam reached the peak, the castellated beam with the Anglo-Saxon pattern supported higher loads, showing significantly higher ductility than the conventional one. Meanwhile, the castellated beams with the Litzka and Anglo-Saxon patterns began to support less load than the solid beam only after reaching a deflection of around 30 mm, in which the Litzka beam had a slightly higher ductility than the Peiner one. Given this, the models with the Litzka and Anglo-Saxons pattern (**Figure 6.16a**) were adopted to apply a thinner slab (h_s= 75mm) with UHPC, as shown in **Figure 6.16b**.

As observed in **Figure 6.16**, the HSS-UHPC composite castellated beam (**Figure 6.16b**) had a slightly higher initial bending stiffness than the HSS-NC composite castellated beams (**Figure 6.16a**). This way, even with a considerably lower slab height, using UHPC, the initial stiffness was slightly enhanced, and the bearing capacity and the appropriate ductility behavior were maintained for both castellated beams with Litzka and Anglo-Saxon patterns (**Figure 6.16b**). The Litzka beam provided a higher M_u value, an option in favor of security (**Figure 6.16b**). Meanwhile, the Anglo-Saxon beam had a similar M_u value to the conventional beam and supported higher loads in almost the whole post-peak range. This way, using a castellated W360x32.9 I-section and S460 high-strength steel diminishes the steel consumption of the solid W360x44.6-S355 I-section by 35.6%, and the use of UHPC made it possible to reduce the concrete consumption by 33.3%, maintaining the hogging bending performance concerning the analyzed conventional NSS-NC composite beam (**Figure 6.16b**).

Figure 6.16: Conventional composite beam with solid W360x44.6-S355 I-section, HSS-NC and HSS-UHPC composite beams with castellated W360x32.9-S460 I-section.

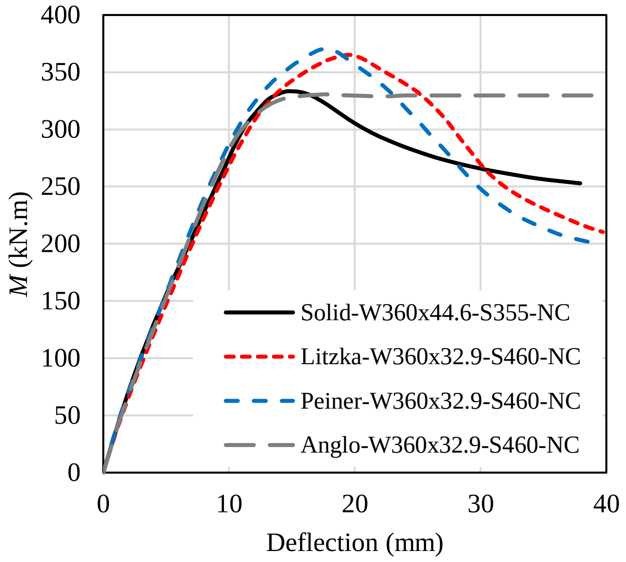

(a) NC slab with h_s= 100mm

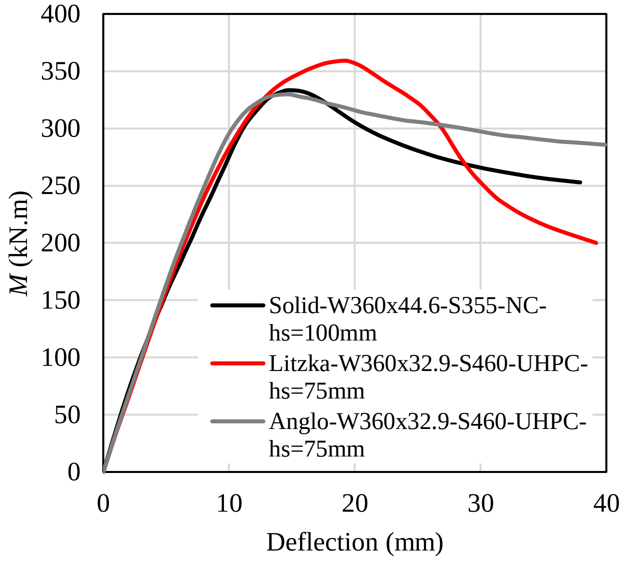

(b) NC slab with h_s= 100mm and UHPC slab with h_s= 75mm
Source: The author (2025).

As noted in **Figure 6.17a**, all composite castellated beams had similar M_u values, which were around 9-10% higher than the conventional composite beam's M_u, and ductility was also higher for the castellated ones. The initial bending stiffness of the castellated beams was slightly higher than that of the conventional beam. Regarding the castellated beams, those with the Litzka and Peiner patterns characterized a similar LDB-WPB interaction in which the WPB phenomenon was not accentuated, resulting in a similarity between their moment-deflection curves (**Figure 6.17a**). On the other hand, the WPB occurrence was more intensive in the Anglo-Saxon beam due its lower web-post width.

Figure 6.17: Conventional composite beam with solid W360x44.6-S355 I-section, steel-NC and steel-UHPC composite beams with castellated W360x39-S355 I-section.

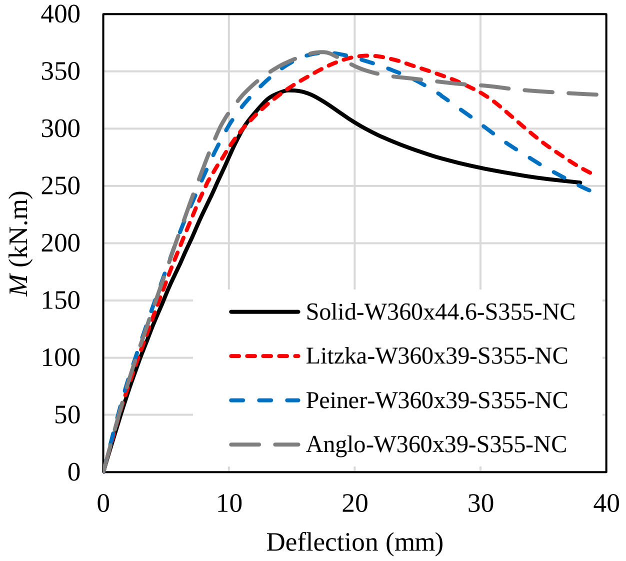

(a) NC slab with h_s= 100mm

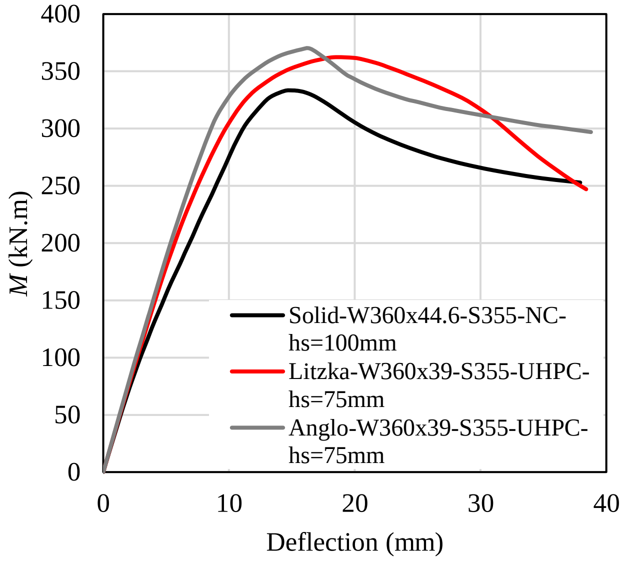

(b) NC slab with h_s= 100mm and UHPC slab with h_s= 75mm

Source: The author (2025).

The composite castellated beams with the Litzka and Anglo-Saxons pattern (**Figure 6.17a**) were adopted to apply a thinner slab (h_s= 75mm) with UHPC, as presented in **Figure 6.17b**. Significant divergences were not obtained between the moment-deflection curves of the composite castellated beams with NC-h_s= 100mm and UHPC-h_s=75mm, and those with UHPC had a slightly enhanced initial bending stiffness. Given this, adopting UHPC made it possible to reduce the concrete consumption by 33.3%, maintaining the hogging bending performance regarding the analyzed conventional NSS-NC composite beam (**Figure 6.17b**). Additionally, there was a 14.4% reduction in I-section steel consumption using only the I-section web expansion approach, as both solid and castellated beams analyzed in this case were made of S355 normal-strength steel.

Figures 6.18-6.19 compare the moment-deflection curves of the conventional composite beam with solid W360x51-S355 I-section and the composite castellated beams with W360x32.9-S690 and W360x39-S460 parent I-sections. The castellated beams addressed in **Figures 6.18-6.19** obtained similar trends in the moment-deflection curves concerning those analyzed in **Figures 6.16-6.17**, respectively. The composite castellated beams assessed in **Figures 6.16** and **6.18** have the W360x32.9 parent I-section, while those addressed in **Figures 6.17** and **6.19** have the W360x39 parent profile, only changing their f_y in both cases.

As noted in **Figure 6.18a**, the HSS-NC composite castellated beams with W360x32.9-S690 I-parent section had a slightly lower initial bending stiffness than the conventional composite beam. On the other hand, the castellated ones had higher M_u values, presenting a higher ductility than the conventional composite beam. The castellated beams with the Litzka and Anglo-Saxons pattern (**Figure 6.18a**) were adopted to apply a thinner slab (h_s= 75mm) with UHPC, as shown in **Figure 6.18b**. Regarding the conventional NSS-NC composite beam, the HSS-UHPC composite castellated beams (**Figure 6.18b**) had a higher agreement in the initial bending stiffness than the HSS-NC composite castellated beams (**Figure 6.18a**). This way, the initial stiffness was slightly enhanced using UHPC even with the concrete slab dematerialization, reducing the concrete consumption by 33.3%. HSS-UHPC composite castellated beams with the Litzka and Anglo-Saxon patterns (**Figure 6.18b**) supported higher loads in almost the whole post-peak range of the conventional composite beam. In addition, these castellated beams with the Litzka and Anglo-Saxon patterns had M_u values of 11.5% and 2.5% higher than the conventional composite beam, respectively. Therefore, adopting a castellated W360x32.9 I-section and S690 high-strength steel reduces the steel consumption of the solid W360x51-S355 I-section by 55%, maintaining the hogging bending performance regarding the assessed conventional NSS-NC composite beam (**Figure 6.18b**).

Figure 6.18: Conventional composite beam with solid W360x51-S355 I-section, HSS-NC and HSS-UHPC composite beams with castellated W360x32.9-S690 I-section.

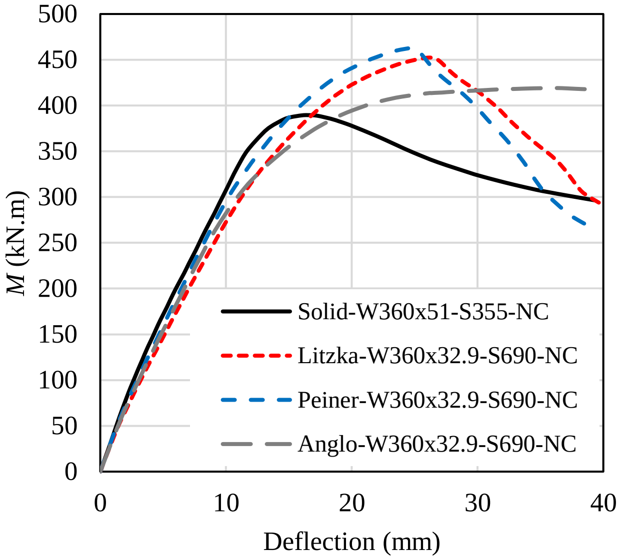

(a) NC slab with h_s= 100mm

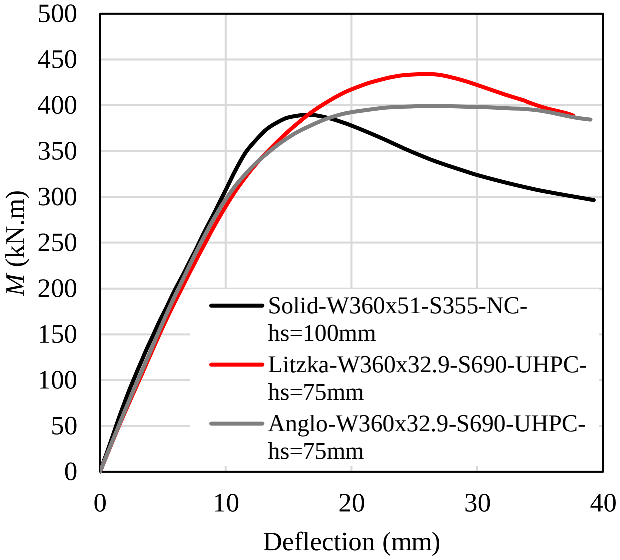

(b) NC slab with h_s= 100mm and UHPC slab with h_s= 75mm
Source: The author (2025).

According to **Figure 6.19a**, the composite castellated beams with the Litzka, Peiner, and Anglo-Saxon patterns had M_u values of 15.5%, 19.5%, and 5.1% higher than the conventional composite beam's M_u. The Anglo-Saxon was more critical to the WPB occurrence due to its lower web-post width, which limited its bearing capacity. In addition, the castellated and conventional beams had similar initial bending stiffness.

Figure 6.19: Conventional composite beam with solid W360x51-S355 I-section, HSS-NC and HSS-UHPC composite beams with castellated W360x39-S460 I-section.

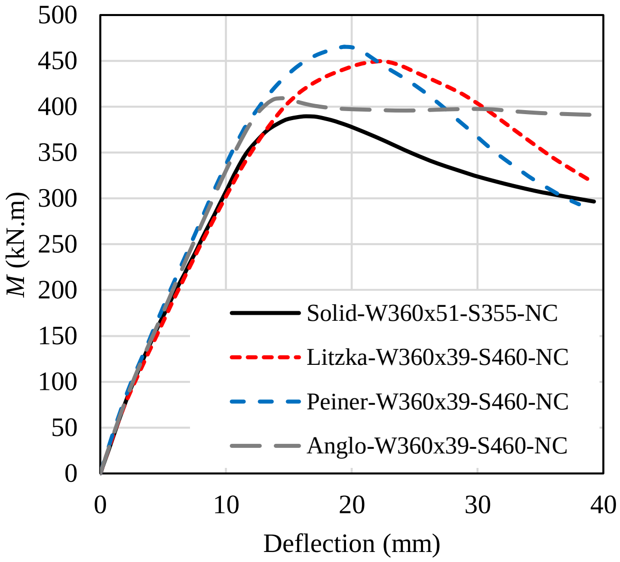

(a) NC slab with h_s= 100mm

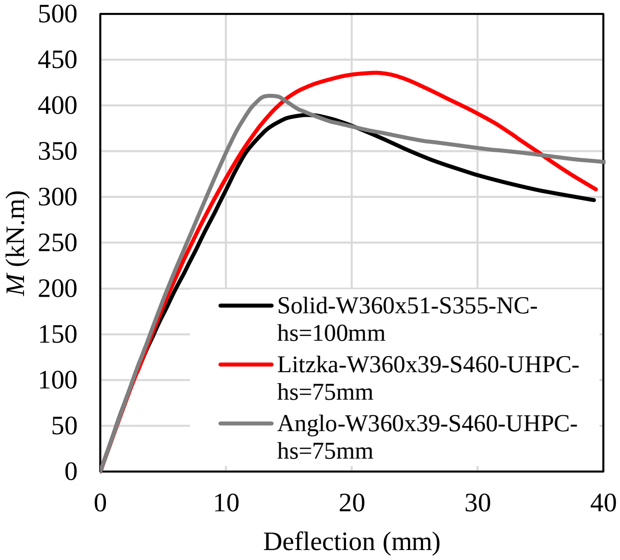

(b) NC slab with h_s= 100mm and UHPC slab with h_s= 75mm

Source: The author (2025).

The composite castellated beams with the Litzka and Anglo-Saxons pattern (**Figure 6.19a**) were also assessed with a thinner slab (h_s= 75mm) with UHPC, as shown in **Figure 6.19b**. As noted in **Figure 6.19**, the composite castellated beams with the slab of UHPC-h_s=75mm (**Figure 6.19b**) had slightly enhanced initial bending stiffness compared to those with NC-h_s=100 mm (**Figure 6.19a**). In addition, significant divergences were not observed between the moment-deflection curves of the composite castellated beams with both analyzed type slabs

(**Figure 6.19a-b**), in which the HSS-UHPC composite castellated beams also had higher M_u values and appropriated ductility behavior concerning the conventional NSS-NC composite beam (**Figure 6.19b**). As a result, the use of UHPC enabled a 33.3% reduction in concrete consumption while preserving the hogging bending performance compared to the analyzed conventional NSS-NC composite beam. Furthermore, utilizing the S460 high-strength steel and the I-section web expansion method in a W360x39 parent I-section led to a 30.8% decrease in steel consumption for I-sections concerning the solid W360x51-S355 profile.

Figures 6.20-6.21 compare the moment-deflection curves of the conventional composite beam with solid W410x60-S355 I-section and the composite castellated beams with W410x38.8-S690 and W410x46.1-S460 parent I-sections. As observed in **Figure 6.20a**, the HSS-NC composite castellated beams with W410x38.8-S690 parent I-section had a slightly lower initial bending stiffness than the conventional composite beam. At the same time, the castellated beams had higher M_u values. Regarding the loads supported by the conventional one after the peak, the castellated beams also supported higher loads in the same deflection range. The castellated beams with the Liztka and Peiner patterns presented similar trends in the moment-deflection curves (**Figure 6.20a**). On the other hand, the Anglo-Saxon beam diverged from the other opening patterns, as this beam was more critical for the WPB occurrence due to its lower web-post width (**Figure 6.20a**). The castellated beams with the Litzka and Anglo-Saxon patterns were adopted to apply a thinner slab (h_s= 75mm) with UHPC (**Figure 6.20b**).

Figure 6.20: Conventional composite beam with solid W410x60-S355 I-section, HSS-NC and HSS-UHPC composite beams with castellated W410x38.8-S690 I-section.

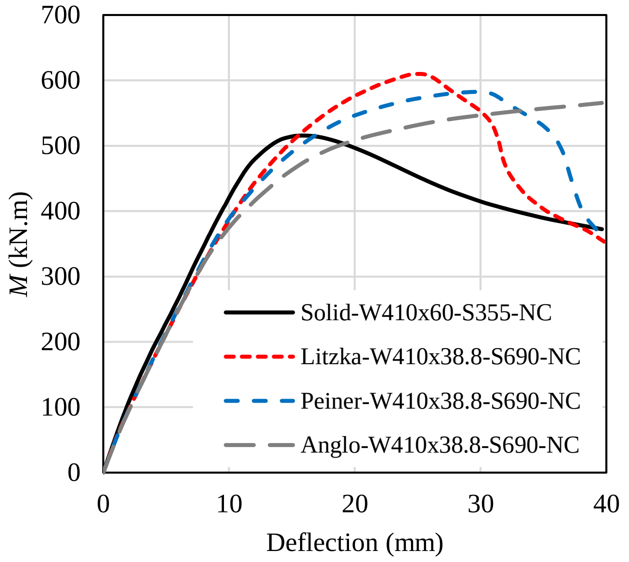

(a) NC slab with h_s= 100mm

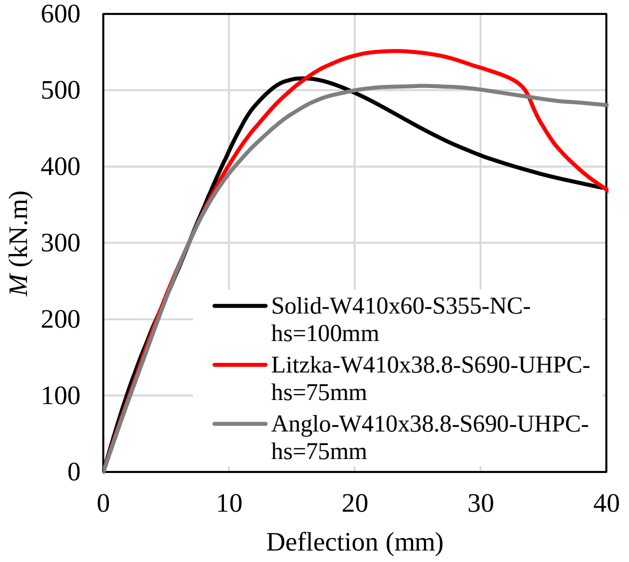

(b) NC slab with h_s= 100mm and UHPC slab with h_s= 75mm
Source: The author (2025).

As noted in **Figure 6.20b**, compared to the conventional NSS-NC composite beam, the HSS-UHPC composite castellated beams exhibited better alignment with the initial bending stiffness than the HSS-NC composite castellated beams (**Figure 6.20a**). Thus, despite the 33.3% reduction in concrete volume due to slab dematerialization, the use of UHPC slightly improved the initial stiffness. Regarding the conventional beam's post-peak behavior, the castellated beams sustained higher loads within the same deflection range. However, a decrease of around 11% was observed in the M_u values of the composite castellated beams with UHPC-h_s= 75mm (**Figure 6.20b**) compared to those with NC-h_s= 100mm (**Figure 6.20a**). As the composite castellated beam with the Litzka pattern and NC-h_s= 100mm had a M_u value of 18.3% higher than the conventional composite beam (**Figure 6.20a**), the Litzka beam with UHPC-h_s= 75mm had a M_u value of 7% higher than the conventional one. In contrast, the Anglo-Saxon beam with UHPC-h_s= 75mm had a M_u value of 1.9% lower than the conventional beam, which is not a considerable divergence. Therefore, the HSS-UHPC composite castellated beams with h_s= 75mm and W410x38.8-S690 parent I-section presented a reduction in concrete and I-section steel consumption of 33.3% and 54.6%, respectively, obtaining an adequate hogging bending performance concerning the conventional composite beam with solid W410x60-S355 profile. On the other hand, the HSS-NC composite castellated beams with h_s= 100mm provided a flexural response that favors security, which had M_u values of around 11% higher than those with UHPC and h_s= 75mm. This occurrence is due to the significant effect of the WPB phenomenon on the failure mode of these castellated beams exhibit, as the castellated W410x38.8 profiles have the highest local web slenderness (h_w/t_w) within the analyzed castellated I-sections, as presented in **Table 6.4**. As observed in **section 6.2.1**, the concrete slab significantly influences the bending behavior of composite castellated beams considerably affected by the WPB phenomenon. This way, the slab height significantly influenced these composite castellated beams' bearing capacity.

According to **Figure 6.21a**, the HSS-NC composite castellated beams with W410x46.1-S460 parent I-section had initial bending stiffness in agreement with the conventional composite beam analyzed, in which the castellated beams had higher M_u values. In addition, the composite castellated beams presented higher ductility than the conventional composite beam. In this analysis (**Figure 6.21a**), the models with the Liztka and Peiner patterns did not show similar trends between their moment-deflection curves, and the Peiner beam had the lowest M_u value within the composite castellated beams. This way, the composite beams with the Liztka and Peiner castellated I-sections were adopted to apply a thinner slab (h_s= 75mm) with UHPC (**Figure 6.21b**) to assess their flexural response.

Figure 6.21: Conventional composite beam with solid W410x60-S355 I-section, HSS-NC and HSS-UHPC composite beams with castellated W410x46.1-S460 I-section.

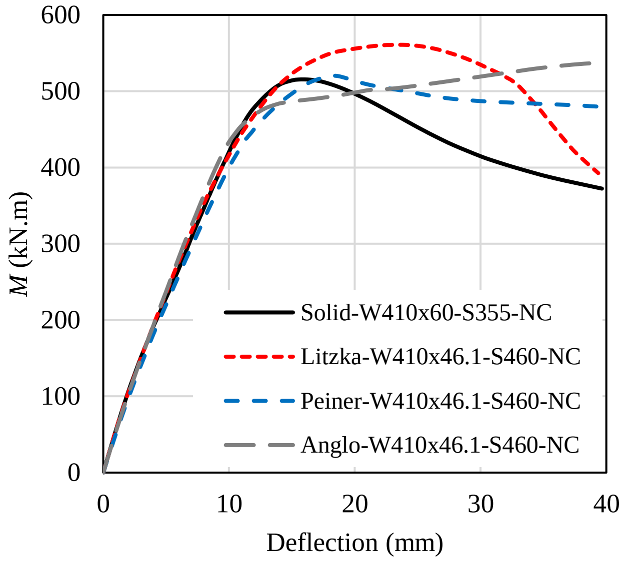

(a) NC slab with h_s= 100mm

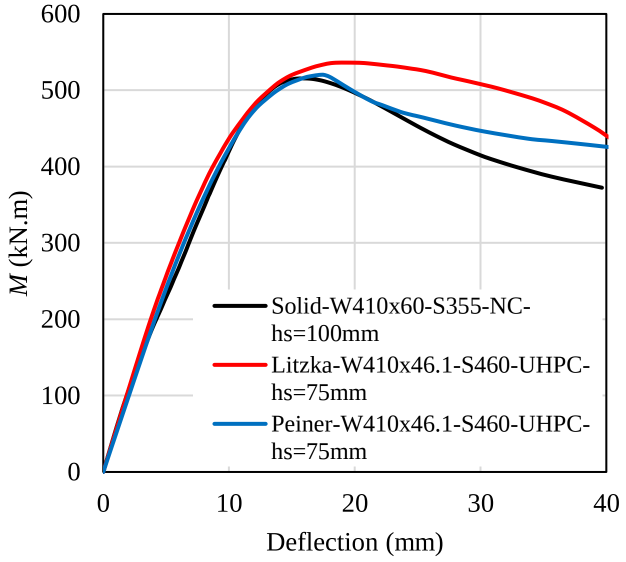

(b) NC slab with h_s= 100mm and UHPC slab with h_s= 75mm
Source: The author (2025).

As shown in **Figure 6.21**, the composite castellated beams with the slab of UHPC and h_s= 75mm (**Figure 6.21b**) demonstrated a slightly higher initial bending stiffness than those with the slab of NC and h_s= 100mm (**Figure 6.21a**). Compared to the conventional composite beam, the HSS-UHPC composite castellated beams had higher M_u values by 4% and 0.9% with Litzka and Peiner patterns (**Figure 6.21b**), respectively. The composite castellated beams also had higher ductility. In contrast to the previous observation in **Figure 6.20**, the composite castellated beams addressed in **Figure 6.21** were not considerably affected by the slab height reduction, in which the Liztka beam's M_u decreased by 4.6%, and the Peiner beam's M_u decreased by 0.02%. This occurrence is due to the lower web local slenderness (h_w/t_w) of the castellated W410x46.1 I-sections than castellated W410x38.8 profiles (**Table 6.4**), which makes them less critical to the WPB phenomenon than the models addressed in **Figure 6.21**. As a result, the use of UHPC enabled a 33.3% reduction in concrete consumption while preserving the hogging bending performance compared to the analyzed conventional NSS-NC composite beam. Furthermore, utilizing the S460 high-strength steel and the I-section web expansion method in a W410x46.1 parent I-section led to a 30.2% decrease in steel consumption for I-sections concerning the solid W410x60-S355 profile.

Figures 6.22-6.23 compare the moment-deflection curves of the conventional composite beam with solid W460x52-S355 I-section and the composite castellated beams with W410x38.8-S460 and W410x46.1-S355 parent I-sections.

As observed in **Figure 6.22a**, the HSS-NC composite castellated beams with W410x38.8-S460 parent I-section had a lower initial bending stiffness than the conventional composite beam, in which this divergence was not elevated. In addition, only the Litzka beam had a higher M_u value (divergence of 1%) than the conventional one. The models with the other opening patterns had lower M_u values, as the WPB phenomenon was more critical in these models due to their lower web-post width, which limited their bearing capacity. Given this, only the composite castellated beam with the Litzka pattern was adopted to apply a thinner slab (h_s= 75mm) with UHPC, as shown in **Figure 6.22b**. **Figure 6.22b** shows that the HSS-UHPC composite castellated beam had an initial bending stiffness in agreement with the conventional composite beam. This castellated beam had a M_u value of 2% lower than the conventional one, which is not a significant divergence. Regarding the conventional beam's post-peak range, the castellated beam began to support less load than the solid beam after reaching a considerable deflection of 30 mm. Therefore, incorporating UHPC allowed for a 33.3% reduction in concrete consumption while maintaining the hogging bending performance when compared to the conventional NSS-NC composite beam analyzed. Additionally, applying S460 high-strength steel and the web expansion technique to a W410x38.8 parent I-section led to a 34% reduction in steel consumption relative to the solid W460x52-S355 profile.

Figure 6.22: Conventional composite beam with solid W460x52-S355 I-section, HSS-NC and HSS-UHPC composite beams with castellated W410x38.8-S460 I-section.

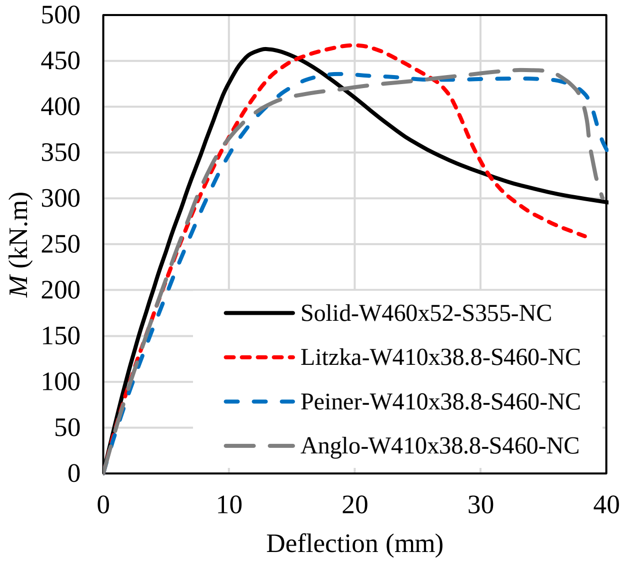

(a) NC slab with h_s= 100mm

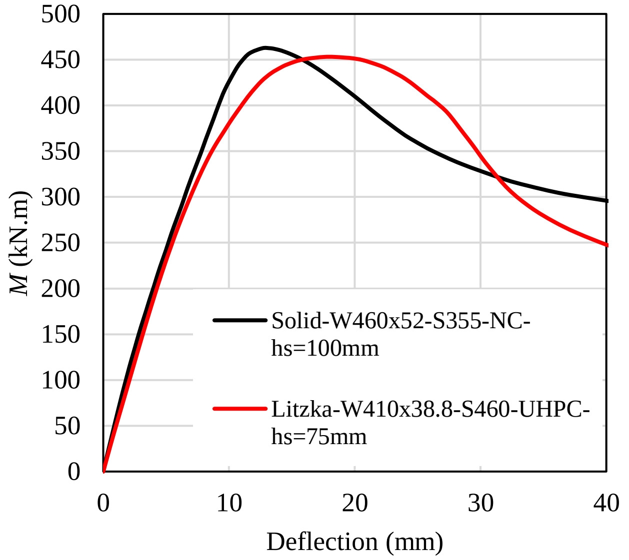

(b) NC slab with h_s= 100mm and UHPC slab with h_s= 75mm
Source: The author (2025).

According to **Figure 6.23a**, the NSS-NC composite castellated beams with W410x46.1-S355 parent I-section had a slightly lower initial bending stiffness than the conventional composite beam analyzed. Only the castellated beam with the Peiner pattern had a higher M_u value than the conventional one, given a divergence of only 0.2%. Those with the Litzka and Anglo-Saxon patterns had M_u values of 0.7% and 2.9%, respectively, lower than the conventional beam. In addition, all composite castellated beams supported higher loads in almost the whole post-peak range of the conventional composite beam. This way, those with the Liztka and Peiner castellated I-sections were used to apply a thinner slab (h_s= 75mm) with UHPC (**Figure 6.23b**) to assess the possibilities of dematerialization in these composite beams.

As observed in **Figure 6.23b**, the NSS-UHPC composite castellated beams had an initial bending stiffness in agreement with the conventional composite beam. This way, the composite castellated beams with the slab of UHPC and h_s= 75mm (**Figure 6.23b**) had a slightly higher initial bending stiffness than those with the slab of NC and h_s= 100mm (**Figure 6.23a**). Compared to the conventional composite beam's post-peak behavior, the NSS-UHPC composite castellated beams supported higher loads in most of this deflection range, as shown in **Figure 6.23b**. On the other hand, these composite castellated beams with the Litzka and Anglo-Saxon patterns had M_u values of 3.3% and 1.3%, respectively, lower than the conventional composite beam. These divergences are not elevated. However, careful analysis must be considered when adopting this dematerialization approach. In these composite castellated beams, the use of UHPC allowed for a 33.3% reduction in concrete consumption while still ensuring adequate hogging bending performance when compared to the conventional NSS-NC composite beam analyzed. Moreover, applying only the web expansion method to a W410x46.1 parent I-section resulted in a 12.8% reduction in steel consumption compared to the solid W420x52-S355 profile.

Figure 6.23: Conventional composite beam with solid W460x52-S355 I-section, steel-NC and steel-UHPC composite beams with castellated W410x46.1-S355 I-section.

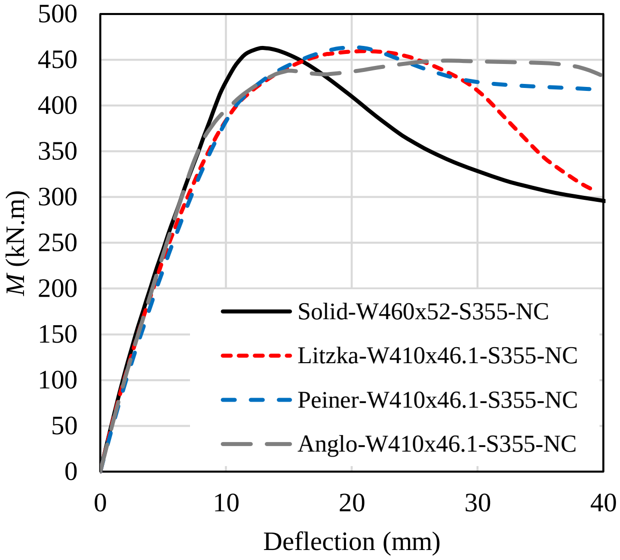

(a) NC slab with h_s= 100mm

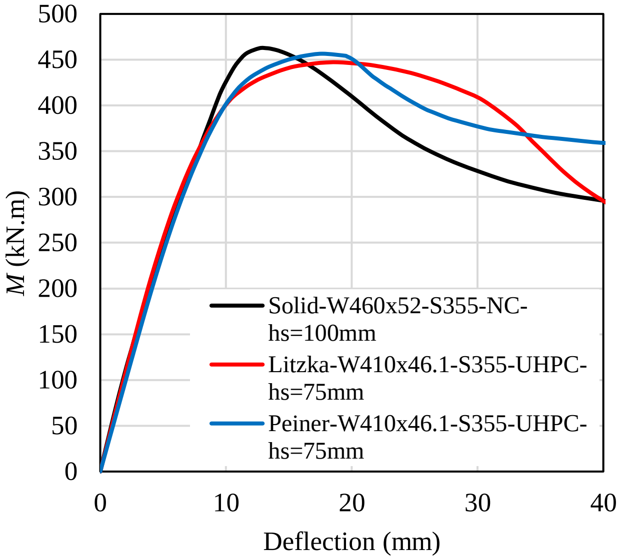

(b) NC slab with h_s= 100mm and UHPC slab with h_s= 75mm

Source: The author (2025).

As previously described, the dematerialization of the steel I-sections was verified by searching for the lowest f_y values possible within the steel grades of the parent I-sections analyzed in the parametric study. In most cases, the higher the I-section steel yield strength (f_y), the higher the cost of the steel profile. This way, the possibilities of the dematerialization were also verified by searching for the lowest steel cost possible. For all dematerialization options discussed in **sections 6.3.1.4.1-6.3.1.4.1.5**, the reduction in the steel consumption is also possible to reach with higher f_y values than those verified. However, it would be a less economical solution in terms of costs. Given this, no economical solution for the dematerialization was verified with the S960 steel due to the following reasons:

- In all cases assessed in **sections 6.3.1.4.1-6.3.1.4.1.5**, when the initial bending stiffness had slight divergence between the composite beams with solid and castellated I-sections, the possibilities of dematerialization was verified using castellated I-sections with lower f_y values than 960MPa, as shown in the example of **Figure 6.24a**;
- When the M_u values of the conventional composite beams with solid I-sections had slight divergence compared to those with castellated I-section and S960 steel, the initial bending stiffness of these castellated beams was significantly lower than the ones with solid I-section, as Young's modulus is equal for normal and high-strength steels. This way, even though it was possible to reach a similar M_u with an elevated reduction in steel consumption by using castellated I-sections of S960 steel, the considerably lower b_f, $tf_,$ and t_w of the castellated profiles resulted in significantly lower initial bending stiffness. This occurrence is shown in **Figure 6.24b**.

Based on the observations made in the present section, the steel-concrete composite beams in hogging moment regions can reach an I-section dematerialization rate of up to 55% by using HSS coupled with the I-section height expansion method. In addition, only adopting the I-section height expansion approach can present an I-section dematerialization rate of up to 17.9%. All these dematerialization rates were obtained even when global and local instability modes occurred in the height-expanded profile (castellated I-section). Finally, the slab concrete can reach the dematerialization rate of 33.3% by utilizing UHPC instead of NC. In all possibilities of dematerialization verified, the initial bending stiffness and M_u had slight divergences, or higher M_u, regarding the reference conventional composite beam.

Figure 6.24: Conventional composite beams with solid I-sections of S335 steel and composite beams with castellated I-sections of S690 and S960 steels.

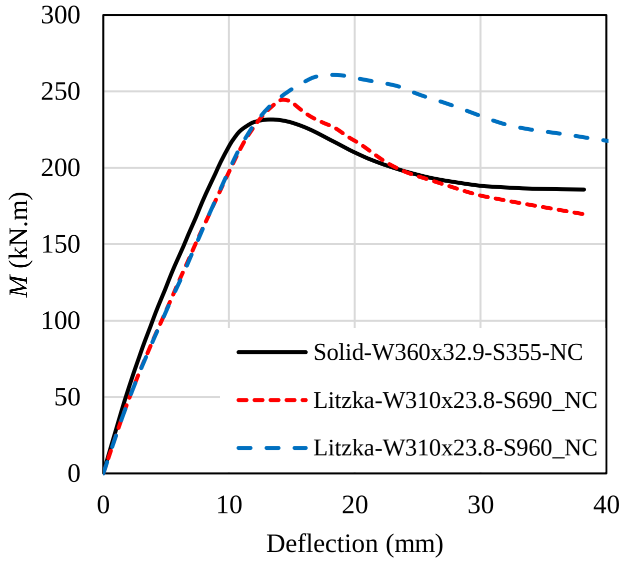

(a) Composite beams with solid W360x32.9 profile of S355 steel and with castellated W310x23.8 I-section of S690 and S960 steels

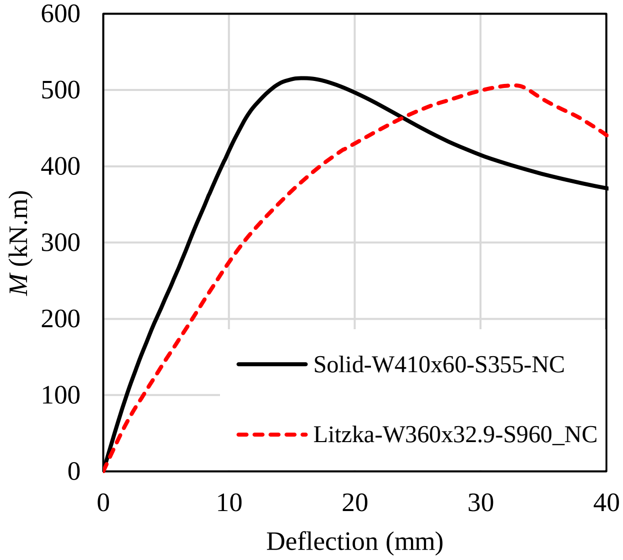

(b) Composite beams with solid W410x60 profile of S355 steel and with castellated W360x32.9 I-section of S960 steels
Source: The author (2025).

6.3.2 Accuracy obtained by LDB resistance formulations

This section deals with the accuracy of the formulations for LDB resistance prediction presented in **section 2.1.2** against the results of the Finite Element Method (FEM) discussed in **sections 6.3.1.1-6.3.1.3**. As all models were submitted to three-point bending with a lateral constraint in the load point, their unrestrained length for the LDB phenomenon is equal to 2m, according to **Figure 6.6**.

The focus of this analysis is verifying the LDB resistance formulations combining different M_{cr} prediction methods and resistance design curves, mainly addressing the updates in European (prEN 1994-1-1 / EN 1993-1-1:2022) and Brazilian codes (ABNT NBR 8800:2024). This way, for determining the M_{cr}, only propositions based on the U-frame model and numerical approach via LBA using the lowest positive eigenvalue are analyzed, and the M_u formulation of Australian codes (AS4100:2020 and AS/NZS2327-2017) are not addressed. The M_{pl} of all models is determined according to **section 2.1.2.2**. For all M_{cr} formulations, the cross-section geometric properties were calculated regarding the central region of the web openings, and the I-section torsional constant (J) was determined according to Sonck and Belis (2017), given by **Eq. 2.1**.

In contrast to the approach analyzed in **section 6.1.2**, in which the coefficient β_{0b} of the M_{cr} proposition of Hanswille *et al*. (1998) was taken equal to 1.0, in the present analysis, the M_{cr} is calculated exactly as proposed by Hanswille *et al*. (1998), as described in **section 2.1.2.1**.

The update in EC3 (EN 1993-1-13:2024) gives an approach for the Lateral-Torsional Buckling (LTB) resistance prediction of non-composite alveolar beams, which fixes the curve "c" of the EC3 design curves (EN 1993-1-1:2022) to calculate the M_u to LTB of steel alveolar beams. Given this, the adoption of curve "c" in LDB resistance prediction is also verified. All numerical models analyzed have castellated I-sections that must use the curve "b" in LDB resistance prediction following the provisions from the previous and current version of EC3 (ENV 1993-1-1:2005 / EN 1993-1-1:2022) given by **Tables 2.11-2.12**, respectively. According to the criteria presented in **Table 2.12**, all models have an imperfection factor α_{LT} equal to 0.34, which is the same value regarding the curve "b", as shown in **Table 2.11**. Therefore, all models' M_u is also calculated using curve "b" of the previous and current versions of EC3 (ENV 1993-1-1:2005 / EN 1993-1-1:2022), which is the same design curve for both versions. The only divergence between these versions of EC3 is the procedure to determine the imperfection factor α_{LT}, as discussed in **section 2.1.2.2** and shown by **Tables 2.11-2.12**. Finally, the resistance curve proposed by Salah (2009) is also adopted in this assessment, given by **Eqs. 2.49-2.50**.

The $M_{u\text{-}Theoretical}/M_{u}\text{-}_{FE}$ ratios (M_u obtained by the analytical formulations about the FEM result) for each combination between the approaches to determine M_{cr} and the resistance design curves given by ABNT NBR 8800:2024, EN 1993-1-1:2022, and Salah (2009) are shown in **Figures 6.25-6.27**, respectively. The $M_{u\text{-}Theoretical}/M_{u}\text{-}_{FE}$ ratio values higher than 1.0 are non-conservative results and vice-versa. In **Figures 6.25-6.27**, the models within the ranges 1–41, 42–82, 83–106, and 107–130 are those with S355, S460, S690 and S960 steels, respectively.

As observed in **Figure 6.25**, for all M_{cr} prediction approaches, $M_{u\text{-}Theoretical}/M_{u}\text{-}_{FE}$ ratio values presented an elevated range variation for the composite castellated beams with S690 and S960 steels (models within 83–130), which shows that the design curve of ABNT NBR 8800:2024 can be not adequate for LDB resistance prediction of composite castellated beams with these HSS. **Figure 6.25** shows that the combination between the M_{cr} proposed by Hanswille *et al*. (1998) and the design curve of ABNT NBR 8800:2024 overestimated the M_u of many models, mainly for those with S690 and S960 steels (models within 83–130), which reached $M_{u\text{-}Theoretical}/M_{u}\text{-}_{FE}$ ratio values up to 1.89. On the other hand, this combination of M_{cr} formulation and design curve had $M_{u\text{-}Theoretical}/M_{u}\text{-}_{FE}$ ratio values in the range from 0.89 to 1.17 for the models with S355 and S460 steels (models within 1–82). However, the proposition of Hanswille *et al*. (1998) considerably overestimates the M_{cr} regarding LBA, which requires more attention to use this M_{cr} formulation, as well as observed by Oliveira *et al*. (2022). The M_{cr} proposition of Dias *et al*. (2019) and Nery *et al*. (2023) combined with the design curve of ABNT NBR 8800:2024 had $M_{u\text{-}Theoretical}/M_{u}\text{-}_{FE}$ ratio values in the range from 0.58 to 1.03, in which the values of around 0.6 were obtained regarding the models with lower I-section dimensions, and the highest values (higher than 0.9) were concerning those with higher I-section dimensions. Meanwhile, using the M_{cr} proposition of Roik *et al*. (1990) with the design curve of ABNT NBR 8800:2024, the range in the $M_{u\text{-}Theoretical}/M_{u}\text{-}_{FE}$ ratio values was from 0.53 to 0.79, also presenting the lowest and highest values of this range for the models with lower and higher I-section dimensions, respectively. Finally, adopting the M_{cr} values via LBA coupling with the design curve of ABNT NBR 8800:2024, the $M_{u\text{-}Theoretical}/M_{u}\text{-}_{FE}$ ratio values were within the range of 0.48 to 0.98, in which the lowest values were given concerning the models with higher I-section dimensions and S960 steel, and the highest values for those with lower I-section dimensions and S960 steel. For this combination, the lowest value of 0.48 was obtained by the model with W410x38.8 I-section, S960 steel, and d_g/d= 1.6, which was the most critical model to WPB occurrence due to its elevated local web slenderness (h_w/t_w) and f_y value. For this model, the LBA result characterized an accentuated WPB in the buckling mode, which limited its M_{cr}. Four buckling modes were analyzed further regarding the lowest positive eigenvalue, which also characterized an elevated influence of local buckling modes in their coupling with LDB in all these eigenvectors.

Figure 6.25: $M_{u\text{-}Theoretical}/M_{u\text{-}FE}$ ratio obtained by the combination between the design curve of ABNT NBR 8800:2024 and different approaches to determine M_{cr}.

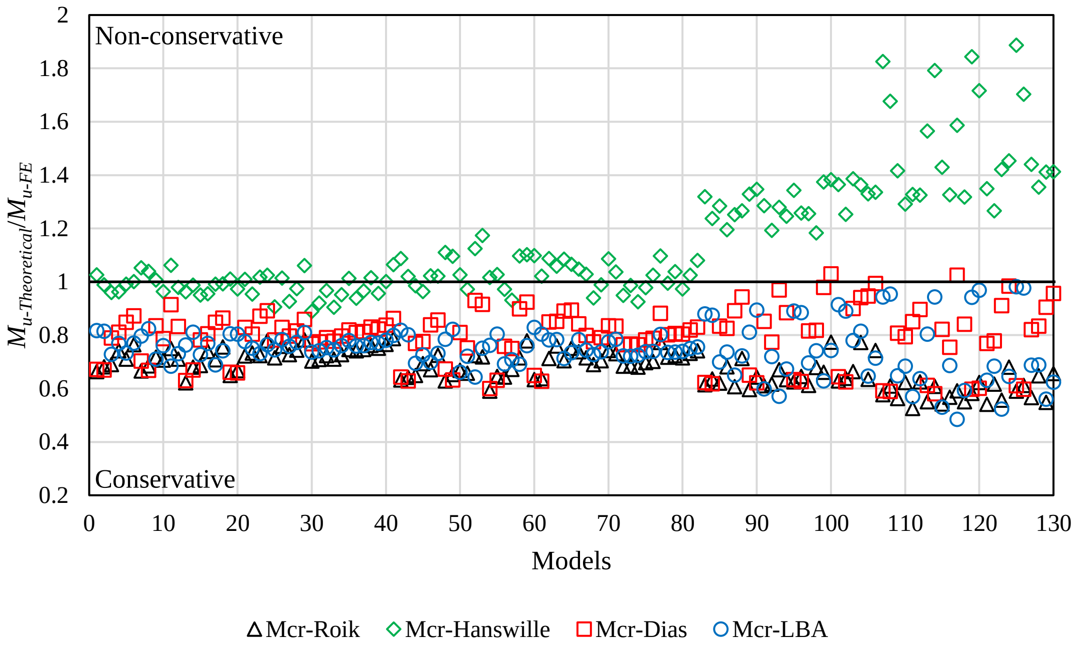

Source: The author (2025).

Regarding the updates in the provisions of Brazilian code, the previous version (ABNT NBR 8800:2008) adopted the M_{cr} formulation proposed by Roik *et al*. (1990), while the current version (ABNT NBR 8800:2024) uses the M_{cr} prediction proposed by Dias *et al*. (2019) and Nery *et al*. (2023). Furthermore, the current version recommends using numerical models to determine M_{cr}, which was not recommended in the previous version. As noted in **Figure 6.25**, in most cases, adopting the M_{cr} formulation proposed by Roik *et al*. (1990), the M_u values were more conservative than utilizing the M_{cr} prediction of Dias *et al*. (2019) and Nery *et al*. (2023). This way, considering only the analytical approaches, the current version of Brazilian code (ABNT NBR 8800:2024), which had $M_{u\text{-}Theoretical}/M_{u\text{-}FE}$ ratio values of around 0.8 for most samples, provided an LDB resistance prediction less conservative than the previous version (ABNT NBR 8800:2008). Using the numerical approach via LBA, the $M_{u\text{-}Theoretical}/M_{u\text{-}FE}$ ratio values were around 0.7 for most samples. However, this approach provided a higher M_u underestimation for composite castellated beams that are more susceptible to the WPB phenomenon. Therefore, for the M_u prediction combining LBA for M_{cr} and the design curve of ABNT NBR 8800:2024, a more critical analysis is needed when the LBA provides eigenmodes with a higher effect of WPB.

Figure 6.26 shows that curve "c" of EC3 (EN 1993-1-1:2022) provides results with higher conservatism than curve "b" for all M_{cr} approaches, as expected. As for the design curve of ABNT NBR 8800:2024, regarding the composite castellated beams with S690 and S960 steels (models within 83–130), the design curves of EC3 (EN 1993-1-1:2022) also presented an elevated range variation in the $M_{u\text{-}Theoretical}/M_{u}\text{-}_{FE}$ ratio values for all M_{cr} prediction methods. Therefore, the EC3's design curves can also not be adequate for LDB resistance prediction of composite castellated beams with these HSS. As observed in **Figure 6.26**, using the M_{cr} proposition of Hanswille *et al*. (1998), as the curve "b" as the curve "c" overestimated the M_u value of the models with S690 and S960 steels (models within 83–130), reaching $M_{u\text{-}Theoretical}/M_{u}\text{-}_{FE}$ ratio values up to 1.78. Meanwhile, for the models with S355 and S460 steels (models within 1–82), the M_{cr} proposition of Hanswille *et al*. (1998) combined with curve "b" and curve "c" had $M_{u\text{-}Theoretical}/M_{u}\text{-}_{FE}$ ratio values in the ranges of 0.87–1.15 and 0.83–1.09, respectively. However, more attention is needed when utilizing this M_{cr} formulation, as it significantly overestimates the M_{cr} (OLIVEIRA *et al*., 2022). Finally, combined with curve "b" and curve "c", the M_{cr} approaches proposed by Roik *et al*. (1990), Dias *et al*. (2019)/Nery *et al*. (2023), and adopting numerical models via LBA provided only conservative results, which were slightly more conservative than using the design curve of ABNT NBR 8800:2024. For these M_{cr} approaches, the same trends observed in their coupling with the design curve of ABNT NBR 8800:2024 were noted with curve "b" and curve "c".

Figure 6.26: $M_{u\text{-}Theoretical}/M_{u\text{-}FE}$ **ratio obtained by the combination between the design curve of EN 1993-1-1:2022 and different approaches to determine** M_{cr}**.**

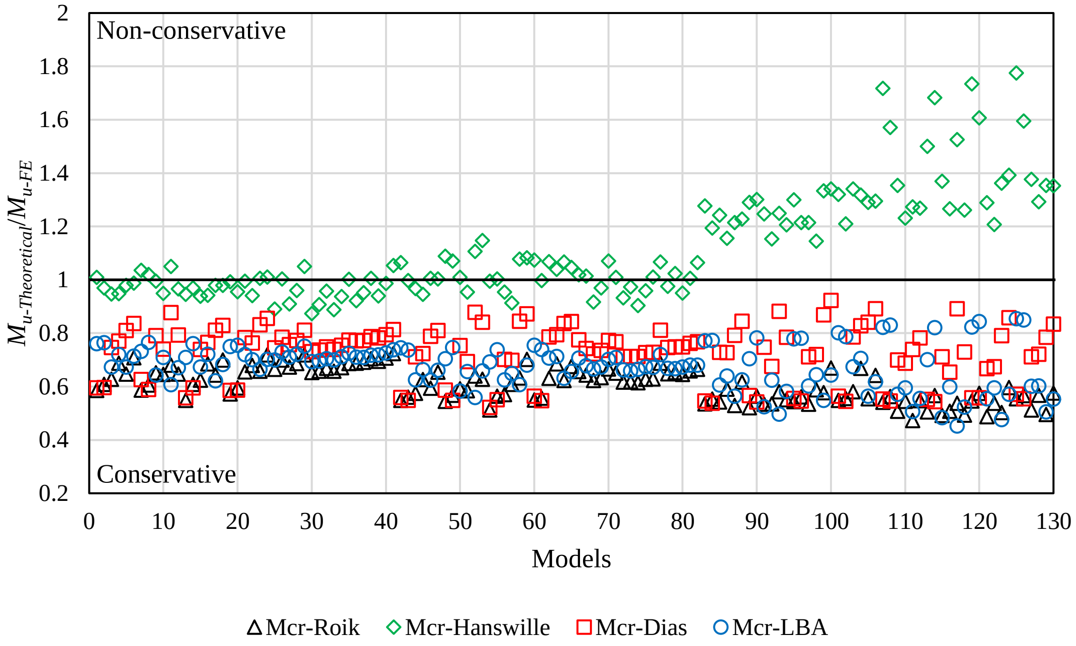

(a) Curve "b"

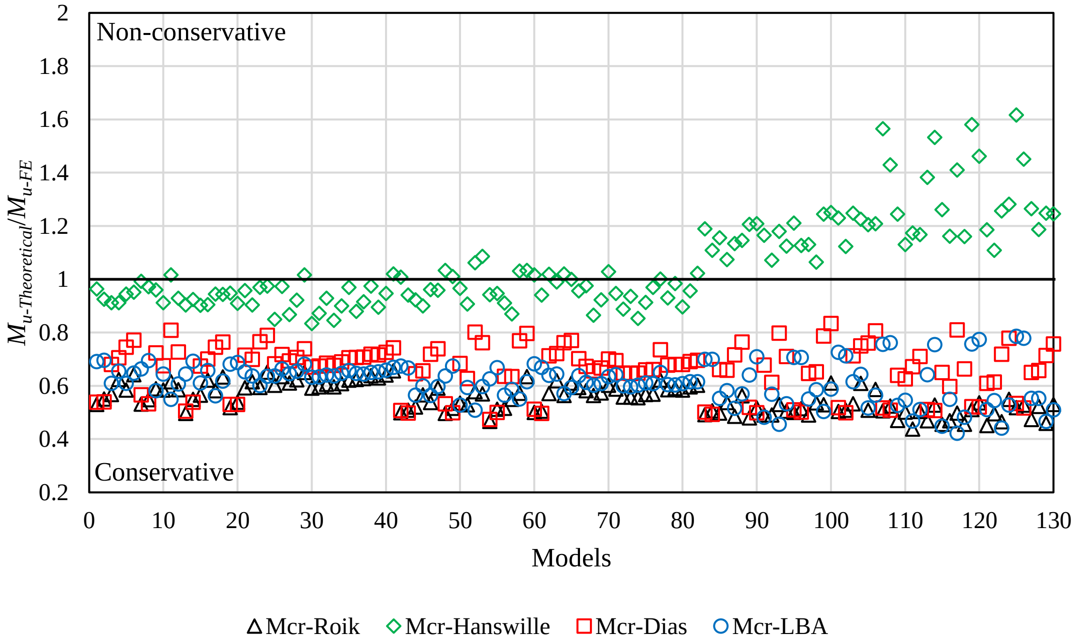

(b) Curve "c"

Source: The author (2025).

Figure 6.27 shows that combining the M_{cr} formulation of Hanswille *et al*. (1998) with the design curve proposed by Salah (2009) overestimated the M_u for all samples. Considering the M_{cr} predictions proposed by Roik *et al*. (1990) and Dias *et al*. (2019)/Nery *et al*. (2023), the design curve of Salah (2009) presented a lower range variation in the $M_{u\text{-}Theoretical}/M_{u}\text{-}_{FE}$ ratio values for the models with S690 and S960 steels than the design curves of ABNT NBR 8800:2024 and EN 1993-1-1:2022 (**Figures 6.25-6.26**). Given this, the design curve of Salah (2009) showed a more appropriate behavior for LDB resistance prediction of composite castellated beams with these HSS than the design curves of Brazilian and European codes. As observed in **Figure 6.27**, using the M_{cr} proposition of Dias *et al*. (2019)/Nery *et al*. (2023), the M_u prediction was less conservative than adopting the M_{cr} formulation of Roik *et al*. (1990) for most samples. For both combinations, the highest $M_{u\text{-}Theoretical}/M_{u}\text{-}_{FE}$ ratio values were obtained regarding the models with higher I-section dimensions, similar to the observations with the other design curves. The combination between the M_{cr} proposition of Dias *et al*. (2019)/Nery *et al*. (2023) and the design curve of Salah (2009) provided only one non-conservative result, in which the $M_{u\text{-}Theoretical}/M_{u}\text{-}_{FE}$ ratio value is equal to 1.04 concerning the model with W410x38.8 I-section, S960 steel, and d_g/d= 1.6. Similar to the observations with other design curves, using LBA to determine M_{cr}, the highest and lowest $M_{u\text{-}Theoretical}/M_{u}\text{-}_{FE}$ ratio values were obtained for the models with lower and higher I-section dimensions, respectively, in which some models with higher I-section dimensions and S960 steel had non-conservative results, presenting $M_{u\text{-}Theoretical}/M_{u}\text{-}_{FE}$ ratio values up to 1.13, as noted in **Figure 6.27**. This occurrence is explained by the same reasons previously mentioned.

Figure 6.27: $M_{u\text{-}Theoretical}/M_{u\text{-}FE}$ ratio obtained by the combination between the design curve of Salah (2009) and different approaches to determine M_{cr}.

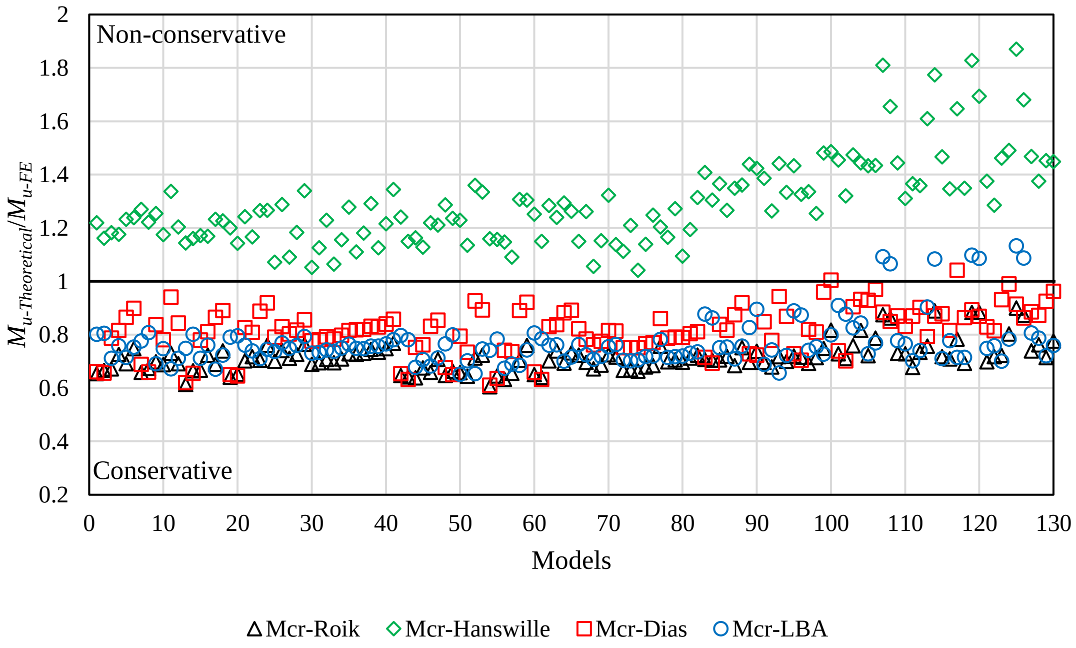

Source: The author (2025).

Figure 6.28 brings the FEM results compared to the LDB resistance formulations combining different M_{cr} predictions and resistance design curves. As noted in **Figure 6.28a**, only conservative results were obtained using the M_{cr} formulation of Roik *et al*. (1990), and its coupling with the design curve of Salah (2009) had the best agreement with the FEM results concerning the other design curves, mainly for the models with S690 and S960 steels. This observation is also made for the M_{cr} proposition of Dias *et al*. (2019)/Nery *et al*. (2023), as shown in **Figure 6.28b**. In addition, for most FEM results compared to the design curve of ABNT NBR 8800:2024, the M_{cr} prediction method proposed by Dias *et al*. (2019)/Nery *et al*. (2023) had a better agreement than the M_{cr} formulation of Roik *et al*. (1990), as observed in **Figure 6.28a-b**. Adopting the numerical approach via LBA (**Figure 6.28c**), the design curve proposed by Salah (2009) also presented a higher agreement with the FEM results than the other design curves. However, the LDB resistance of seven models was overestimated by up to 13%. For the LBA approach, considering only conservative results, the design curve of ABNT NBR 8800:2024 had the best agreement with the FEM results. At the same time, it considerably overestimated the M_u of the model, which had a higher influence on the WPB phenomenon. For all combinations addressed in **Figure 6.28a-c**, EC3's curves "b" and "c" (EN 1993-1-1:2022) provided only conservative results, and the curve "c" had the highest conservatism. Finally, **Figure 6.28d** shows that the M_{cr} calculation method of Hanswille *et al*. (1998) only provided non-conservative results for all design curves concerning the models with S690 and S960 steels. In addition, this M_{cr} approach overestimated the M_u of most models, mainly with the design curve of Salah (2008), which only had non-conservative results.

Figure 6.28: Numerical results compared to the LDB resistance formulations combining different M_{cr} predictions and resistance design curves.

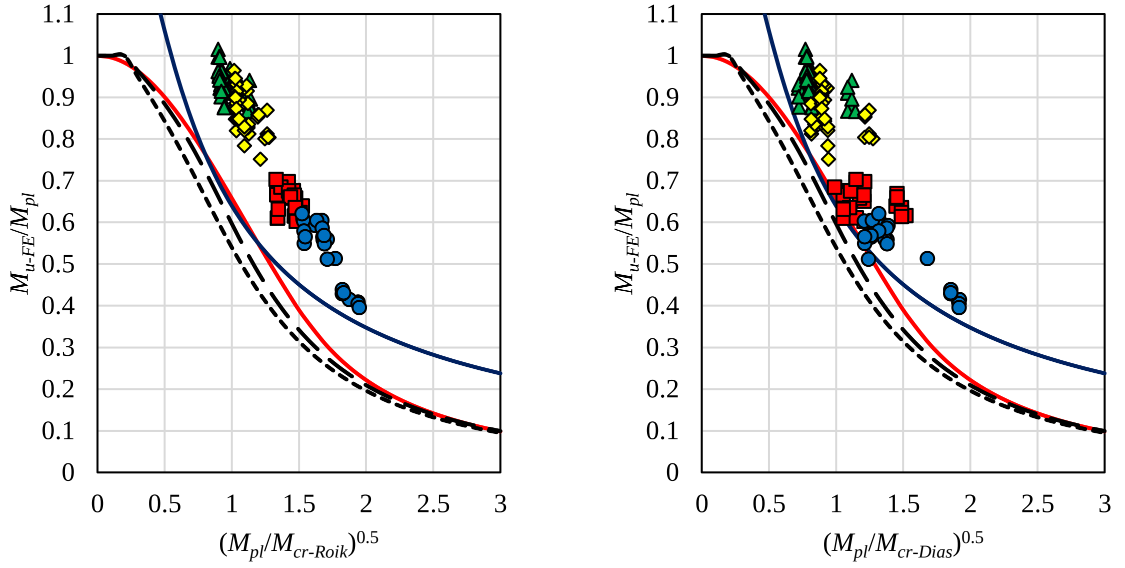

(a) M_{cr} proposed by Roik *et al*. (1990)

(b) M_{cr} proposed by Dias *et al*. (2019)/ Nery *et al*. (2023)

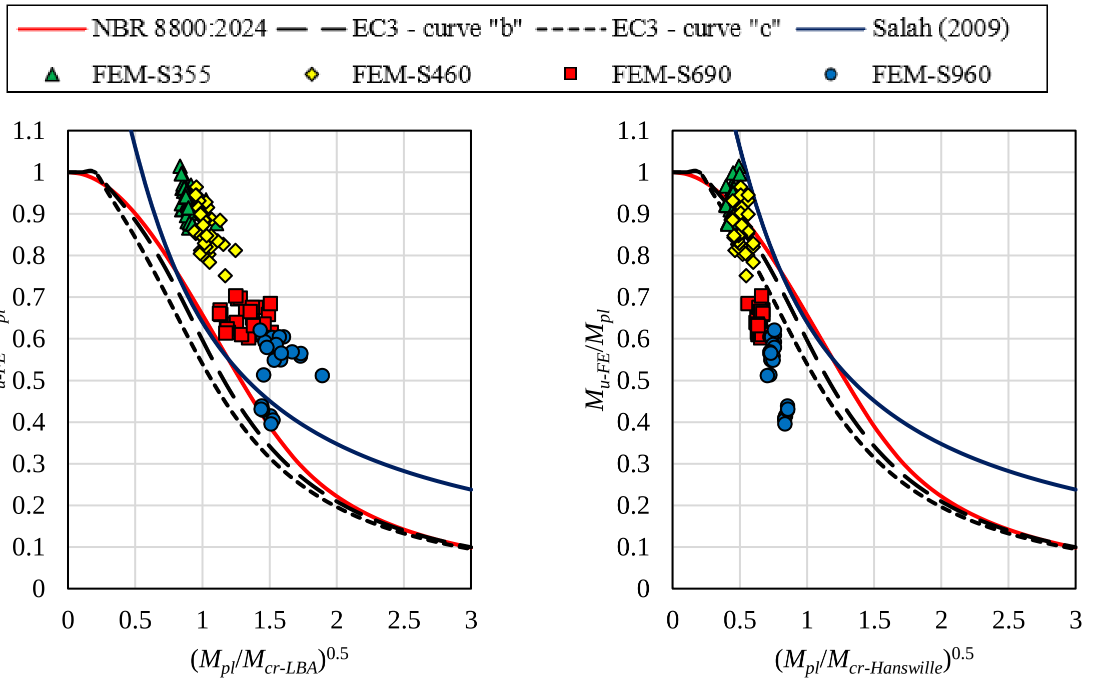

(c) M_{cr} obtained by LBA

(d) M_{cr} proposed by Hanswille *et al*. (1998)

Source: The author (2025).

Table 6.11 presents the statistical analysis of the $M_{u\text{-}Theoretical}/M_{u\text{-}FE}$ ratio for each combination of the approaches to determine M_{cr} and the resistance design curves. As noted, all combinations with the M_{cr} proposition of Hanswille *et al*. (1998) had a mean $M_{u\text{-}Theoretical}/M_{u\text{-}FE}$ ratio higher than 1.0 and the highest standard deviation (SD) and variance (VAR). Regarding the ABNT NBR 8800:2024, the M_{cr} formulation of Dias *et al.* (2019)/Nery *et al.* (2023) had the highest mean, SD and VAR. In contrast, the M_{cr} calculation proposed by Roik *et al.* (1990) had the lowest mean, SD, and VAR, and the numerical approach via LBA presented an intermediate case. Despite the M_{cr} formulation of Dias *et al.* (2019)/Nery *et al.* (2023) have obtained the highest SD and VAR for ABNT NBR 8800:2024, it was not significantly overestimated the Mu of the models, which is a positive point for a safety analysis. Regarding the EC3's design curves, curve "b" had higher means than curve "c" for all M_{cr} approaches, and except for the one proposed by Hanswille *et al.* (1998), only had conservative results, showing a higher accuracy using the curve "b" for the provisions by Eurocode 3 and 4 (prEN 1994-1-1/EN 1993-1-1:2022/EN 19931-13:2024). Only considering means of the $M_{u\text{-}Theoretical}/M_{u\text{-}FE}$ ratio lower than 1.0, the highest mean (equal to 0.81) was obtained by combining the M_{cr} formulation of Dias *et al.* (2019)/Nery *et al.* (2023) and the design curve of Salah (2009). This combination had only one non-conservative result: a $M_{u\text{-}Theoretical}/M_{u\text{-}FE}$ ratio of 1.04. Using the design curve of Salah (2009), the numerical approach via LBA also presented considerable agreement with the FEM results with a mean of the $M_{u\text{-}Theoretical}/M_{u\text{-}FE}$ ratio of 0.77. However, it had a higher SD and VAR than the M_{cr} proposition of Dias *et al.* (2019)/Nery *et al.* (2023). For the analyzed samples, the combination of the M_{cr} formulation of Dias *et al.* (2019)/Nery *et al.* (2023) and the design curve of Salah (2009) had the highest agreement with the FEM results for the LDB resistance prediction.

Table 6.11: Statistical analysis of $M_{u\text{-}Theoretical}/M_{u\text{-}FE}$ ratio.

Resistance design curve	Statistical	Calculation methods for M_{cr}			
		Roik *et al.* (1990)	Hanswille *et al.* (1998)	[a]Dias *et al.* (2019)	[b]LBA
NBR 8800	Mean	0.68	1.15	0.79	0.75
	SD. (10^2)	6.32	22.31	10.69	8.96
	VAR (%)	0.40	4.98	1.14	0.80
EC3 curve "b"	Mean	0.61	1.12	0.72	0.68
	SD. (10^2)	6.23	20.00	10.42	8.18
	VAR (%)	0.39	4.00	1.09	0.67
EC3 curve "c"	Mean	0.55	1.06	0.66	0.62
	SD. (10^2)	5.33	16.96	9.39	7.31
	VAR (%)	0.28	2.88	0.88	0.53
Salah (2009)	Mean	0.71	1.30	0.81	0.77
	SD. (10^2)	5.57	16.38	8.92	9.24
	VAR (%)	0.31	2.68	0.80	0.85

[a]Methodology proposed by Nery *et al.* (2023); [b]Obtained by FEM

Source: The author (2025).

6.4 SUMMARY AND CONCLUSIONS OF THE CHAPTER

This chapter presents the development of parametric studies and their respective results and discussions. The parametric studies discussed in sections 6.1-6.2 were published by Oliveira *et al*. (2023b, 2025), respectively. The research article regarding the parametric study described in section 6.3 is under development. As a summary and conclusion of the chapter, the main observations of each parametric study are presented separately.

According to the parametric study described in **section 6.1**, it was concluded that:

- Except for two composite cellular beams, all others showed LDB in the buckling mode due to the hogging moment. The ones without LDB presented Tee Local Buckling (TLB) and its coupling with the Web Local Buckling (WLB) at the end-post;
- The flange width, flange thickness, web depth, and web thickness were the parameters that had the greatest influence on the elastic critical load, as the web slenderness is significant in the models that reached LDB and WPB;
- The beams subjected to considerable shear force presented WPB in buckling mode, and the web-post width, as well as the opening diameter, had a significant influence on the critical buckling load;
- Some composite cellular beams with lower opening diameter characterized TLB, as these have higher "tee" depth in the region of the alveolus, and consequently, the ones have a slenderer web of the tee;
- WLB was observed in the ones with higher values of end-post width (b_{we}), as in those with smaller b_{we}, there is a shorter frame of end-post, which decreases the possibility of WLB occurrence;
- As the opening diameter decreased and web-post width increased, there was an increase in the elastic critical moment to LDB;
- In most, the uniform hogging moment was the most critical case, and the gradient moment 1-0 was the least. Except for the composite cellular beams that showed more influence of WPB than LDB in the buckling mode. In these beams, the gradient moment 1-0 was the most critical case due to the shear force;
- Some M_{cr} calculation procedures provided considerable non-conservative results for models subjected to the gradient moment 1-0, such as Svensson (1985), Williams and Jemah (1987) and Australian codes (AS4100:2020 and AS/NZS2327-2017);

- The M_{cr} analytical procedures that provided only conservative results were the adaptation of the methodology of Hanswille *et al*. (1998) by using the coefficient β_{0b} equal to 1.0, and the M_{cr} formulations proprosed by Roik *et al*. (1990) and Dias *et al*. (2019)/Oliveira (2018).

Based on the parametric study discussed in **section 6.2**, it was observed that:

- WPB-VM interaction is sensitive to the variation of opening and web-post geometries;
- The lower the web-post width is, the higher the susceptibility to the WPB occurrence. On the other hand, the higher the tee length is, the greater the sensitivity to the VM phenomenon;
- As these opening and web-post parameters of castellated beams vary simultaneously in practice, intermediate dimensions for these parameters provided a higher ultimate load regarding the WPB and VM interaction;
- All composite beams with UHPC slabs had higher initial bending stiffness and ultimate loads than those with NC slabs, even the WPB and VM phenomenon limiting the composite beams' bearing capacity;
- Regarding the accuracy of the procedures for WPB resistance predictions, Steel Design Guide 31 provided non-conservative results in most cases and overestimated the WPB resistance of castellated beams considerably affected by VM;
- The procedure from EN 1993-1-13:2024 had conservative results in most cases and significantly underestimated the WPB resistance of castellated beams with thinner web thickness.

According to the parametric study discussed in **section 6.3**, it was observed that:

- All models presented lateral displacement at the compressed flange, which characterizes the LDB occurrence;
- In most models, the "S" shape in the web-post was also characterized by the WPB phenomenon, with some presenting WPB as more accented than others;
- The composite castellated beams with lower local web slenderness (h_w/t_w ratio) were less susceptible to WPB, characterizing only LDB in most cases;
- The increase in the castellated I-section's expansion ratio (d_g/d) resulted in a higher susceptibility to WPB, as the local web slenderness is also increased;

- For the same I-section and d_g/d value, the higher the f_y is, the greater the WPB characterization in the instability mode, as the models with higher f_y present higher bearing capacity, which makes them reach shear loads more critical for the WPB phenomenon;
- The castellated beams with parent profiles of lower cross-section dimensions were less sensitive to the d_g/d ratio variation, as they did not reach shear loads for a critical WPB, and the LDB was predominant in their failure modes;
- In contrast, the ones with parent profiles of higher cross-section dimensions were more sensitive to the d_g/d ratio variation, as they characterized a significant WPB occurrence in their failure modes;
- The width of the end web-post (b_{we}) had a significant influence on the models that characterized a considerable WPB occurrence, in which the higher the b_{we} is, the higher M_u;
- For the models that showed a significant WPB, the lower the web-post width is, the lower the bearing capacity;
- The models' M_u was significantly affected by the f_y variation, as all models had M_u increase with the increase in f_y;
- The effect of the f_y variation on the M_u was higher for the castellated beams with greater I-section dimensions for all opening patterns, as those with higher I-section dimensions present a higher variation in the M_{pl} for changing the f_y value;
- The diameter and steel yield strength of the longitudinal reinforcement bars did not considerably affect the hogging bending behavior of the composite castellated beams;
- Changing the compressive strength of the concrete from NC (f_{ck}= 30MPa) to UHPC (f_{cm}= 139.8MPa), the gains with this UHPC in the hogging bending performance were a considerably higher initial bending stiffness and increases in the M_u values up to 4.8%;
- The slab height (h_s) also had a considerable influence on the behavior of the models;
- Comparing the models with the combinations of NC-h_s= 100mm and UHPC-h_s= 75mm, those with UHPC-h_s= 75mm had a lower M_u value of up to 3.6% of divergence, and these divergences decreased with the increase in the diameter of the longitudinal reinforcement bars;

- For a similar hogging bending performance, the conventional composite beams can be significantly dematerialized by using HSS castellated I-sections and thinner slabs with UHPC;
- Even when instability modes occur in the castellated I-section, an I-section dematerialization rate of up to 55% can be reached by using HSS coupled with the I-section height expansion method. In addition, only adopting the I-section height expansion approach can present an I-section dematerialization rate of up to 17.9%;
- The slab concrete can reach the dematerialization rate of 33.3% by utilizing UHPC instead of NC;
- The M_{cr} proposition of Hanswille *et al*. (1998) with the coefficient β_{0b} equal to the proposed by the authors provided an M_u overestimation for all the design curves;
- The updates in the Brazilian code from the previous version (ABNT NBR 8800:2008) to the current version (ABNT NBR 8800:2024) presented a more accurate formulation for the current version;
- The formulation of the European code (EN 1994-1-1:2004/prEN 1994-1-1) had conservative results when the M_{cr} is obtained via LBA and by the formulations of Roik *et al*. (1990) and Dias *et al*. (2019)/Nery *et al*. (2023);
- Analyzing composite castellated beams with I-sections of S690 and S960 high-strength steels, the design curve of Salah (2009) showed a better agreement with the numerical results for all analyzed M_{cr} approaches, except with the M_{cr} formulation of Hanswille *et al*. (1998);
- The combination between the M_{cr} proposition of Dias *et al*. (2019)/Nery *et al*. (2023) and the design curve of Salah (2009) had the highest agreement with the numerical results.

CHAPTER 7
FINAL REMARKS

After achieving the study's objectives, this chapter presents final considerations, summarizes key conclusions, and suggests future research on the stability behavior of steel-concrete composite alveolar beams using conventional and high-performance materials.

7.1 CONCLUSIONS

The present study addressed steel-concrete composite alveolar beams formed by solid concrete slabs, castellated and cellular I-profiles, and conventional and high-performance materials, such as Normal-Strength Steels (NSS), High-Strength Steel (HSS), Normal Concrete (NC) and Ultra-High-Performance Concrete (UHPC), focusing on the hogging moment regions of continuous and cantilever composite beams. This way, the occurrence of Lateral-Distortional Buckling (LDB) and Web-Post Buckling (WPB) in these beams was assessed.

The assessment of the hogging bending behavior of these structures was carried out through experimental tests and numerical analyses. As described, three-point bending tests are performed to investigate the WPB behavior of two steel-UHPC composite castellated beams. Additionally, nonlinear numerical models were developed and calibrated against the test results, which obtained significant agreement concerning the experimental results with divergences of up to 4.1% regarding the ultimate loads. This way, numerical parametric studies encompass the influence on the LDB and WPB phenomenon of parameters such as: the expansion factor of the alveolar profiles, opening geometric parameters, I-section dimensions, unrestrained length, concrete slab thickness, the influence of high-performance materials, and loading conditions. Finally, a numerical study assessed some possibilities for dematerializing conventional NSS-NC composite beams of solid I-sections using HSS castellated I-sections and UHPC. In this context, the following findings can be stated:

- According to the Linear Buckling Analyses (LBA) performed with the numerical models, some calculation procedures to determine the elastic critical moment to LDB (M_{cr}) provided non-conservative results, such as Svensson (1985), Williams and Jemah

(1987) and Australian codes (AS4100:2020 and AS/NZS2327-2017). In contrast, the following M_{cr} analytical procedures provided only conservative results: the adaptation of the methodology of Hanswille *et al*. (1998) by using the coefficient β_{0b} equal to 1.0, and the M_{cr} formulations proposed by Roik *et al*. (1990) and Dias *et al*. (2019)/Oliveira (2018);

- Based on the theoretical study, many analyzed approaches for composite alveolar beams' LDB resistance prediction provide non-conservative results when the cross-section properties are not calculated regarding only the central region of the openings. In addition, the I-section torsional constant proposed by Sonck and Belis (2015, 2017) can be adopted. Using the provisions of the current version of EC4 (EN 1994-1-1:2004) combined with the elastic critical moment to LDB (M_{cr}) proposed by Hanswille *et al*. (1998) overestimates the composite alveolar beams' LDB resistance. In addition, the LDB resistance prediction proposed by Salah (2009) combined with the M_{cr} formulations developed by Svensson (1985), Williams and Jemah (1987), and Hanswille *et al*. (1998) overestimates the composite alveolar beams' LDB resistance, as well as the provision given by the Australian codes (AS4100:2020 and AS/NZS2327-2017). Finally, the LDB resistance prediction given by the previous version of the Brazilian code (ABNT NBR 8800:2008), which adopts the M_{cr} formulation proposed by Roik *et al*. (1990), provides conservative results;
- According to the nonlinear numerical analyses, using the M_{cr} proposition of Hanswille *et al*. (1998) with the coefficient β_{0b} calculated by the formulas proposed by the authors, the composite castellated beams' LDB resistance is overestimated when all the analyzed design curves are adopted. In addition, the updates in the Brazilian code from the previous version (ABNT NBR 8800:2008) to the current version (ABNT NBR 8800:2024) show a more accurate formulation for the current version. The formulation of the European code (EN 1994-1-1:2004/prEN 1994-1-1) provides conservative results when the M_{cr} is determined via LBA and by the propositions of Roik *et al*. (1990) and Dias *et al*. (2019)/Nery *et al*. (2023). Regarding composite castellated beams with I-sections of S690 and S960 high-strength steels, the design curve proposed by Salah (2009) presents a better agreement with the numerical results for all analyzed M_{cr} approaches, except with the M_{cr} formulation of Hanswille *et al*. (1998). Finally, the highest agreement with the numerical results is given by the combination between the M_{cr} proposition of Dias *et al*. (2019)/Nery *et al*. (2023) and the design curve of Salah (2009);

- According to the theoretical study, the proposition of Lawson *et al.* (2006) and the EN 1993-1-13: 2024 procedure provide conservative results for the composite cellular beams' WPB resistance;
- Based on the theoretical, experimental, and numerical analyses, the methodology for WPB resistance of composite castellated beams proposed by Aglan and Redwood (1974), which is adopted by the Steel Design Guide 31, overestimates the WPB resistance of composite castellated beams more susceptible to Vierendeel mechanism (VM). In addition, EN 1993-1-13: 2024 procedure provides, at the same time, conservative and slightly non-conservative results for the WPB resistance of composite castellated beams and significantly underestimated the WPB resistance of castellated beams with thinner web thickness;
- As concerns the experimental and nonlinear numerical analyses on the WPB behavior of steel-UHPC composite castellated beams, the models reached failure by WPB coupled with VM. The opening and web-post geometry significantly influence the ultimate load. As noted, the higher the tee length is, the lower the bearing capacity because the VM occurrence is more critical in castellated beams with higher tee length. In addition, the lower the web-post width is, the higher the susceptibility to the WPB occurrence, and, in most cases, a lower ultimate load is obtained. As the opening and web-post parameters of castellated I-sections vary simultaneously in practice, intermediate dimensions for these parameters provide a higher ultimate load regarding the WPB and VM interaction. The composite beams with UHPC slabs present higher initial bending stiffness and ultimate loads than those with NC slabs, even the WPB and VM phenomenon limiting the composite beams' bearing capacity. Finally, as observed in the experimental tests, the UHPC slab presents cracking localization after multiple cracking, a typical behavior of UHPC;
- Based on the numerical assessment of LBA, the flange width, flange thickness, web depth, and web thickness are parameters that have an elevated influence on the elastic critical load. For composite cellular beams susceptible to WPB, the web-post width, as well as the opening diameter, have a significant effect on the critical buckling load. In addition, composite cellular beams with lower opening diameters can reach Tee Local Buckling (TLB), as these cellular I-sections have higher "tee" depth in the region of the opening. Consequently, these have a slenderer web of the tee. The composite cellular beams with higher values of end-post width (b_{we}) are susceptible to Web Local Buckling

(WLB) in these end-posts. In contrast, with smaller b_{we}, there is a shorter frame of end-post, which decreases the possibility of WLB occurrence. Regarding the elastic critical moment (M_{cr}) to LDB, the lower the opening diameter is, the higher the M_{cr}. Meanwhile, the larger the web-post width is, the higher the M_{cr}. Finally, in most cases, the uniform hogging moment is the most critical case, and the gradient moment 1-0 is the least. On the other hand, when the composite cellular beam is considerably susceptible to the WPB occurrence, the gradient moment 1-0 is the most critical case due to the shear force.

- According to the nonlinear numerical analyses on the stability of behavior of composite castellated beams with I-sections of NSS and HSS and slabs of NC and UHPC, these composite beams can reach failure by LDB coupled with WPB. The composite castellated beams with lower local web slenderness are less susceptible to WPB, reaching failure only by LDB in most cases. The higher the I-section's expansion ratio for these beams, the higher their susceptibility to WPB occurrence due to the higher local web slenderness. However, when the castellated beams are made of parent I-sections with lower cross-section dimensions, the castellated I-section's expansion ratio does not have a significant effect on their hogging bending performance. The I-section steel yield strength (f_y) has an elevated impact on the ultimate moment and ductility of the composite castellated beams, increasing them with the increase in f_y. At the same time, it was observed that with increasing the f_y, the susceptibility to the WPB occurrence also increases as the composite castellated beams reach critical shear loads for this instability mode. For the composite castellated beams more susceptible to WPB occurrence, the end-post width (b_{we}) shows a significant influence, in which the higher the b_{we} is, the higher M_u. In addition, the lower the web-post width is, the lower the bearing capacity. The effect of the f_y variation on the M_u is higher for the castellated beams made of parent I-sections of higher cross-section dimensions. This is because the higher I-section dimensions present a higher variation in the M_{pl} for changing the f_y value.
- The diameter and steel yield strength of the longitudinal reinforcement bars do not significantly affect the composite castellated beams' ultimate moment, only influencing their ductility. Varying the compressive strength of the concrete from NC (f_{ck}= 30MPa) to UHPC (f_{cm}= 139.8MPa), the initial bending stiffness is considerably increased with UHPC, and, for the slab analyzed, increases in the ultimate moment up to 4.8% is obtained. The slab height (h_s) also affects the initial bending stiffness and ultimate

moment, in which, for the same concrete, the increase in h_s provides a higher initial bending stiffness and ultimate moment.

- Searching for the slab dematerialization, the composite castellated beams with slabs of NC and h_s= 100mm compared to those with UHPC and h_s= 75mm present lower divergences in their ultimate moment when longitudinal reinforcements of higher diameters are used. However, when the composite castellated beams present a critical WPB occurrence, more attention is needed for this dematerialization, as the considerable reduction in the slab height can significantly reduce the bearing capacity of these castellated beams, even using the UHPC. At the same time, in other cases, the divergences are not significant, enabling an elevated reduction in concrete consumption with dematerialization rates of up to 33.3%;
- For a similar hogging bending performance, the conventional composite beams can be significantly dematerialized by using HSS castellated I-sections and thinner slabs with UHPC. Even when instability modes occur in the castellated I-section, an I-section dematerialization rate of up to 55% can be reached using HSS coupled with the I-section height expansion method. In addition, only adopting the I-section height expansion approach can present an I-section dematerialization rate of up to 17.9%. Finally, the slab concrete can reach the dematerialization rate of 33.3%, as already stated, by utilizing UHPC instead of NC.

Given the exposure and the main question addressed in the present work, the present thesis sustains the statement that elevated dematerialization rates in continuous conventional composite beams can be reached by using HSS alveolar I-sections and slabs of UHPC, even when instability occurs, while maintaining initial bending stiffness and ultimate loads.

7.2 SUGGESTIONS FOR FUTURE RESEARCH

The potential for future work adopting the following approaches is identified to further the investigations presented in this study:

- Four-point bending tests of steel-UHPC composite alveolar beams under hogging bending focusing on the LDB behavior;
- Experimental and numerical assessments on the WPB behavior of steel-UHPC composite alveolar beams subjected to sagging bending;

- Analyses on the dematerialization of simply supported composite beams under sagging bending by using HSS alveolar I-sections and slabs of UHPC;
- Studies on the LDB and WPB behavior of composite beams under hogging bending with hybrid alveolar I-sections;
- Experimental and numerical investigation on the hogging bending performance of composite alveolar beams at elevated temperatures.

REFERENCES

ADAWI, A.; YOUSSEF, M. A.; MESHALY, M. E. Experimental investigation of the composite action between hollowcore slabs with machine-cast finish and concrete topping. **Engineering Structures**, v. 91, p. 1–15, 2015.

ADAWI, A.; YOUSSEF, M. A.; MESHALY, M. E. Finite element modeling of the composite action between hollowcore slabs and the topping concrete. **Engineering Structures**, v. 124, p. 302–315, 2016.

ALMEIDA, A.C.B., **Análise inelástica de pórticos planos considerando a plasticidade distribuída e o efeito das tensões residuais nos perfis estruturais de aço**. 2006. Dissertação (Mestrado em Engenharia de Estruturas) - Universidade Federal de Minas Gerais.

ALPSTEN, G. A. **Thermal residual stresses in hot-rolled steel members (Residual stresses in thick welded plates)**. n. December, 1968.

ALPSTEN, G., **Prediction of thermal residual stresses in hot-rolled plates and shapes of structural steel**, Swedish Inst. Of Steel Const. Rep. 16.4., 1972b.

ALPSTEN, G. A.; TALL, L. Residual Stresses in Heavy Welded Shapes. **Welding Journal, res. Supl.**, v. 49, n. 3, p. 93–105, 1970.

ABAMBRES, M. *et al*. Neural Network-Based Formula for the Buckling Load Prediction of I-Section Cellular Steel Beams. **Computers**, v. 8, n. 1, 2019.

ABAMBRES, M.; QUACH, W. M. Residual stresses in steel members: A review of available analytical expressions. **International Journal of Structural Integrity**, v. 7, n. 1, p. 70–94, 2016.

AGLAN, A.; REDWOOD, R. **Web Buckling in Castellated Beams**. Proceedings of the Department of Civil Engineering and Applied Mechanics. **Anais**...McGill University, Montreal, Canada: 1974.

ALPSTEN, G. A. Prediction of thermal residual stresses in hot- rolled plates and shapes of structural steel. **IABSE Ninth Congress**, 1972.

ALPSTEN GA; TALL L. Residual Stresses in Heavy Welded Shapes. **Welding Journal (NY)**, v. 49, n. 3, 1970.

AMARAL, T. V *et al*. Lateral-distortional buckling of continuous steel-concrete composite beam. **IBRACON Structures and Materials Journal**, v. 11, n. 4, p. 719–737, 2018.

AMAYREH, L.; SAKA, M. P. Failure load prediction of castellated beams using artificial neural networks. **Asian Journal of Civil Engineering (Building and Housing)**, v. 6, n. 1–2, p. 35–54, 2005.

AMERICAN ASSOCIATION OF STATE AND HIGHWAY TRANSPORTATION OFFICIALS. (AASHTO) (2017). **AASHTO LRFD Bridge Design Specifications**, 8th ed. with 2017 Interim Provisions, AASHTO, Washington, DC.

AMERICAN INSTITUTE OF STEEL CONSTRUCTIONANST/AISC - **AISC 360-16**: Specification for Structural Steel Buildings. Chicago, EUA, 2016.

REFERÊNCIAS BIBLIOGRÁFICAS

AMERICAN INSTITUTE OF STEEL CONSTRUCTIONANST/AISC - **AISC 360-22**: Specification for Structural Steel Buildings. Chicago, EUA, 2022.

ARAUJO, H. F. *et al*. Lateral-distortional buckling of steel-concrete composite beams: Kinematics, constrained-mode GBT and analytical formulae. **Journal of Constructional Steel Research**, v. 192, n. February, p. 107210, 2022.

ARCELORMITTAL. **ACB and Angelina beams - A new generation of beams with large web openings**. Disponível em: <https://constructalia.arcelormittal.com/en/products/cellular_beams>. Acesso em: 1 out. 2023.

ASSOCIAÇÃO BRASILEIRA DE NORMAS TÉCNICAS. **ABNT NBR 8800.** Projeto de Estruturas de Aço e de Estruturas Mistas de Aço e Concreto de Edifícios, Rio de Jaineiro, Brasil, 2008.

ASSOCIAÇÃO BRASILEIRA DE NORMAS TÉCNICAS. **ABNT NBR 8800.** Projeto de Estruturas de Aço e de Estruturas Mistas de Aço e Concreto de Edificações, Rio de Jaineiro, Brasil, 2024.

ASTM A370-24. Standard Test Methods and Definitions for Mechanical Testing of Steel 599 Products, **ASTM International**, 2024.

ASTM C1856/C1856M-17. Standard Practice for Fabricating and Testing Specimens of Ultra-High Performance Concrete, **ASTM International**, West Conshohocken, 2017.

BADALASSI, M. *et al*. Influence of variability of material mechanical properties on seismic performance of steel and steel – concrete composite structures. **Bull Earthquake Eng**, v. 15, p. 1559–1607, 2017.

BAKER, T. N. Microalloyed steels. **Ironmaking and Steelmaking**, v. 43, n. 4, p. 264–307, 2016.

BAN, H. *et al*. Research progress on the mechanical property of high strength structural steels. **Advanced Materials Research**, v. 250–253, p. 640–648, 2011.

BAN, H. *et al*. Overall buckling behavior of 460 MPa high strength steel columns: Experimental investigation and design method. **Journal of Constructional Steel Research**, v. 74, p. 140–150, 2012.

BAN, H. *et al*. Residual stress of 460 MPa high strength steel welded i section: Experimental investigation and modeling. **International Journal of Steel Structures**, v. 13, n. 4, p. 691–705, 2013.

BAN, H.; SHI, G. A review of research on high-strength steel structures. **Proceedings of the Institution of Civil Engineers: Structures and Buildings**, v. 171, n. 8, p. 625–641, 2018.

BÄRNKOPF, E.; JÁGER, B.; KÖVESDI, B. Lateral–torsional buckling resistance of corrugated web girders based on deterministic and stochastic nonlinear analysis. **Thin-Walled Structures**, v. 180, n. June, p. 109880, 2022.

BARTH, K. E.; WHITE, D. W. Finite element evaluation of pier moment-rotation characteristics in continuous-span steel I Girders. **Engineering Structures**, v. 20, n. 8, p. 761–778, 1998.

BATTERMAN, R. H.; JOHNSTON, B. G. Behavior and maximum strength of metal columns. **Journal of the Structural Division**, v. 93, n. 2, p. 205–230, 1967.

BEER, H.; SCHULZ, G. The theoretical basis of the new column curves of the European Convention for Constructional Steelwork. **Construction Metallique**, v. 3, 1970.

BEG, D.; HLADNIK, L. Slenderness Limit of Class 3 I Cross-sections Made of High Strength Steel. **Journal of Constructional Steel Research**, v. 38, n. 3, p. 201–217, 1996.

BENEDETTY, C. A. *et al*. Flexural and shear behavior of steel-UHPC composite beams: a review. **Engineering Structures**, v. 293, n. July, 2023.

BENEDITO, A. V. *et al*. Effects of Niobium Addition on the Mechanical Properties and Corrosion Resistance of Microalloyed Steels: A Review. **Buildings**, v. 14, n. 5, p. 1–18, 2024.

BENINCÁ, M. E.; MORSCH, I. B. Numerical simulation of composite steel-concrete alveolar beams: Web-post buckling, vierendeel and flexural mechanisms. **Latin American Journal of Solids and Structures**, v. 17, n. 5, p. 1–28, 2020.

BJORHOVDE, R. *et al*. Residual Stresses in Thick Welded Plates. **Weld J**, v. 51, n. 8, p. 392-s, 1972.

BJORHOVDE, R. Columns: From Theory To Practice. **Engineering Journal**, v. 25, n. 1, p. 21–34, 1988.

BRADFORD, M. A. Distortional buckling of elastically restrained cantilevers. **Journal of Constructional Steel Research**, v. 47, n. 1–2, p. 3–18, 1998.

BRADFORD, M. A. Strength of compact steel beams with partial restraint. **Journal of Constructional Steel Research**, v. 53, n. 2, p. 183–200, 2000.

BRADFORD, M. A.; GAO, Z. DLSTORTIONAL BUCKLING SOLUTIONS FOR Restraint by slab Distortion of web Flange remains rigid. **Journal of Structural Engineering**, v. 118, n. 1, p. 73–89, 1992.

BRADFORD, M. A.; JOHNSON, R. P. Inelastic Buckling of Composite Bridge Girders Near Internal Supports. **Proceedings of the Institution of Civil Engineers (London)**, v. 83, n. pt 2, p. 143–159, 1987.

BRAGA, J. J. V. *et al*. Failure mode and strength prediction of laterally braced Litzka-type castellated beams. **Journal of Constructional Steel Research**, v. 184, n. June 2021, p. 106796, 2021.

BRITISH STANDARDS INSTITUTION. **BS 4360:1990:** Weldable structural steels, BSI, London, UK. 1990.

BUI, V. T. *et al*. Fully nonlinear analysis of steel-concrete composite girder with web local buckling effects. **International Journal of Mechanical Sciences**, v. 184, n. April, p. 105729, 2020.

CAI, M. *et al*. Cracking control technique for continuous steel-concrete composite girders under negative bending moment. **Archives of Civil Engineering**, v. 69, n. 3, p. 239–251, 2023.

CARREIRA, D.; CHU, K. Stress-strain relationship for plain concrete in compression. **ACI Journal Proceedings**, v. 82, n. 6, 1985.

CARREIRA, D. J.; CHU, K. H. Stress-Strain Relationship for Reinforced Concrete in Tension. **ACI Journal Proceedings**, v. 83, n. 1, 1986.

CARVALHO, A. S. DE *et al*. Moment gradient factor for steel I-beams with sinusoidal web openings. **Journal of Constructional Steel Research**, v. 202, n. October 2022, p. 107775, 2023.

CEN. **EN 1090-2:** Execution of Steel and Aluminium Structures – Part 2: Technical Requirements for Steel Structures, European Committee for Standardization, 2018.

CHACÓN, R.; MIRAMBELL, E.; REAL, E. Influence of designer-assumed initial conditions on the numerical modelling of steel plate girders subjected to patch loading. **Thin-Walled Structures**, v. 47, p. 391–402, 2009.

CHACÓN, R.; SERRAT, M.; REAL, E. The influence of structural imperfections on the resistance of plate girders to patch loading. **Thin-Walled Structures**, v. 53, p. 15–25, 2012.

CHEN, H. *et al*. High-strength steel beams with hexagonal web openings under impact load. **Journal of Constructional Steel Research**, v. 207, n. April, 2023.

CHEN, S. **Instability of composite beams in hogging bending**. University of Warwick, 1992.

CHEN, S. *et al*. Experimental and numerical investigations of Q690D H-section columns under lateral cyclic loading. **Journal of Constructional Steel Research**, v. 121, p. 268–281, 2016.

CHEN, S.; JIA, Y. Numerical investigation of inelastic buckling of steel–concrete composite beams prestressed with external tendons. **Thin-Walled Structures**, v. 48, n. 3, p. 233–242, 2010.

CHEN, S.; LIU, J. ZHI; CHAN, T. M. Material properties and residual stresses of welded high strength steel and hybrid I-sections. **Engineering Structures**, v. 276, n. December 2022, p. 115293, 2023.

CHEN, S.; WANG, X. Finite element analysis of distortional lateral buckling of continuous composite beams with transverse web stiffeners. **Advances in Structural Engineering**, v. 15, n. 9, p. 1607–1616, 2012.

CHUNG, K. F.; LAWSON, R. M. Simplified design of composite beams with large web openings to Eurocode 4. **Journal of Constructional Steel Research**, v. 57, n. 2, p. 135–164, 2001.

CLARIN, M. **High strength steel: local buckling and residual stresses**. Lulea University of Technology, 2004.

COUTO, C. Neural network models for the critical bending moment of uniform and tapered beams. **Structures**, v. 41, n. February, p. 1746–1762, 2022.

COUTO, C.; VILA REAL, P. Numerical investigation on the influence of imperfections in the lateral-torsional buckling of beams with slender I-shaped welded sections. **Thin-Walled Structures**, v. 145, n. October, p. 106429, 2019.

DA SILVA, L. V.; MESQUITA, L. M. R. Elastic lateral-torsional buckling of cellular beams. **Structures**, v. 63, n. April, p. 106392, 2024.

DE ANGELIS, A.; PECCE, M. R.; LOGORANO, G. Evaluation of the plastic hinge length of steel-concrete composite beams under hogging moment. **Engineering Structures**, v. 191, n. April, p. 674–685, 2019.

DE CARVALHO, A. S. *et al*. New formulas for predicting the lateral–torsional buckling strength of steel I-beams with sinusoidal web openings. **Thin-Walled Structures**, v. 181, n. June, p. 110067, 2022.

DE CARVALHO, A. S. *et al*. Elastic lateral-torsional buckling behavior of steel I-beams with sinusoidal web openings. **Structures**, v. 47, n. November 2022, p. 23–36, 2023.

DE CARVALHO, A. S.; ROSSI, A.; MARTINS, C. H. Assessment of lateral–torsional buckling in steel I-beams with sinusoidal web openings. **Thin-Walled Structures**, v. 175, n. March, p. 109242, 2022.

DE OLIVEIRA, J. P.; CARDOSO, D. C. T.; SOTELINO, E. D. Elastic flexural local buckling of Litzka castellated beams: Explicit equations and FE parametric study. **Engineering Structures**, v. 186, n. November 2018, p. 436–445, 2019.

DE SOUSA, A. M. D. *et al*. Behavior and punching capacity of flat slabs with the rational use of UHPFRC: NLFEA and analytical predictions. **Engineering Structures**, v. 244, n. March, p. 112774, 2021.

DEEPHA, R.; JAYALEKSHMI, S.; JAGADEESAN, K. Nonlinear analysis of castellated ISMB150 – I beam with hexagonal openings – A finite element approach. **Materials Today: Proceedings**, n. xxxx, 2020.

DEGTYAREV, V. V.; TSAVDARIDIS, K. D. Buckling and ultimate load prediction models for perforated steel beams using machine learning algorithms. **Journal of Building Engineering**, v. 51, n. March, p. 104316, 2022.

DEKKER, N. W.; KEMP, A. R.; TRINCHERO, P. Factors influencing the strength of continuous composite beams in negative bending. **Journal of Constructional Steel Research**, v. 34, n. 2–3, p. 161–185, 1995.

DIAS, J. V. F. **Determination of the elastic critical moment to lateral distortional buckling of continuous and semicontinuous composite beams**. Federal University of Minas Gerais, 2018.

DIAS, J. V. F. *et al*. Elastic Critical Moment of Lateral-Distortional Buckling of Steel-Concrete Composite Beams under Uniform Hogging Moment. **International Journal of Structural Stability and Dynamics**, v. 19, n. 7, 2019.

DING, J. *et al*. Mechanical properties and engineering application of single-span steel-concrete double-sided composite beams. **Journal of Building Engineering**, v. 40, n. January, p. 102644, 2021.

DWIGHT, J. B.; WHITE, J. D. **Prediction of weld shrinkage stresses in plate structures**. Preliminary Report, 2nd International Colloquium on Stability of Structures. **Anais**...Belgium: Liège, ECCS-IABSE, 1977. Disponível em: <http://refhub.elsevier.com/S0263-8231(21)00092-6/sb74>

EARLS, C. J. Effects of material property stratification and residual stresses on single angle flexural ductility. **Journal of Constructional Steel Research**, v. 51, p. 147–175, 1999.

EBRAHIMI, S.; ZAHRAI, S. M.; MIRGHADERI, S. R. Cyclic Performance Evaluation of Hollow Structural Section (HSS) and Concrete-Filled Tube (CFT) Braces. **International Journal of Structural Stability and Dynamics**, v. 19, n. 11, 2019.

ECCS – **European Convention for Constructional Steelwork**. Ultimate Limit State Calculations of Sway Frames with Rigid Joints. No. 33, 1984.

ELLOBODY, E. Nonlinear analysis of cellular steel beams under combined buckling modes. **Thin-Walled Structures**, v. 52, p. 66–79, 2012a.

ELLOBODY, E. Behaviour of normal and high-strength castellated steel beams. **Proceedings of the Institution of Civil Engineers - Structures and Buildings**, v. 165, n. 10, p. 529–542, 2012b.

ERDAL, F.; SAKA, M. P. Ultimate load carrying capacity of optimally designed steel cellular beams. **Journal of Constructional Steel Research**, v. 80, p. 355–368, 2013.

EUROCODE 2. EN 1992-1-1:2023 - Design of concrete structures - Part 1-1: General ruels and rules for buildings, standard, European Committee for Standardization, 2023.

EUROCODE 3. EN 1993-1-1:2022 - Design of steel structures - Part 1-1: General rules and rules for buildings, standard, European Committee for Standardization, 2022.

EUROCODE 3. EN 1993-1-5:2006 - Design of steel structures – Part 1-5: Plated Structural Elements Buildings, standard, European Committee for Standardization, 2006.

EUROCODE 3. EN 1993-1-12:2007 - Design of steel structures – Part 1-12: Additional rules for the extension of EN 1993 up to steel grades S700, standard, European Committee for Standardization, 2007.

EUROCODE 3. EN 1993-1-13:2024 - Design of steel structures — Part 1-13: Beams with large web openings, standard, European Committee for Standardization, 2024.

EUROCODE 3. ENV 1993-1-1:2005 - Design of steel structures - Part 1-1: General rules and rules for buildings, standard, European Committee for Standardization, 2005.

EUROCODE 4. EN 1994-1-1:2004 - Design of composite steel and concrete structures —Part 1-1: General rules and rules for buildings, standard, European Committee for Standardization, 2004.

EUROCODE 4. ENV 1994-1-1:1992 - Design of composite steel and concrete structures — Part 1-1: General rules and rules for buildings, standard, European Committee for Standardization, 1992.

EUROCODE 4. prEN 1994-1-1 - Design of composite steel and concrete structures —Part 1-1: General rules and rules for buildings, standard, European Committee for Standardization, 2024.

FAN, C. X. R. **Buckling in continuous composite beams**. University of Warwick, 1990.

FAN, J. *et al.* Experimental and analytical research on the flexural behaviour of steel–ECC composite beams under negative bending moments. **Engineering Structures**, v. 210, n. February 2020, p. 110309, 2020.

FANG, J. *et al.* Behaviour of composite beams with beam-to-girder end-plate connection under hogging moments. **Engineering Structures**, v. 235, n. 230, p. 112030, 2021.

FANG, Z. *et al.* Interfacial shear and flexural performances of steel–precast UHPC composite beams: Full-depth slabs with studs vs. demountable slabs with bolts. **Engineering Structures**, v. 260, n. April, p. 114230, 2022a.

FANG, Z. *et al.* Static behavior of grouped stud shear connectors in steel–precast UHPC composite structures containing thin full-depth slabs. **Engineering Structures**, v. 252, n. October 2021, p. 113484, 2022b.

FARES, S. S.; COULSON, J.; DINEHART, D. W. Castellated and Cellular Beam Design 31. **American Institute of Steel Construction**, p. 1–116, 2016.

FERREIRA, F. P. V. *et al*. Buckling and post-buckling analyses of composite cellular beams. **Composite Structures**, v. 262, p. 113616, 2021a.

FERREIRA, F. P. V. *et al*. Composite action on web-post buckling shear resistance of composite cellular beams with PCHCS and PCHCSCT. **Engineering Structures**, v. 246, n. August, p. 113065, 2021b.

FERREIRA, F. P. V. *et al*. Ultimate strength prediction of steel–concrete composite cellular beams with PCHCS. **Engineering Structures**, v. 236, n. January, p. 112082, 2021c.

FERREIRA, F. P. V. *et al*. Buckling and post-buckling analyses of composite cellular beams. **Composite Structures**, v. 262, 2021d.

FERREIRA, F. P. V. *et al*. Steel-concrete-composite beams with precast hollow-core slabs: A sustainable solution. **Sustainability (Switzerland)**, v. 13, n. 8, 2021e.

FERREIRA, F. P. V. *et al*. EC3 design of web-post buckling resistance for perforated steel beams with elliptically-based web openings. **Thin-Walled Structures**, v. 175, n. January, p. 245–262, 2022a.

FERREIRA, F. P. V. *et al*. Lateral–torsional buckling resistance prediction model for steel cellular beams generated by Artificial Neural Networks (ANN). **Thin-Walled Structures**, v. 170, n. September 2021, p. 108592, 2022b.

FERREIRA, F. P. V. *et al*. Web-post buckling resistance calculation of perforated high-strength steel beams with elliptically-based web openings for EC3. **Structures**, v. 55, n. June 2023, p. 245–262, 2023.

FERREIRA, F. P. V.; MARTINS, C. H. LRFD for Lateral-Torsional Buckling Resistance of Cellular Beams. **International Journal of Civil Engineering**, v. 18, n. 3, p. 303–323, 2020.

FERREIRA, F. P. V.; MARTINS, C. H.; NARDIN, S. **Advances in composite beams with web openings and composite cellular beams**. **Journal of Constructional Steel Research**Elsevier Ltd, , 2020a. Disponível em: <https://doi.org/10.1016/j.jcsr.2020.106182>

FERREIRA, F. P. V.; MARTINS, C. H.; NARDIN, S. Sensitivity Analysis of Composite Cellular Beams to Constitutive Material Models and Concrete Fracture. **International Journal of Structural Stability and Dynamics**, v. 21, n. 01, 2020b.

FERREIRA, F. P. V.; MARTINS, C. H.; NARDIN, S. A parametric study of steel-concrete composite beams with hollow core slabs and concrete topping. **Structures**, v. 28, n. July, p. 276–296, 2020c.

FERREIRA, F. P. V.; MARTINS, C. H.; NARDIN, S. Assessment of web post buckling resistance in steel-concrete composite cellular beams. **Thin-Walled Structures**, v. 158, n. October 2020, p. 106969, 2021.

FERREIRA, F. P. V.; ROSSI, A.; MARTINS, C. H. Lateral-torsional buckling of cellular beams according to the possible updating of EC3. **Journal of Constructional Steel Research**, v. 153, p. 222–242, 2019.

FERREIRA FILHO, J. O. *et al*. Experimental and numerical flexural buckling resistance of high strength steel columns and beam-columns. **Engineering Structures**, v. 265, n. April, p. 114414, 2022.

FRANÇA, G. M. *et al*. An appraisal of the Vierendeel mechanism capacity of cellular beams with sinusoidal openings. **Journal of Constructional Steel Research**, v. 198, n. September, p. 107539, 2022.

GALAMBOS, T. V. Inelastic Lateral Buckling of Beams. **Journal of the Structural Division**, v. 89, n. 5, p. 217–242, out. 1963.

GALAMBOS, T. V. **Guide to stability design criteria for metal structures**. Fourth ed. ed. John Wiley & Sons, 1988.

GALAMBOS, T. V.; KETTER, R. L. Columns under combined bending and thrust. **Journal of the Engineering Mechanics Division**, v. 85, p. 1–30, 1959.

GENG, K. *et al*. Experimental study on the mechanical behaviour of castellated composite beams under a negative bending moment. **Structures**, v. 47, p. 953–965, 2023.

GHOLIZADEH, S.; PIRMOZ, A.; ATTARNEJAD, R. Assessment of load carrying capacity of castellated steel beams by neural networks. **Journal of Constructional Steel Research**, v. 67, n. 5, p. 770–779, 2011.

GIZEJOWSKI, M. A.; SALAH, W. A. Numerical modeling of composite castellated beams. **Composite Construction in Steel and Concrete VI - Proceedings of the 2008 Composite Construction in Steel and Concrete Conference**, p. 554–565, 2008.

GIZEJOWSKI, M. A.; SALAH, W. A. **Stability and ductility of castellated composite beams subjected to hogging bending**. Proceedings of SDSS' Rio 2010: International Colloquium Stability and Ductility of Steel Structures. **Anais**...2010a. Disponível em: <https://www.scopus.com/inward/record.uri?eid=2-s2.0-84890254428&partnerID=40&md5=f6ea14864e95e160d941b5c43734afd5>

GIZEJOWSKI, M. A.; SALAH, W. A. Restrained distortional buckling strength of steel-concrete composite beams - A review of current practice and new developments. **10th International Conference Modern Building Materials, Structures and Techniques**, n. November, p. 604–612, 2010b.

GRACIANO, C.; CASANOVA, E.; MARTÍNEZ, J. Imperfection sensitivity of plate girder webs subjected to patch loading. **Journal of Constructional Steel Research**, v. 67, n. 7, p. 1128–1133, 2011.

GRILO, L. F. *et al*. Design procedure for the web-post buckling of steel cellular beams. **Journal of Constructional Steel Research**, v. 148, p. 525–541, 2018.

GUEZOULI, S.; LACHAL, A. Numerical analysis of frictional contact effects in push-out tests. **Engineering Structures**, v. 40, p. 39–50, 2012.

GÜNTHER, H.-P. **Use and application of high-performance steel for steel structures**. [s.l: s.n.].

GUO, D. *et al*. Residual stresses of Q235 steel wallboard - Q460 high-strength steel column structural system. **Journal of Constructional Steel Research**, v. 197, n. April, p. 107450, 2022.

GUO, J. *et al*. Mechanical performance of hybrid high-strength steel composite cellular beam under low cyclic loading. **Journal of Constructional Steel Research**, v. 203, n. October 2022, 2023.

HAMODA, A. *et al*. Behaviour of composite high performance concrete slab on steel I-beams subjected to static hogging moment. **Engineering Structures**, v. 140, p. 51–65, 2017.

HANSWILLE, G.; LINDNER, J.; MÜNICH, D. Lateral Torsional Buckling of Composite Beams [in German]. **Stahlbau**, v. 67, p. 525–535, 1998.

HASSANEIN, M. F. *et al*. Effect of using slender flanges on EN 1993-1-5 design model of mono-symmetric S460 corrugated web bridge girders. **Structures**, v. 33, n. April, p. 330–342, 2021.

HE, S. *et al*. Effective width evaluation for HSS-UHPC composite beams with perfobond strip connectors. **Engineering Structures**, v. 295, n. December 2022, p. 116828, 2023.

HECHLER, O.; MÜLLER, C.; SEDLACEK, G. Investigations on beams with multiple regular web openings. **Composite Construction in Steel and Concrete V**, p. 390–401, 2006.

HILLERBORG, A.; MODÉER, M.; PETERSSON, P.-E. Analysis of crack formation and crack growth in concrete by means of fracture mechanics and finite elements. **Cement and Concrete Research**, v. 6, n. 6, p. 773–781, 1976.

HOPE-GILL, M. C.; JOHNSON, R. P. Tests on three-span continuous composite beams. **Proc. Instn Civ. Engrs**, v. 61, p. 367–381, 1976.

HOSSEINPOUR, M. *et al*. New predictive equations for LDB strength assessment of steel–concrete composite beams. **Engineering Structures**, v. 258, n. February, p. 114121, 2022.

HOSSEINPOUR, M.; SHARIFI, Y. Finite element modelling of castellated steel beams under lateral-distortional buckling mode. **Structures**, v. 29, n. October 2020, p. 1507–1521, 2021.

HOSSEINPOUR, M.; SHARIFI, Y.; SHARIFI, H. Neural network application for distortional buckling capacity assessment of castellated steel beams. **Structures**, v. 27, n. July 2020, p. 1174–1183, 2020.

HRADIL, P. *et al*. Evaluation of ductility limits for structural steel design. **Journal of Constructional Steel Research**, v. 135, n. September 2016, p. 1–10, 2017.

HU, Y. *et al*. Flexural performance of steel-UHPC composite beams with shear pockets. **Structures**, v. 27, n. May, p. 570–582, 2020.

HUANG, B.; ZHANG, W. F. Lateral-Torsional Buckling Performance of High Strength Steel Welded I-Section Beam-Columns. **Journal of Failure Analysis and Prevention**, v. 22, n. 4, p. 1478–1494, 2022.

HUANG, Y. *et al*. Strengthening of concrete structures with ultra high performance fiber reinforced concrete (UHPFRC): A critical review. **Construction and Building Materials**, v. 336, n. April, 2022.

HUBER, A. W.; BEEDLE, L. S. Residual stress and the compressive strength of steel. **Welding Journal**, v. 33, n. 12, p. 589–614, 1954.

HUNG, C.-C.; EL-TAWIL, S.; CHAO, S.-H. A Review of Developments and Challenges for UHPC in Structural Engineering: Behavior, Analysis, and Design. **Journal of Structural Engineering**, v. 147, n. 9, p. 1–19, 2021.

ITO, M. *et al*. Experimental Study on Moment – Plastic Rotation Capacity of Hybrid Beams. **JOURNAL OF BRIDGE ENGINEERING**, v. 10, n. 4, p. 490–496, 2005.

J. MURZEWSKI. **Random load carrying capacity of rod structures [in Polish]**. PWN, Serie ed. Warszawa, 1976.

JOHNSON, R. P. **Composite Structures of Steel and Concrete**. 2004.

JOHNSON, R. P.; CHEN, S. Stability of continuous composite plate girders with U-frame action. **Proceedings of the Institution of Civil Engineers: Structures and Buildings**, v. 99, n. 2, p. 187–197, 1993.

JOHNSON, R. P.; FAN, C. K. R. Distortional lateral buckling of continuous composite beams. **Proceedings - Institution of Civil Engineers. Part 2. Research and theory**, v. 91, n. pt 2, p. 131–161, 1991.

JÖNSSON, J.; STAN, T. C. European column buckling curves and finite element modelling including high strength steels. **Journal of Constructional Steel Research**, v. 128, p. 136–151, 2017.

JURKIEWIEZ, B.; TOUT, F.; FERRIER, E. Push-out and bending tests of steel-concrete adhesively bonded composite elements. **Engineering Structures**, v. 231, n. September 2020, p. 111717, 2021.

KABIR, M. I. *et al*. Flexural behaviour of ECC-LWC encased slender high strength steel composite beams. **Journal of Constructional Steel Research**, v. 173, p. 106253, 2020.

KABIR, M. I.; LEE, C. K.; ZHANG, Y. X. Numerical and analytical investigations of flexural behaviours of ECC–LWC encased steel beams. **Engineering Structures**, v. 239, n. April, p. 112356, 2021.

KALA, Z.; VALEŠ, J. Global sensitivity analysis of lateral-torsional buckling resistance based on finite element simulations. **Engineering Structures**, v. 134, p. 37–47, 2017a.

KALA, Z.; VALEŠ, J. Sensitivity assessment and lateral-torsional buckling design of I-beams using solid fi nite elements. **Journal of Constructional Steel Research**, v. 139, p. 110–122, 2017b.

KALA, Z.; VALEŠ, J.; MARTINÁSEK, J. Inelastic finite element analysis of lateral buckling for beam structures. **Procedia Engineering**, v. 172, p. 481–488, 2017.

KANG, L.; HONG, S.; LIU, X. Shear behaviour and strength design of cellular beams with circular or elongated openings. **Thin-Walled Structures**, v. 160, n. July 2020, p. 107353, 2021.

KANG, L.; MENG, L.; LIN, Y. Experimental and numerical investigation of lateral torsional buckling behavior and capacity of welded Q460 beams. **Journal of Constructional Steel Research**, v. 172, p. 106166, 2020.

KANG, S. B. *et al*. Global buckling of laterally-unrestrained Q460GJ beams with singly symmetric I-sections. **Journal of Constructional Steel Research**, v. 145, p. 341–351, 2018.

KERDAL, D.; NETHERCOT, D. A. Failure Modes for Castellated Beams. **Journal of Constructional Steel Research**, v. 4, p. 295–315, 1984.

KHAPLE, S. *et al*. Effect of Niobium Addition on Microstructure and Mechanical Properties of Fe–7Al–0.35C Low-Density Steel. **Metallography, Microstructure, and Analysis**, v. 9, n. 2, p. 127–139, 2020.

KIM, D. K. *et al*. Strength and residual stress evaluation of stub columns fabricated from 800 MPa high-strength steel. **Journal of Constructional Steel Research**, v. 102, p. 111–120, 2014.

KITAOKA, S. *et al*. Strength of lateral-torsional buckling of a composite steel beam subjected to reverse curvature bending. **Composite Construction in Steel and Concrete VIII - Proceedings of the 8th International Conference on Composite Construction in Steel and Concrete, 2017**, n. August, p. 334–345, 2017.

KÖVESDI, B.; MECSÉRI, B. J.; DUNAI, L. Imperfection analysis on the patch loading resistance of girders with open section longitudinal stiffeners. **Thin Walled Structures**, v. 123, n. August 2017, p. 195–205, 2018.

KRAHL, P. A. *et al*. Effect of curing age on pullout behavior of aligned and inclined steel fibers embedded in UHPFRC. **Construction and Building Materials**, v. 266, p. 121188, 2021.

KRAHL, P. A.; CARRAZEDO, R.; EL DEBS, M. K. Mechanical damage evolution in UHPFRC: Experimental and numerical investigation. **Engineering Structures**, v. 170, n. May, p. 63–77, 2018.

LAWSON; HICKS. **Design of Composite Beams with Large web openings**. [s.l.] The Steel Constrution Institute, 2011.

LAWSON, R. M. *et al*. Design of composite asymmetric cellular beams and beams with large web openings. **Journal of Constructional Steel Research**, v. 62, n. 6, p. 614–629, 2006.

LAWSON, R. M.; SAVERIRAJAN, A. H. A. Simplified elasto-plastic analysis of composite beams and cellular beams to Eurocode 4. **Journal of Constructional Steel Research**, v. 67, n. 10, p. 1426–1434, 2011.

LE, T. *et al*. Buckling of welded high-strength steel I-beams. **Journal of Constructional Steel Research**, v. 168, p. 105938, 2020a.

LE, T. *et al*. Residual stresses in welded high-strength steel I-Beams. **Journal of Constructional Steel Research**, v. 167, p. 105849, 2020b.

LE, T. .; BRADFORD, M. A. .; VALIPOUR, H. R. **Experimental and Numerical Study of Flexural-Torsional Buckling of Web-Tapered High-Strength Steel I-Beams**. Wang, C.M., Dao, V., Kitipornchai, S. (eds) EASEC16. Lecture Notes in Civil Engineering, vol 101. Springer. **Anais**...2021. Disponível em: <https://doi.org/10.1007/978-981-15-8079-6_2>

LEBASTARD, M. *et al*. Impact of the fabrication process on the lateral–torsional buckling of welded I-section beams. **Thin-Walled Structures**, v. 188, n. December 2022, p. 110761, 2023.

LEE, C.-H. *et al*. Flexural Strength and Rotation Capacity of I-Shaped Beams Fabricated from 800-MPa Steel. **Journal of Structural Engineering**, v. 139, n. 6, p. 1043–1058, 2013.

LEE, J.; FENVES, G. L. Plastic-Damage Model for Cyclic Loading of Concrete Structures. **Journal of Engineering Mechanics**, v. 124, n. 8, p. 892–900, 1998.

LEE, S. H.; CHOI, B. J. Mechanical properties of astm a572 grades 50 and 60 steels at high temperatures. **Applied Sciences (Switzerland)**, v. 11, n. 24, 2021.

LI, B. V. C.; LEUNG, C. K. Y. Steady-State and Multiple Cracking of Short Random Fiber Composites. **Journal of Engineering Mechanics**, v. 118, n. 11, p. 2246–2264, 1993.

LI, L. *et al*. O.I.C.-based design of mono-symmetric I-sections under simple load cases. **Thin-Walled Structures**, v. 174, n. July 2021, p. 109134, 2022.

LI, L. *et al*. Fire local stability of steel I-sections under simple load cases. **Engineering Structures**, v. 283, n. July 2022, p. 115874, 2023.

LI, L.; BOISSONNADE, N. Design of mono-symmetric I-sections under combined load cases by the Overall Interaction Concept. **Thin-Walled Structures**, v. 182, n. June 2022, p. 110280, 2023.

LI, T. J.; LI, G. Q.; WANG, Y. B. Residual stress tests of welded Q690 high-strength steel box- and H-sections. **Journal of Constructional Steel Research**, v. 115, p. 283–289, 2015.

LIEW, J. Y. R.; YAN, J. B.; HUANG, Z. Y. Steel-concrete-steel sandwich composite structures-recent innovations. **Journal of Constructional Steel Research**, v. 130, p. 202–221, 2017.

LIMBACHIYA, V.; SHAMASS, R. Application of Artificial Neural Networks for web-post shear resistance of cellular steel beams. **Thin-Walled Structures**, v. 161, n. September 2020, p. 107414, 2021.

LIU, M. *et al*. Web-post buckling of bolted castellated steel beam with octagonal web openings. **Journal of Constructional Steel Research**, v. 164, n. October 2019, p. 105794, 2020.

LIU, X. *et al*. Finite element modelling of steel-concrete composite beams with high-strength friction-grip bolt shear connectors. **Finite Elements in Analysis and Design**, v. 108, p. 54–65, 2016.

LIU, X. *et al*. Experimental and Numerical Studies on the Negative Flexural Behavior of Steel-UHPC Composite Beams. **Advances in Civil Engineering**, v. 2021, 2021.

LIU, X. *et al*. Behaviour of continuous steel–concrete composite beams strengthened with CFRP sheets at hogging-moment region. **Composite Structures**, v. 291, n. April, p. 115695, 2022.

LIU, Y. *et al*. Three failure modes of High-Strength Steel (HSS) perfobond connector embedded in UHPC. **Engineering Structures**, v. 286, n. December 2022, p. 116147, 2023a.

LIU, Y. *et al*. Shear performance and failure process of perfobond connector in steel-UHPC composite structures. **Structures**, v. 50, n. November 2022, p. 1461–1475, 2023b.

LU, W. L. *et al*. Study on mechanical behavior of steel-UHPC-NC composite beams under negative bending moment. **Case Studies in Construction Materials**, v. 17, n. August, p. e01593, 2022.

LUBLINER, J. *et al*. A plastic-damage model for concrete. **International Journal of Solids and Structures**, v. 25, n. 3, p. 299–326, 1989.

MA, Y. *et al*. Experimental and analytical investigation on shear mechanism of steel-UHPC composite T-Perfobond shear connectors. **Engineering Structures**, v. 286, n. November 2022, p. 116061, 2023.

MANSUR, M. A.; CHIN, M. S.; WEE, T. H. Stress-Strain Relationship of High-Strength Fiber Concrete in Compression. **Journal of Materials in Civil Engineering**, v. 11, n. 1, p. 21, 1999.

MARTIN, P. O. *et al*. An analytical method for the resistance of cellular beams with sinusoidal openings. **Engineering Structures**, v. 143, p. 113–126, 2017.

MCFALLS, R. K. **A study of welded columns manufactured from flame-cut plates**. Lehigh University, 1967.

MELA, K.; HEINISUO, M. Weight and cost optimization of welded high strength steel beams. **Engineering Structures**, v. 79, p. 354–364, 2014.

MEN, P. *et al*. Behaviour of steel–concrete composite girders under combined negative moment and shear. **Journal of Constructional Steel Research**, v. 179, p. 106508, 2021a.

MEN, P. *et al*. Web shear buckling of steel–concrete composite girders in negative-moment regions. **Engineering Structures**, v. 237, n. December 2020, 2021b.

MEN, P. *et al*. Experimental Investigation of the Shear Behavior of Slender Continuous Steel–Concrete Composite Girders in Hogging Moment. **Journal of Structural Engineering**, v. 149, n. 1, p. 1–16, 2023.

MENG, L.; KANG, L. Numerical investigation on lateral torsional buckling of welded Q460 steel beams. **Procedia Engineering**, v. 210, p. 220–227, 2017.

MINISTRY OF CONSTRUCTION. **GB 50017-2017: Code for Design of Steel Structures. (China Architecture & Building Press, Beijing, 2018)**.

MIRANDA, L. G. J. *et al*. Comparative analysis of fire-adapted models for the shear buckling strength of web-posts in castellated steel beams. **Fire Safety Journal**, v. 138, n. December 2022, p. 103796, 2023.

MOGHBELI, A.; SHARIFI, Y. New predictive equations for lateral-distortional buckling capacity assessment of cellular steel beams. **Structures**, v. 29, n. October 2020, p. 911–923, 2021.

MOHEBKHAH, A.; AZANDARIANI, M. G. Shear resistance of retrofitted castellated link beams: Numerical and limit analysis approaches. **Engineering Structures**, v. 203, n. May 2019, 2020.

MORKHADE, S. G.; GUPTA, L. M. Experimental investigation for failure analysis of steel beams with web openings. **Steel and Composite Structures**, v. 23, n. 6, p. 647–656, 2017.

MORKHADE, S. G.; GUPTA, L. M.; MARTINS, C. H. Effect of Web Post Width on Strength Capacity of Steel Beams with Web Openings: Experimental and Analytical Investigation. **Practice Periodical on Structural Design and Construction**, v. 27, n. 2, 2022.

MÜLLER, C. *et al*. **Large web openings for service integration in composite floors**. Technical Steel Research. European Comission, Contract No 7210-PR/315. Final report: [s.n.].

NAAMAN, A. E.; CHANDRANGSU, K. Innovative bridge deck system using high performance fiber-reinforced cement composites. **ACI Structural Journal**, v. 101, n. 1, p. 57–64, 2004.

NAWAR, M. T.; ARAFA, I. T.; ELHOSSEINY, O. Numerical investigation on e ff ective spans ranges of perforated steel beams. **Structures**, v. 25, n. November 2019, p. 398–410, 2020.

NERY, L. S. *et al*. Novo Procedimento para Cálculo do Momento Crítico de Flambagem Lateral com Distorção de Vigas Mistas de Aço e Concreto. **Revista da Estrutura de Aço**, v. 12, n. 02, 2023.

NGUYEN, C. L.; LEE, C. K. Flexural behaviours of Engineered Cementitious Composites – High strength steel composite beams. **Engineering Structures**, v. 249, n. August, p. 113324, 2021.

NGUYEN, T. A.; LY, H. B.; TRAN, V. Q. Investigation of ANN Architecture for Predicting Load-Carrying Capacity of Castellated Steel Beams. **Complexity**, v. 2021, 2021.

NSEIR, J. *et al*. **Lateral torsional buckling of cellular steel beams**. Proceedings of the Annual

Stability Conference Structural Stability Research Council (SSRC2012). **Anais**...Grapevine, Texas: 2012. Disponível em: <http://hdl.handle.net/1854/LU-2130334>

ODESSKII, P. D. *et al*. High-strength hot-rolled I-beams for the construction industry. **Steel in Translation**, v. 47, n. 6, p. 412–420, 2017.

OLIVEIRA, J. P. S. DE *et al*. Resistant bending moment to lateral-torsional buckling of continuous steel and concrete composite beams with transverse stiffeners. **Revista IBRACON de Estruturas e Materiais**, v. 14, n. 4, p. 1–18, 2021.

OLIVEIRA, V. M. DE *et al*. Stability behavior of steel–concrete composite cellular beams subjected to hogging moment. **Thin-Walled Structures**, v. 173, n. February, p. 108987, 2022.

OLIVEIRA, V. M. DE. **Avaliação do comportamento de vigas celulares mistas de aço e concreto em regiões de momento fletor negativo**. [s.l.] Universidade Estadual de Maringá, 2022.

OLIVEIRA, V. M. DE *et al*. Lateral Distortional Buckling Resistance Predictions of Composite Alveolar Beams: A Review. **Buildings**, v. 13, n. 3, 2023a.

OLIVEIRA, V. M. DE *et al*. Elastic and inelastic analyses of composite cellular beams in hogging moment regions. **Thin-Walled Structures**, v. 184, n. July 2022, p. 110513, 2023b.

OLIVEIRA, V. M. DE *et al*. Comparative analysis of geometric imperfections and residual stresses on the global stability behavior of cantilever composite alveolar beams. **Structures**, v. 65, n. January, p. 106634, 2024.

OLIVEIRA, V. M. DE *et al*. Steel-UHPC composite castellated beams under hogging bending: Experimental and numerical investigation. **Engineering Structures**, v. 331, n. February, 2025.

OLIVEIRA, J. P. S. **New proposition for verification of lateral distortional buckling of steel-concrete composite beams [in Portuguese]**. [s.l.] Federal University of Minas Gerais, 2018.

ORIBI, S. B. *et al*. Behaviour of cellular steel beams at ambient and high-temperature conditions. **Journal of Constructional Steel Research**, v. 207, n. February, p. 107969, 2023.

OSORIO, E.; BAIRÁN, J. M.; MARÍ, A. R. Lateral behavior of concrete under uniaxial compressive cyclic loading. **Materials and Structures**, v. 46, n. 5, p. 709–724, 2013.

PANEDPOJAMAN, P.; SAE-LONG, W.; CHUB-UPPAKARN, T. Cellular beam design for resistance to inelastic lateral-torsional buckling. **Thin-Walled Structures**, v. 99, p. 182–194, 2016.

PANEDPOJAMAN, P.; THEPCHATRI, T.; LIMKATANYU, S. Novel design equations for shear strength of local web-post buckling in cellular beams. **Thin-Walled Structures**, v. 76, p. 92–104, 2014.

PANEDPOJAMAN, P.; THEPCHATRI, T.; LIMKATANYU, S. Novel simplified equations for Vierendeel design of beams with (elongated) circular openings. **Journal of Constructional Steel Research**, v. 112, p. 10–21, 2015.

PRESSMAIR, N. *et al*. Non-linear material modelling strategy for conventional and high-performance concrete assisted by testing. **Cement and Concrete Research**, v. 161, n. March, p. 106933, 2022.

QI, J. *et al*. Flexural behavior of steel-UHPFRC composite beams under negative moment.

Structures, v. 24, n. January, p. 640–649, 2020.

QIAO, H.; GUO, Z.; CHEN, Y. Experimental investigation of a substructure in a frame with castellated steel beams in case of a column loss. **Engineering Structures**, v. 255, n. January, p. 113926, 2022.

QIU, M. *et al*. Flexural cracking behavior of steel-NC-UHPC composite beam under negative bending moment. **Engineering Structures**, v. 322, n. PA, p. 119071, 2025.

RAJANA, K.; TSAVDARIDIS, K. D.; KOLTSAKIS, E. Elastic and inelastic buckling of steel cellular beams under strong-axis bending. **Thin-Walled Structures**, v. 156, n. December 2019, p. 106955, 2020.

RAO, N.; ESTUAR, N. .; TALL, L. Residual stresses in welded shapes. **AWS Weld J**, p. 295, 1964.

ROIK, K.; HANSWILLE, G.; KINA, J. Solution for the lateral torsional buckling prob lem of composite beams [in German]. **Stahlbau**, v. 59, n. 59, p. 327–332, 1990.

ROSSI, A. *et al*. Lateral distortional buckling in steel-concrete composite beams : A review. **Structures**, v. 27, n. June, p. 1299–1312, 2020a.

ROSSI, A. *et al*. Numerical assessment of lateral distortional buckling in steel-concrete composite beams. **Journal of Constructional Steel Research**, v. 172, p. 106192, 2020b.

ROSSI, A. *et al*. Reassesement of lateral torsional buckling in hot-holled I-beams. **Structures**, v. 26, n. March, p. 524–536, 2020c.

ROSSI, A. *et al*. Assessment of lateral distortional buckling resistance in welded I-beams. **Journal of Constructional Steel Research**, v. 166, 2020d.

ROSSI, A. *et al*. Numerical Analysis of the Elastic Critical Moment To Lateral Distortional Buckling of Steel-Concrete Composite Beams. **Holos**, v. 8800, p. 1–28, 2021a.

ROSSI, A. *et al*. Stability behavior of Steel–concrete Composite Beams subjected to hogging moment. **Thin-Walled Structures**, v. 167, n. April, p. 108193, 2021b.

ROSSI, A. *et al*. The influence of structural and geometric imperfections on the LDB strength of steel – concrete composite beams. **Thin-Walled Structures**, v. 162, n. October 2020, p. 107542, 2021c.

ROSSI, A. *et al*. The influence of structural imperfections on the LTB strength of I-beams. **Structures**, v. 29, n. December 2020, p. 1173–1186, 2021d.

ROSSI, A. *et al*. The influence of structural and geometric imperfections on the LDB strength of steel–concrete composite beams. **Thin-Walled Structures**, v. 162, n. December 2020, p. 1173–1186, 2021e.

ROSSI, A. *et al*. A New Formula for Predicting Lateral Distortional Buckling Strength of I-Beams Subjected to Different Loading Conditions. **International Journal of Structural Stability and Dynamics**, v. 2250129, p. 1–29, 2022.

ROSSI, A. *et al*. A Parametric Study on the LDB Strength of Steel-Concrete Composite Beams. **Eng**, v. 4, n. 3, p. 2226–2253, 2023.

SALAH, W. A. **Modelling of instability behavior in hogging moment regions of steel-concrete composite beams**. [s.l.] Warsaw University of Technology, 2009.

SALAH, W. A. Performance of Hybrid Castellated Beams Prediction Using Finite Element Modeling. **Technology & Applied Science Research**, v. 12, n. 2, p. 8444–8451, 2022.

SCHAPER, L. *et al*. A novel residual stress model for welded I-sections. **Journal of Constructional Steel Research**, v. 188, n. October 2021, 2022.

SCHULZ, G. **The Maximum Strength of Axially Loaded Columns Considering Geometrical Imperfections and Material in Homogeneities**. [s.l.] Technical University Graz, Áustria, 1968.

SEGHIER, M. E. A. BEN *et al*. Numerical analysis and prediction of lateral- torsional buckling resistance of cellular steel beams using FEM and least square support vector machine optimized by metaheuristic algorithms. **Alexandria Engineering Journal**, v. 67, p. 489–502, 2023.

SHAMASS, R. *et al*. Web-post buckling prediction resistance of steel beams with elliptically-based web openings using Artificial Neural Networks (ANN). **Thin-Walled Structures**, v. 180, n. June, p. 109959, 2022.

SHAMASS, R.; GUARRACINO, F. Numerical and analytical analyses of high-strength steel cellular beams: A discerning approach. **Journal of Constructional Steel Research**, v. 166, p. 105911, 2020.

SHAO, Y. B.; ZHANG, Y. M.; HASSANEIN, M. F. Strength and behaviour of laterally-unrestrained S690 high-strength steel hybrid girders with corrugated webs. **Thin-Walled Structures**, v. 150, n. February, p. 106688, 2020.

SHARIF, A. M. *et al*. Use of CFRP to Maintain Composite Action for Continuous Steel–Concrete Composite Girders. **Journal of Composites for Construction**, v. 20, n. 4, p. 1–10, 2016.

SHARIFI, Y. *et al*. Study of Neural Network Models for the Ultimate Capacities of Cellular Steel Beams. **Iranian Journal of Science and Technology - Transactions of Civil Engineering**, v. 44, n. 2, p. 579–589, 2020.

SHARIFI, Y.; TOHIDI, S. Lateral-torsional buckling capacity assessment of web opening steel girders by artificial neural networks – elastic investigation. **Front. Struct. Civ. Eng.**, v. 8, n. 2, p. 167–177, 2014.

SHEEHAN, T. *et al*. Experimental study on long spanning composite cellular beam under flexure and shear. **Journal of Constructional Steel Research**, v. 116, p. 40–54, 2016.

SHI, F. W. *et al*. Flexural behavior of prefabricated composite beam with cast-in-situ UHPC: Experimental and numerical studies. **Structures**, v. 45, n. April, p. 670–684, 2022.

SHI, G.; HU, F.; SHI, Y. Recent research advances of high strength steel structures and codification of design specification in China. **International Journal of Steel Structures**, v. 14, n. 4, p. 873–887, 2014.

SHIN, D. K.; KIM, K. Flexural Strength of Composite HSB690 I-Girders in Negative Moment. **International Journal of Steel Structures**, v. 19, n. 6, p. 1875–1894, 2019.

SHOKOUHIAN, M.; SHI, Y. Flexural strength of hybrid steel I-beams based on slenderness. **Engineering Structures**, v. 93, p. 114–128, 2015.

SILVA, C. C. *et al*. Web rotational stiffness of continuous steel-concrete composite castellated beams. **Frattura ed Integrita Strutturale**, v. 13, n. 50, p. 264–275, 2019.

SILVA, C. C. *et al*. Elastic Critical Moment of Lateral Distortional Buckling of Castellated Composite Beams under Uniform Hogging Moment. **Practice Periodical on Structural Design and Construction**, v. 25, n. 4, p. 04020032, 2020.

SILVA, J.; DALCANAL, P.; MESQUITA, L. Numerical analysis of cellular steel beams failure modes in fire conditions. **Lecture Notes in Civil Engineering**, v. 1, p. 78–92, 2020.

SILVEIRA, E. G. DA. **Study of alveolar beams with emphasis on collapse modes by yielding [in Portuguse]**. Federal University of Viçosa, 2011.

SIMULIA, D. S. **ABAQUS**. 2016.

SJAARDA, M. *et al*. Fatigue Behavior of Welded Shear Studs in Precast Composite Beams. **Journal of Bridge Engineering**, v. 22, n. 11, p. 04017089, 2017.

SKOGLUND, O.; LEANDER, J.; KAROUMI, R. Optimizing the steel girders in a high strength steel composite bridge. **Engineering Structures**, v. 221, n. February, p. 110981, 2020.

SONCK, D. **Global buckling of castelled and cellular steel beams and columns**. [s.l.] Ghent University, 2014.

SONCK, D.; BELIS, J. Lateral-torsional buckling resistance of cellular beams. **Journal of Constructional Steel Research**, v. 105, p. 119–128, 2015.

SONCK, D.; BELIS, J. Lateral-Torsional Buckling Resistance of Castellated Beams. **Journal of Structural Engineering**, v. 143, n. 3, p. 1–9, 2017.

SONCK, D.; BOISSONNADE, N.; VAN IMPE, R. Instabilities of cellular members loaded in bending or compression. **Structural Stability Research Council Annual Stability Conference 2012**, n. September 2014, p. 509–526, 2012.

SONCK, D.; IMPE, R. VAN; BELIS, J. Experimental investigation of residual stresses in steel cellular and castellated members. **Construction and Building Materials**, v. 54, p. 512–519, 2014.

SONG, A. *et al*. Residual deflection analysis in negative moment regions of steel-concrete composite beams under fatigue loading. **Construction and Building Materials**, v. 158, n. October 2017, p. 50–60, 2018.

SONG, C. Y.; TENG, J. G.; ROTTER, J. M. Imperfection sensitivity of thin elastic cylindrical shells subject to partial axial compression. **International Journal of Solids and Structures**, v. 41, p. 7155–7180, 2004.

SONG, Y. *et al*. Behaviour and design of stainless steel-concrete composite beam-to-column joints. **Journal of Constructional Steel Research**, v. 184, p. 106800, 2021.

SPOORENBERG, R. C. *et al*. Experimental investigation on residual stresses in heavy wide flange QST steel sections. **Journal of Constructional Steel Research**, v. 89, p. 63–74, 2013.

SPOORENBERG, R. C.; SNIJDER, H. H.; HOENDERKAMP, J. C. D. Experimental investigation of residual stresses in roller bent wide flange steel sections. **Journal of Constructional Steel Research**, v. 66, n. 6, p. 737–747, 2010.

SPOORENBERG, R. C.; SNIJDER, H. H.; HOENDERKAMP, J. C. D. Proposed residual stress model for roller bent steel wide flange sections. **Journal of Constructional Steel Research**, v. 67, n. 6, p. 992–1000, 2011.

STANDARD ASSOCIATION OF AUSTRALIA/STANDARD ASSOCIATION OF NEW ZEALAND. **AS/NZS 2327** COMPOSITE STRUCTURES - COMPOSITE STEEL CONCRETE CONSTRUCTION IN BUILDINGS. Sydney (Australia), 2017.

STANDARD ASSOCIATION OF AUSTRALIA/STANDARD ASSOCIATION OF NEW ZEALAND. **AS/NZS 3678** STRUCTURAL STEEL - HOT-ROLLED PLATES FLOORPLATES AND SLABS. **Sydney (Australia)**, 2016.

STANDARDS ASSOCIATION OF AUSTRALIA. **AS 4100 (R2016)** Steel structures. Sydney, Australia, 2016.

STANDARDS ASSOCIATION OF AUSTRALIA. **AS 4100 (R2020)** Steel structures. Sydney, Australia, 2020.

SUBRAMANIAN, L.; WHITE, D. W. Resolving the disconnects between lateral torsional buckling experimental tests, test simulations and design strength equations. **Journal of Constructional Steel Research**, v. 128, p. 321–334, 2017.

SVENSSON, S. E. Lateral buckling of beams analysed as elastically supported columns subject to a varying axial force. **Journal of Constructional Steel Research**, v. 5, n. 3, p. 179–193, 1985.

SZALAI, J.; PAPP, F. A new residual stress distribution for hot-rolled I-shaped sections. **Journal of Constructional Steel Research**, v. 61, n. 6, p. 845–861, 2005.

TANKOVA, T. *et al*. Experimental buckling behaviour of web tapered I-section steel columns. **Journal of Constructional Steel Research**, v. 147, p. 293–312, 2018a.

TANKOVA, T. *et al*. Experimental lateral-torsional buckling behaviour of web tapered I-section steel beams. **Engineering Structures**, v. 168, n. May, p. 355–370, 2018b.

TANKOVA, T. *et al*. Residual stresses in welded I section steel members. **Engineering Structures**, v. 197, n. May, p. 109398, 2019.

TANKOVA, T. *et al*. Lateral-torsional buckling of high strength steel beams: Experimental resistance. **Thin-Walled Structures**, v. 164, n. May, p. 107913, 2021.

TARAS, A. **Contribution to the development of consistent stability design rules for steel members**. TU Graz, 2010.

TARAS, A.; GREINER, R. New design curves for lateral-torsional buckling-Proposal based on a consistent derivation. **Journal of Constructional Steel Research**, v. 66, n. 5, p. 648–663, 2010.

TAŞ, S. *et al*. Effect of geometry on flexural behavior of optimal designed web-expanded beams. **Journal of Constructional Steel Research**, v. 215, n. December 2023, 2024.

TEBEDGE, N.; ALPSTEN, G.; TALL, L. Residual-stress measurement by the sectioning method. **Experimental Mechanics**, v. 13, n. 2, p. 88–96, 1973.

TOHIDI, S.; SHARIFI, Y. Neural networks for inelastic distortional buckling capacity assessment of steel I-beams. **Thin-Walled Structures**, v. 94, p. 359–371, 2015.

TONG, L. *et al*. Experimental investigation on mechanical behavior of steel-concrete composite beams under negative bending [in Chinese]. **Journal of Building Structures**, v. 35, n. 10, p. 1–10, 2014.

TONG, L. *et al*. Experiment and finite element analysis of bending behavior of high strength steel-UHPC composite beams. **Engineering Structures**, v. 266, n. February, p. 114594, 2022.

TONG, L. *et al*. Experimental and numerical study on residual stress distributions in welded H-sections of High-strength steel. **Advances in Structural Engineering**, v. 26, n. 12, p. 2248–2264, 2023.

TSAVDARIDIS, K. D.; MELLO, C. D. Web buckling study of the behaviour and strength of perforated steel beams with different novel web opening shapes. **Journal of Constructional Steel Research**, v. 67, n. 10, p. 1605–1620, 2011.

TSAVDARIDIS, K. D.; MELLO, C. D. Vierendeel Bending Study of Perforated Steel Beams with Various Novel Web Opening Shapes through Nonlinear Finite-Element Analyses. **Journal of Structural Engineering**, v. 138, n. October, p. 1214–1230, 2012.

TÜMER, M.; SCHNEIDER-BRÖSKAMP, C.; ENZINGER, N. Fusion welding of ultra-high strength structural steels – A review. **Journal of Manufacturing Processes**, v. 82, n. July, p. 203–229, 2022.

UNSWORTH, D.; DRIVER, R. G.; LI, L. Measurement and prediction of residual stresses in welded girders. **Journal of Constructional Steel Research**, v. 169, p. 106007, 2020.

VAROL, H.; CASHELL, K. A. Numerical modelling of high strength steel beams at elevated temperature. **Fire Safety Journal**, v. 89, n. February, p. 41–50, 2017.

VASDRAVELLIS, G. *et al*. Behaviour and design of composite beams subjected to negative bending and compression. **Journal of Constructional Steel Research**, v. 79, p. 34–47, 2012a.

VASDRAVELLIS, G. *et al*. The effects of axial tension on the hogging-moment regions of composite beams. **Journal of Constructional Steel Research**, v. 68, n. 1, p. 20–33, 2012b.

VELJKOVIC, M.; JOHANSSON, B. Design of hybrid steel girders. **Journal of Constructional Steel Research**, v. 60, n. 3–5, p. 535–547, 2004.

VIEIRA, W. B. **Numerical-experimental study of web-post buckling in steel castellated beams [in Portuguse]**. [s.l.] Federal University of Viçosa, 2015.

VILLALOBOS, J. C. *et al*. Microalloyed steels through history until 2018: Review of chemical composition, processing and hydrogen service. **Metals**, v. 8, n. 5, 2018.

VRCELJ, Z.; BRADFORD, M. A. Elastic Bubble Augmented Spline Finite Strip Method in Analysis of Continuous Composite Beams. **Australian Journal of Structural Engineering**, v. 7, n. 2, p. 75–84, 2007.

VRCELJ, Z.; BRADFORD, M. A. Inelastic restrained distortional buckling of continuous composite T-beams. **Journal of Constructional Steel Research**, v. 65, n. 4, p. 850–859, 2009.

WAN, Z. *et al*. Structural performance of steel–concrete composite beams with UHPC overlays under hogging moment. **Engineering Structures**, v. 270, n. September, p. 114866, 2022.

WANG, K. *et al*. Fully-scale test and analysis of fully dry-connected prefabricated steel-UHPC composite beam under hogging moments. **Engineering Structures**, v. 197, n. March, p. 109380, 2019.

WANG, W. *et al*. A Simplified Approach for Fire Resistance Design of High Strength Q460 Steel Beams Subjected to Non-uniform Temperature Distribution. **Fire Technology**, v. 54, n. 2, p. 437–460, 2018.

WANG, Y.-H. *et al*. Experimental study on assembled monolithic steel-prestressed concrete composite beam in negative moment. **Journal of Constructional Steel Research**, v. 167, n. February 2020, p. 105667, 2020.

WANG, Y. B.; LI, G. Q.; CHEN, S. W. Residual stresses in welded flame-cut high strength steel H-sections. **Journal of Constructional Steel Research**, v. 79, p. 159–165, 2012.

WANG, Y.; BRADFORD, M. A.; LIU, X. Strength design of welded high-strength steel beams considering coupled local and global buckling. **Thin-Walled Structures**, v. 149, n. August 2019, p. 106391, 2020.

WARD, J. K. **Design of composite and non-composite cellular beams**. [s.l.] Steel Construction Institute, Silwood Park, Ascot, UK, 1990.

WARREN, J. **Ultimate Load and Deflection Behaviour of Cellular Beams**. [s.l.] University of Natal, South Africa, 2001.

WEIDLICH, C. M.; SOTELINO, E. D.; CARDOSO, D. C. T. An application of the direct strength method to the design of castellated beams subject to flexure. **Engineering Structures**, v. 243, n. January, p. 112646, 2021.

WEN, C. *et al*. Influence of fibers on the mechanical properties and durability of ultra-high-performance concrete: A review. **Journal of Building Engineering**, v. 52, n. March, p. 104370, 2022.

WIJESIRI PATHIRANA, S. *et al*. Flexural behaviour of composite steel-concrete beams utilising blind bolt shear connectors. **Engineering Structures**, v. 114, p. 181–194, 2016.

WILLIAMS, F. W.; JEMAH, A. K. Buckling curves for elastically supported columns with varying axial force, to predict lateral buckling of beams. **Journal of Constructional Steel Research**, v. 7, n. 2, p. 133–147, 1987.

WU, F. *et al*. Comparative study of the negative bending behaviour of corrugated web steel – concrete composite beams using NC , ECC and UHPC. **Engineering Structures**, v. 283, n. March 2023, p. 115925, 2023.

XIONG, G. *et al*. Experimental and numerical studies on lateral torsional buckling of welded Q460GJ structural steel beams. **Engineering Structures**, v. 126, p. 1–14, 2016.

XIONG, G. *et al*. Lateral-torsional buckling behaviour of 690 MPa high strength steel beams. **Structures**, v. 33, n. July, p. 3999–4010, 2021.

XIONG, G. *et al*. Lateral–torsional buckling behaviour of welded Q690 steel I-beams with double lateral restraints along the length. **Thin-Walled Structures**, v. 170, n. November 2021, 2022.

XU, C. *et al*. Shrinkage effect and mechanical performance of steel-ultra-high performance concrete composite deck under negative bending action. **Engineering Structures**, v. 273, n. September, 2022a.

XU, Q. *et al*. Performance of large-diameter studs in thin ultra-high performance concrete slab. **Structures**, v. 34, n. November, p. 4936–4951, 2021.

XU, Q. *et al*. Shear behaviour and calculation model for stud-UHPC connections: Finite element and theoretical analyses. **Engineering Structures**, v. 254, n. November 2021, p. 113838, 2022b.

XU, Q. *et al*. Parametric Experimental Study of Ultra-Short Stud Connections for Lightweight Steel–UHPC Composite Bridges. **Journal of Bridge Engineering**, v. 27, n. 2, p. 1–13, 2022c.

XUHONG ZHOU *et al*. **Distortional buckling behavior and design consideration of castellated beams considering residual stresses**. Structural Stability Research Council Annual Stability Conference 2019, SSRC 2019. **Anais**...2019.

YAN, J. B. *et al*. Numerical studies on shear resistance of headed stud connectors in different concretes under Arctic low temperature. **Materials and Design**, v. 112, p. 184–196, 2016.

YAN, J. B.; LI, Z. X.; XIE, J. Numerical and parametric studies on steel-elastic concrete composite structures. **Journal of Constructional Steel Research**, v. 133, p. 84–96, 2017.

YAN, X. L. *et al*. Experimental and numerical investigation on flexural-torsional buckling of Q460 steel beams. **Journal of Constructional Steel Research**, v. 174, p. 106276, 2020.

YANG, B. *et al*. Residual stresses in welded I-shaped sections fabricated from Q460GJ structural steel plates. **Journal of Constructional Steel Research**, v. 122, p. 261–273, 2016.

YANG, B. *et al*. Experimental and numerical study on lateral-torsional buckling of singly symmetric Q460GJ steel I-shaped beams. **Thin-Walled Structures**, v. 113, n. January, p. 205–216, 2017.

YANG, B. *et al*. Global buckling investigation on laterally-unrestrained Q460GJ steel beams under three-point bending. **Engineering Structures**, v. 181, n. November 2018, p. 271–280, 2019.

YANG, Z. *et al*. Effect of fire exposure on residual stresses relief in welded high strength Q690 steel sections. **Journal of Constructional Steel Research**, v. 177, p. 106455, 2021.

YOUNG, B. W. Residual stresses in hot rolled members. **Proceedings IABSE Colloquium: On Column Strength.**, v. 23, p. 25–38, 1975.

YUN, X.; GARDNER, L. Stress-strain curves for hot-rolled steels. **Journal of Constructional Steel Research**, v. 133, p. 36–46, 2017.

ZAHER, O. F. *et al*. Structural behaviour of arched steel beams with cellular openings. **Journal of Constructional Steel Research**, v. 148, n. July 2018, p. 756–767, 2018.

ZEWUDIE, B. B. Nonlinear Finite Element Analysis and Comparison of In-Plane Strength of Circular and Parabolic Arched I-Section Cellular Steel Beam. **Advances in Civil Engineering**, v. 2022, n. August 2022, p. 13, 2022.

ZEYTINCI, B. M. *et al*. A practical design formulation for perforated beams with openings strengthened with ring type stiffeners subject to Vierendeel actions. **Journal of Building Engineering**, v. 43, n. June, 2021.

ZHANG, Y. *et al*. Flexural responses of steel-UHPC composite beams under hogging moment. **Engineering Structures**, v. 206, p. 110134, 2020.

ZHAO, Q. *et al*. Behavior and design of steel-UHPC composite beams subjected to negative moment. **Structures**, v. 57, n. August, 2023.

ZHOU, W.-B.; YAN, W.-J. Refined nonlinear finite element modelling towards ultimate bending moment calculation for concrete composite beams under negative moment. **Thin-Walled Structures**, v. 116, p. 201–211, 2017.

ZHOU, X. *et al*. Experimental investigation of the vertical shear performance of steel–concrete composite girders under negative moment. **Engineering Structures**, v. 228, n. November 2020, p. 111487, 2021.

ZHU, J. *et al*. Flexural Behavior of Steel–UHPC Composite Beams with Waffle Slabs under Hogging Moment. **Journal of Bridge Engineering**, v. 27, n. 11, p. 1–15, 2022.

ZHU, J. S. *et al*. Shear behaviour of steel-UHPC composite beams in waffle bridge deck. **Composite Structures**, v. 234, n. September 2019, p. 111678, 2020a.

ZHU, Y. *et al*. Flexural Study on UHPC–Steel Composite Beams with Joints under Negative Bending Moment. **Journal of Bridge Engineering**, v. 25, n. 10, p. 1–17, 2020b.

APPENDIX A
DEVELOPED ARTICLES

In parallel with the development of this thesis, a review paper and research articles have been published and written for journals and international conference proceedings. **Chart A.1** presents the references of the developed articles that compose the present thesis, which includes four published articles and one under development. Finally, **Charts A.2-A.3** show the related studies published in journals and international conference proceedings, respectively.

Chart A.1: **Summary of the developed articles that composes the thesis.**

1. Oliveira, V. M., Carvalho, A. S., Rossi, A., Ferreira, F. P. V. & Martins, C. H. (2023). *Elastic and inelastic analyses of composite cellular beams in hogging moment regions*. ***Thin-Walled Structures***, 184, 110513. https://doi.org/10.1016/j.tws.2022.110513.

2. Oliveira, V. M., Rossi, A., Ferreira, F. P. V., Carvalho, A. S. & Martins, C. H. (2023). *Lateral distortional buckling resistance predictions of composite alveolar beams: A review*. ***Buildings***, 13, 808. https://doi.org/10.3390/buildings13030808.

3. Oliveira, V. M., Prates, L. M. S., Rossi, A., Martins, J. P., Simões da Silva, L. A. P. & Martins, C. H. (2024). *Comparative analysis of geometric imperfections and residual stresses on the global stability behavior of cantilever composite alveolar beams*. ***Structures***, 65, 106634. https://doi.org/10.1016/j.istruc.2024.106634.

4. Oliveira, V. M., Santos, V. B., Rossi, A., Benedito, A. V., Krahl, P. A., Martins, C. H., Andrade Silva, F. & Cardoso, D. C. T. (2025). *Steel-UHPC composite castellated beams under hogging bending: Experimental and numerical investigation*. ***Engineering Structures***, 331, 120012. https://doi.org/10.1016/j.engstruct.2025.120012.

5. Oliveira, V. M., Santos, V. B., Rossi, A., Krahl, P. A., Martins, C. H., Andrade Silva, F. & Cardoso, D. C. T. *Stability and dematerialization of continuous composite beams using HSS castellated I-sections and UHPC slabs*. ***Thin-Walled Structures*** (in development).

Chart A.2: **Related studies published in journals.**

1. Oliveira, V. M., Prates, L. M. S., Christoforo, A. L., Martins, C. H., Rossi, A., & Ferreira, F. P. V. (2023). *Regression models for ultimate hogging moment prediction of composite cellular beams*. ***Australian Journal of Structural Engineering***. https://doi.org/10.1080/13287982.2023.2280275.

2. Oliveira, V. M., Carvalho, A. S., Rossi, A., Hosseinpour, M., Sharifi, Y. & Martins, C. H. (2024). *Data-driven design approach for the lateral-distortional buckling in steel-concrete composite cellular beams using machine learning models*. ***Structures***, 61, 106018. https://doi.org/10.1016/j.istruc.2024.106018.

Chart A.3: **Related studies published in international conference proceedings.**

1. Oliveira, V. M., Rossi, A., Santos, V. B., Krahl, P. A. & Martins, C. H. (2024). *The influence of different steel grades on the lateral-distortional buckling resistance of steel-concrete composite cellular beams*. **10th International Conference on Steel and Aluminium Structures (ICSAS24)**, Rio de Janeiro, Brazil, June 5-7. http://www.labciv.eng.uerj.br/icsas2024/index.php?menu=proceedings.

2. Martins, C. H., Oliveira, V. M., Prates, L. M. S., Rossi, A., & Ferreira, F. P. V. (2024). *Nonlinear finite element analysis of steel-concrete composite beams with cellular I-section under hogging moment*. **Proceedings of the joint XLVIbero-Latin-American Congress on Computational Methods in Engineering (CILAMCE-2024)**, ABMEC, Maceió, Brazil, November 11-14. https://publicacoes.softaliza.com.br/cilamce/article/view/10417.